APPLIED AND FUNDAMENTAL HETEROGENEOUS CATALYSIS STUDIES ON HYDRODECHLORINATION OF TRICHLOROETHYLENE AND STEAM REFORMING OF ETHANOL

DISSERTATION

Presented in Partial Fulfillment of the Requirements for the Degree

Doctor of Philosophy in the Graduate School of The Ohio State University

By

Hyuntae Sohn, M.S.

Graduate Program in Chemical Engineering

The Ohio State University

2016

- Dissertation Committee -

Prof. Umit S. Ozkan, Advisor

Prof. Andre Palmer

Prof. Lisa Hall

Prof. T.V. (Babu) RajanBabu

ABSTRACT

The dissertation herein reports heterogeneous catalysis studies conducted on two different projects, (1) Hydrodechlorination of trichloroethylene and (2) Ethanol steam reforming. The former is associated with the process for trichloroethylene waste treatment and groundwater remediation technology whereas the latter pertains to hydrogen production. The presented work involves not only investigations on the catalytic activity, but also fundamental studies to understand how and why a catalyst works for a particular reaction. This dissertation is composed of two major parts.

(1) Part I (Chapter 1-4): Trichloroethylene (TCE) is a chlorinated hydrocarbon solvent which has been widely used as a vapor degreaser for metal cleaning. TCE contains high level of toxicity, also known as a carcinogen. Recently, contamination of groundwater due to untreated TCE is a rapidly rising environmental issue, affecting the drinking water quality. The current waste treatment process for removal of TCE are mostly based on adsorption and extraction techniques. However, these processes do not provide a complete destruction of the TCE chemical structure; hence, it requires an additional incinerator to convert TCE into non harmful products.

Hydrodechlorination (HDC) of TCE is a catalytic chemical reaction where TCE is converted to ethane and hydrochloric acid using hydrogen as a reducing agent. The treatment is a single step process, also can be performed in situ in groundwater. The most

extensively used catalysts for this reaction are based on Pd metal. The main purpose of this study is to investigate the catalytic activity and stability of Pd supported on swellable organically modified silica (SOMS) for HDC of TCE. SOMS is a highly hydrophobic and adsorptive material. The material was recently developed and was reported in the literature. An interesting characteristic of SOMS is "swelling", i.e., the volume of SOMS expands while adsorbing organics. The expansion of SOMS leads to generation of new pores thereby increasing its pore volume and surface area. When SOMS is treated with heat, contraction of SOMS occurs resulting a decrease in volume to its original size. Another important characteristic is its high hydrophobicity.

It was deduced that Pd/SOMS showed promising catalytic activity compared to commercial Pd/Al_2O_3 in liquid phase HDC of TCE. This was attributed to the adsorptive and swelling properties of Pd/SOMS and its hydrophobicity, which helped to concentrate the TCE reactants in the vicinity of the active Pd sites. The increase in concentration near the active sites resulted in better kinetics for HDC reaction obtaining high TCE conversion. Furthermore, the strong hydrophobicity of SOMS helped to secure the Pd sites from ionic poisons such as sulfur and chlorine containing groups without losing its catalytic activity, e.g., when Pd/SOMS and Pd/Al_2O_3 was treated with 1 M HCl, Pd/SOMS retained its catalytic performance whereas Pd/Al_2O_3 was completely degraded because of Pd leaching under HDC of TCE conditions.

On the other hand, better catalytic activity was observed over Pd/Al_2O_3 compared to Pd/SOMS for gas phase HDC of TCE. It was found that the swelling of SOMS in gas phase, in other words, the expansion of the catalyst due to TCE vapors was not enough so that most of the embedded Pd sites were not accessible to the TCE reactants. To resolve

this issue, Pd was impregnated on a pre-calcined SOMS which was treated under inert condition at high temperatures (H-SOMS). With respect to Pd/H-SOMS, the Pd accessibility in gas phase to the TCE molecules were improved drastically. A significant increase in Pd dispersion as well as decreased in Pd particle size was observed. When tested for HDC of TCE activities, higher TCE conversions were obtained over Pd/H-SOMS catalyst compared to Pd/SOMS.

(1) Part II (Chapter 5-10): Hydrogen has been considered as the next alternative and renewable energy carrier that can be utilized for many industrial applications. The production of energy from hydrogen is typically conducted through a fuel cell, which only generates water as a product. Among many other hydrogen production processes, ethanol steam reforming (ESR), a catalytic chemical reaction, has gained a lot of attention since it provides a closed carbon loop cycle when ethanol is derived from environmentally friendly sources such as bio-mass. With respect to catalysts, noble metals such as Pt, Pd, Rh and Ru have been tested under ESR conditions and have shown excellent catalytic activities obtaining high hydrogen yield and ethanol conversion. However, noble metals are expensive thereby increase the overall operating cost.

In this dissertation, the catalytic performance and stability of non-noble metals such as Co supported on CeO_2 (cerium oxide) was investigated. According to the results obtained in our laboratory during the past decade, Co/CeO_2 with 10 wt % cobalt loading, had significant activity for ESR at relatively lower temperatures, around 350 to 600 °C. Some of the findings include 1) high oxygen mobility of CeO_2 reduces carbon deposition, 2) transition of Co_3O_4 to CoO and metallic Co was observed during steam reforming, 3)

reducibility of Co and surface activity, morphology and particle size of CeO_2 significantly influence the catalytic activity of Co/CeO_2 for ESR.

Herein, a detailed kinetic analysis to acquire activation energies of reduction and re-oxidation processes of cobalt was conducted. Moreover, reducibility of CeO_2 was studied in two different particle sizes where nano-sized CeO_2 contained more Ce^{3+} reduced sites compared to micro-sized CeO_2 both in bulk and surface of the catalyst under ESR conditions. The difference in extent of reduction of CeO_2 led to a more basic surface for nano-sized CeO_2 resulting better catalytic activity for ESR. When cobalt was present on the catalyst surface (Co/CeO_2), the oxidation state of Ce was lower in comparison to a bare CeO_2 support under same reaction conditions. This was attributed to the reduction of cobalt taking precedence over the reduction of CeO_2. Lastly, the effect of microgravity on synthesis of CeO_2 was studied. It was found that CeO_2 prepared in microgravity consists lower surface area and pore volume compared to the CeO_2 prepared in normal-gravity. A significant difference in particle shape was observed where microgravity-CeO_2 was more like rods whereas normal-gravity-CeO_2 contained polyhedral particles.

Dedication

To my parents and my grumpy sister.

ACKNOWLEDGMENTS

I have worked as an undergraduate research assistant as well as a Ph.D. graduate student with Dr. Ozkan for seven years. It has been a long time, but during those days, there was not a single moment that made me regret my decision. I was a very lucky person to have Dr. Ozkan as my advisor. I really appreciate Dr. Ozkan who has continuously encouraged and supported me along my journey not only related to research but also my personal life. I always have enjoyed having a discussion with Dr. Ozkan whenever I was frustrated reaching a dead end in my research. Your guidance has always let me see the light at the end of this tunnel. I will always remember the inspiration you provided for me. Thank you!

It is a pleasure for me to thank Ilgaz Ibrahim Soykal who was a senior researcher, a mentor, and a great friend. He taught me all the basics of heterogeneous catalysis research and also showed me how to level up faster in World of Warcraft. We have published six papers together so what can I say more. He was the most hard-working and intelligent graduate student I have ever met. I would like to thank the SOMS research group, especially Dr. Edmiston who actually brought the idea of using Pd/SOMS for groundwater remediation technology. Without your support and tremendous contribution to the project, this dissertation would not have been possible. Also, thanks to Gokhan, Seval and Saruabh who will continue to push this project forward for the future. I am indebted to all my colleagues especially Sreshtha and Gokhan who had to listen to my singing of "I love you baby~, not Sreshtha" by Frank Sinatra for 5 years. I like both of you guys equally? Katja who taught me English slang, Kuldeep (carbon man), Seval and Doruk who came from Turkey and etc. people (Deeksha, Saurabh and Dhruba - who have just begun their descent into darkness). I owe you all for the great ideas that you guys provided me.

Finally, and most importantly, I love my family a lot, I have no space to write abou

VITA

September 18, 1984 .....Born, Seoul, Republic of Korea (South)

August, 2011 .....B.S. Chemical Engineering
The Ohio State University, Columbus, OH

December, 2014 .....M.S. Chemical Engineering
The Ohio State University, Columbus, OH

August, 2011 to Present .....Ph.D. Graduate Research Associate
Chemical Engineering
The Ohio State University, Columbus, OH

PUBLICATIONS

1. **Sohn, H**.; Celik, G.; Gunduz, S.; Majumdar, S. S.; Dean, S. L.; Edmiston, P.; Ozkan, U. S., Effect of High-temperature-treated Swellable Organically-Modified Silica (H-SOMS) and Its Application to Gas-Phase Hydrodechlorination of Trichloroethylene. *Manuscript in Preparation*

2. **Sohn, H**.; Celik, G.; Gunduz, S.; Shan, J.; Tao, F.; Miller, J. T.; Ozkan, U. S., *in situ* AP-XPS studies over cobalt supported on nano-ceria under ethanol steam reforming conditions. *Manuscript in Preparation*

3. **Sohn, H**.; Celik, G.; Gunduz, S.; Dean, S. L.; Painting, E.; Edmiston, P.; Ozkan, U. S., Hydrodechlorination of Trichloroethylene over Swellable Organically-Modified Silica (SOMS). *Submitted to Applied Catalysis B: Environmental*

4. **Sohn, H**.; Soykal, I. I.; Zhang, S.; Shan, J.; Tao, F.; Miller, J. T.; Ozkan, U. S., Effect of Cobalt on Reduction Characteristics of Ceria under Ethanol Steam Reforming Conditions: AP-XPS and XANES Studies. The Journal of Physical Chemistry C 2016. *June-Published*

5. **Sohn, H**.; Ozkan, U. S., Cobalt-Based Catalysts for Ethanol Steam Reforming: An Overview. Energy & Fuels 2016. *April-Published*

6. Soykal, I. I.; **Sohn, H**.; Bayram, B.; Gawade, P.; Snyder, M.; Levine, S.; Oz, H.; Ozkan, U., Effect of Microgravity on Synthesis of Nano Ceria. Catalysts 2015, 5 (3), 1306-1320.

7. Soykal, I. I.; **Sohn, H**.; Singh, D.; Miller, J. T.; Ozkan, U. S., Reduction Characteristics of Ceria under Ethanol Steam Reforming Conditions: Effect of the Particle Size. ACS Catalysis 2014, 4 (2), 585-592.

8. Soykal, I. I.; **Sohn, H**.; Miller, J. T.; Ozkan, U. S., Investigation of the Reduction/Oxidation Behavior of Cobalt Supported on Nano-ceria. Topics in Catalysis 2013, 57 (6-9), 785-795.

9. Soykal, I. I.; **Sohn, H**.; Ozkan, U. S., Effect of Support Particle Size in Steam Reforming of Ethanol over Co/CeO_2 Catalysts. ACS Catalysis 2012, 2 (11), 2335-2348.

10. Soykal, I. I.; Bayram, B.; **Sohn, H**.; Gawade, P.; Miller, J. T.; Ozkan, U. S., Ethanol steam reforming over Co/CeO_2 catalysts: Investigation of the effect of ceria morphology. Applied Catalysis A: General 2012, 449, 47-58.

FIELDS OF STUDY

Major Field: Chemical Engineering

Specialization: Heterogeneous Catalysis

TABLES OF CONTENTS

LIST OF TABLES

LIST OF FIGURES

PART I

HYDRODECHLORINATION OF TRICHLOROETHYLENE

CHAPTER 1

INTRODUCTION

1.1 Chlorinated Hydrocarbons (CHCs)

Chlorinated organic substances have been widely used for various industrial applications in the Unites States. For example, chlorofluorocarbons (CFCs), which were banned in 1970s, were heavily used as refrigerants until researchers found that it causes ozone depletion. Another example can be chlorinated hydrocarbons (CHCs) such as polychlorinated biphenyls (PCBs) that were used as heat transfer fluids and dielectric fluids. The utilization of PCBs was also prohibited in the United States because of its deleterious impact on environment and health. Other CHCs such as tetrachloroethylene (TTCE/PCE), trichloroethylene (TCE), 1,1,1-trichloroethane (TCA), tetrachloride (CTC), chloroform (CLF), dichloromethane (DCM) are still being used primarily as metal degreasers, either in liquid or vapor phase, under stringent regulations stipulated by the U. S. Environmental Protection Agency (EPA).

Chlorinated compounds were used initially as dry-cleaning agents in early 1900s.[1] In those times, the industry of synthetic organic chemistry had not been established well in the United States, thus all chemicals were imported from European countries.[1] However, throughout World War I, the difficulty in importing the chemicals and raw materials from

Europe had risen, therefore the government recognized the significance of having chemical production facilities in the United States.[1] Although the outcome of World War I affected the appearance of major producers of chlorinated compounds, the supply of these chemicals were still in deficiency because of the high domestic demand.[1] Moreover, during World War II, chlorinated solvents such as TTCE, TCE and ethylene dichloride was assigned as first priority for military uses by the priorities of the United States Office of Production Management.[1] For these reasons, major manufacturers such as Dow Chemical, dupont, and Warner-Klipstein chemical companies increased their production of chlorinated solvents continuously and substantially.[1]

Currently, the reason for rigorously enforced regulations on the production and utilization of chlorinated compounds is that most of them are carcinogens. For instance, the recent toxicological review for TCE by the U.S. EPA states that TCE may cause kidney and liver cancer.[2] Likewise, the human exposure to TTCE and DCM is likely associated with bladder cancer, and kidney and lung cancer, respectively.[3] Most of the aforementioned chlorinated compounds are highly active as carcinogens. In addition to that, the contribution of gas phase CHCs to smog formation and global warming has been reported.[4] Therefore, an appropriate CHC waste treatment system is essential and important to protect the environment and public health.

CHCs typically have low boiling points and high vapor pressures. Although CHCs mainly exist as liquids at room temperature, they are still very volatile. Moreover, the solubility of CHCs in water is fairly low. Therefore, when considering these chlorinated organic wastes, emitted from industrial facilities such as vapor degreasing, metal finishing

and textile cleaning sites, the treatment of waste CHCs should be considered in both liquid and gas phase.

The conventional technique to treat chlorinated effluent gases at industrial plants is absorption using activated carbon followed by a thermal incineration at very high temperatures.[5] Since chlorinated compounds are molecularly stable, thermal destruction of CHCs requires temperatures above 1000 ℃, which significantly increases the overall operating cost.[6] Additional cost to regenerate the used activated carbons at temperatures above 700 ℃, is another factor that makes the process economically unfeasible. Also, incomplete combustion of CHCs in the incinerator leads to toxic by-products such as dioxins and PCBs.[7]

Alternative treatment processes such as catalytic oxidation and steam reforming of CHCs have been investigated.[7-8] However, it was reported that the partial oxidation of CHCs generated hazardous by-products such as $COCl_2$ and Cl_2. For steam reforming process, high reaction temperature is desired to convert CHCs into hydrogen and carbon dioxide. Other methods such as bio-filtration and membrane-filtration are not effective.[9]

With respect to chlorinated solvents in liquid phase, the general waste treatment methods are somewhat similar to gas phase in which an incinerator is utilized. The chlorinated waste solvents require more careful control due to the direct influence on human health issues through groundwater contamination. In the past, before the U.S. EPA was founded, these greatly concentrated CHC liquid wastes were not handled properly. Some of them were just spilled on the ground or illegally disposed to the rivers. Also incidents such as leaking storage tanks and sewer pipelines were a part of the environmental release of hazardous CHCs. Eventually, these untreated CHC solvents

infiltrated deeper into the groundwater level and contaminated the most useful drinking water source in the United States. The groundwater contamination due to chlorinated compounds is regarded as a long-term environmental issue due to its high volatility, e.g., CHC vapors which are vaporized from groundwater remain in the unsaturated zone.[10] Surprisingly, although it has been almost 30 years since the U.S. EPA regulated CHC emissions as well as the production rate, ground water contamination due to chlorinated compounds is an on-going environmental issue even now. For example, according to the U. S. geological survey,[11] among 51 volatile organic compounds (VOCs) detected in ground and drinking water, chlorinated solvents were the most frequently found contaminants at high concentrations.

A variety of groundwater remediation techniques are being employed nowadays. Although most methods lead to promising results, different remedial approaches have their own benefits and drawbacks. In here, four of the most popular pilot-scale groundwater treatment technologies are discussed:[12] (1) air stripping, (2) soil venting, (3) in-well aeration, (4) bioremediation.

Air stripping is a method in which a continuous flow of air is used to evaporate a particular liquid component from a solvent mixture.[12] The principle behind is closely related to the low water-solubility and high vapor pressure of CHCs. However, the exhausted air from this process contains toxic CHC vapors, thus, further treatment is needed before releasing the vapor mixture to the atmosphere. This can be done in combination with activated carbon (AC) adsorption after air stripping,[13] which is widely used in the industry. The process is cost effective and an appropriate way to remove contaminants from groundwater, especially for CHCs that are quite insoluble in water.

A similar approach is soil venting. Soil vapor extraction is an *in situ* air stripping process to remove large amounts of CHCs in the underground unsaturated zone.[12] As mentioned before, the vaporized CHCs exist in the subsurface soil above the groundwater level (unsaturated zone). When a pressurized air stream is injected to this area, the CHC vapors are collected by several extraction wells located underground, and delivered to a secondary vapor treatment system. One disadvantage of this technique is that the permeability of soil to air may drastically hinder the performance.

In-well aeration falls into the same category with the methods explained above.[14] However, a difference is that the vertical well is located in between the upper unsaturated zone and the lower saturated zone where groundwater is present. As air is injected into the vertical well, the aerated groundwater is circulated with oxygen, thus, volatile contaminants start to arise as vapors, whereas water is forced back into the saturated zone. The process is repeated continuously using a hydraulic circulation system resulting a rapid minimization of contaminant concentration.

As all three examples are more associated with extraction and absorption, bioremediation is a biological method where microorganisms are used to destroy contaminants in groundwater and degrade CHCs into nontoxic species. More importantly, the feasibility of complete transformation of CHCs into CO_2, water and other harmless microscopic organisms, is very attractive.[12] However, the efficiency and reaction rate of bioremediation strongly depends on how fast the microorganisms grow and how effectively they can react with various contaminants in groundwater.[15] Moreover, undesired products such as chlorine-based compounds might exist after treatment. Therefore, more research is needed in this area.

Until now, air stripping is known as the most cost-effective and efficient process.[12] However, in any case, further treatment on the collected CHC vapors is necessary; which is predominantly incineration today. Hence, alternative remediation method is strongly recommended. The process ought to be: (1) environmentally clean - minimal production of toxins, (2) economically viable - fast reaction rate at low temperature and pressure and (3) efficient - complete destruction of the reactants with high conversion and selectivity. Herein, the proposed technique is catalytic hydrodechlorination (HDC), which has been known as a popular methodology to eliminate chlorinated compounds in both liquid and gas phase. This process involves hydrogen and metal-based catalysts which significantly increase the reaction rate and reduce toxic by-products by lowering the activation energy. Moreover, it leads to a complete destruction of chlorinated compounds so that no further treatment is needed.

1.2 Swellable Organically-Modified Silica (SOMS)

The motivation of this study is to use a highly hydrophobic support, thereby enhancing the resistance to catalyst deactivation. The proposed material has never been studied or characterized as a catalyst scaffold. There have been only four publications in the literature with respect to the material but mostly on its chemical properties. It is our intention to use this material as an alternative support for metal-based catalysts thereby obtaining better catalytic stability and activity for HDC reactions. The technical name of the material is “swellable organically modified silica (SOMS)”, which is commercialized

by ABS material Inc. The company was co-founded by Professor. Edmiston in Wooster College, OH. The commercialized name for SOMS is called “Osorb”.

SOMS is basically synthesized by a sol-gel synthesis method.[16] A detailed synthesis procedure is provided in Chapter 3.2.1 and Appendix D. The special characteristics of SOMS can be divided into three. First, SOMS is a very hydrophobic and adsorptive material. It adsorbs all kinds of organic molecules but repels water. In a recent study from Edmiston’s group,[17] it was shown that the SOMS adsorbs both polar and non-polar organics, whereas activated carbon, which is the most widely used adsorbent, tends to adsorb only non-polar molecules. The adsorbing capacity of SOMS was investigated on various organic solvents such as PCE, TCE, toluene, methyl t-butyl ether (MTBE), acetone, naphthalene, and 1- butanol, dissolved in water. The results showed that SOMS was capable of adsorbing all the samples in the range of extraction percentages between 20-99%. Almost complete removal of PCE and toluene and a 92 % of TCE extraction were achieved using 120 ppm solution.[17]

Another interesting aspect of SOMS is that while it adsorbs organic molecules, the volume of SOMS expands more than 6 times of its original size.[18] In other words, SOMS physically takes the organics into its structure, as a consequence, the material mechanically expands. It is found that the swelling phenomena creates extra surface areas and pores thereby increasing the adsorption capacity as well as the pore volumes. Besides, the swelling generates forces more than 100 N/g.[18] Figure 1 shows the swelling process when acetone was added drop-wise to SOMS.

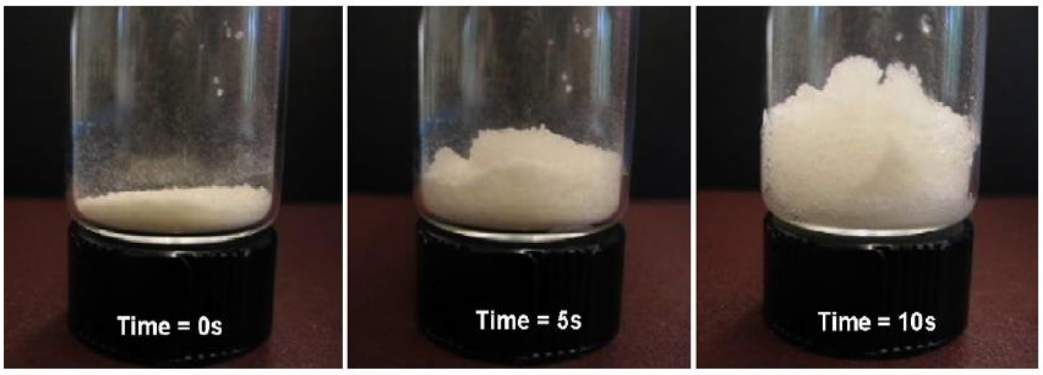

Figure 1. Swelling process of Osorb[17] *(cited from "Edmiston, P. L.; Underwood, L. A., Absorption of dissolved organic species from water using organically modified silica that swells. Sep. Purif. Technol. 2009, 66, 532-540.")*

Lastly, the adsorbed molecules can be easily removed through evaporation. This aspect is significantly advantageous compared to activated carbon which requires temperature above 700 ℃ for regeneration. Also, interestingly, the swelling is reversible, therefore releasing of the adsorbed organics from SOMS leads to a decrease in volume returning to its original size.

Due to its exceptional characteristics, the utilization of SOMS can be applicable in many different industries. Today, ABS materials Inc. is predominantly using SOMS as an adsorbent for drinking water and waste water treatment systems. For example, bio-modified SOMS is installed near the sewer drain thereby removing the toxins before they enter the sewer system. The bio-related functionality is there to accelerate plant growth regardless of the amount of pollutants passing through it. This material can be incorporated with rain gardens especially in the cities. Not only as an adsorbent, but also SOMS was tested for *in situ* groundwater treatment. The type of SOMS employed for this application

is Iron-SOMS where a trace amount of Pd was mixed with nano-scale zerovalent iron (ZVI) and placed on the SOMS support.[19] Edmiston and coworkers transported Iron-SOMS using an injection drill all the way down to at least 20 feet from the ground. The results indicated that Iron-SOMS was effective to treat TCE contaminant in groundwater for more than 120 days. However, partially dechlorinated products were observed which is likely attributed to the slow kinetics of the HDC reaction.

** Information in this chapter was partially reproduced/adapted from " Sohn, H.; Celik, G.; Gunduz, S.; Dean, S. L.; Painting, E.; Edmiston, P.; Ozkan, U. S., Hydrodechlorination of Trichloroethylene over Swellable Organically-Modified Silica (SOMS). Submitted to Applied Catalysis B: Environmental"*

CHAPTER 2

LITERATURE REVIEW

2.1 Pd-Based Catalysts

Hydrodechlorination (HDC) of chlorinated compounds using catalysts has been gaining a lot of attention from many different journals since the late 1970s. The process involves hydrogen as a reducing agent and mostly heterogeneous metal-based catalysts to accelerate the dechlorination reaction at moderate temperatures and pressures. The reaction has been found to be slightly exothermic. Lots of chlorinated compounds such as TTCE, TCE, CTC, TCA and PCBs have been extensively studied for their implications on HDC reaction either in liquid or gas phase. In this study, the literature review was done mostly focusing on trichloroethylene (TCE) that has been extensively studied. Figure 2 describes the chemical structure of TCE and its corresponding HDC reaction. As it can be seen, the reaction produces hydrogen chloride and ethane as major products. Hydrogen chloride could be easily removed after reaction by neutralization using NaOH. However, intermediate products such as 1,1 dichloroethylene (DCE), 1,2 cis-DCE, 1,2 trans-DCE and vinyl chloride (VC) can also be detected in notable amounts due to partial dechlorination. Among various precious metals, a consensus has been reached in the literature that Pd metal-based catalysts have exhibited promising catalytic activity for HDC

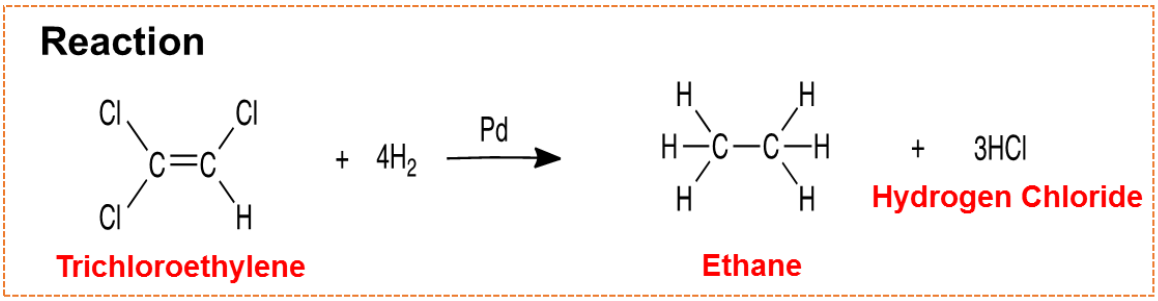

Figure 2. Hydrodechlorination of Trichloroethylene (TCE)

of TCE.[20] Commonly, palladium metal (Pd) is known as a good hydrogenation initiator where its catalyst surface favors dissociation of hydrogen molecules into chemisorbed surface hydrogen atoms. Since the catalytic HDC is a surface-mediated reaction, the surface hydrogen participates in cleavage of C-Cl bond of chlorinated compounds by substituting Cl to H atom. For this reason, Pd supported catalysts have also been frequently employed for removal of C-F, C-Br and C-I bonds as hydrodehalogenation catalysts.[21]

First of all, Ordóñez and Diez's group in University of Oviedo (Spain) have conducted quite a lot of work on exploring the catalytic activity and stability of Pd supported on Al_2O_3 on HDC of chlorinated compounds.[20, 22-28] In one of their early studies in 2000, eight different commercial catalysts including noble metals such as Pd, Pt, Rh and Ru impregnated on either alumina or activated carbon were tested for their catalyst activity on HDC of TTCE and TCE. The reaction was carried out in gas phase at 50 bar and 300 ℃.[23] The conclusion was that both Pt and Pd catalyst similarly showed high conversion of more than 90%. Later on, the authors performed a follow-up study on Pt and Pd supported on activated carbon with a 0.5% metal loading for HDC of TTCE in a continuous fixed bed reactor under reaction conditions of 250 ℃ and 5 bar.[25] Results indicated that

the Pd catalyst demonstrated better catalytic activity and stability due to high resistance from catalyst deactivation such as coking when compared to the Pt based catalyst.

Reinhard and colleagues in Stanford University have proposed similar works on Pd based catalysts for HDC of chlorinated hydrocarbons such as TCE, TTCE and DCEs in aqueous phase.[29-33] For example, two commercially available catalysts, 1% Pd/Al_2O_3 and Pd black powder were tested for TCE HDC. 97% TCE conversion was obtained over Pd/Al_2O_3 while ethane and HCl were detected as the only products. The reaction was performed at ambient temperature and pressure with much diluted TCE.[29] In another recent study of theirs in 2008,[33] authors presented an *ex-situ* catalytic reductive dechlorination (CRD) system which was tested in a real contaminated site located in the Edwards air force base in Southern California. The CRD system consisted of a pilot-scale fixed bed reactor combined with a hydrogen feed and catalyst regeneration system. The contaminated groundwater was pumped above ground, rinsed and bleached, then introduced to the reactor where Pd catalyst bed was located. Results indicate that more than 99% of TCE was removed constantly during 100 days of operation time.

Reducing the metal particle size to nanometer range has been considered as a suitable way to enhance the catalyst performance. The increase in catalytic activity has been attributed to: (1) increase in metal surface area (2) higher dispersion of metal particles which increases the exposed surface active sites (3) less mass transfer limitation to the catalyst pores. However, catalyst sintering is problematic because metal nanoparticles tend to agglomerate to larger size particles under actual reaction conditions, especially in groundwater. Therefore, Pd capping agents that allow immobilization of Pd nanoparticles on the catalyst surface such as sodium carboxymethyl cellulose (CMC) has been

investigated.[34-37] Liu et al.[34] performed a comparative study for 0.15 wt.% CMC stabilized Pd nanoparticles, 0.15 wt.% glucose capped Pd, and neat Pd black nanoparticles on liquid phase TCE HDC. The addition of CMC stabilizer to Pd nanoparticles indicated high catalytic activity towards TCE conversion due to increase in Pd metal dispersion on the catalyst surface. Another study from Zhang et al.[35] also showed that 0.33 wt. % CMC-Pd nanoparticles over Al_2O_3 support was 7.3 times active than the commercial Pd/Al_2O_3 for liquid phase HDC of TCE.

To the best of our knowledge, Pd supported on gold (Au) nanoparticles has exhibited the highest reaction rate on TCE dechlorination in the literature. Nutt and coworkers were the first group who impregnated Pd on Au nanoparticles in different Pd metal loadings from 1% to 35%.[38-39] A comparison was mainly made between Pd black powders, Pd/Al_2O_3, Pd nanoparticles and Pd/Au nanoparticles, but other forms such as Au/Al_2O_3, $Au/Pd/Al_2O_3$ and $Pd/Au/Al_2O_3$ were also examined for their overall catalytic activity. The results exhibited that Pd/Au nanoparticles were significantly more active than any other catalysts under aqueous phase HDC of TCE at atmospheric pressure and temperature. The rate constant obtained from the experiment was more than 70 times higher than the commercially available Pd/Al_2O_3 catalysts. They explained that this is probably due to a combination of electronic and geometric effect of Pd and Au nanoparticles. Since then, the utilization of Pd/Au NP for HDC of TCE has been acknowledged in the literature, and more studies on Pd/Au nanoparticles in terms of DFT calculation,[40] bio-modification[41] and activity comparison to other catalysts[42] have been conducted.

There are three major limitations that make catalytic hydrodechlorination process less practical for pilot-scale ground water remediation as well as chlorinated waste treatment applications. First, the cost of Pd metal is very expensive. Using 1 wt. % Pd metal loading seems reasonable for bench scale experiments; however, when it is scaled-up to industrial size which uses several kilograms of Pd metal, the operating cost increases tremendously. Secondly, storage and transportation of hydrogen is difficult for some contaminated sites. Safety issue can be a huge concern due to high flammability of hydrogen, which may lead to explosions under careless maintenance. Lastly and most importantly, the extent of catalyst deactivation is severe which degrades the activity significantly. This is due to several causes such as chlorine and sulfur poisoning and catalyst coking.[20]

To reduce the operational cost, non-noble metals have been tested for their implications on catalyst activity under HDC TCE conditions. This is to either substitute Pd metal or for use as a reducing agent to replace hydrogen. For example, studies on zero valent iron (ZVI) has been well documented for *in situ* groundwater remediation as it can act as electron donor to produce hydrogen from water.[43-44] The overall dechlorination reaction is described in the following equations where R is alkyl group.

$$Fe^0 + 2H_2O \rightarrow Fe^{2+} + H_2 + 2OH^-$$

$$R\text{-}Cl + Fe^0 + H^+ \rightarrow RH + Fe^{2+} + Cl^-$$

However, it has been reported that ZVI itself is not very effective for HDC TCE showing very slow reaction rates. Thus to enhance the reaction kinetics, a trace amount of Pd was utilized as the second dopant metal which increased the overall catalytic activity.[45]

For example, Lin et al. tested iron supported noble metals such as Pd, Ru, Pt and Au for TCE HDC.[46] The reaction was in aqueous phase in absence of hydrogen gas at room temperature and pressure. 1000 mg/L of TCE was completely removed from the solution using 0.25% Pd/Fe within 20 minutes of reaction. Pd/Fe has been also extensively studied for hydrodechorination of PCBs,[47] dichlorophenol,[48] chlorobenzens[49] and chlorinated methane[50] in aqueous phase. Another non-noble metal that has been well investigated for ZVI based catalysts is Nickel (Ni). Similar to Pd metal, Ni is also known as a good hydrogenation metal which is capable of dissociating hydrogen into chemisorbed surface hydrogen.[51] In the literature, a consensus has been reached that Ni and Pd act as catalyst whereas Fe and Zn are employed as reducing agents.[52-53] Thus, Ni/Fe has been extensively studied as alternative catalysts to replace Pd/Fe for ground water remediation process. Several researches have been proposed that Ni/Fe have shown reasonable catalytic activity for liquid phase TCE HDC.[53-55]

The implementation of a bimetallic catalytic system often changes the mechanism due to modification of electronic inter-relation between two metals and catalyst surface structure. Therefore, including ethane, the unique characteristic of bimetallic catalysts is that they can also create hydrocarbons such as propane, butane, hexane and octane resulting from HDC of TCE over Pd/Fe and Ni/Fe catalysts.[52, 56] Schrick et al.[52] studied Ni/Fe catalysts for HDC of TCE and found out that hydrocarbon products with even number of carbons were formed during reaction along with ethane. The production of hydrocarbons can be due to the formation of methyl and ethyl radicals resulting from C-C bond scission on Pd catalyst. These radicals then float around on the catalyst surface and likely bind to excess surface hydrogen generating C_2-C_4 alkanes.[57] Not only can the formation of

hydrocarbons, but also valuable olefins such as ethylene be produced. Pt/Cu,[58] Pt/Sn,[59] Pd/Ag,[60] Pd/NiMgAl,[61] PdCu alloy[62] and Pt and Pd contacting Cu-hydrotalcite[63] have shown selectivity towards ethylene under HDC of TCE reaction conditions. Meshesha and coworkers have observed close to 100% ethylene selectivity which was obtained at 300 ℃ using PdCu alloy nanoparticles supported over Al_2O_3.[62]

Several additional techniques have been implemented to make the HDC process more economical. The latest employed method could be microwave heating that has been presented as an alternative way to heat the reactor up to desired reaction temperature of TCE HDC.[64-66] This technology is environmentally clean and involves less operational costs compared to other heating sources. In addition, alternative organic hydrogen donors have been explored such as 2-propanol,[67] humic acid[68] and formic acid[69-70] in liquid phase HDC reactions. These organic solvents not only provide a hydrogen source, but also slightly enhance the kinetic rate of HDC. Moreover, cathodic hydrogen produced using electrolytic cell has been stated in the literature.[71]

2.2 Catalyst Deactivation

The catalyst deactivation is a crucial aspect to be taken into account for HDC processes. This is because the degradation of catalyst is directly related to the catalytic activity, stability and durability. Regarding the HDC reactions, there have been four major deactivation sources found for Pd metal-based catalysts. These are as follow: (i) chloride poisoning (ii) catalyst coking (carbon deposition) (iii) sulfide poisoning and (iv) bicarbonate poisoning.

Chloride poisoning and catalyst coking is unavoidable since it is driven from the HDC reaction itself. Through the C-Cl and C-C bond cleavage of the chlorinated reactants, it generates carbons and chloride radicals on the catalyst surface, which predominantly interacts with Pd active sites. Deposited carbons can cause physical fouling due to blockage of active sites which decrease the accessibility of the Pd metal to the reactants. Likewise, hydrogen chloride and chloride ions could cause significant degradation of the catalysts activity and stability. Numerous papers have indicated the inhibition effect of chloride poisoning during HDC reactions.[15, 20, 27, 51, 63, 72] This can be attributed to the stabilization of Pd^{+2} species on the catalyst surface by chlorine ions, which is not a preferred oxidation state for high catalytic activity for HDC reactions. It should be noted that metal phase Pd^{0} is more active than its oxidized form of Pd^{+2} for TCE HDC reaction. Ordóñez and coworkers performed a XPS analysis on fresh and used Pd based catalysts and compared the Pd^{+2}/Pd ratio between the two.[20] The results indicate that this ratio was increased from 0.3 to 0.75 after the catalysts were used for HDC of TCE in liquid phase. The oxidation of Pd^{0} to Pd^{+2} is not thermodynamically favorable under rich hydrogen environment, thus the conclusion was that released chloride ions stabilize initial Pd^{+2} by forming $PdCl^{3-}$ and $PdCl_4^{2-}$ and stimulates the oxidation by surface protons.[20]

With respect to *in situ* HDC in groundwater, deactivation sources vary a lot because of different impurities dissolved in water. Among them, sulfur-containing groups such as sulfates have expressed significant effect on the deactivation of the catalyst.[22, 26, 33, 71] This can occur through a reduction of sulfate species to hydrogen sulfide by sulfate-reducing bacteria.[33] Hydrogen sulfide and even bisulfide that are often dissolved in water form a thin layer on the Pd sites and inhibit the reaction.[32]

$$SO_4^{2-} + 4H_2 \rightarrow HS^- + OH^- + 3H_2O$$

$$Pd + HS^- + H_2O \rightarrow \mathbf{Pd\text{-}S} + H_2 + bOH^- \text{ (b is constant)}$$

$$Pd + H_2S \rightarrow \mathbf{Pd\text{-}S} + H_2$$

Another ionic molecule that degrades the catalyst performance is bicarbonate.[30] This is because conversion of bicarbonate to formates is feasible over Pd catalysts with hydrogen. The reaction is shown in equation. Therefore, the reaction competes with HDC and eventually slows down the HDC reaction rate.

$$HCO_3^- + H_2 \rightarrow HCO_3^- + H_2O$$

To overcome all the obstacles mentioned above, using different supports is a good methodology in general. For example, the interaction between metal and support oxides can make the active sites more resistant to coking. This is attributed to the abundance of oxygen on the catalyst surface, which diffuses from the support through oxygen vacancies. Yuan and Keane have shown that Pd supported on Al_2O_3 was more coke resistant than supported on activated carbon for HDC of 2,4-dichlorophenol.[73] Barrabés et al. investigated Pt/CeO_2, which is another well-known support for its high oxygen mobility, for HDC of TCE.[74-75] Interestingly, the results express higher selectivity towards ethylene than ethane. Authors established that this is probably because of oxygen vacancies that showed activity for scission of C-Cl bond by forming Ce-O-Cl phase.

Modification of support acidity and basicity are known to alleviate deactivation from chloride poisoning. Ordóñez et al. suggested that the more acidic the support is, the more the affinity towards chloride ions.[20] Having more surface chlorides lead to high chance of forming Pd-Cl bonds, which eventually oxidizes Pd^0 to Pd^{+2}, thus decreases the

catalyst performance drastically. Their results indicated that Al_2O_3, which is more acidic, showed faster deactivation than activated carbon for TCE HDC.

In order to minimize the contact between Pd metal and poisons such as chloride and sulfide-containing species, coating materials such as poly dimethylsiloxane (PDMS) have been developed.[76-77] This is to enhance the hydrophobicity of the catalysts thereby repelling ionic poisons dissolved in groundwater. However, an associated issue is that hydrogen chloride produced from the HDC reaction degrades the polymers.

Finally, regarding the mechanism of TCE HDC, it follows a Langnuir-Hinshelwood mechanism where a series of chlorine atoms are eliminated by addition of hydrogen.[40, 78] The dechlorination rate is proportional to the number of chlorine atoms present in the compound, thus the reaction rate for less chlorinated compounds such as DCE and VC is slower than TCE. The rate-limiting step for HDC of TCE is still disputed. One assertion is that the addition of hydrogen to double bond is the rate-limiting step and C-Cl cleavage occurs later.[40] Another argument is that cleavage of the first C-Cl bond by Pd is the rate-determining step.[79] The most reasonable statement is that the rate-limiting step is the electron transfer to the adsorbed reactants. This explains the slow dechlorination rate for more chlorinated species such as TCE, which is a weak electron acceptor.[52]

Figure 3 shows the well-accepted mechanism for TCE HDC. As can be seen, TCE is dechlorinated to DCE products which then again lose one more chlorine resulting in the formation of VC molecule. After that, through another dechlorination process, finally ethane is obtained as product. The other route is acetylene pathway where acetylene exists as surface intermediate product. As mentioned earlier cleaved surface carbon and hydrogen interacts with acetylene producing alkanes.

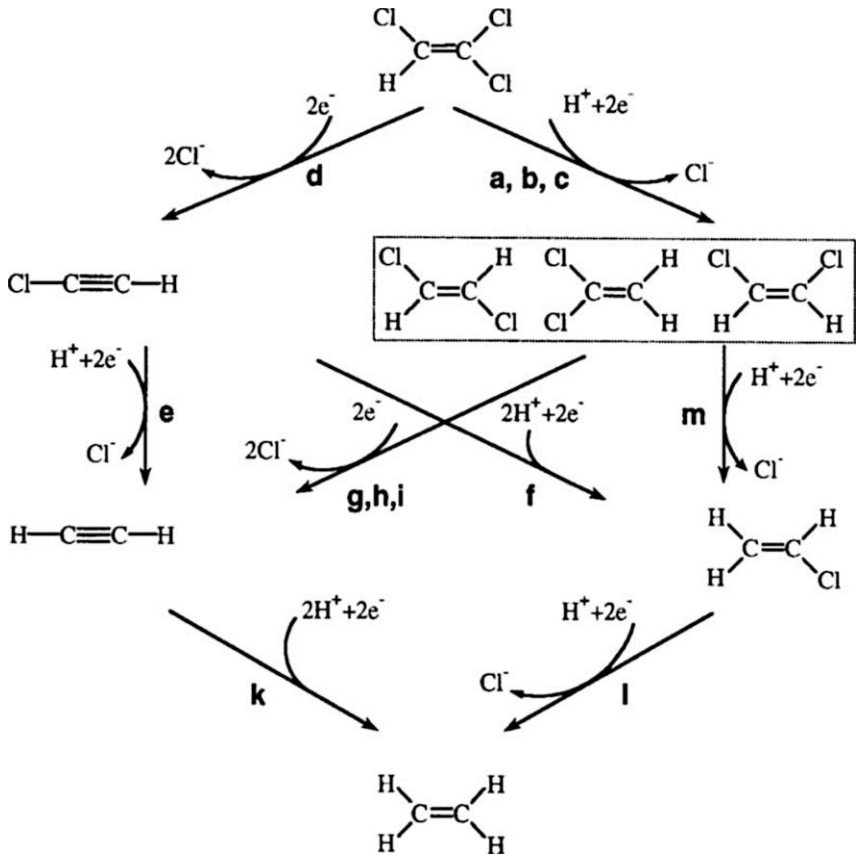

Figure 3. Proposed Mechanism for HDC of Trichloroethylene (TCE)[80] *(cited from "Reinhard, M.; Semadeni, M.; Sharma, P. K.; Haag, W. R., Dehalogenation of haloaliphatic hydrocarbon compounds in the aquatic and terrestrial environment. Bioremediation of Contaminated Soils 1999, 133-174.")*

** Information in this chapter was partially reproduced/adapted from " Sohn, H.; Celik, G.; Gunduz, S.; Dean, S. L.; Painting, E.; Edmiston, P.; Ozkan, U. S., Hydrodechlorination of Trichloroethylene over Swellable Organically-Modified Silica (SOMS). Submitted to Applied Catalysis B: Environmental"*

CHAPTER 3

HYDRODECHLORINATION OF TRICHLOROETHYLENE OVER PD SUPPORTED ON SWELLABLE ORGANICALLY-MODIFIED SILICA (SOMS)

3.1 Summary of Chapter 3

The catalytic activity and resistance to poisoning of Pd catalysts supported on swellable organically-modified silica (SOMS) were investigated for hydrodechlorination (HDC) of trichloroethylene (TCE). The promising catalytic activity of 1% Pd/SOMS sample was attributed to the high affinity of SOMS for organics and its remarkably high hydrophobicity. While latter characteristic repels water, the adsorptive capacity for organics allows TCE dissolved in aqueous media to concentrate inside the pores, in the vicinity of the active sites, thus helping the kinetics. In the liquid phase, using a continuous flow reactor, higher TCE conversion was obtained over the 1% Pd/SOMS compared to the commercial 1% Pd/Al_2O_3 catalyst. When the pores of 1% Pd/SOMS sample were fully opened by pre-treating it with ethanol prior to the reaction, HDC activity significantly increased. In the gas phase, the extent of adsorption was less, reducing the concentration of reactants near the active sites. To determine their resistance to poisoning, 1% Pd/SOMS and 1% Pd/Al_2O_3 catalysts were poisoned ex-situ with Li_2S. The ex-situ poisoned Pd/SOMS sample maintained its catalytic activity for HDC of TCE. However, a significant

loss in catalytic activity of the Pd/Al_2O_3 catalyst was observed after poisoning. Protection from aqueous phase sulfide poisoning was attributed to the hydrophobicity of the Pd/SOMS, which would exclude anionic species from the embedded Pd particles. The XPS, STEM and ICP-OES results indicated that when Pd/Al_2O_3 and Pd/SOMS were treated with 1 M HCl, most of the Pd metal was leached from the Pd/Al_2O_3 catalyst in contrast to Pd/SOMS, which had negligible leaching. Overall, due to hydrophobicity and high affinity for organics, SOMS has potential to be used as a catalyst scaffold for different reactions in groundwater remediation applications.

3.2 Experimental Section

3.2.1 Catalyst Preparation

The synthesis procedure for SOMS was reported previously by Edmiston and co-workers.[16-18, 81-82] In brief, it involves a sol-gel synthesis consisting of polycondensation of an aromatically bridged silane precursor (monomer) with flexible linkages between the aryl group and the silicon centers (e.g., [bis(trimethoxysilylethyl) benzene (BTEB) shown in Figure 4), followed by hydrolysis and condensation reactions initiated by fluoride ion (e.g., tetrabutyl ammonium fluoride) as a catalyst (leading to Si-O-Si bond formation). Organization of the polycondensed BTEB is aided by π-π stacking interactions of the aryl rings and assembling of particles into generally amorphous, but flexibly crosslinked clusters that interlink to form a continuous colloidal gel through kinetic control. After aging the gel for 6 days, residual silanol groups are derivatized by end-capping them with organic functional groups (e.g., chlorosilane ($R\text{-}Si(CH_3)_2Cl$)) which prevents Si-O-Si bond

formation during drying, preserving flexibility in the matrix. The crucial step in the synthesis is the choice of the monomer since swelling behavior is observed only when flexible linkages between the aryl group and the silicon centers exist.

1% wt. Pd/SOMS was prepared using Pd(II) acetate (Sigma-Aldrich 98%) through incipient wetness impregnation (IWI) technique. The Pd acetate was first dissolved in acetone and stirred rigorously to obtain a homogenous Pd precursor solution. The mixture was then added to the SOMS support drop-wise using a micropipette at which point the volume of SOMS expanded (swelled) about 2.5x. Once the expansion was reached to a maximum state, SOMS was dried at 25℃ with constant agitation. The swelling and drying process was repeated until all the precursor solution was added to the SOMS support. Pd^{2+} was reduced by swelling the material with a saturated solution of $NaBH_4$ in 95% ethanol. The Pd/SOMS particles were then filtered and extensively rinsed with ethanol and then with deionized water, and dried at 60℃. The particle size was of the Pd/SOMS was ~150 μm.

Commercial 1% Pd/Al_2O_3 was purchased from Sigma-Aldrich. The 1% Pd/Al_2O_3 was reduced using 5% H_2/He gas at 400 ℃ for 1 h. The reduction was carried out either ex-situ or in situ for liquid phase and gas phase reactions, respectively. To desorb any species that may be adsorbed from the atmosphere, the sample was first treated with helium at 450 ℃ for 30 min.

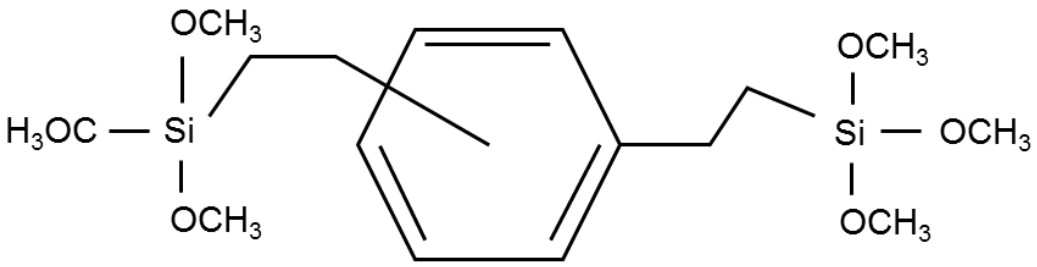

Figure 4. Bis(trimethoxysilylethyl)benzene (BTEB)

3.2.2 Catalyst Characterization

3.2.2.1 Raman and Infrared (IR) spectroscopy

Raman spectra were collected with a Renishaw-Smiths Detection Combined Raman-IR Microprobe equipped with Leica and CCD detector (400 X 576). SOMS material was placed on a stainless steel sample holder where a helium-neon laser (633 nm) beam was focused on a particular spot (x20 objective). The spectra were collected using an exposure time of 50 s^{-1} in the 300-4000 cm^{-1} range. FT-IR-ATR spectra were measured using a Thermo Nicolet 6700 FTIR Spectrometer with a diamond attenuated total reflectance accessory.

3.2.2.2 Temperature Programmed Oxidation (TPO)

SOMS was placed in a 4 mm-ID quartz reactor, which was then loaded into a Carbolite MTF 10/15/130 furnace. A gas mixture of 5% O_2/He was introduced to the reactor at 30ml/min at RT and the outlet stream was connected to a mass spectrometer (MKS-Cirrus II) operated in scanning ion mode. The signals from m/z=2 to 60 were all monitored in order to detect various products. TPO was performed using a 10 ℃/min temperature ramp rate at which the temperature was increased from RT to 800 ℃.

3.2.2.3 Surface Area, Pore Size and Pore Volume

Micromeritics ASAP 2020 (accelerated surface area and porosimetry) instrument was used to obtain nitrogen adsorption/desorption isotherms of the SOMS, 1% Pd/SOMS and 1% Pd/Al_2O_3 catalysts. First, the sample was degassed for 12 h at 130 ℃ under 2 µm

Hg of vacuum in order to remove any gas molecules captured inside the pores and impurities on the surface. The degassed sample was then transferred to the analysis port where the nitrogen adsorption took place at liquid nitrogen temperature. The collected isotherms were used to calculate the Brunauer-Emmett-Teller (BET) surface area and Brunauer-Joyner-Helena (BJH) pore volumes of the samples. The pore size distribution was obtained from the desorption curve of the isotherm.

3.2.2.4 High angle annular dark field (HAADF) scanning transmission electron microscopy (STEM) and Energy-Dispersive X-ray Analysis (EDAX)

HADDF-STEM images were taken by FEI Tecnai F20 instrument equipped with a high brightness field emission electron gun (FEG) operated at 200 kV and a HADDF detector. Prior to the imaging, the Pd/SOMS and Pd/Al_2O_3 samples were suspended in ethanol and sonicated for 5 min. After obtaining a homogeneous mixture a drop of it was added on a Tedpella, Inc. 200 mesh copper grid sample holder, which was coated with lacey carbon. For identification of Pd particles, EDAX spectra were collected over all the samples.

3.2.2.5 Static Vapor-Phase Adsorption

Static vapor equilibrium adsorption at 25 ℃ was measured over time using Pyris 1 Perkin-Elmer thermo-gravimetric analyzer. A mass of sample was placed on the balance and a neat liquid or solid was added to the sealed analysis chamber to yield a static condition of saturated vapor. Mass was measured every 6 s until equilibrium was reached.

3.2.2.6 X-ray photoelectron spectroscopy (XPS)

XPS spectra were collected over the Pd/SOMS and Pd/Al_2O_3 catalysts by using a Kratos AXIS Ultra X-ray photoelectron spectrometer with a monochromatized Al K_α X-ray source operated at 13 kV and 10 mA. The sample was loaded in the chamber using carbon tape and was evacuated overnight. For each sample, a survey scan was taken in order to identify all the elements present on the catalyst surface. After the survey scan, spectra for the specific C 1s, O 1s, Cl 2p, Pd 3d and Si 2p regions were collected. Prior to the data analysis, the charging effect was corrected based on the C 1s binding energy of 284.5 eV. The background subtraction, normalization and peak fitting of the data were performed in CasaXPS software.

3.2.2.7 Inductively Coupled Plasma Optical Emission Spectrometry (ICP-OES)

To examine leaching characteristics of the active metal in pre-reduced 1% Pd/Al_2O_3 and 1% Pd/SOMS, samples 1 M HCl poisoning was conducted by stirring each of the two samples in 40 ml of of 0, 0.1 and 1 M HCl solutions for 20 min at RT. The resulting mixture was then filtered to remove all the residual solids. The elemental analysis of Pd in the HCl solution was conducted utilizing a Perkin-Elmer Optima 4300DV ICP-OES.

3.2.3 Catalyst Activity Testing

3.2.3.1 HDC of TCE in the Liquid Phase

A continuous flow, fixed bed reactor was constructed using a LCC-500 fast flow liquid chromatography system (Pharmacia). All the experiments were based on equal liquid

hour space velocity (LHSV = reactant flow rate/reactor volume). The liquid feed consisted of water, TCE, H_2 and methanol. Deionized water was saturated with H_2 by continuously sparging the 4 L source water reservoir. TCE was dissolved in methanol (5.18 mg/mL), to allow rapid dissolution, introduced by a syringe pump. TCE solution feed rates were either 2.4 mL/hr when TCE was limiting or 9.6 mL/hr when the dissolved H_2 was the limiting reagent. A 50-60 Hz mixer upstream of the catalyst bed ensured a homogenous solution. Catalyst was added to a 15 mm diameter water-jacketed chromatography column (GE-Pharmacia) so that the bed thickness remained constant at 4 mm which required 2.0 g of Pd/Al_2O_3, 0.40 g of Pd/SOMS, and 0.27 g of pre-swollen Pd/SOMS. Catalyst bed was maintained at 30 ℃. Flow rate was 20 mL/min (~40 bed volumes per min).

Reaction progress was monitored by measuring the conductivity of the water in the effluent of the catalytic bed (HCl production) using a Pharmacia Biotech 18-1500 conductivity monitor with 1 Hz data acquisition. In addition, a sampling port was used to collect water samples for analysis of chlorinated solvents by headspace gas chromatography-mass spectrometry (GC-MS) using an 6980/5973 instrument (Agilent).

3.2.3.2 HDC of TCE in the Gas Phase

The catalytic activity of the 1% Pd/SOMS and 1% Pd/Al_2O_3 in the gas phase for HDC of TCE was measured using a bench-scale fixed-bed flow reactor system. The catalyst was first placed inside a 4 mm-ID quartz reactor using quartz wool plugs to support the catalyst bed. The reactor was then positioned in the center of a furnace (Carbolite, MTF 10/15/130) whose temperature was adjusted by an Omega CSC232 PID temperature

controller. The outlet of the reactor was connected to an online gas chromatographer (Shimadzu Scientific 2010) equipped with a Q-bond column and a flame ionization detector (FID) for separation, identification, and quantification of all the products. The inlet stream to the reactor contained 0.7% TCE, excess hydrogen (1:30, TCE-to-hydrogen molar ratio), and nitrogen as the balance gas. The TCE vapors were generated by using a stainless-steel bubbler, which contained pure TCE and which was held at 35 ℃ using nitrogen as a carrier gas. The effluent gas mixture from the bubbler was then mixed with additional nitrogen and excess hydrogen to obtain 0.7% TCE in feed stream. In order to investigate the effect of water on the catalytic activity of the samples, water was added to the reactant stream. Similar to the TCE, a water bubbler, which was maintained at 35 ℃, was to generate water vapor. The total water concentration used in the feed stream was 4%.

All the gas lines (Swagelok) were held at temperatures above 200 ℃ to prevent any condensation of the reactants and products. Prior to the HDC reaction experiment, the 1% Pd/Al_2O_3 was pre-reduced in situ by using 5% H_2/He at 400℃ for 1 h. The Pd/SOMS was chemically reduced using $NaBH_4$. The quantification of the products and reactants was done based on calibration curves that were obtained periodically. The catalytic activity comparison between the two samples was based on equal gas hour space velocity (GHSV).

3.3 Results and Discussion

3.3.1 Structure of SOMS

SOMS is synthesized using a bis(trimethoxysilylethyl)benzene (BTEB) silane monomer precursor which contains a benzene ring directly connected to silicon (Figure 4). The poly-condensation of BTEB during sol-gel synthesis creates a highly cross-linked polymer matrix including covalent linkages between the aryl group and silicon. In a recent study, Edmiston and co-workers[16, 18] have examined the effect of various parameters such as the choice of precursor, solvent, catalysts, aging time and silane concentration to investigate the principle behind the swelling behavior. Interestingly, the swelling behavior of SOMS was only obtained by the two precursors that included a covalent bond between the aryl groups connected to the silicon center. Thus, the flexibility of SOMS is possibly correlated to the Si-C-aryl bonds. To obtain a better understanding of the chemical structure of SOMS, two different spectroscopy techniques were used.

3.3.1.1 Raman Spectroscopy

Raman spectrum was collected over the bare SOMS support. Figure 5 (a) shows the spectrum region of 300-1800 cm^{-1}. The band with the strongest intensity at 1000 cm^{-1} is attributed to mono, 1,3 and 1,3,5 substituted benzenes.[83] This indicates that the aromatic ring originating from the BTEB precursor was stable throughout the synthesis process. The Si-O-Si asymmetric stretching[84-85] was observed as a sharp feature at 1079 cm^{-1} whereas the Si-O-Si symmetric stretching[86-87] was assigned to a peak at 640 cm^{-1}. Several other peaks appeared around the lower wavelength region below 1000 cm^{-1}. The bands at 484

and 603 cm^{-1} are possibly related to three- or four-membered rings of the Si-O-Si symmetric stretching mode, which are typically found in silica Raman spectra.[88-89] However, the intensity of these peaks were much lower. The features for Si-CH_3 appear as a sharp peak at 1240 cm^{-1} ascribed to the CH_3 symmetric deformation.[85] Peaks at 812 and 842 cm^{-1} were associated to two methyl groups in Si-$(CH_3)_2$ binding to the silicon center and the band at 1412 cm^{-1} was attributed to the asymmetric stretching of the CH_3 species.[85] It is likely that Si-CH_2-R bonds are present in the structure. The 692 and 743 cm^{-1} bands were assigned to the rocking vibration of CH_2.[85] Si-O-CH_3 bonds were also identified as a strong peak at 1181 cm^{-1}.[85] The CH_3 symmetric stretching in C-CH_3 group were also seen at 1334 cm^{-1}.[85] The higher wavenumber range above 1400 cm^{-1} are mostly due to adsorption of aromatic groups. The 1452, 1588 and 1606 cm^{-1} peaks are due to aromatic rings with different substituents.[85, 90]

The high wavenumber-region of the spectrum led to similar observations as seen in Figure 5 (b). The adsorption due to C-H stretching in aromatic rings were observed at 3004 and 3057 cm^{-1}.[85, 90] The peaks at 2956, 2901 and 2876 cm^{-1} are attributed to C-H vibration in CH_3 or CH_2 groups of aliphatic compounds,[85, 90] or Si-O-CH_3 groups.[91]

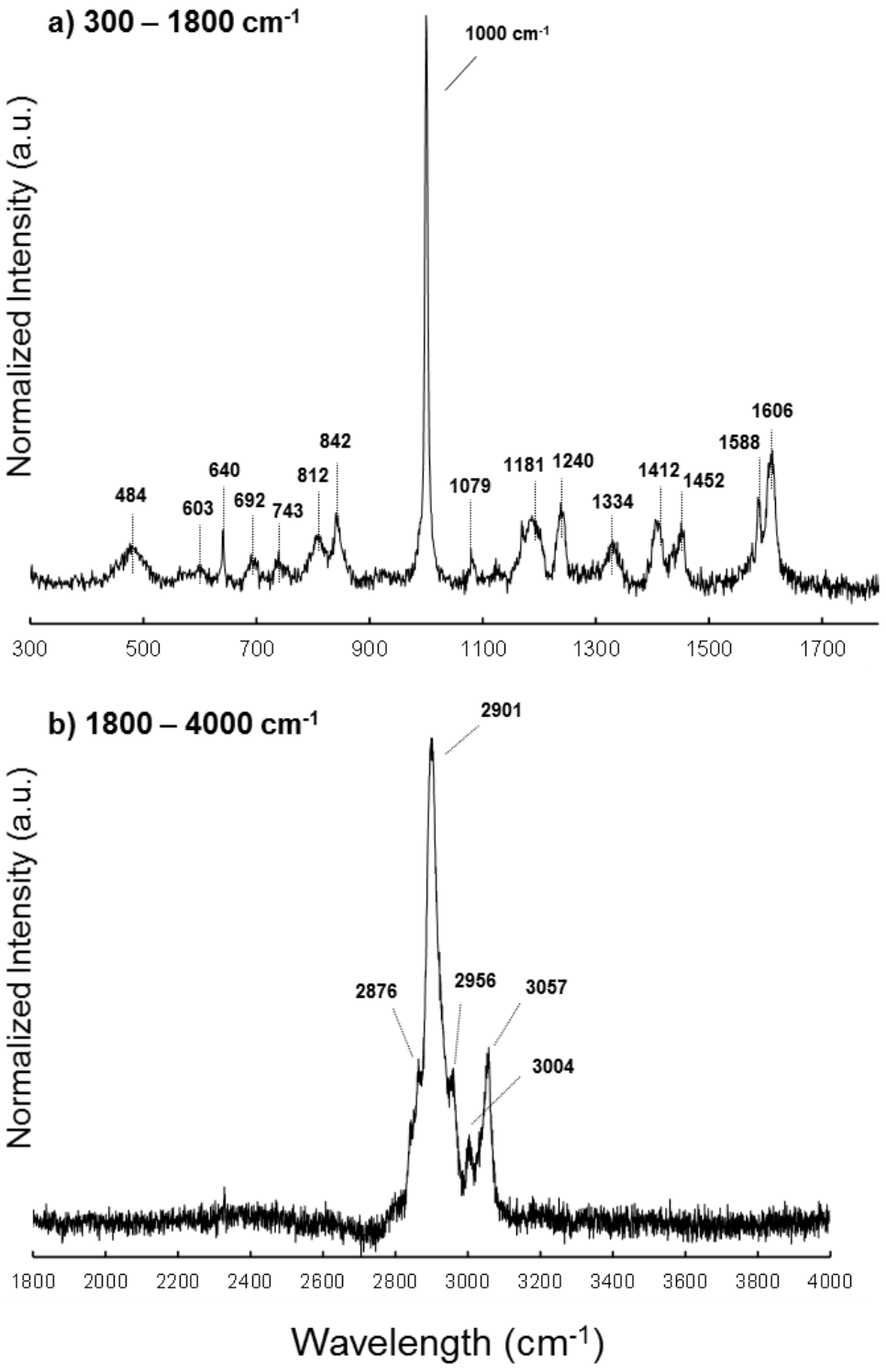

Figure 5. Raman spectra of SOMS, a) 300 - 1800 cm^{-1} and b) 1800 - 4000 cm^{-1}

3.3.1.2 IR Spectroscopy

The structural characteristics of the SOMS materials were also examined using IR spectroscopy (Figure 6). The two overlapping peaks at 1034 and 1093 cm^{-1} indicate Si-O-Si stretching.[92] The shoulder of Si-O-Si band is characteristic of SOMS and due to longitudinal-optic (LO)-transverse-optical (TO) splitting of the vibrational modes. LO-TO splitting has been attributed to long range coupling of Coulomb interactions.[93-95] Specifically, the antisymmetric stretching LO_3 (1188)-TO_3 (1093) cm^{-1} bands observed in SOMS are likely explained as scattering in larger pore structures.[96]

The Si-OH groups were not observed, i.e. showing no notable peaks around the 3000-3600 cm^{-1} or 950 cm^{-1} regions.[92] This is due to the Si-OH groups being capped by treatment with chlorotrimethysilane in the synthesis of SOMS[16] leading to O-Si-$(CH_3)_3$ groups which were detected by Raman and observed in the IR by three distinctive peaks at 764, 845 and 1252 cm^{-1}.[92] Multiple bands associated with the aromatic ring were shown in the spectrum. Two strong peaks at 688 and 754 cm^{-1} exhibit features that correspond to out-of-plane C-H bending or wagging vibrations of mono and meta substituted benzenes.[92, 97] The in-plane C-H bending was observed around 1400-1700 cm^{-1} region. The five peaks at 1406, 1448, 1489, 1512, and 1606 cm^{-1} can be related to a combination of mono, ortho, meta and para substituted benzenes of the SOMS structure.[97]

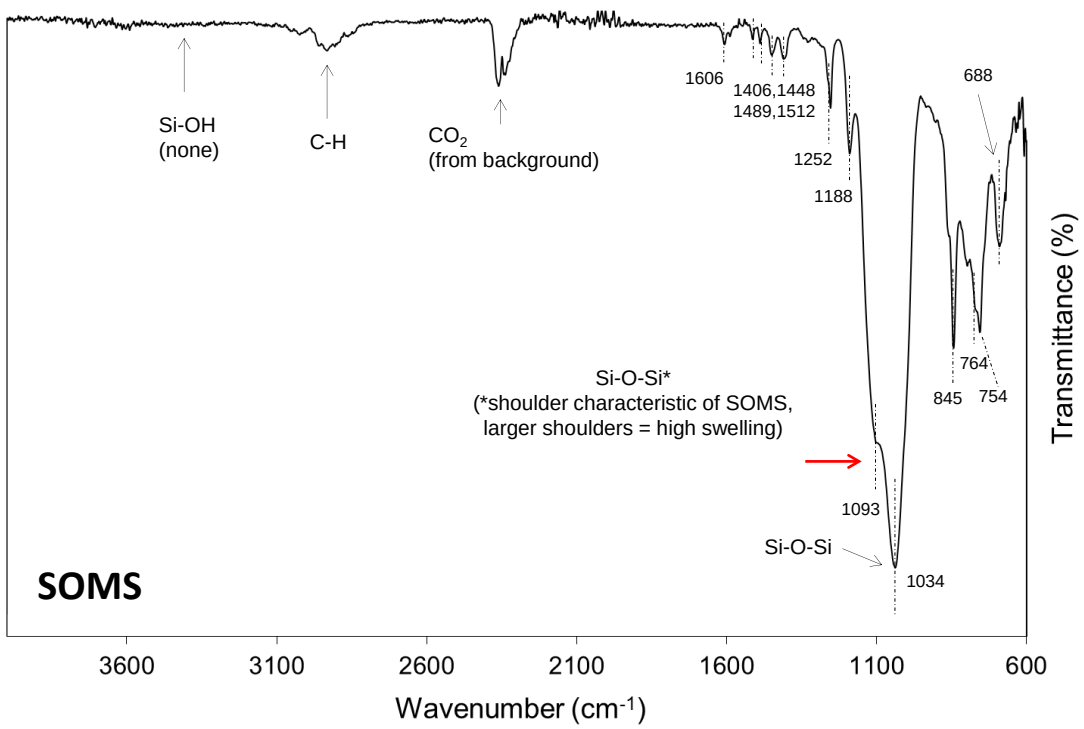

Figure 6. IR spectra of SOMS ***(Data was collected by ABS Materials)***

3.3.2 Thermal Stability of SOMS

SOMS is an organosilicates-based material which consists of a crosslinked network. It is expected that under extreme thermal treatment, the structure of SOMS collapses due to decomposition of the organic groups, resulting in the loss of the swelling capability and hydrophobicity. Hence, a TPO experiment was conducted to determine an accurate decomposition temperature of the SOMS material. As shown in Figure 7, a significant oxygen consumption feature was observed around 500 ℃, simultaneously producing a large amount of CO_2. This clearly shows that the decomposition of SOMS with C-C bond cleavage. Some amount of H_2O and CH_4 was also detected as products. Interestingly, the swelling property and hydrophobicity in the post-TPO SOMS sample was still present (data not shown). However, the degree of physical volume expansion was significantly reduced compared to the fresh SOMS support. The weak thermal stability of the SOMS support limited its utilization in the H_2 pre-reduction process, which requires high temperatures. Thus, for this study, all of the Pd/SOMS samples were pre-reduced using $NaBH_4$ at room temperature.

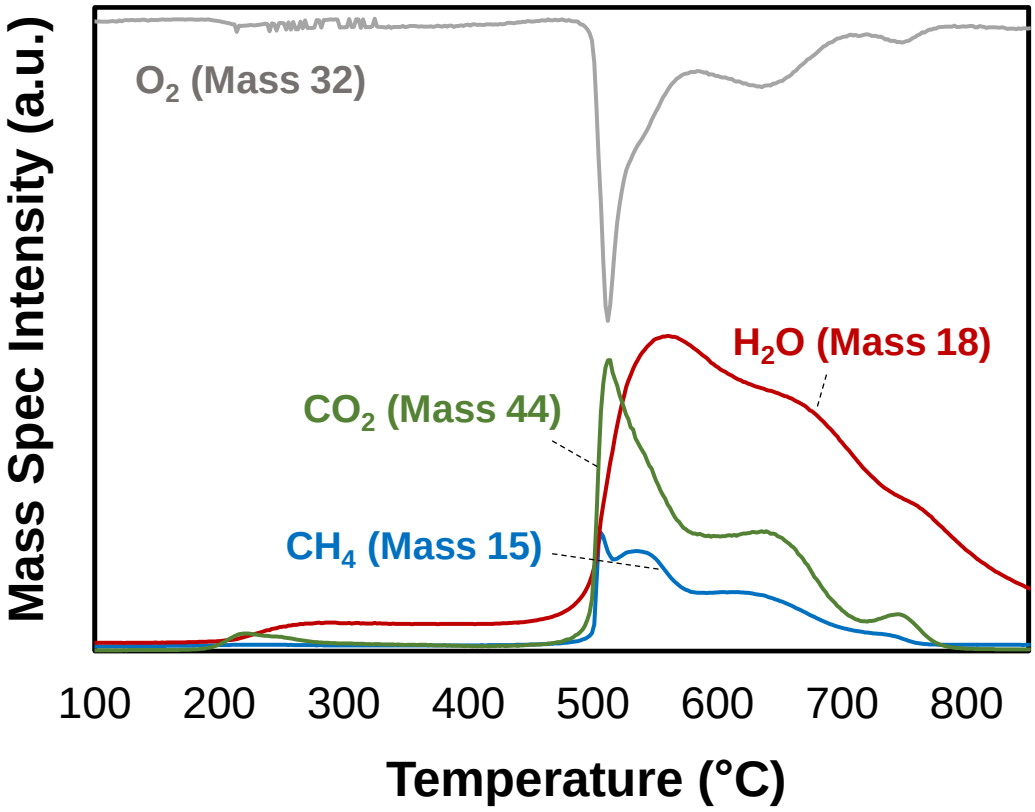

Figure 7. Temperature-programmed oxidation (TPO) profiles showing decomposition of SOMS at high temperatures (> 450 ℃)

3.3.3 Surface Area, Pore Size and Pore Volume

The nitrogen isotherms of the samples were collected using an ASAP 2020 instrument to obtain BET surface area, BJH pore volume and averaged pore diameter. The calculated values are shown in Table 1. The impregnation of Pd on the SOMS support showed reduction in surface area, pore volume and averaged pore diameter. This is likely attributed to the filling/blockage of the pores of the SOMS support by Pd particles. The surface area of 1% Pd/SOMS was higher than that of the 1% Pd/Al_2O_3 commercial catalyst. However, 1% Pd/Al_2O_3 exhibited a higher pore volume and a higher average pore. The BJH pore size distributions are shown in Figure 8. As it can be seen, a significant decrease in number of pores of 50-200 Å over the SOMS support was observed after the Pd impregnation process. For Pd/SOMS sample, most of the pores detected were close to 50 Å (mesopores) whereas a wide pore size distribution in the range of 50-400 Å was obtained for Pd/Al_2O_3.

All the SOMS and 1% Pd/SOMS samples tested here were in their closed state, i.e., before any physical expansion of the material has taken place. The open-state of these samples were not subjected for the analysis due to the degassing and analysis conditions. However, it should be noted that the surface area and pore volume of the open-SOMS and open-1% Pd/SOMS are expected to be significantly greater compared to the closed state of the two samples. This is attributed to the generation of the inner surface area during swelling of the samples, hence, the actual surface area, pore volume and pore size would be higher under reaction conditions.

Table 1. BET Surface area, pore volume and average pore diameter of SOMS, 1% Pd/SOMS and 1% Pd/Al_2O_3 catalysts

	Surface Area	Pore Volume	Averaged Pore Diameter
	(m^2/g)	(cm^3/g)	(Å)
SOMS	493	1.03	84
1% Pd/SOMS	479	0.56	47
1% Pd/Al_2O_3	156	0.85	217

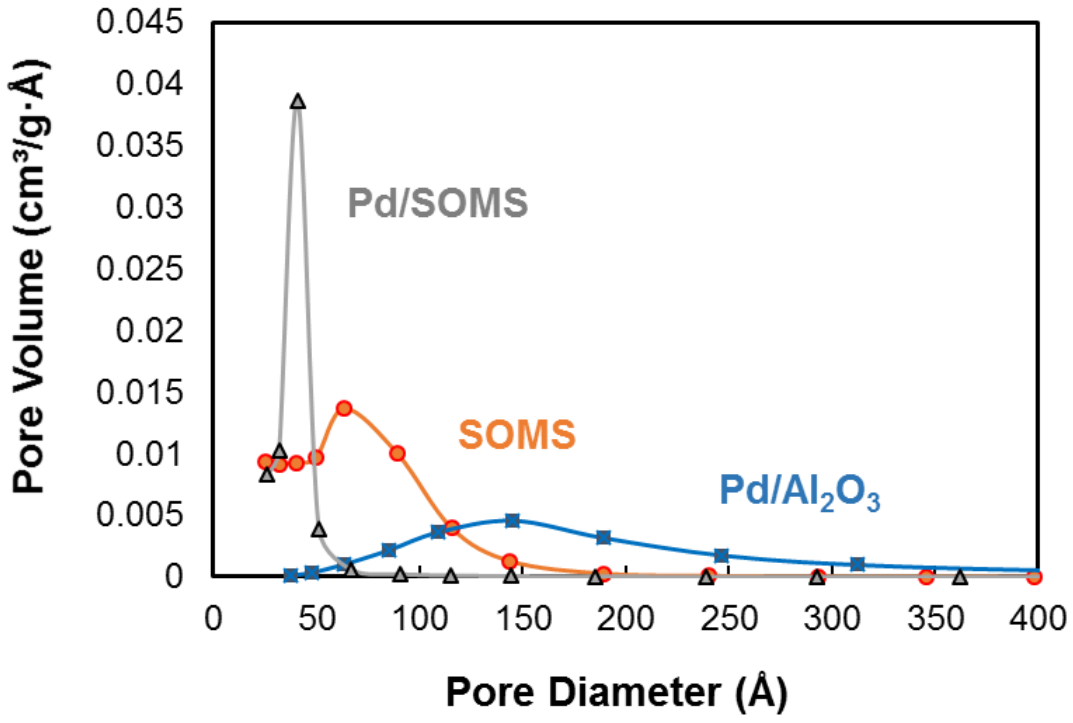

Figure 8. BJH Pore size distribution of SOMS, 1% Pd/SOMS and 1% Pd/Al_2O_3

3.3.4 Hydrophobicity and Adsorption Capacity of 1% Pd/SOMS vs 1% Pd/Al_2O_3

Adsorption capacity of SOMS for different organics (acetone, heptane, methanol, TCE, and benzene) was measured at room temperature using the static vapor adsorption technique and compared to that for water vapor. The term adsorption here refers to physisorption and involves pore filling. The mass intake profiles for these organics and for water are shown in Figure 9. The results indicate SOMS had adsorptive capacity for organic vapors between 60-100% w/w. Capacity after 120 min exposure time was generally non-selective across all organic vapors. In contrast, water vapor adsorption was <7% w/w, verifying the high hydrophobicity of SOMS.

In an earlier study by Edmiston and co-workers,[17] SOMS was shown to be capable of adsorbing both polar and non-polar organic substances dissolved in aqueous phase. The study reported adsorption capacity for several organics, including PCE, TCE, toluene, methyl t-butyl ether (MTBE), acetone, naphthalene, and 1-butanol. Especially several compounds that are very relevant to water contamination problem such as PCE, TCE and toluene were adsorbed from water by SOMS at extraction levels of 92% or above.[17]

Figure 9 (b) shows a comparison of 1% Pd/SOMS and 1% Pd/Al_2O_3 catalysts and their adsorption uptake capacities for acetone and water. The adsorption selectivity of acetone to water, i.e., ratio of the weight of acetone adsorbed to that of water adsorbed, was seen to be much higher for Pd/SOMS than it was for Pd/Al_2O_3 as seen in the inset. It also shows that SOMS is much more hydrophobic than Al_2O_3 and the Pd impregnation of the reduction step with $NaBH_4$ does not change the hydrophobic nature of this material.

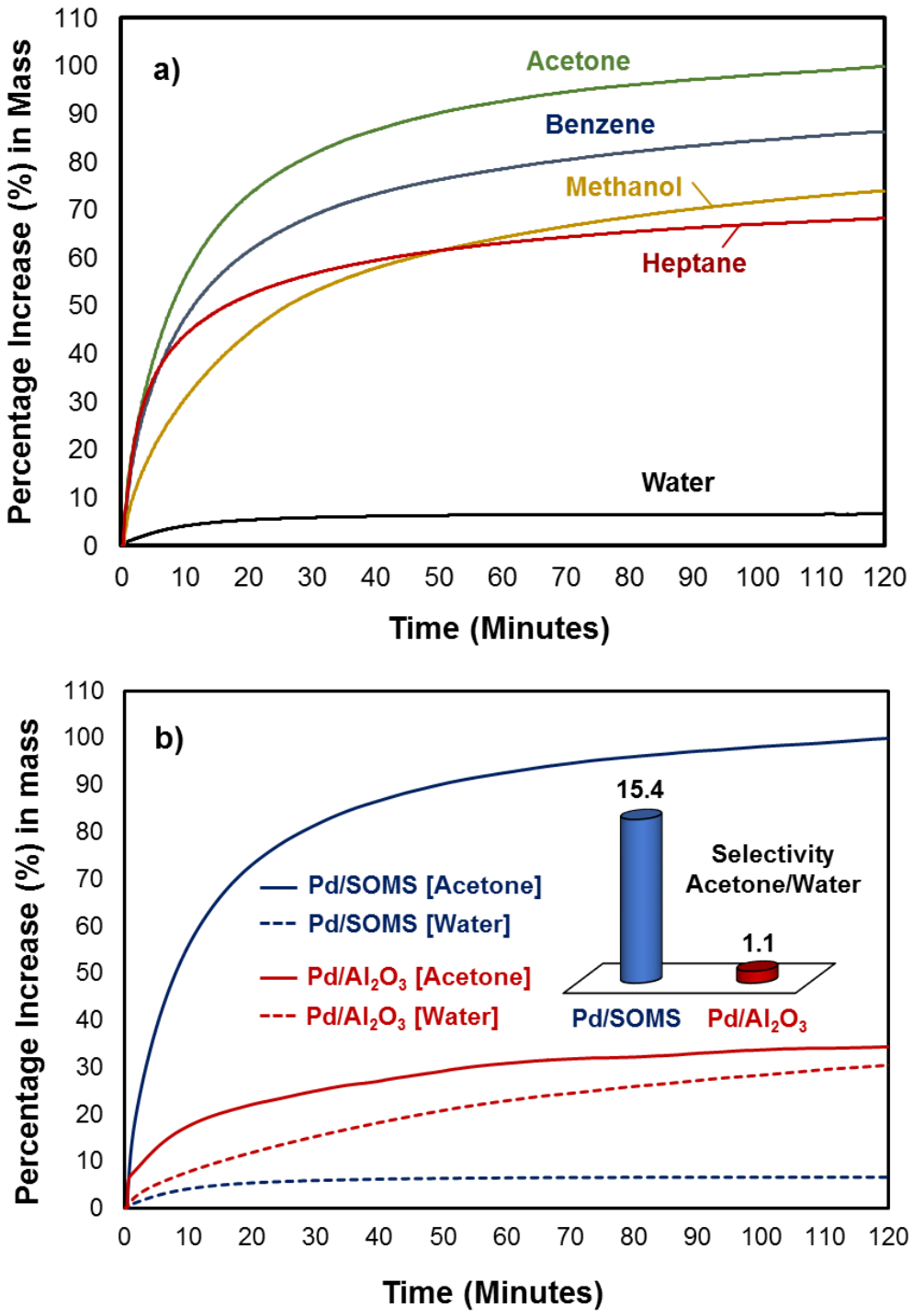

Figure 9. a) Adsorption of different organic groups on 1% Pd/SOMS, b) Adsorption of water and acetone on 1% Pd/SOMS and 1% Pd/Al_2O_3 catalysts ***(Data was collected by ABS Materials)***

3.3.5 HDC of TCE in Liquid Phase

3.3.5.1 Pd/SOMS vs. Pd/Al_2O_3

The catalytic activity of Pd/SOMS and Pd/Al_2O_3 was investigated in liquid phase for HDC of TCE using a continuous flow reactor system where the aqueous phase reactant mixture (TCE + water), was introduced into a fixed catalyst bed. A thin bed of supported catalyst was used to give a short residence time to better assess the kinetics of the HDC reaction. The effluent stream from the reactor was monitored by a conductivity detector, where the concentration of HCl was directly correlated to hydrodechlorination activity of the catalyst. These experiments were conducted in three parts: (i) with 180 μM TCE (24 ppm) in the feed, i.e., TCE is the limiting reactant; (ii) with 320 μM TCE (42 ppm) in the feed, i.e., H_2 is the limiting reactant; (iii) ending with TCE-free feed. In all three parts of the experiment, H_2 concentration in the feed was kept constant at 775 μM.

Figure 10 (a) shows the liquid-phase hydrodechlorination of TCE over 1% Pd/Al_2O_3 at three different TCE concentrations. The green bar at the top of each section indicates the theoretical HCl concentration when complete hydrodechlorination of TCE is achieved. When 180 μM of TCE was introduced to the reactor, after a transient period of 290 s, a steady-state percent hydrodechlorination (HDC) of around 35% was obtained over the 1% Pd/Al_2O_3 catalyst. Here %HDC is defined as 100 x (moles of HCl produced) / (3 x moles of TCE fed). The %HDC slightly increased to 40% as TCE concentration was increased to 320 μM. As expected, when there was no TCE in the reactor feed, as shown in the third section of the graph, the HCl concentration in the effluent quickly dropped to 0 μM. Water collected during the steady-state period (t = 1,200 s) was tested for the

presence of chlorinated solvents by GC-MS. At steady state, TCE (C_{out}/C_{in} = 0.25), and a range of partially dechlorinated compounds including dichloroethylene, and vinyl chloride were detected in the effluent, supporting incomplete HDC reaction as included by sub-stoichiometric HCl production.

Pd/SOMS catalyst showed a different performance from Pd/Al_2O_3 (Figure 10 (b)). For Pd/SOMS, the transient period was much longer (850 s) as the HCl concentration gradually rose to the steady-state value. The hydrodechlorination activity was higher than that of Pd/Al_2O_3, with 63 and 79% HDC conversion levels, for 180 μM and 320 μM of TCE inlet concentrations, respectively. It should be noted that the Pd/SOMS initially loaded into the bed was in the closed (unswollen) state. In other words, the catalyst was not pre-treated with an organic solvent, which would swell the pores prior to the reaction. The collapsed initial pore architecture may account for the slow approach to steady-state and the long transient period, during which the pores of the SOMS support are expected to be filled by TCE adsorption. In other words, during this period TCE would be concentrating inside the pores. Another interesting observation from these experiments is that HCl formation continued for an extended time (1500 s) after discontinuing TCE addition to the deionized feed water. Continued HCl production can be explained by the reaction continuing from the reservoir of adsorbed TCE. The amount of chlorinated solvents in the reactor effluent was measured at t = 1000, 2500, 5000 s ($[TCE]_{in}$ = 180, 320, and 0 μM, respectively). At all-time points the amount of TCE in the reactor effluent water was undetectable by GC-MS. An amount of vinyl chloride approximately 10% of the TCE effluent concentration was detected when TCE was in stoichiometric excess of H_2 (t = 2500 s). Ethane was detected at all-time points, but was not quantified.

The result shown for Pd/SOMS is surprising and significant as it was deduced that the SOMS support itself has a large adsorptive capacity for TCE, resulting in a high concentration of the reactant inside the pores and the ability to "buffer" TCE input loads. An amount of vinyl chloride likely escapes during the elevated TCE input since the vinyl chloride is more soluble in water and likely builds up in the pores due to H_2 starvation. The high storage capacity is a unique feature which is facilitated by the swelling and adsorptive characteristics of SOMS. The hydrophobic nature of SOMS, which repels water, but allows adsorption of organics inside the pores appears to improve the kinetics, since local concentration of TCE inside the pores, i.e., in the vicinity of the active sites would be much higher than in the bulk of the liquid.

To examine the effect of volumetrically expanding the pores, Pd/SOMS was first pretreated with ethanol in order to reach its maximum swollen state to make the catalyst pores fully opened prior to reaction. The Pd/SOMS-open was then tested for HDC of TCE (Figure 10 (c)). When the pores are volumetrically expanded by ethanol pre-treatment, a significant increase in the HDC conversion was obtained over the 1% Pd/SOMS-open compared to 1% Pd/SOMS-closed and 1% Pd/Al_2O_3 catalysts in both TCE feed concentrations. The HCl concentration obtained with 180 μM TCE feed reached a maximum value at 94% of HDC conversion. This is 31% greater compared to Pd/SOMS-closed sample. In the second region where 42 ppm of TCE feed was utilized, %HDC reached 84%. An important observation is that the approach to steady-state i.e., transient period was much shorter (420 s) for the Pd/SOMS-open sample since the pores were already fully opened when the feed was introduced and the TCE could concentrate inside the pores much faster. Similarly, the production of HCl was continued for a shorter time

(900 s) after addition of TCE to reactant stream was stopped, compared to the Pd/SOMS-closed. This is likely due to the higher conversion rate of the reactant, which results in a faster depletion rate of the TCE "stored" in the pores. Chlorinated solvent concentrations in the effluent were measured at t = 1800, 3000, 4500 s. TCE and all partially dechlorinated compounds were undetectable at 1800 s ($[TCE]_{in}$= 180 μM) and 4500 s ($[TCE]_{in}$= 0 μM, post addition). When TCE was in excess (t = 3000 s) a small amount of TCE (C_{out}/C_{in} = 0.02) and vinyl chloride were detected, however, the open state-SOMS has capability of adsorbing and TCE was still adsorbed by the SOMS.

The faster kinetics due to concentration of TCE inside the pores is seen more clearly when the results obtained over Pd/Al_2O_3 and Pd/SOMS (both open and closed) are compared. In these experiments, the feed flow rate and concentration were kept constant, but the amount of Pd/Al_2O_3 in the reactor was more than 5and 7 times that of the Pd/SOMS and Pd/SOMS-open, respectively. This result shows that the high hydrodechlorination rates obtained over Pd/SOMS (both open and closed) cannot be explained by their higher surface areas.

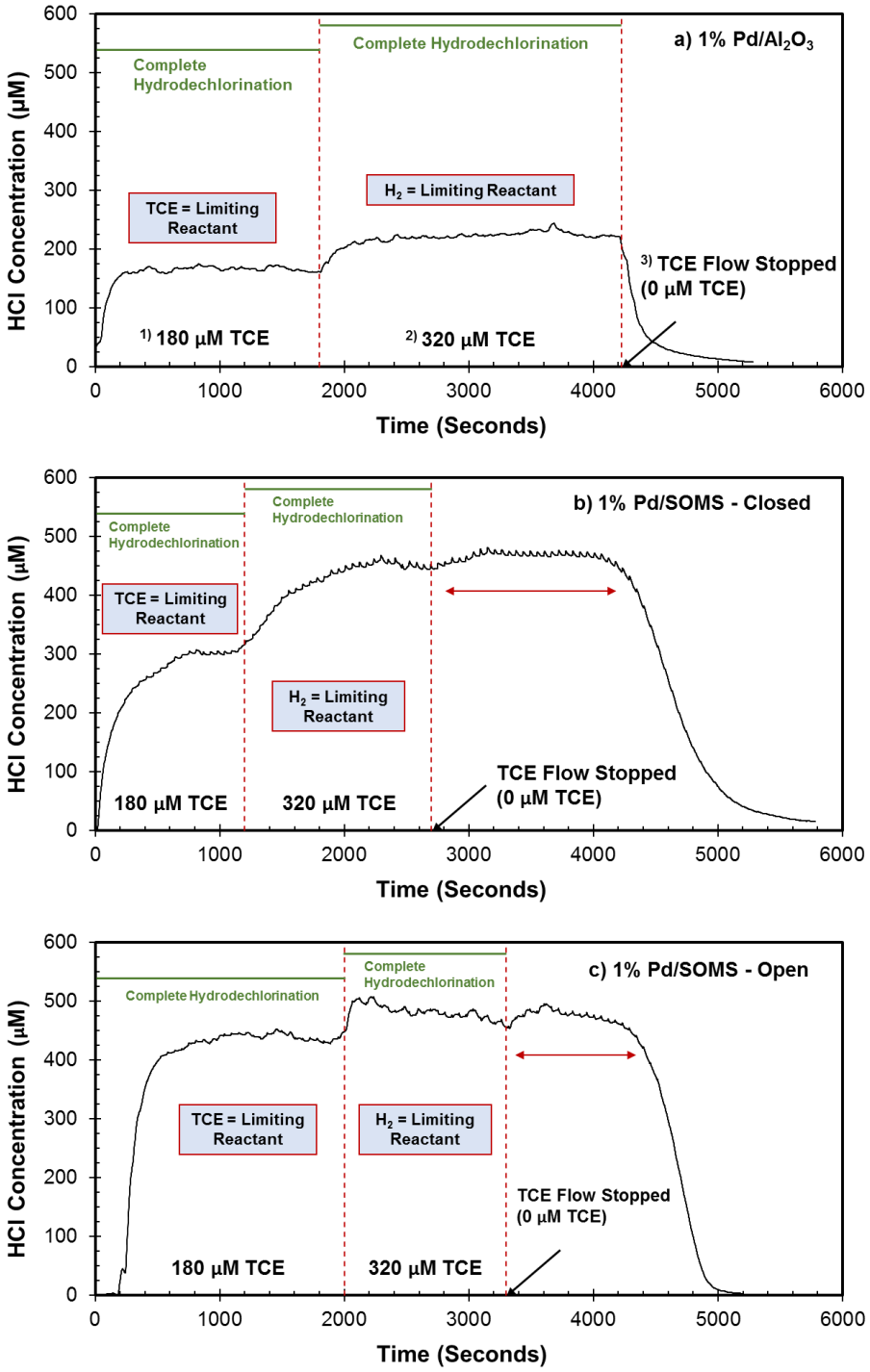

Figure 10. Catalytic activity data for a) 1% Pd/Al_2O_3, b) 1% Pd/SOMS-closed and c) Pd/SOMS-open for HDC of TCE in continuous flow liquid-phase reactor ***(Data was collected by ABS Materials)***

3.3.5.2 Catalytic activity of Li_2S poisoned Pd/SOMS and Pd/Al_2O_3

Another advantageous aspect of SOMS material is the hydrophobicity which makes the Pd/SOMS catalyst considerably resistant to ionic poisons. Various ionic poisons, which exist in groundwater, decrease the performance of the catalyst. Among them, several studies have shown that sulfur containing groups have a significant impact on the stability of Pd-based catalysts used for HDC of TCE. In this study, lithium sulfide (Li_2S) was used as a model poison compound in order to investigate the effectiveness of the hydrophobic SOMS support in protecting the Pd active sites from poisoning.

HDC activity was measured for 1% Pd/SOMS was poisoned ex-situ by soaking in a solution containing 5 ppm of Li_2S and 1 ppm Na_2CO_3 for 1 hr. As a comparison, 1% Pd/Al_2O_3 was also poisoned using Li_2S under the same conditions. Figure 11 (a) and (b) show the catalytic activity data collected over the two Li_2S-poisoned-samples for HDC of TCE. It is clear that a complete deactivation was observed for the Pd/Al_2O_3 catalyst after poisoning whereas Pd/SOMS remained partially active.

As previously mentioned, the observed initial time lag over Pd/SOMS catalyst was ascribed to the adsorption time of TCE into the pores of the support. However, compared to the fresh 1% Pd/SOMS-closed, the approach to steady state was slower (850 s vs 4100 s), i.e., more time was required to reach to the same conversion at steady-state for the poisoned sample. The vapor phase adsorption of TCE to Pd/Al_2O_3 and Pd/SOMS before and after poisoning was measured (Figure 12). Similar to other organic vapors, Pd/SOMS has a high adsorption capacity for TCE, 125% w/w, which is 10x more that the amount of TCE adsorbed by Pd/Al_2O_3. Exposure of Pd/SOMS to Li_2S had no deleterious effect on

the TCE adsorption, indicating that the slower activity is due to changes in catalyst activity and not the affinity of the sorbent support. The slower rise time is likely due to poisoning of Pd particles near the surface of the SOMS support whereas particles deeper in the hydrophobic matrix appear to be protected from sulfide. TCE must adsorb further into the pores to reach active catalyst. A longer time-lag was also seen when the TCE flow was stopped in which more than 50 min was spent to release all the adsorbed TCE molecules. These data indicate that the SOMS matrix can exclude anionic poisons, especially if the particles are embedded in the matrix where aqueous solutions cannot penetrate.

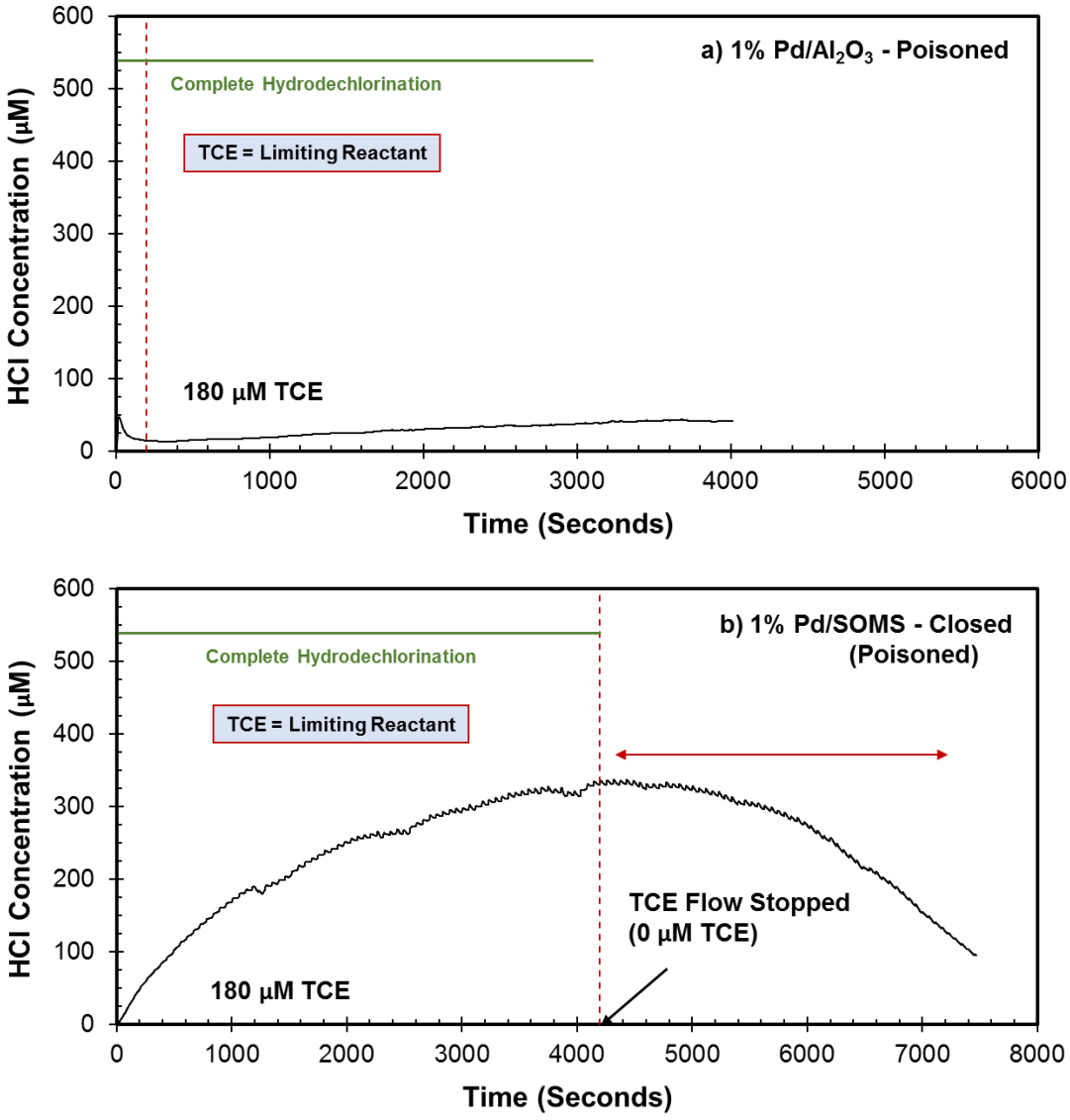

Figure 11. Catalytic activity data for a) Li_2S-poisoned 1% Pd/Al_2O_3 and b) Li_2S-poisoned 1% Pd/SOMS-closed for HDC of TCE in continuous flow liquid-phase reactor ***(Data was collected by ABS Materials)***

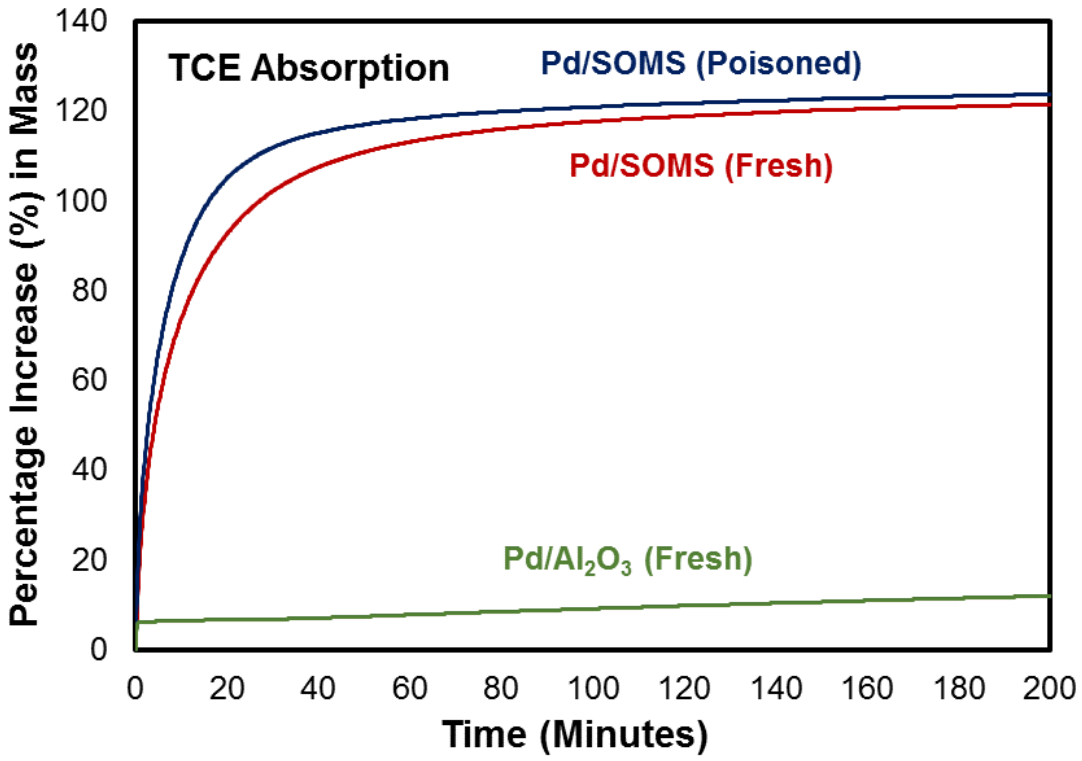

Figure 12. TCE adsorption profile for fresh and Li_2S-poisoned 1% Pd/SOMS-closed and fresh 1% Pd/Al_2O_3 catalysts ***(Data was collected by ABS Materials)***

3.3.6 Pd leaching with HCl

Catalyst deactivation due to HCl was investigated since HCl is a potential inhibitory product of the HDC of TCE reaction. The chloride ions interact with Pd active sites, they may affect the oxidation state of Pd, or facilitate the carbon deposition on the catalyst surface.[20, 61] Besides, Pd leaching has been reported due to decrease in pH during hydrodechlorination reactions.[73, 76] Similar to the previous sulfur poisoning studies, it was expected that the hydrophobicity of the Pd/SOMS catalyst provide some protection by repelling the Cl^- ions. However, it is possible that the resistance to chlorides may decay when high concentration of HCl is used. To allow comparison, both Pd/SOMS and Pd/Al_2O_3 were treated ex-situ using 1 M HCl and characterized using XPS, STEM/EDAX and ICP-OES techniques.

3.3.6.1 XPS Results

Figure 13 (a) shows the Cl 2p spectra collected over the HCl-treated Pd/SOMS and Pd/Al_2O_3 samples. The high intensity of the peak validates that Cl ions were adsorbed on the Pd/Al_2O_3 catalyst surface in contrast to Pd/SOMS sample where no Cl signal was detected. Regarding the Si 2p spectra, no oxidation state change of the Si was observed. The peak at 102.5 eV indicates that Si species consist lower oxidation state (1+ and 2+) including features of SiC peak.[98-100] The spectra for Pd 3d for Pd/Al_2O_3 in Figure 13 (c) were deconvoluted in order to perform quantification of the oxidation state of Pd particles and to understand the change in oxidation states due to HCl treatment. The peak assignments for Pd^0 and Pd^{2+} were determined based on the literature.[101-103] The constraints

used in fitting the spectra were that the ratio of the intensities of $3d_{3/2}$ and $3d_{5/2}$ was 2:3 and the two peaks were 5.26 eV apart from each other. Since the majority of the Pd particles were located inside the SOMS structure, no Pd was observed for Pd/SOMS (data not shown). However, using the same Pd loading, two distinctive peaks were found in the Pd 3d spectra over the pre-reduced Pd/Al_2O_3 catalyst. These results demonstrate that the Pd is embedded in the SOMS support. The effect of HCl treatment on the oxidation state of Pd on the Al_2O_3 support was apparent where a significant decrease in Pd signal intensity was observed due to Pd leaching. Furthermore, the oxidation state of Pd was increased from 0.12 (pre-reduced) to 1.98 after HCl treatment. This may be attributed to the formation of $PdCl^{3-}$ and $PdCl_4^{2-}$ complexes, which indirectly affect the change of oxidation state from Pd^0 to Pd^{2+} by stabilizing Pd in the higher oxidation state.[20]

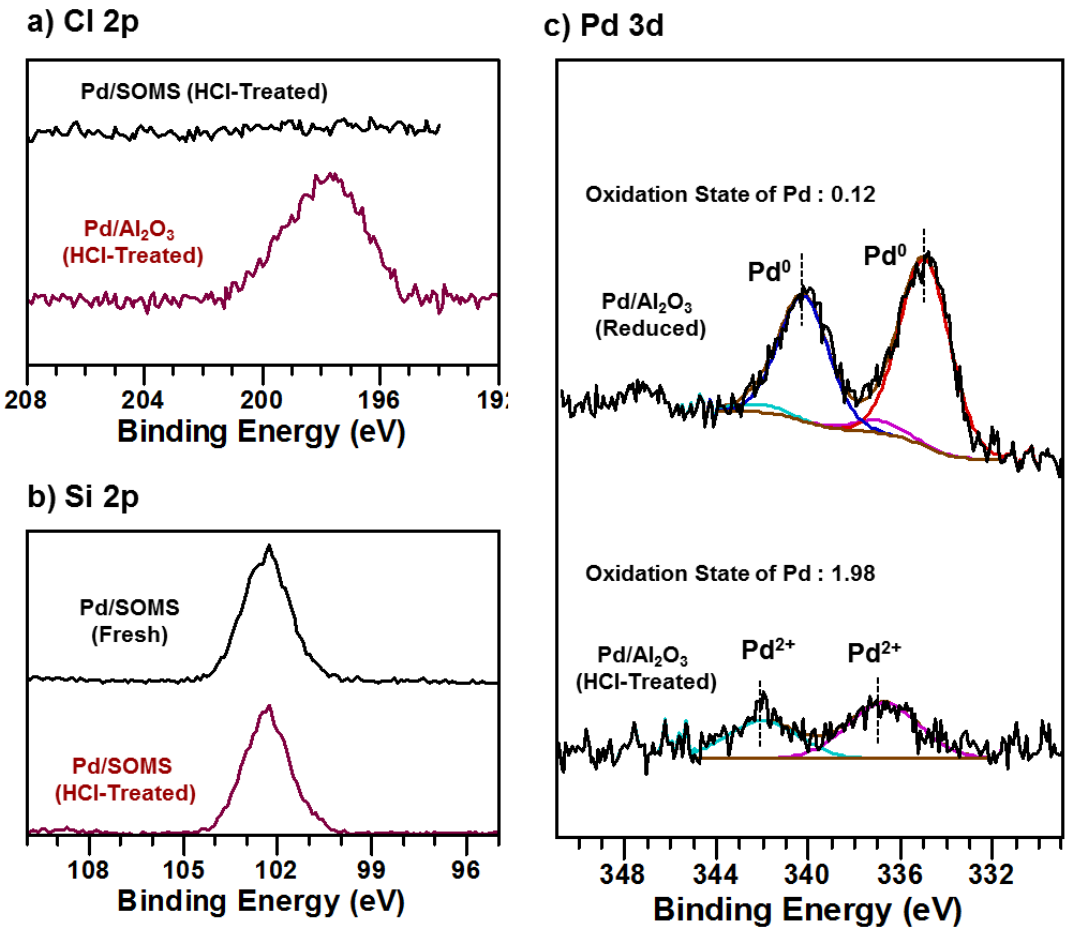

Figure 13. XPS spectra collected over fresh and HCl-treated 1% Pd/Al_2O_3 and 1% Pd/SOMS catalysts: a) Cl 2p, b) Si 2p and c) Pd 3d

3.3.6.2 STEM/EDAX and ICP-OES Results

STEM and TEM images were taken to observe the particle size and Pd dispersion on SOMS and Al_2O_3 supports. Figure 14 (a) presents STEM images of the fresh 1% Pd/SOMS where white dots represent Pd metals. The Pd metal particles are not homogeneously dispersed on the SOMS support. The particles size varies from in the 5-30 nm range. In some areas, Pd particles were seen to agglomerate forming aggregates. Heterogeneity may be due to non-uniform Pd distribution post-drying and/or the chemical reduction process where BH_4^- must penetrate the pores to reduce Pd^{2+}. In contrast to Pd/SOMS, the fresh 1% Pd/Al_2O_3 catalyst (Figure 14 (b)), exhibits a uniform dispersion of Pd metal with a very narrow particle size range of 2-5 nm.

STEM images and EDAX spectra were obtained over the HCl-treated Pd/Al_2O_3 catalysts. After the 1 M HCl treatment, most of the Pd particles were leached from the Al_2O_3 support as it is shown in the EDAX spectra which no longer displays a Pd peak (Figure 14 (d)). On the other hand, most of the Pd metal was still present in the HCl-treated Pd/SOMS sample (Figure 14 (c)). These results show that the hydrophobicity of the SOMS support plays an important role in protecting the Pd particles from chloride ions.

ICP-OES experiment was carried out to quantify the Pd leaching as well as to compare the chloride resistance of the Pd/SOMS and Pd/Al_2O_3 catalysts. The concentration of the Pd in the filtered solution (post-treatment) was acquired and compared to the original amount of Pd (1%). Based on these measurements, the percentage of Pd leaching was calculated and are shown in Table 2. Results from a control experiment where the catalysts were soaked in water only are also included to isolate the degradation effect due to HCl.

As it can be seen, no Pd leaching was observed using the 0 M HCl (pure water). When the HCl concentration was increased to 0.1 M, 74.4% of Pd leached out to the HCl solution from the Al_2O_3 support in contrary to the Pd/SOMS in which only 1.6% of Pd was leached. At 1 M HCl concentration, all the Pd particles were removed from the Al_2O_3 support as opposed to 6.4% of Pd/SOMS. These results show that the Pd sites over Pd/SOMS are better protected against leaching compared to Pd/Al_2O_3.

Table 2. ICP-OES results showing percentages of Pd leached from 1% Pd/Al_2O_3 and 1% Pd/SOMS samples after they were exposed to different concentrations of HCl

Pd leached (%)			
	0 M HCl	0.1 M HCl	1 M HCl
1%Pd/Al_2O_3	0	74.4	> 99
1%Pd/SOMS	0	1.6	6.4

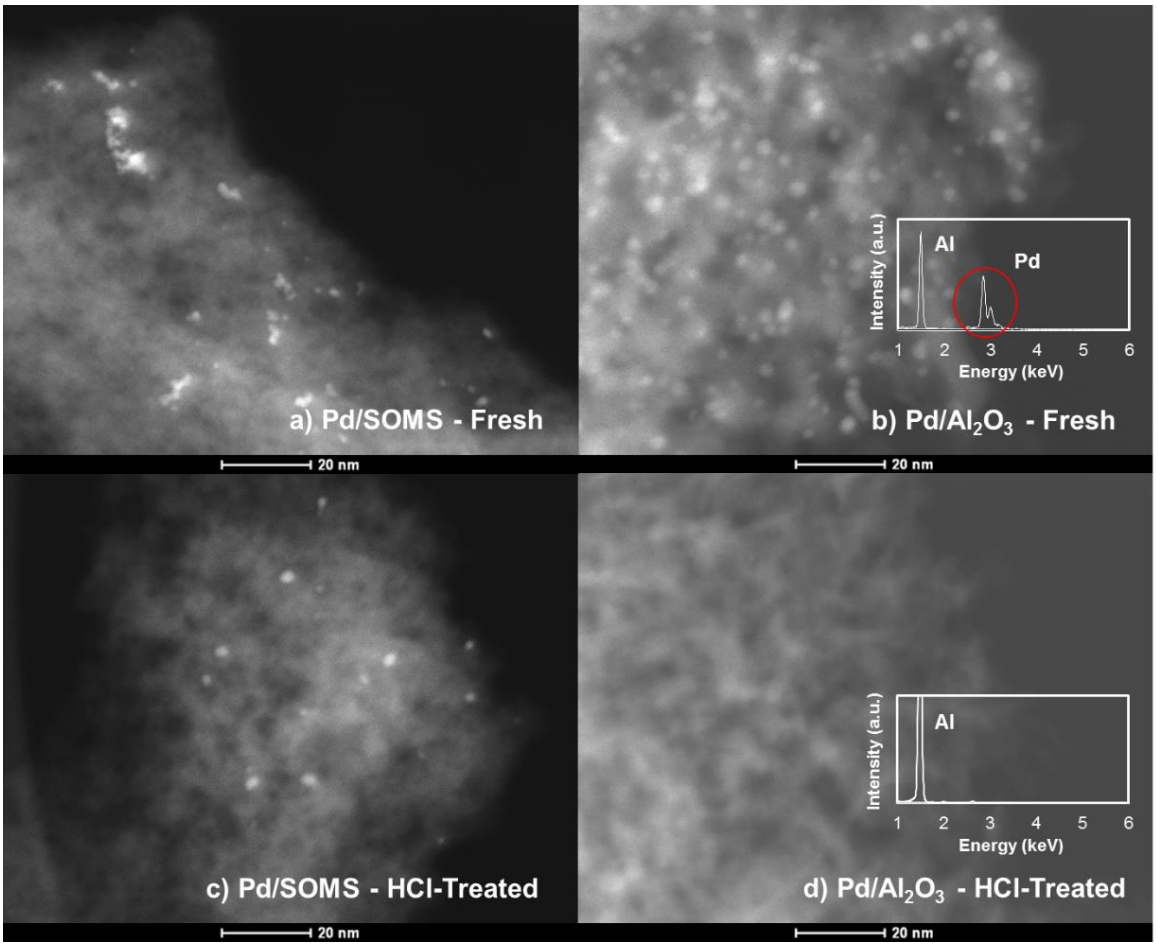

Figure 14. STEM images of fresh and HCl-treated Pd/Al_2O_3 and Pd/SOMS catalysts

3.3.7 HDC of TCE in the Gas Phase

In the gas phase, the degree of swelling of SOMS is much smaller and slower than it is in the liquid phase. Part of this is also due to the higher temperatures used in the gas-phase experiments. As mentioned earlier, the pore-opening process may play an important role for obtaining high catalytic activity since it impacts the accessibility of the Pd active sites and facilitates the concentration of the reactant (TCE) near the active sites (and potentially allowing HCl egress). Figure 15 shows a comparison of the TCE conversion on the Pd/SOMS and Pd/Al_2O_3 catalysts. In fresh form, 1% Pd/Al_2O_3 sample exhibited significantly higher catalytic performance at all temperatures tested compared to Pd/SOMS (fresh). The difference in catalytic activity of the Pd/SOMS between liquid and gas phase suggests that opening of the pores in SOMS is a key to its superior catalytic performance in the liquid phase HDC of TCE. The fact that Pd is embedded in SOMS helps the kinetics (including protection from anionic poisons), but may lead to a barrier to activity unless there is sufficient adsorption of TCE inside the pores.

The samples treated by 1 M HCl were also tested for gas-phase HDC of TCE. Due to strong Pd leaching over the Pd/Al_2O_3 catalyst, no conversion of TCE was observed. On the other hand, although the TCE conversion is low, there was almost no difference in terms of the catalytic activity between the fresh and HCl-treated Pd/SOMS. Figure 15 (c) shows the percent loss in TCE conversion over the two samples at 50, 100 and 150, 200 ℃. These results are significant in reiterating the importance of the pore architecture in SOMS as well as its ability to protect the Pd sites from leaching.

Lastly, the effect of water on the hydrodechlorination activity of Pd/Al_2O_3 and Pd/SOMS was examined, by adding water to the reactant stream. In the presence of water (4%), significant decrease in TCE conversions were observed over the Pd/Al_2O_3 catalyst in comparison with the case when the feed was water-free. There appears to be a strong inhibition effect with water over Pd/Al_2O_3.

In contrast, no decrease in TCE conversions were observed for Pd/SOMS sample with water. This indicates that the strong hydrophobicity of the SOMS support plays an important role for alleviating the water inhibition effect. Figure 16 (c) indicates the percent loss in TCE conversion in the presence of water in the TCE reactant stream. Interestingly, when the reaction temperature was increased to 200 ℃, Pd/Al_2O_3 showed better catalytic performance compared to Pd/SOMS in the presence of water. This is likely due to a decrease in the hydrophobicity of the SOMS at higher temperatures. When the %HDC values were compared (not shown), very similar trends were observed in all cases.

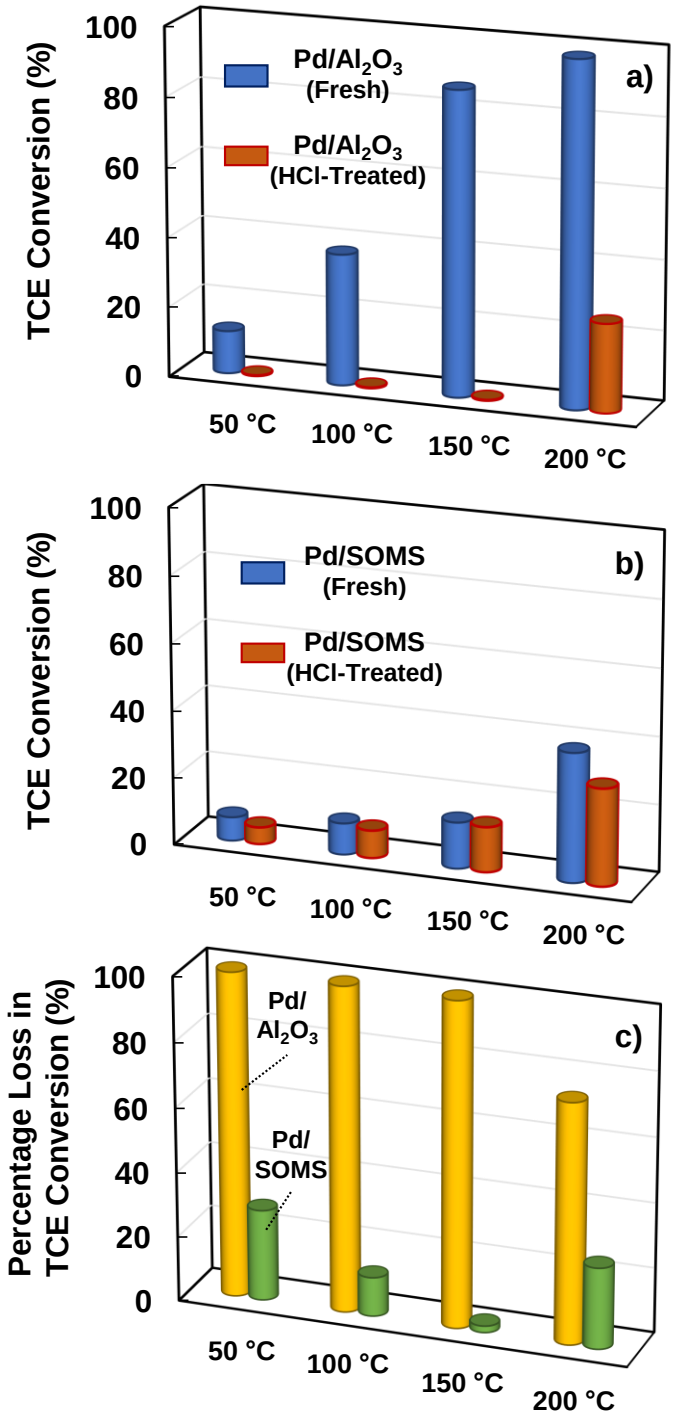

Figure 15. Catalytic activity data for fresh and HCl-treated of a) 1% Pd/Al_2O_3 and b) 1%Pd/SOMS samples for HDC of TCE in continuous flow gas-phase reactor, c) percentage loss in TCE conversion due to HCl treatment

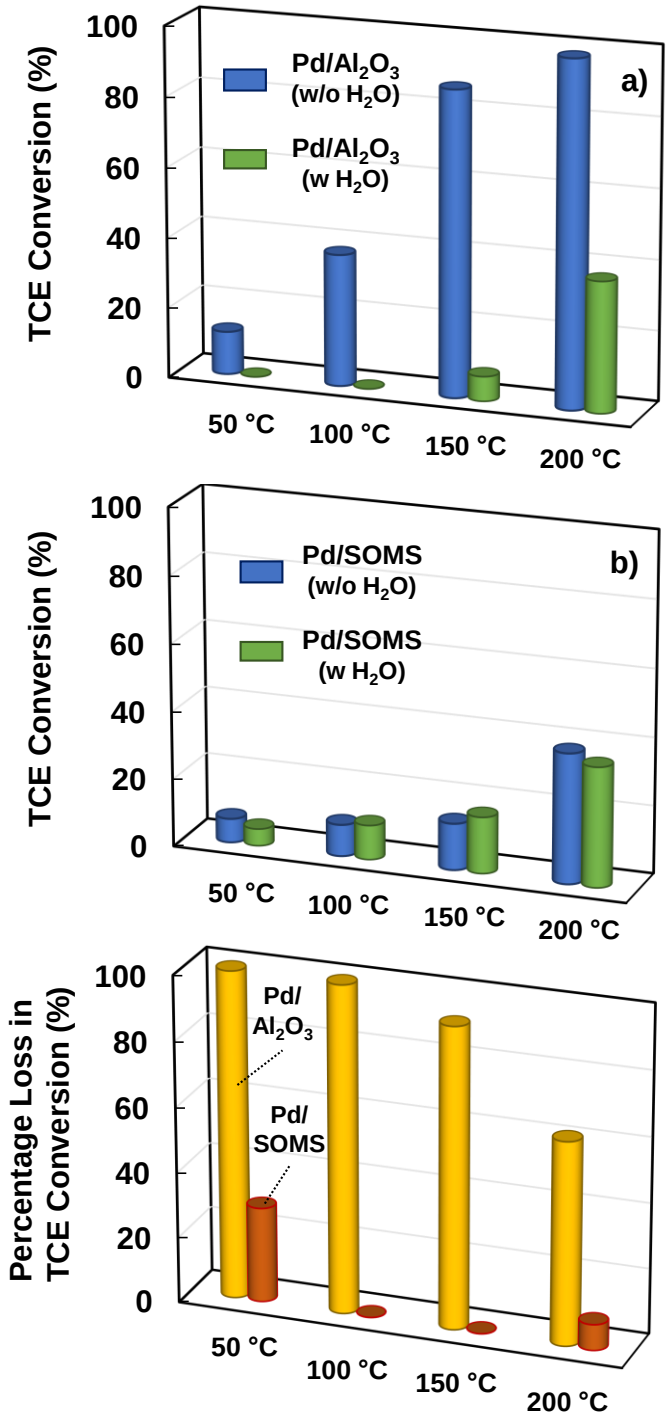

Figure 16. Catalytic activity data for a) 1% Pd/Al_2O_3 and b) 1%Pd/SOMS for HDC of TCE in the presence/absence of water in continuous flow gas-phase reactor, c) percentage loss in TCE conversion due to water in the feed

3.4 Conclusion of Chapter 3

Swellable organically-modified silica was shown to be a promising support for catalysts used for catalytic treatment of water contaminated with chlorinated hydrocarbons, specifically TCE. Both the swelling capability of SOMS and it high hydrophobicity play a role in improving the kinetics of hydrodechlorination of the reaction, by concentrating the organic contaminants inside the pores in the close vicinity of the pores. Pd catalysts supported on SOMS showed a higher HDC activity in the liquid phase compared to Pd/Al_2O_3 catalysts. Pd/SOMS catalysts were also shown to be more resistant to deactivation by sulfur compounds or chloride ions than those supported on alumina. Pd species inside the pores of the SOMS support were also shown to be protected against poisoning and leaching in lower pHs. This study demonstrates the high potential of these materials as catalyst scaffolds in many applications for catalytic water treatment.

** Information in this chapter was reproduced/adapted from " Sohn, H.; Celik, G.; Gunduz, S.; Dean, S. L.; Painting, E.; Edmiston, P.; Ozkan, U. S., Hydrodechlorination of Trichloroethylene over Swellable Organically-Modified Silica (SOMS). Submitted to Applied Catalysis B: Environmental"*

CHAPTER 4

HIGH-TEMPERATURE-TREATED SWELLABLE ORGANICALLY-MODIFIED SILICA (H-SOMS) AND ITS APPLICATION TO GAS-PHASE HYDRODECHLORINATION OF TRICHLOROETHYLENE

4.1 Summary of Chapter 4

Pd supported on swellable organically-modified silica (SOMS) and high-temperature-treated swellable organically-modified silica (H-SOMS) were tested for its catalytic activities under gas-phase hydrodechlorination (HDC) of trichloroethylene (TCE) conditions. High-temperature treatment on SOMS resulted in increase in surface area and pore diameter of the SOMS material (H-SOMS). In addition, the dispersion of Pd on H-SOMS was significantly improved with smaller Pd particle sizes compared to Pd/SOMS catalyst. The reduction and re-oxidation of Pd were investigated using XANES technique. It was found that the Pd sites in the pores of SOMS was accessible to small molecules such as H_2 indicating reduction of Pd, whereas oxidation of Pd was limited even at higher temperatures when O_2 was used. The selective adsorption according to the particle size of a molecule was only obtained over Pd/SOMS catalyst. For Pd/H-SOMS, because the pores were widely open than Pd/SOMS, both reduction and oxidation of Pd were observed. The order of catalytic activity towards gas-phase HDC of TCE was obtained as Pd/H-SOMS >

Pd/SOMS, but both catalysts were less active compared to Pd/Al_2O_3. However, when water was added to the reactant stream (TCE+H_2O), significant water inhibition effect was revealed for Pd/Al_2O_3, leading to a complete degradation of the catalyst. On the other hand, Pd/SOMS and Pd/H-SOMS maintained its catalytic performances due to hydrophobic property of the supports. When all the samples were treated with 1 M HCl, most of the Pd particles were leached out from the Al_2O_3 support contradictory to Pd/SOMS where no Pd leaching was observed. With respect to Pd/H-SOMS, although the support was hydrophobic, a fair amount of Pd was removed from the support (Pd/Al_2O_3 > Pd/H-SOMS > Pd/SOMS).

4.2 Experimental Section

4.2.1 Catalyst Preparation

A detailed sol-gel synthesis method to prepare SOMS was reported by Edmiston and coworkers.[16-18, 81-82] First of all, a solution of 0.144 mol of bis(trimethoxysilylethyl) benzene (BTEB) was dissolved in 220 ml of acetone. The solution was added to another solution which contains 1.5 ml of 1 M tetrabutylammo-nium fluoride in 7.8 ml of water. The mixing initiated gelation and the resulting gel was kept at room temperature (RT) for 6 days. Through evaporation of the solvents, the remaining solids were filtered and rinsed with acetone. The solids were then grounded and derivatized using 5 v/v % solution of cyanopropyltrimethylsilane in acetonitrile for 24 h. Finally, the solution was filtered and the remaining solids were washed with acetone and dried at 110 ℃ to acquire SOMS with a white color.

The high-temperature-treated SOMS, referred to as H-SOMS in this paper, was prepared by calcining SOMS under inert conditions. The SOMS was first saturated with acetone until no more volume expansion was observed (fully swollen). This was to increase the surface area and pore volume of the SOMS to its maximum state before the calcination was carried out. The saturated SOMS was placed into a sealed horizontal quartz tube which was flushed with nitrogen for 5 min to remove oxygen inside. The quartz tube was then transferred into the center of a heated furnace at 600 ℃ while nitrogen was flowing through the tube. SOMS was calcined for 2 hr under inert conditions (nitrogen). Afterwards, the calcined SOMS, i.e. H-SOMS, was obtained as brown-colored solids.

Incipient wetness impregnation (IWI) technique was utilized to place Pd particles on SOMS support. A known amount of Pd acetate solids were dissolved in acetone solution in order to obtain 1% wt Pd. The Pd precursor solution was then added drop-wise until SOMS was saturated reaching its maximum expansion state. At this point, the volume of SOMS was about 2.5 times compared to its original size. The Pd impregnated SOMS was then dried at 25℃ with constant agitation to prevent migration of the Pd particle towards a certain direction during evaporation (observed only over SOMS). The entire process was repeated multiple times to use all the precursor solution. The 1% Pd/SOMS was obtained after drying at the end. For H-SOMS, similar preparation steps were employed, except that the solids were dried at 100 ℃.

The reduction of Pd (Pd^{2+} to Pd^{0}) was carried out chemically using a saturated solution of $NaBH_4$ in 95% ethanol in the case of 1% Pd/SOMS. After Pd/SOMS was soaked in the $NaBH_4$ solution, it was filtered and rinsed with ethanol followed by deionized water. The remaining solids were dried at 60 ℃. In regards to 1% Pd/H-SOMS, 5% H_2/He

gas was utilized at which the catalyst was reduced in situ at 400 ℃ for 1 h. The reduced Pd/H-SOMS was then treated with helium at 450 ℃ for 30 min for surface clean-up. For comparison purposes, 1% Pd/Al_2O_3 was also purchased from Sigma-Aldrich and went through the same pre-reduction process as Pd/H-SOMS.

4.2.2 Catalyst Characterization

4.2.2.1 Temperature Programmed Desorption (TPD)

TPD experiment was performed using a Carbolite MTF 10/15/130 furnace where a 4 mm-ID quartz reactor located at the center of the furnace. SOMS was first placed inside the quartz reactor supported by quartz wools. A continuous flow of pure helium was then introduced to the reactor at 30 ml/min at RT and reached a mass spectrometer (MS - MKS-Cirrus II) operated in scanning ion mode. Once a stable MS signal of helium was obtained, the furnace temperature was increased gradually at a ramp rate of 10 ℃/min from RT to 800 ℃ and stayed there for few hours. For identification of the products, signals from m/z=2 to 60 were collected.

4.2.2.2 ^{29}Si Nuclear magnetic resonance (NMR) and Infrared (IR) Spectroscopy

^{29}Si MAS (Magic Angle Spinning) NMR spectra were collected over Pd/SOMS and Pd/H-SOMS samples using Bruker DPX 300 MHz NMR instrument at a resonance frequency of 59.6 MHz. A standard of TMS was used as a reference for 0 ppm. SpinWorks 4.2.3.0 © 2016 software was utilized for line broadening of the spectra. FTIR-ATR spectra

of SOMS and H-SOMS were acquired using a Thermo Nicolet 6700 FTIR Spectrometer with a diamond attenuated total reflectance accessory.

4.2.2.3 Surface Area, Pore Size and Pore Volume

(BET) surface area and Brunauer-Joyner-Helena (BJH) pore volumes of SOMS, H-SOMS, Pd/SOMS, Pd/H-SOMS and Pd/Al_2O_3 were measured using Micromeritics ASAP 2020 (accelerated surface area and porosimetry) instrument. The samples were first degassed for 12 h at 130 ℃ under 2 μm Hg of vacuum and transferred to the analysis port to obtain nitrogen adsorption/desorption isotherms of the samples. The analysis was conducted at liquid nitrogen temperature and the saturation pressure of nitrogen was measured frequently to improve accuracy of the relative pressure calculation. The BJH pore size distribution was acquired using the desorption branch of the isotherm.

4.2.2.4 High Angle Annular Dark Field (HAADF) Scanning Transmission Electron Microscopy (STEM)

Identification and particle size information of Pd were obtained by taking HADDF-STEM images. A small amount of Pd/SOMS, Pd/H-SOMS and Pd/Al_2O_3 was first dissolved in ethanol and stirred rigorously for 5 min using a sonicator. The resulted solution was then placed drop-wise on a Tedpella, Inc. 200 mesh copper grid coated with lacey carbon sample holder. After a drying step at RT for 1 hr, the sample holder was transferred to FEI Tecnai F20 instrument equipped with a high brightness field emission electron gun

(FEG) operated at 200 kV and a HADDF detector. Multiple images were taken in different spots of the TEM grid to ensure uniformity of the Pd particle sizes.

4.2.2.5 Static Vapor-Phase Adsorption

Pyris 1 Perkin-Elmer thermogravimetric analyzer (TGA) was exploited to obtain acetone adsorption profiles of the Pd/SOMS, Pd/H-SOMS and Pd/Al_2O_3 catalyst. The sample was placed inside a seal container in which a saturated acetone vapor was introduced. The mass of the sample was first measured at 0 s and collected continuously every 6 s until no mass increased was observed. Percentage increase in mass (%) was calculated for each sample (increased mass / original mass × 100).

4.2.2.6 CO Chemisorption

Carbon monoxide (CO) were used as a probe molecule in order to obtain the dispersion of Pd particles on SOMS, H-SOMS and Al_2O_3 supports. A similar reactor system used in the TPD experiment was employed with an addition of a 6-port valve which allows to send CO gases in pulses. All the samples were first pre-reduced prior to CO chemisorption. Pd/SOMS was reduced chemically using $NaBH_4$ solution while the other two were pre-reduced in situ under 5% H_2/He at 400 ℃. The CO chemisorption started at RT sending a known amount of CO to the catalyst bed in several pulses until equilibrium was reached. The outlet of the reactor was connected to a MS and the amount of CO uptake at each pulse was quantified based on the feed (250 µl sample loop) which was calibrated before the reaction. The Pd dispersion was calculated as "number of moles of Pd reacted

with CO / number of moles Pd in the sample". The calculation was performed assuming 1:1 ratio of Pd to CO.

4.2.2.7 *In Situ* X-ray Absorption Near Edge Structure (XANES) Spectroscopy

In situ XANES spectra were collected at the insertion device (Sector 10-ID) beamline of the Materials Research Collaborative Access Team (MRCAT) located at the Advanced Photon Source (APS) - Argonne National Laboratory. The measurements were performed in transmission mode using a Si (111) monochromator with a harmonic rejection mirror covered with Pt and Rh. The 1% Pd/SOMS, 1% Pd/H-SOMS and 1% Pd/Al_2O_3 samples were first finely ground with/without addition of silica as a diluent to obtain a proper Pd K edge (24.36 KeV) jump. The prepared three samples were then pressed gently into a six-well sample holder made of stainless steel which was inserted horizontally to a 45 cm long quartz tube (2 cm ID). The inlet and outlet of the quartz tube were connected to Swagelok gas lines to allow *in situ* experiments.

All the samples went through the same treatment conditions as follow: (1) pre-oxidation at 150 ℃, (2) oxidation at 250 ℃ (3) reduction at 150 and 250 ℃, (4) re-oxidation at 150 and 250 ℃. The sample was kept at each temperature for 30 min. The gases used for oxidation and reduction were 5 % O_2/He and 3.6 % H_2/He, respectively. The switch between gases was made after the existing gas in the lines was flushed with helium. It should be noted that it was not possible to collect the XANES spectra for all three samples simultaneously. Since only 15 s was spent to collect XANES spectrum for each sample, there is a 15 s time delay between the first and second sample. Likewise, the first

and third sample has a 30 s time delay. Lastly, the quantification of Pd oxidation states was obtained using WinXAS software by linear combination between the spectra of Pd metal foil and PdO standard.

4.2.2.8 X-ray photoelectron spectroscopy (XPS) and Inductively Coupled Plasma Optical Emission Spectrometry (ICP-OES)

XPS and ICP-OES techniques were exploited to investigate Pd leaching of 1 M HCl-treated Pd/SOMS, Pd/H-SOMS and Pd/Al_2O_3 catalysts. Samples were first soaked in 1 M HCl solutions and stirred extensively for 20 min at RT. The sample was then filtered and subjected to XPS analysis while the remaining solution was tested for elemental analysis for Pd using Perkin-Elmer Optima 4300DV ICP-OES instrument. The XPS spectra of the samples in C 1s and Pd 3d region were obtained by a Kratos AXIS Ultra X-ray photoelectron spectrometer with a monochromatized Al K_α X-ray source operated at 13 kV and 10 mA. CasaXPS software was utilized to perform peak-fitting and quantification of Pd oxidation states of the spectra collected.

4.2.3 Catalyst Activity Testing

Gas-phase HDC of TCE was performed over 1% Pd/SOMS, 1% Pd/H-SOMS and 1% Pd/Al_2O_3 catalysts in a bench-scale fixed bed flow reactor system. TCE vapors were generated using a bubbler heated at 35 ℃ by flushing with nitrogen as a carrier gas. The TCE and nitrogen gas compound was then mixed with more nitrogen in order to lower the concentration of TCE. Afterwards, hydrogen was added to the mixture resulting reactants

of 0.7% TCE in excess hydrogen at 1:30, TCE-to-hydrogen molar ratio. For HDC of TCE experiments in the presence of water vapor, the water concentration in the feed was 4%. The reactants were then sent to the catalyst bed located inside the 4 mm-ID quartz reactor. The gas-phase HDC of reaction was carried out at 100, 150 and 200 ℃. The reactor temperature was increased/decreased by an Omega CSC232 PID temperature controller which adjusts the temperature of the surrounding furnace (Carbolite, MTF 10/15/130). All the catalysts were pre-reduced prior to the reaction (Pd/SOMS → $NaBH_4$, Pd/H-SOMS and Pd/Al_2O_3 → *in situ* H_2). For accurate comparison, the catalytic activities of the samples were obtained at equal gas hour space velocity (GHSV). The end of the reactor was connected to online gas chromatography (Shimadzu Scientific 2010) which constitutes a Q-bond column and a flame ionization detector (FID). The oven temperature, injector pressure/linear velocity of the He carrier gas were altered to obtain widespread separation of the product peaks including TCE, partially dechlorinated compounds, short-chain hydrocarbons especially the major product ethane. The carbon contacting product yield and TCE conversion were calculated by the following equations.

$$Carbon\ Containing\ Product\ Yield = \frac{Number\ of\ Carbon\ in\ Product\ \times\ Moles\ of\ Product}{2\ \times\ Moles\ of\ TCE\ Fed} \times 100$$

$$TCE\ Conversion = \frac{Moles\ of\ TCE\ Fed - Unreacted\ Moles\ of\ TCE}{Moles\ of\ TCE\ Fed} \times 100$$

4.3 Results and Discussion

4.3.1 Calcination of SOMS

The preparation for H-SOMS involves a calcination process under inert atmosphere in which SOMS is instantly calcined at 600 ℃ for 2 hr. A temperature-programmed desorption (TPD) experiment was conducted under helium environment to identify the species that were evolved from the SOMS during calcination. Figure 17 shows the spectra which follow different mass-to-charge ratio (m/z) intensities of 2 (H_2), 15 (CH_4), 18 (H_2O), 28 (C_2H_6), 29 (C_3H_8), 32(O_2) and 44(CO_2). The m/z values were selected considering the fragmentations of molecular ions of the gases so that there are no contributions in the intensities to each other. As it is demonstrated in the TPD results, the decomposition of SOMS started around 450 ℃ releasing short chain hydrocarbons such as methane, ethane and propane as well as hydrogen, oxygen and water. The fact that majority of the products are methane and ethane indicates the C-C bond cleavages of aromatic rings composing the SOMS structure. This resulted in a significant amount of carbon deposition on the SOMS surface as the color of the material changed completely black after calcination. After the reactor temperature was increased to 800 ℃, the temperature was maintained for few more hours. By then, most of the gases were liberated from the SOMS material at which the m/z signals returned to its original intensities.

The absence of oxygen in the atmosphere led to trivial amount of CO_2 formation, although slight increase in CO_2 intensity was observed which can be due to remaining surface oxygen. It is important to note that the synthesis of H-SOMS is not an oxidation; therefore, the carbon-containing organic groups are still present in the SOMS matrix.

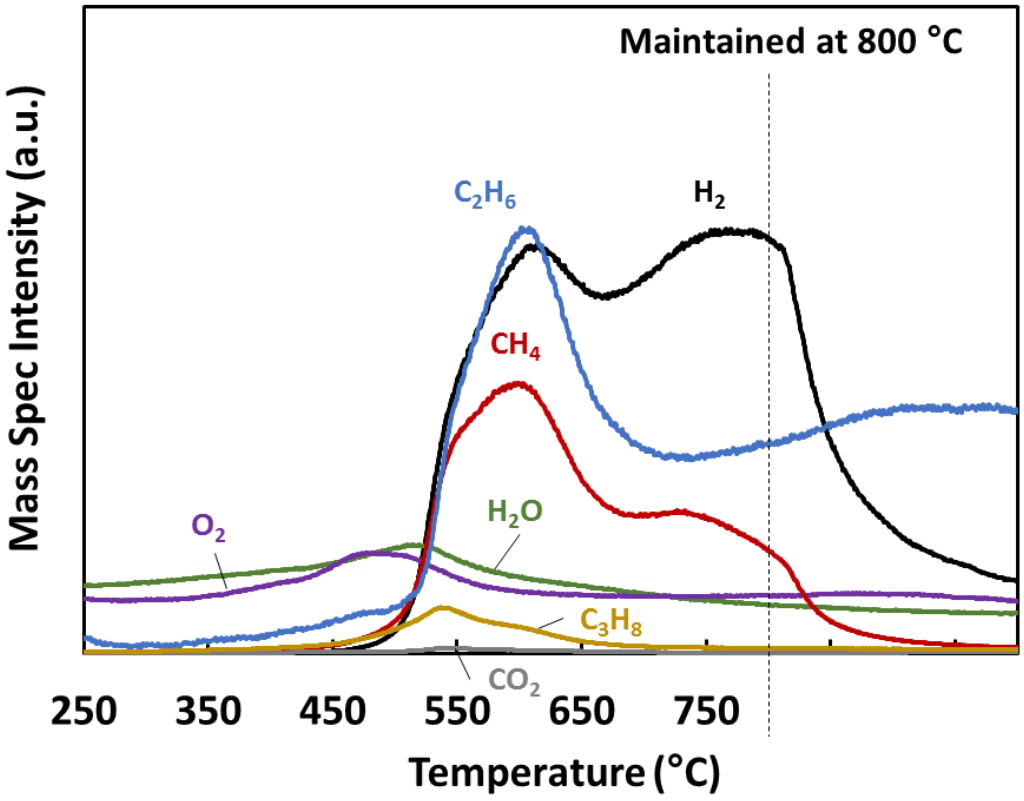

Figure 17. Desorbed species during calcination of SOMS under helium environment

4.3.2 Chemical Structure of H-SOMS

4.3.2.1 IR results

IR spectra over SOMS and H-SOMS were obtained to understand the change in structural properties of the materials. Figure 18 (a) shows the spectra collected in the range of 600 to 1800 cm^{-1} and (b) from 600 to 3600 cm^{-1}. With respect to SOMS, the two peaks located at 1034 and 1093 cm^{-1} are correlated to eh Si-O-Si stretching.[92] The 1093 cm^{-1} peak is assigned to longitudinal-optic (LO)–transverse-optical (TO) splitting with an additional peak at 1188 cm^{-1},[96] specifically, indicating LO3-TO3 antisymmetric stretching which was reported due to long range coupling of Coulomb interactions.[93-95] These bands are not present in the H-SOMS spectra. It was found that the antisymmetric stretching LO3 (1188)–TO3 (1093) cm^{-1} vibration was related to the swelling capability of the SOMS material. Thus, based on the disappearance of the peaks, the data evidently indicates that H-SOMS does not involve swelling (expansion and contraction of the material) during absorption of organic molecules.

Near the lower wavelength region of the SOMS spectrum, peaks 688 and 754 cm^{-1} were likely to be assigned to out-of-plane C-H bending/wagging vibrations of mono and meta substituted benzene compounds.[92, 97] Similarly, for 1400 to 1700 cm^{-1} region, several peaks were appeared which were linked to in-plane C-H bending of substituted benzenes.[97] These bands are not visible for H-SOMS which leads to a conclusion that almost all of the aromatic rings were decomposed due to high temperature treatment.

Lastly, IR bands at 764, 845 and 1252 cm^{-1} of the SOMS spectrum indicates that O-Si-$(CH_3)_3$ are present in the SOMS material.[92] The formation of trimethylsilyl group is

likely resulted from the derivatization process during SOMS synthesis (chlorotrimethysilane treatment).[16] This eliminates the residual Si-OH groups which helps to prevent Si-O-Si bond formation as well as to maintain the flexibility of the SOMS structure. However, the intensities of 763 and 1252 cm^{-1} peaks significantly decreases for H-SOMS; instead, two peaks of 795 and 1273 cm^{-1} appear in the spectrum. The shifts of 763 to 795 cm^{-1} and 1252 to 1273 cm^{-1} is relevant to generation of dimethyl groups (O-Si-$(CH_3)_2$-).[92] This shows that the calcination of SOMS under inert conditions causes the destruction of the end-capped trimethylsiyl and forms more linkages of the polysiloxane network.

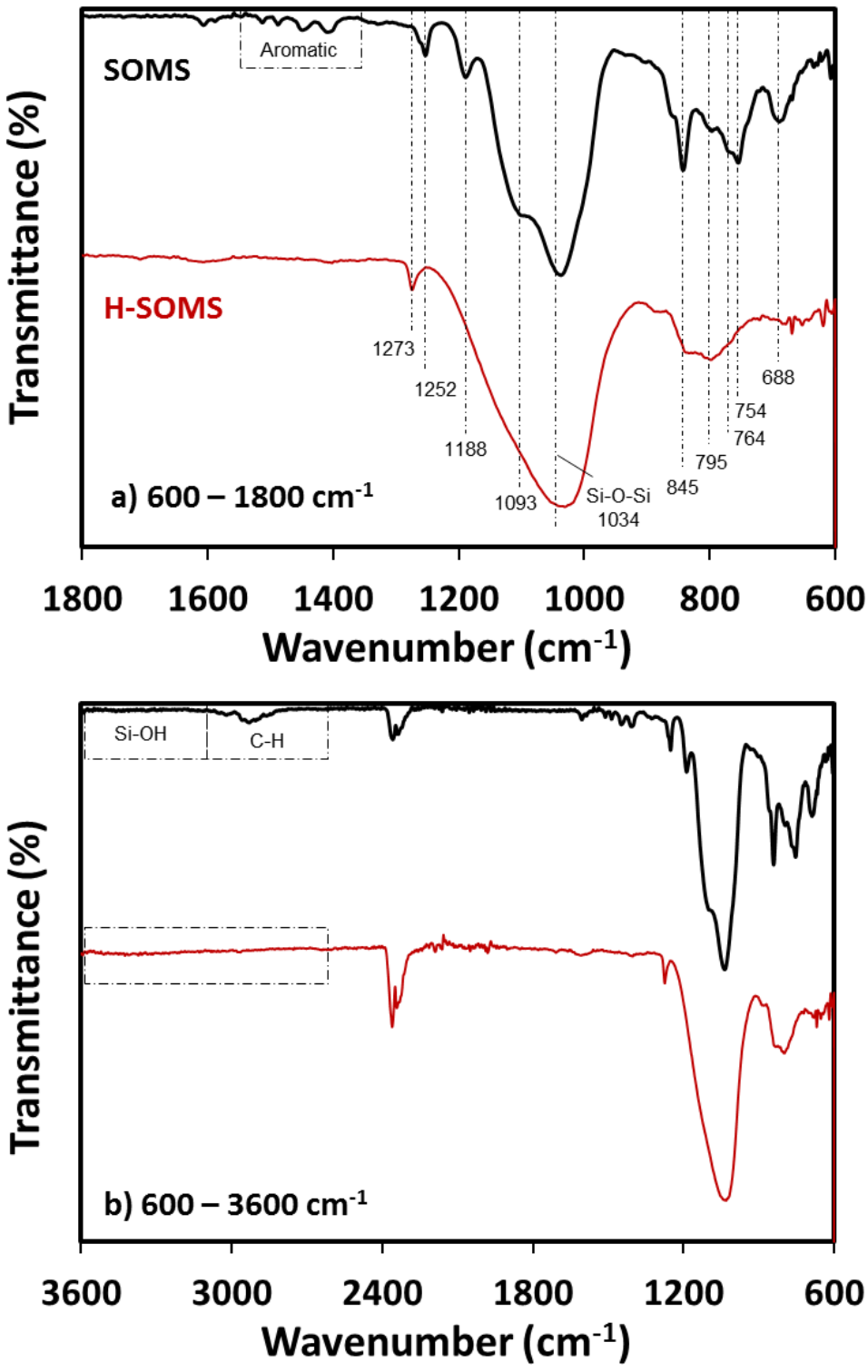

Figure 18. IR spectra for SOMS and H-SOMS in the range of a) 600 - 1800 cm^{-1} and b) 600 - 3600cm^{-1} ***(Data was collected by ABS Materials)***

4.3.2.2 Si^{29} NMR results

The structure characteristic of SOMS and H-SOMS were investigated in detail using Si^{29} NMR. Figure 19 expresses the collected spectra over the Pd/SOMS and Pd/H-SOMS materials. The NMR spectrum of Pd/SOMS consists of three distinctive peaks, one at 8 ppm and the other two at -59 ppm and -68 ppm. The first lower region around 8 ppm corresponds to the (SiO)-Si*-RR'R" where the center Si* is attached to a SiO group and three substituents.[104] In this case, all three substituents are methyl groups of (SiO)-Si*-$(CH_3)_3$ which agrees with the IR data.[104-106] The peak at -59 and -68 ppm are due to $(SiO)_2$-Si*-(OCH_3)R[106] and $(SiO)_3$-Si*-R[107] chemical sites where Si* is bonded to three oxygens (O).[108] Specifically, it is likely that the substituted benzenes may contribute to the intensity of these two peaks.[109]

With regards to H-SOMS, the high temperature treatment was revealed to have a significant impact on the chemical structure of SOMS. The appearance of peak around -105 ppm region indicates $(SiO)_4$-Si* at which Si*is linked to four SiO groups.[107] The formation of additional Si-O bonds was certainly due to decomposition of SOMS releasing mostly hydrocarbons in gas phase, not oxygen-containing species. It can be concluded that the thermal treatment process under inert condition transferred SOMS into a more silica-like material (SiO_2), however, it should be noted that the peak at around -65 ppm for H-SOMS still indicates the presence of organic species in the H-SOMS support matrix.

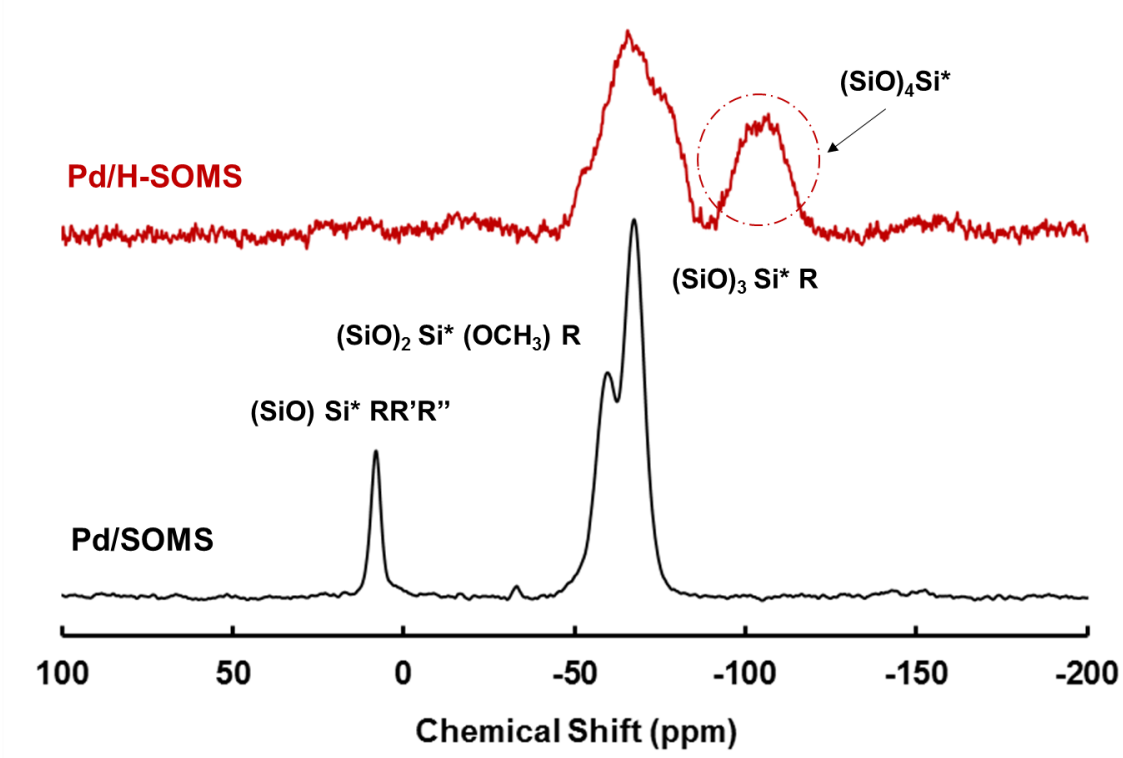

Figure 19. NMR spectra for SOMS and H-SOMS

4.3.3 Surface Area, Pore Volume and Averaged Pore Diameter

Table 3 shows the BET surface area, pore volume and averaged pore diameter of the samples used for this study. It was observed that the BET surface area of SOMS was increased significantly after high-temperature treatment was performed (493 $m^2/g \rightarrow 682$ m^2/g). Likewise, the increase in pore volume and averaged pore diameter possibly indicates formation of larger pores during calcination process. The increase in these values are not common to other materials where a structural contraction is more often observed after calcination. The impregnation of Pd particles on SOMS and H-SOMS supports led to a decrease in BET surface area, pore volume and averaged pore diameter compared to its bare SOMS and H-SOMS supports. This assures that the Pd particles are located inside the pores of the catalyst. The BET surface area of 1% Pd/Al_2O_3 was lower compared to other samples whereas the average pore diameter was significantly larger.

4.3.4 Particle Size

The Pd particle sizes of 1% Pd/H-SOMS and 1% Pd/SOMS samples were measured using STEM technique (Figure 20). With respect to Pd/SOMS, Pd particles (shown as white dots) on SOMS support are not well distributed compared to Pd/H-SOMS catalyst. The average Pd particle size for Pd/SOMS was estimated around 9 nm. Also, larger Pd particles above 20 nm were observed (not shown in the figure). The non-homogeneous distribution of Pd particles and formation of larger Pd clusters are most likely attributed to the expansion/compression of the SOMS matrix during the Pd impregnation, drying and/or $NaBH_4$ chemical reduction processes. Especially, while SOMS returns to its tensioned

matrix due to evaporation of the organic solvents (acetone/ethanol), it may cause relocation and agglomeration of the Pd particles.

On the other hand, the Pd particles on the H-SOMS support were smaller than on SOMS with an average Pd particle size of 4 nm. The Pd particles were more homogenously dispersed on H-SOMS with narrower particle size distribution compared to Pd/SOMS catalyst. As it is shown, between Figure 20 (a) and (b), significantly more Pd particles are seen in the same scale image. It is worth to note that the process of Pd impregnation on H-SOMS does not accompany with any physical expansion/compression (swelling) of the support matrix; therefore, it can be speculated that the swelling behavior strongly affects in determination of the Pd particle size.

Table 3. BET Surface area, pore volume and average pore diameter of SOMS and H-SOMS

	BET Surface Area	Pore Volume	Averaged Pore Diameter
	(m^2/g)	(cm^3/g)	(Å)
SOMS	493	1.03	84
H-SOMS	682	2.07	122
1% Pd/SOMS	479	0.56	47
1% Pd/H-SOMS	546	1.09	75
1% Pd/Al_2O_3	156	0.85	217

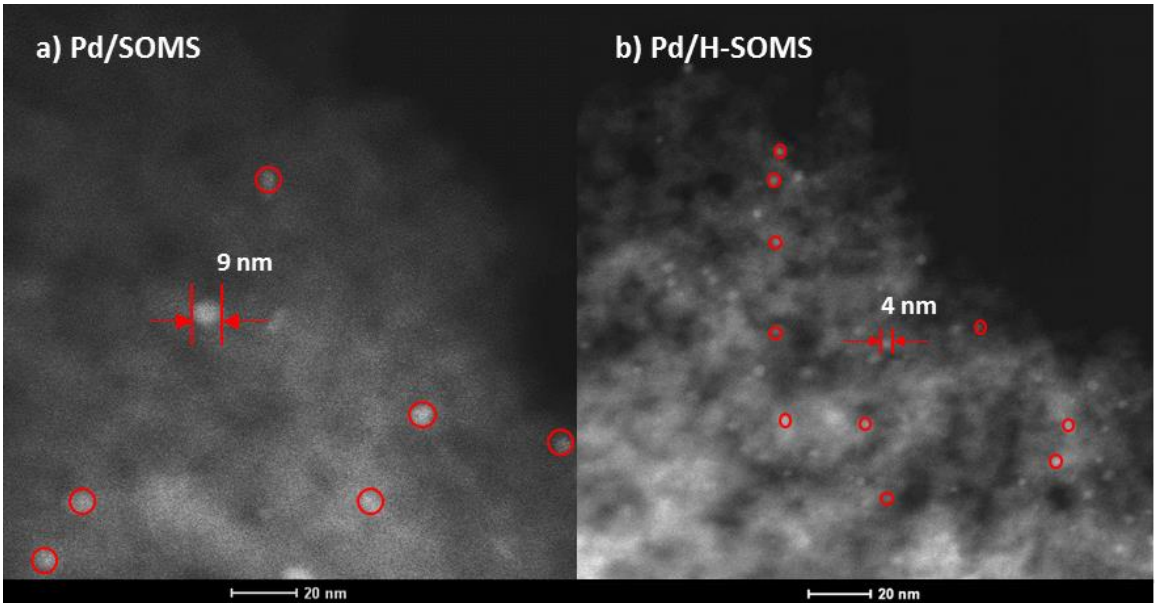

Figure 20. STEM images of Pd/SOMS and Pd/H-SOMS (white dots represents Pd particles)

4.3.5 Acetone Vapor Adsorption in Static Condition

The adsorption capacity and affinity of 1% Pd/SOMS, 1% Pd/H-SOMS and commercial 1% Pd/Al_2O_3 catalysts to acetone were examined in a static condition. In Figure 21, the percentage increase in mass of the three samples are plotted with respect to exposure time to the acetone vapor. The highest affinity to acetone was obtained over the Pd/SOMS catalyst. At 120 min of adsorption time, the mass of the Pd/SOMS increased twice as before the original. The adsorption capacity at this point is roughly 4 times higher as opposed to the Pd/Al_2O_3 sample. With regard to the Pd/H-SOMS sample, the adsorption capacity and affinity to acetone is in between that of Pd/SOMS and Pd/Al_2O_3. As mentioned earlier, the calcination of SOMS results in reduction of extent of swelling and hydrophobicity. The swelling of the SOMS structure is closely associated with the formation of new pores and surface areas which increase the adsorption capacity of the material. Therefore, these results are expectable since the degree of swelling for Pd/H-SOMS are much lesser than Pd/SOMS catalyst. However, the adsorption capacity and affinity of Pd/H-SOMS to acetone are still greater compared to the commercial Pd/Al_2O_3.

An interesting observation was that the rate of adsorption of acetone is significantly higher over the Pd/H-SOMS than other catalysts. In the red dotted region in the figure, a rapid rise of the mass of Pd/H-SOMS can be seen which indicates a fast adsorption of the acetone vapors. This was also visible by human eye when a drop of acetone solvent (liquid phase) was added to all the samples. The adsorption of acetone in liquid phase over the Pd/H-SOMS sample was taken place relatively quickly, i.e. the drop was immediately adsorbed by the sample, compared to others without leaving any wetted areas of the catalyst.

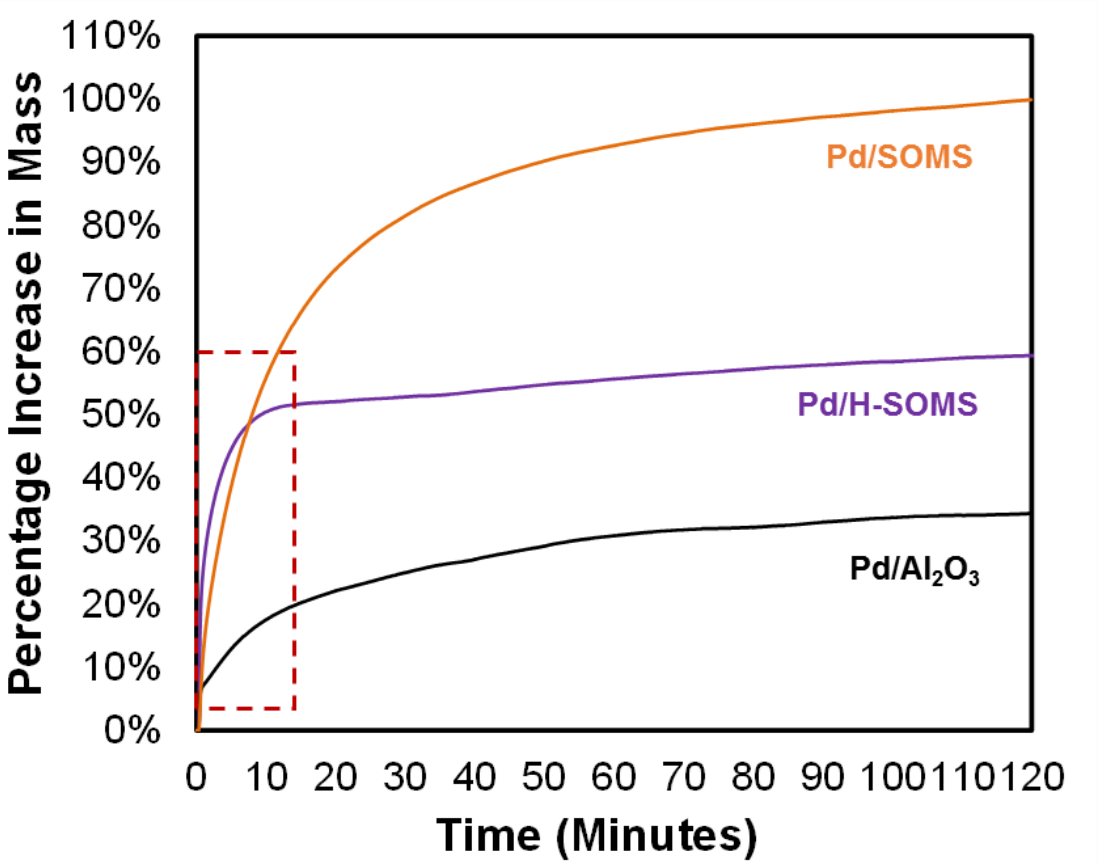

Figure 21. Adsorption of acetone over Pd/SOMS, Pd/H-SOMS and Pd/Al_2O_3 ***(Data was collected by ABS Materials)***

4.3.6 Accessibility of Pd to CO, O_2 and H_2

4.3.6.1 CO chemisorption results

CO chemisorption technique has been employed in many studies in order to investigate the Pd dispersion on a catalyst surface.[110-112] For this study, a known amount of CO molecules was continuously introduced to the catalyst bed in pulses. All the catalysts were pre-reduced prior to the reaction, either chemically (Pd/SOMS) or thermally using hydrogen (Pd/H-SOMS and Pd/Al_2O_3). Figure 22 indicates the MS intensity for m/z=28 which is linked to CO. Each peak corresponds to a CO pulse and the number in the numerical order signifies the number of pulses made during the experiment. As can be seen, all the CO molecules in the first pulse were adsorbed by the 1% Pd/Al_2O_3, specifically by the reduced Pd sites of the catalyst, whereas no consumption of CO was detected for 1% Pd/SOMS. This reaches to a conclusion that all the reduced Pd particles are not accessible to the incoming CO molecules in case of the Pd/SOMS. In other words, Pd particles were entirely protected by the SOMS support thereby resulting no Pd-CO bond formation; CO was not able to open up the catalyst pores of the Pd/SOMS. In regards to H-SOMS, the CO uptake for the first CO pulse was greater than Pd/SOMS but lesser than Pd/Al_2O_3. Consequently, this undoubtedly explains that the high-temperature treatment on SOMS led to an increasing Pd dispersion.

As the CO pulses were continued, more CO molecules were adsorbed on the Pd/Al_2O_3 surface in contrast to Pd/SOMS and Pd/H-SOMS where the intensity of the CO peaks leveled off to the original value of the feed. The third, fourth and fifth CO pulses share the same intensity for all samples, hence, reaching to a saturating of CO on the

catalyst surface. The dispersion values were calculated based on chemisorption stoichiometry of 1:1 ratio of Pd to CO[113-114] and are shown in the inset table of Figure 22.

The 0% Pd dispersion for Pd/SOMS is not a realistic value under reaction conditions according to the previous catalytic activity studies for HDC of TCE in liquid-phase (at least some Pd active sites were available for the reaction to convert TCE). It should be remembered that the actual number of Pd metal particles for Pd/SOMS during the HDC reaction is certainly higher due to swelling of the SOMS support. The adsorption of TCE increases the availability of the Pd metal in the SOMS matrix by opening up the catalyst pores while physical expansion of the Pd/SOMS catalyst proceeds. However, for gas-phase HDC of TCE, a significantly lower catalyst performance of 1% Pd/SOMS was obtained compared to 1% Pd/Al_2O_3 (section 4.3.7.1). Thus, whether the pores are opened enough so that Pd active sites are all available for the HDC reaction is questionable in gas-phase. In addition, the fact that an opposite trend was obtained in liquid-phase HDC of TCE where the 1% Pd/SOMS catalyst was more active than 1% Pd/Al_2O_3 (data not shown) supports the statement that the swelling, i.e. expansion of the volume of SOMS, is somewhat limited in gas-phase.

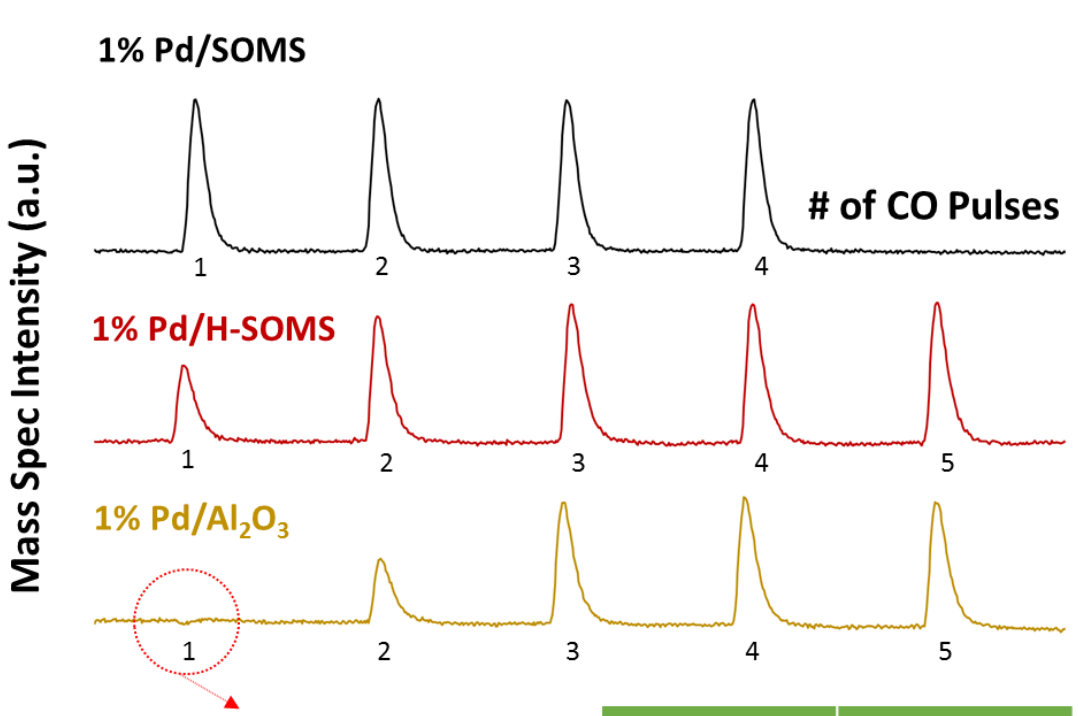

Sample	Pd Dispersion
1% Pd/Al_2O_3	41 %
1% Pd/H-SOMS	17 %
1% Pd/SOMS	Not Accessible

Figure 22. Results of CO Chemisorption

4.3.6.2 XANES results for oxidation, reduction and re-oxidation

The oxidation state of Pd was followed by XANES technique while the catalyst was under oxidizing and reducing environments. The switches from O_2 to H_2 and H_2 to O_2 were made at 30 min and 90 min, respectively. All the catalyst were pre-oxidized at 150 ℃ under 5% O_2/He. The starting oxidation states of Pd after pre-oxidation were converged to a similar value of +1 for all samples (Figure 23). When the temperature was increased to 250 ℃ under oxidizing environment, a sudden rise in Pd oxidation state in Pd/Al_2O_3 was observed whereas no oxidation of Pd was seen over the Pd/SOMS catalyst. This suggests a severe mass transfer limitation for oxygen molecules to enter the catalyst pores in the SOMS support structure. In other words, it proves that most of the Pd particles are embedded inside the SOMS matrix thereby being not accessible to the incoming molecules unless the gas/liquid are organics. With respect to Pd/H-SOMS, a drastic increase in oxidation state of Pd was obtained compared to Pd/SOMS. The difference is ascribed to the open-pores of the H-SOMS chemical structure where majority of the Pd particles are placed on the catalyst surface.

The reduction was performed subsequently using 3.6% H_2 at 150 ℃. After 15 min of reduction, all the samples were significantly reduced to metallic Pd, although the Pd/SOMS catalyst was slightly more oxidized compared to others. Likewise, at 250 ℃, the extent of reduction of Pd/Al_2O_3, Pd/H-SOMS and Pd/SOMS were maintained as close to Pd^0. The reduction of Pd of Pd/SOMS catalyst is interesting, especially considering the fact that oxygen was not able to access the Pd sites. Therefore, it is probable that the adsorption takes place depending on the size of the molecule, i.e. hydrogen molecule is much smaller

than oxygen. The SOMS support acts as a molecular sieve where larger molecules are not allowed to pass through to get in contact with the Pd particles located inside the SOMS matrix. However, it should be pointed out that this is only valid when swelling of the Pd/SOMS does not occur. Regardless of the molecular size, at least a large portion of the Pd metal is presumably accessible to the reactants if the SOMS is in the swollen state.

Re-oxidation of the samples was carried out following the reduction treatment. Again, similar to the conclusion made previously, only Pd/SOMS catalyst was not oxidized obtained less than +1 oxidation state. With regards to the Pd/H-SOMS sample, the approachability of Pd to oxygen improved considerably in contrast to the case of Pd/SOMS. The actual XANES spectra collected at 90 min and 150 min are shown in Figure 24.

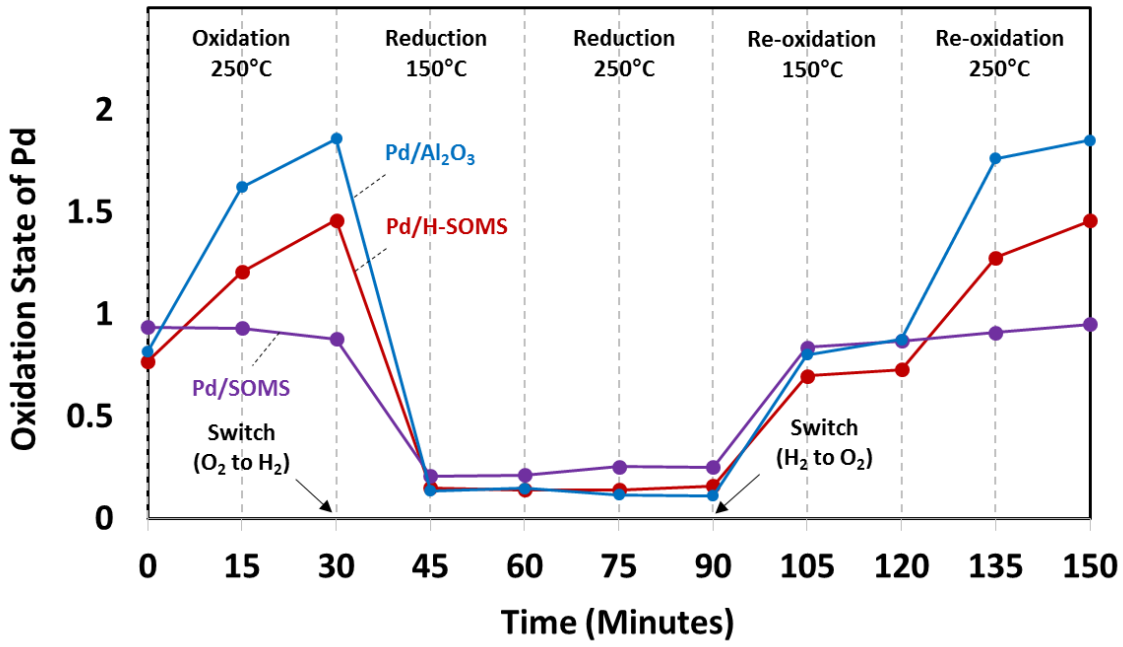

Figure 23. Change in oxidation states of Pd for SOMS, H-SOMS and Al_2O_3 in reducing and oxidizing reaction conditions

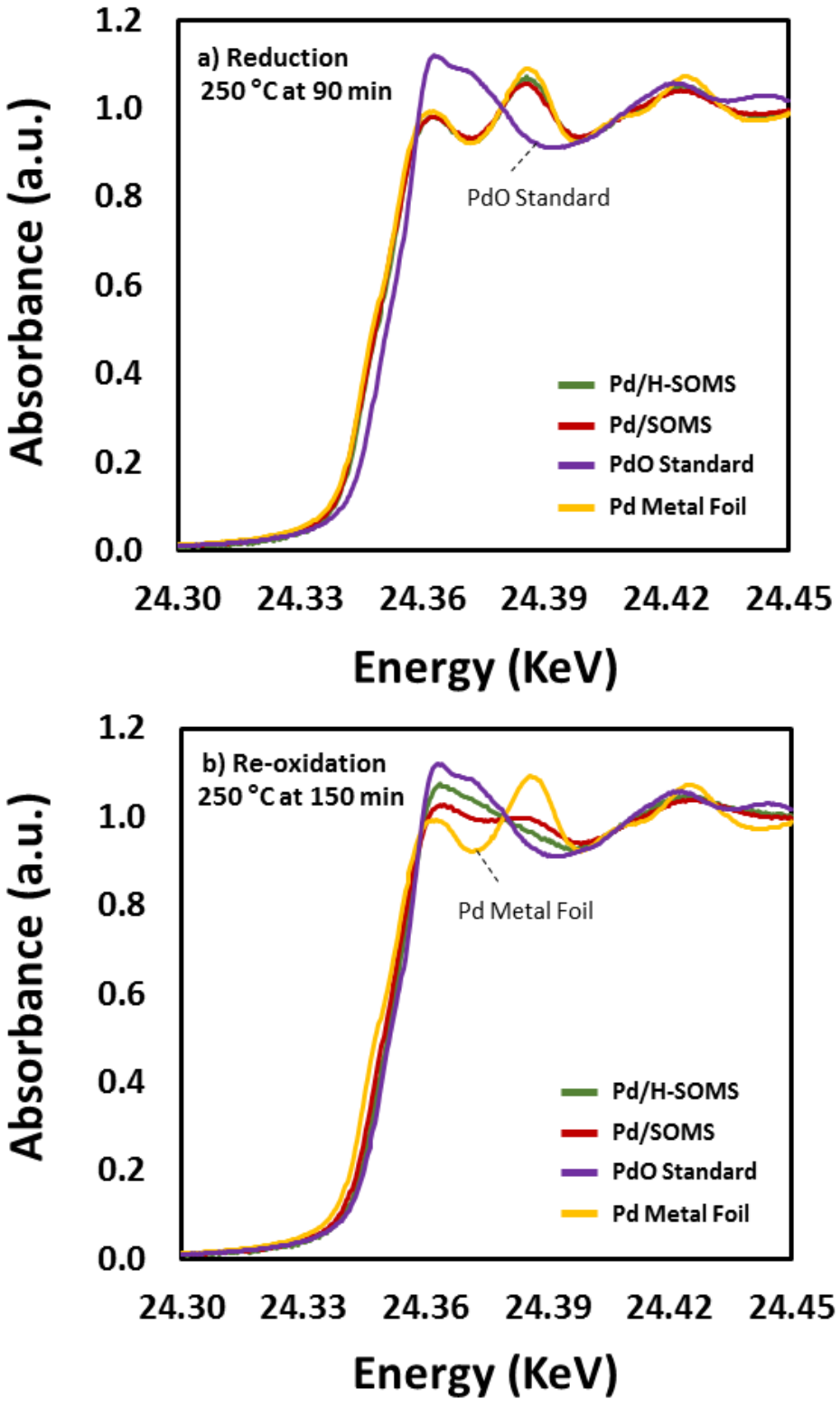

Figure 24. XANES spectra collected under reducing and oxidizing reaction conditions

4.3.7 Gas-Phase HDC of TCE

4.3.7.1 Catalytic Activity

The catalytic performances of 1% Pd/SOMS, 1% Pd/H-SOMS and 1% Pd/Al_2O_3 were investigated for gas-phase HDC of TCE. The reactants include 0.7% of TCE balanced in nitrogen in excess hydrogen condition. The Pd/H-SOMS and Pd/Al_2O_3 catalyst were pre-reduced in situ prior to the HDC reaction while Pd/SOMS was pre-reduced chemically using $NaBH_4$ as a reducing agent. The reaction was performed in a continuous gas-phase fixed bed reactor system at reaction temperatures of 100, 150 and 200 ℃. The TCE conversions obtained over the three samples are exhibited in Figure 25. As expected, 1% Pd/SOMS was significantly less active for gas-phase HDC of TCE reaction in the entire temperature range compared to the commercial 1% Pd/Al_2O_3 catalyst. This is attributed to the lower degree of swelling in gas-phase, resulting in a decrease in the number of Pd active sites available for the HDC of TCE. However, when Pd was impregnated on calcined SOMS under inert conditions (Pd/H-SOMS), a significant improvement of the catalytic activity was observed compared to regular Pd/SOMS. This is in good agreement with the CO chemisorption results where more Pd metallic sites are accessible to the TCE molecules thus increasing the conversion levels. At 200 ℃, the TCE conversion obtained over the Pd/H-SOMS catalyst is almost as similar as that of Pd/Al_2O_3.

The main products of HDC of TCE is hydrogen chloride (HCl) and ethane (C_2H_6). As shown in the figure, based on the ethane yields, similar order of activities of the catalysts were found (Pd/Al_2O_3>Pd/H-SOMS>Pd/SOMS). With respect to by-products, partially dechlorinated products such as cis-1,2 DCE was predominantly detected compared to 1,1

DCE and trans-1,2 DCE, especially when lower TCE conversions were obtained. For example, close to 16% yield of cis-1,2 DCE was obtained over Pd/Al_2O_3 catalyst with 39% TCE conversion at 100 ℃. Ethylene was acquired in small amounts over the Pd/SOMS and Pd/H-SOMS at 200 ℃. Also, vinyl chloride was produced although it was in negligible amounts. Even number of carbon products such as n-butane and n-hexane were observed.[52] More n-butane was obtained over the Pd/Al_2O_3 catalyst compared to Pd/SOMS and Pd/H-SOMS. Also, catalyst coking was observed at a reaction temperature of 200 ℃ for both Pd/Al_2O_3 and Pd/H-SOMS catalysts. This indicates that Pd metal has both C-Cl and C-C bond cleavage capabilities.

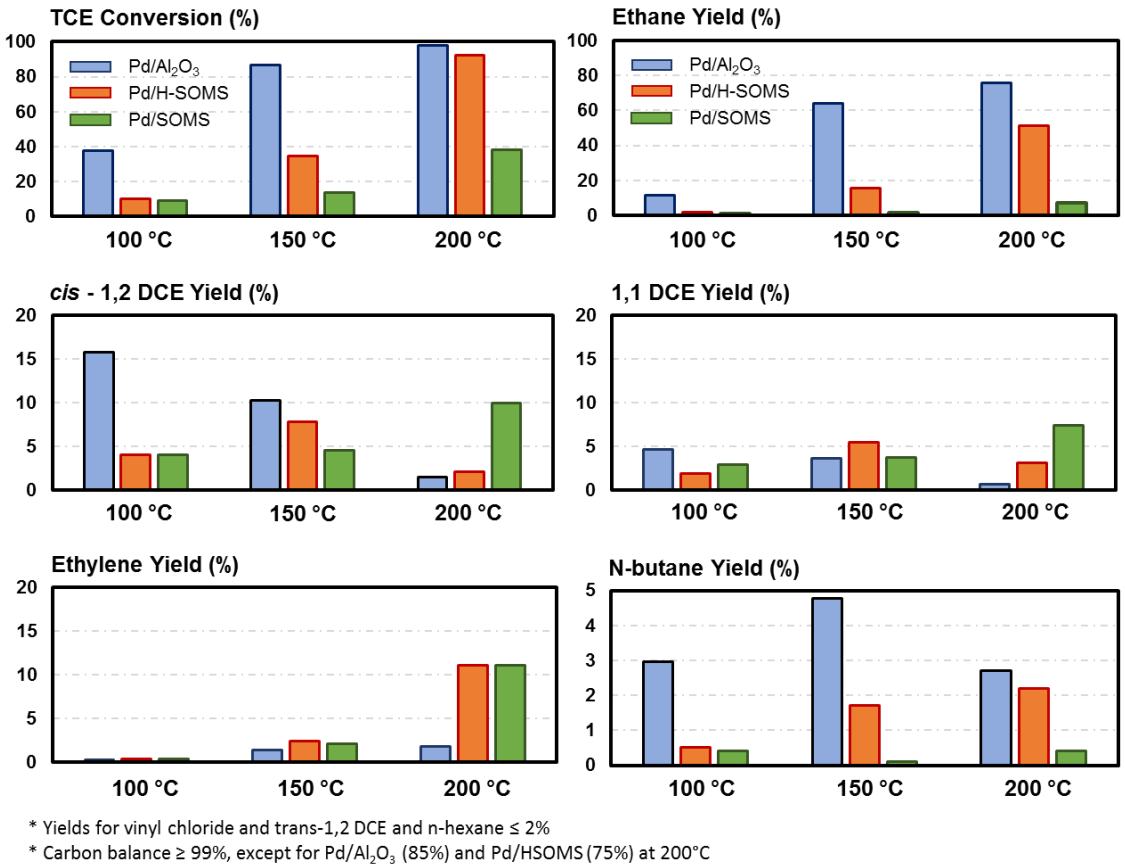

Figure 25. Gas-phase catalytic activity data of Pd/Al_2O_3, Pd/H-SOMS and Pd/SOMS for HDC of TCE

4.3.7.2 Effect of Addition of Water

The effect of adding water vapors to the reactant stream on catalytic activities of of 1% Pd/SOMS, 1% Pd/H-SOMS and 1% Pd/Al_2O_3 were examined. The reactant mixture in gas-phase comprised 0.7% of TCE and 4% of water balanced with nitrogen in excess hydrogen. It was found that Pd/Al_2O_3 suffered from significant catalyst degradation in the presence of water vapors (Figure 26). Comparing between the cases of with/without water addition, the TCE conversions obtained over the Pd/Al_2O_3 catalyst clearly shows the water inhibition effect taking place during hydrodechlorination. On the other hand, the addition of water to the reactants did not affect the catalytic performance of the Pd/H-SOMS and Pd/SOMS catalysts. At all reaction temperatures, the achieved TCE conversions in the absence/presence of water vapors reached to similar values. This is mainly attributed to the strong hydrophobicity of SOMS and H-SOMS supports that repels the water molecules thereby restricts the adsorption of water on the catalyst surface. Even though, the degree of hydrophobicity of the H-SOMS was fairly reduced compared to SOMS, the results still indicate that inhibition effect of water on the catalytic activity of Pd/H-SOMS is negligible. However, at 200 ℃, as observed before, severe carbon deposition on the Pd/H-SOMS catalyst was encountered due to extensive coking activities. The experiment had to be ceased after 1 hr of reaction because of significant pressure build-up in the reactor.

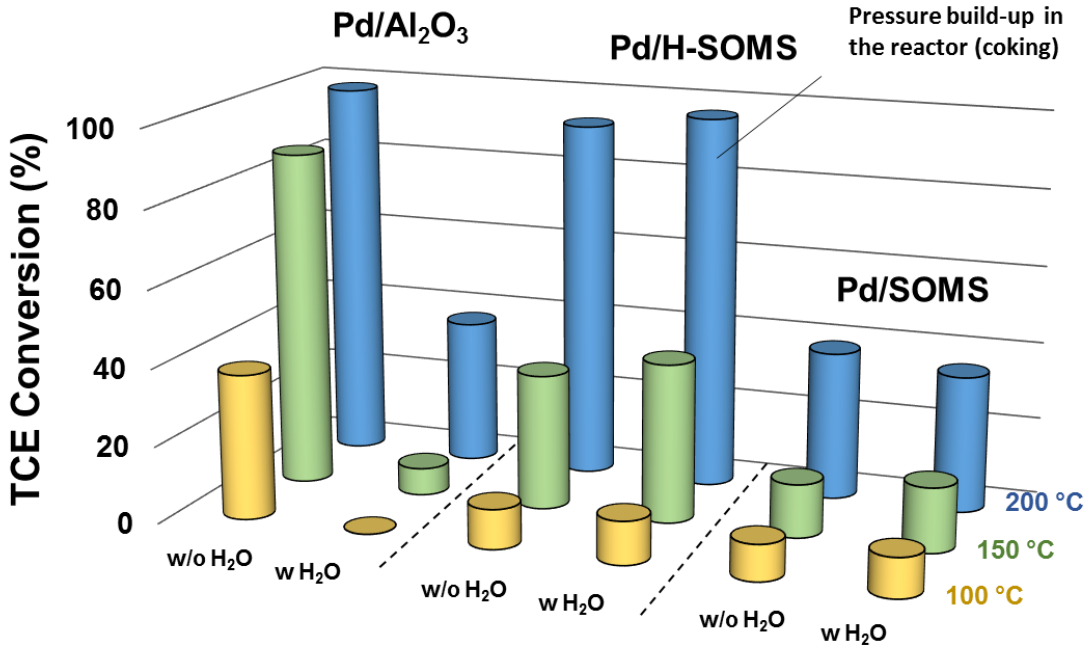

Figure 26. Effect of addition of water in the reactant stream on catalytic activity of Pd/Al_2O_3, Pd/H-SOMS and Pd/SOMS

4.3.8 Pd leaching due to 1 M HCl

4.3.8.1 XPS and ICP-OES results

Pd leaching has been reported in many studies under hydrodechlorination reaction conditions especially in aqueous phase.[73, 115-117] This is mostly due to HCl production from the reaction itself. To understand how resistant to Pd leaching the Pd/SOMS, Pd/H-SOMS and Pd/Al_2O_3 are, all the catalysts were treated with 0.1M and 1M HCl and stirred rigorously for 20 min in an aqueous solution. For a control experiment, all the samples were treated with pure water additionally. It should be noted that the intent for using 0.1 and 1M HCl was to determine how well the Pd particles are protected by the SOMS/H-SOMS support under severe treatment conditions, thus, for the actual HDC of TCE reaction, the concentration of produced HCl would be much lower than 0.1 M.

Once the experiment was completed, the remaining solutions and dried catalysts were used in ICP-OES and XPS analyses, respectively. As can be seen in Table 4, when the Pd/SOMS, Pd/H-SOMS and Pd/Al_2O_3 samples were soaked in water, no Pd was leached out from the catalysts indicating 0 % Pd leaching. When the HCl concentration was increased to 0.1 M, only 1.6% Pd leached out from Pd/SOMS whereas 74.4 % of Pd leaching was observed over the Pd/Al_2O_3 sample. With 1M HCl treatment, almost all of the Pd were removed from the Pd/Al_2O_3 catalyst which is significantly greater compared to Pd/SOMS where only 6.4% of the Pd particles were removed. From these results, it can be deduced that the strong hydrophobicity of the Pd/SOMS catalyst certainly helps preventing the chloride ions entering the pores. In case of Pd/H-SOMS, because the pores were opened leading to higher Pd dispersion compared to Pd/SOMS, the Pd leaching

percentage was increased to 43.2% and 61.6% for 0.1 M and 1 M HCl, respectively. However, these values are still lower as compared to that of Pd/Al_2O_3 catalyst.

The 1M HCl-treated Pd/SOMS, Pd/H-SOMS and Pd/Al_2O_3 catalysts were analyzed using XPS and Pd 3d spectra were collected for quantification of the Pd oxidation state was performed (Figure 27). The oxidation state of Pd is important since metallic Pd is the desired form to obtain high catalytic activity for HDC of TCE. Unfortunately, Pd signal over Pd/SOMS was not detected due Pd particles being inside the pores of the catalyst and not on the surface. Since XPS only probes the surface and sub-surface of a catalyst, this shows that most of the Pd particles are located inside the SOMS support. With respect to Pd/Al_2O_3, the treatment with 1 M HCl oxidized the Pd particles, exhibiting close to +2 oxidation state. When compared to pre-reduced Pd/Al_2O_3, the difference in peak location is clearly noticeable. Similarly, for Pd/H-SOMS, Pd was also partially oxidized showing +0.85 oxidation state.

Table 4. Percentages of Pd leaching using 0 M, 0.1 M and 1 M HCl

Pd leached (%)	0 M HCl	0.1 M HCl	1 M HCl
$1\%Pd/Al_2O_3$	0	74.4	> 99
1% Pd/HSOMS	0	43.2	61.6
1%Pd/SOMS	0	1.6	6.4

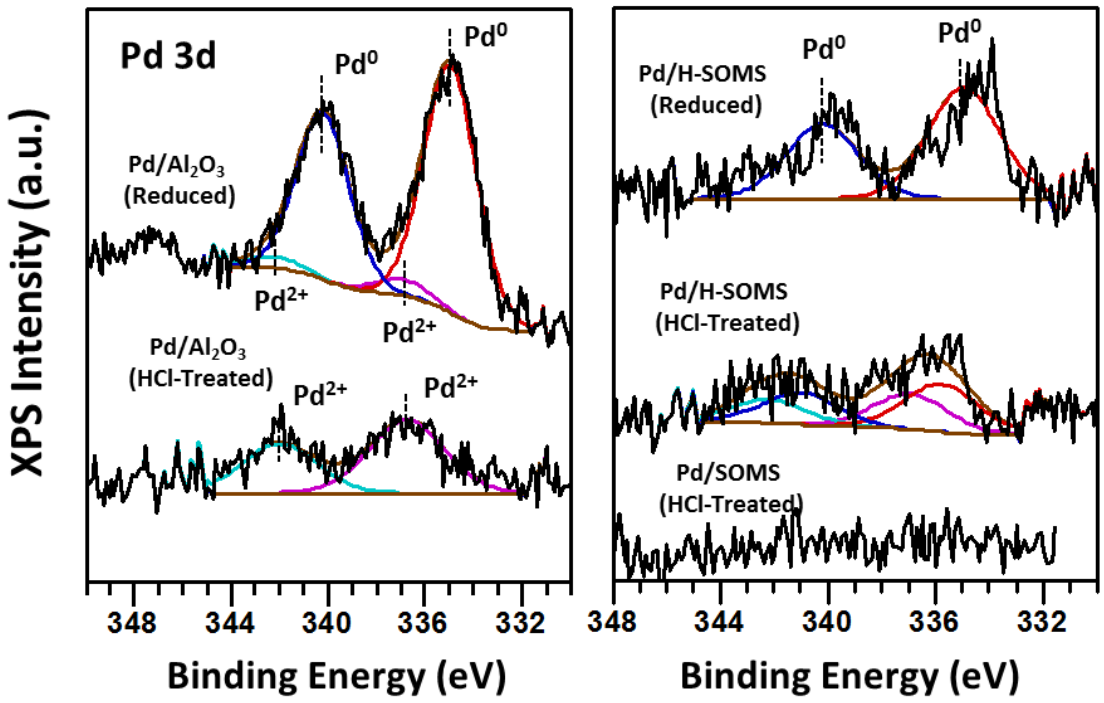

Figure 27. XPS Pd 3d spectra collected for 1M HCl-treated Pd/Al_2O_3, Pd/H-SOMS and Pd/SOMS

4.3.8.2 Catalytic Activity of Fresh and 1M HCl treated samples

The catalytic activities of 1M HCl-treated Pd/SOMS, Pd/H-SOMS and Pd/Al_2O_3 for HDC of TCE were measured and compared to their fresh counterparts (Figure 28). As aforementioned, the catalyst performances of the samples increase in the order of Pd/Al_2O_3 > Pd/H-SOMS > Pd/SOMS at all temperatures tested. However, interestingly, when treated with 1 M HCl an opposite order of Pd/SOMS > Pd/H-SOMS > Pd/Al_2O_3 was observed. This is in good agreement with the results obtained from ICP-OES and XPS analysis where most of the Pd particles were remained on the SOMS support thereby leading to higher TCE conversions compared to Pd/Al_2O_3. Again, the strong hydrophobicity was the key factor in order to retain the catalyst performance of the Pd/SOMS sample. For 1 M HCl-treated Pd/H-SOMS, as expected, degradation of the catalytic activity was observed due to Pd leaching and oxidation. However, the percentage loss in TCE conversion was lower in contrast to Pd/Al_2O_3 catalyst. This indicates that the hydrophobicity of H-SOMS was not able to facilitate the catalyst to maintain its reactivity by repelling 1 M HCl.

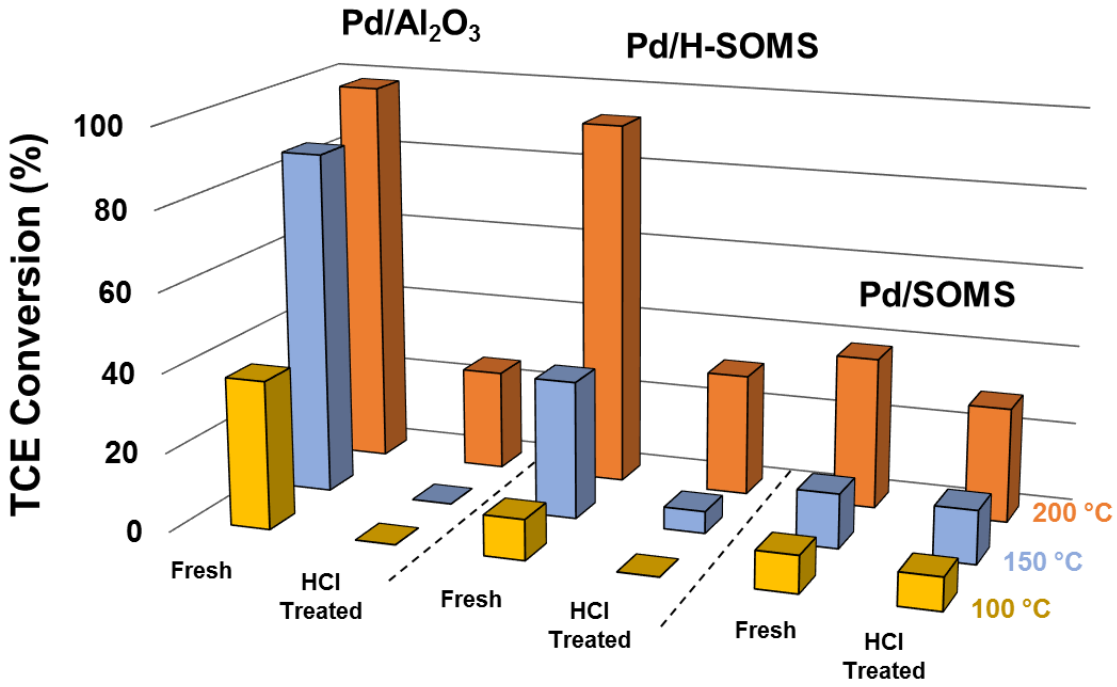

Figure 28. TCE conversions obtained over fresh and HCl-treated Pd/Al_2O_3, Pd/H-SOMS and Pd/SOMS for HDC reaction

4.4 Conclusion of Chapter 4

The catalytic activities of Pd supported on SOMS and high-temperature treated SOMS (H-SOMS) were investigated for gas-phase HDC of TCE. In our previous results, it was reported that 1% Pd/SOMS shown significantly better catalytic performance compared to 1% Pd/Al_2O_3 catalyst under liquid-phase HDC of TCE conditions. This was attributed to the swelling capability of SOMS which concentrated the TCE reactants in the vicinity of the Pd active sites. However, in the gas-phase, the catalyst pores of Pd/SOMS were significantly restricted to the adsorption TCE thereby leading to lower catalytic activity of Pd/SOMS than Pd/Al_2O_3. Thus, in this study, a saturated SOMS with acetone was calcined under inert conditions at high temperature in order to retain its maximum swollen state resulting better pore accessibility. The surface analysis results exhibited higher BET surface area, pore volume and averaged pore diameter over the H-SOMS material compared to SOMS. After Pd was placed on both supports, the Pd dispersion of Pd/H-SOMS was greatly improved than that of Pd/SOMS based on the STEM images. Also, the average Pd particle size was smaller for Pd/H-SOMS. XANES results exhibited that Pd sites on H-SOMS were accessible to both H_2 and O_2 leading to reduction and oxidation of the Pd particles. However, reduction of Pd was only observed over the Pd/SOMS catalyst whereas oxidation of Pd was significantly limited to +1 oxidation state even at higher temperatures. The selective adsorption is likely due to the particle size of the adsorbate which explains lower extent of adsorption of TCE which is a relatively larger molecule. For gas-phase HDC of TCE, higher TCE conversions were achieved over the Pd/H-SOMS catalyst compared to Pd/SOMS. However, both Pd/SOMS and Pd/H-SOMS

showed lower catalytic activities then Pd/A_2O_3. In the presence of water in the reactant mixture, a complete deactivation of Pd/Al_2O_3 catalyst was obtained. On the contrary, Pd/SOMS and Pd/H-SOMS catalyst retained its catalytic activities which was attributed to the hydrophobicity of the supports. All the samples were treated with 1 M HCl to examine the quantity of Pd leaching. Almost close to 100% of Pd was leached out from the Al_2O_3 support after the treatment whereas only 6.5% Pd leaching was obtained for Pd/SOMS. Although Pd/H-SOMS was hydrophobic, with 1 M HCl treatment, 61.6 % of Pd was removed from the H-SOMS support.

** Information in this chapter was reproduced/adapted from "Sohn, H.; Celik, G.; Gunduz, S.; Majumdar, S. S.; Dean, S. L.; Edmiston, P.; Ozkan, U. S., High-temperature-treated Swellable Organically-Modified Silica (SOMS) and Its Application to Gas-Phase Hydrodechlorination of Trichloroethylene. Manuscript in Preparation"*

PART II

STEAM REFORMING OF ETHANOL

CHAPTER 5

INTRODUCTION

5.1 Ethanol Steam Reforming (ESR)

The rapid increase in the world population and industrialization has led to a significant rise in energy consumption demands. Because most of the energy is generated by combustion of fossil fuels today, the amount of greenhouse gases and toxic pollutants produced continues to rise as well. For these reasons, there have been attempts to use alternative and renewable energy sources as the next generation of energy carriers. Among many other sources of energy, hydrogen has garnered a lot of attention because of its high energy storage capacity (120.7 kJ/mol)[118] and environmentally friendly combustion process, which generates only water as the product. Especially, use of hydrogen as a feedstock for a proton exchange membrane (PEM) fuel cell is an attractive technology, which converts chemical energy to electrical energy with higher efficiency without producing any pollutants.[119] Currently, a large fraction of hydrogen is produced from natural gas steam reforming.[120] However, natural gas is also a fossil fuel and contributes to the carbon dioxide emissions. To have a closed carbon loop cycle, it is essential to use reactants originating from renewable sources, such as biomass. In that sense, ethanol, which can be obtained through fermentation of biomass, is a good candidate.

Although ethanol steam reforming produces carbon dioxide, it can be consumed by photosynthesis of plants, which then are used as a feedstock for biomass production, potentially completing the carbon loop cycle. Also, its nontoxicity and high solubility in water make ethanol an attractive reactant for steam reforming processes.[121]

The chemical reaction for ethanol steam reforming can be represented as follows:

$$\mathbf{C_2H_5OH + 3H_2O \rightarrow 6H_2 + 2CO_2} \quad \textbf{(complete reforming of ethanol)}$$

Ethanol steam reforming is an endothermic process, which requires energy input in the form of heat during the reaction (ΔH = 348 kJ/mol at 25 ℃), with the two major products being H_2 and CO_2.

A thermodynamic equilibrium analysis of the product distribution for different feed conditions is presented in Figure 29. Reaction parameters, such as the temperature, pressure, and molar ratio of ethanol/water, are altered, and the resulting hydrogen yield and ethanol conversion are shown. With regard to the reaction temperature and pressure, it was found that an increase in both parameters improves the hydrogen yield. However, at higher temperatures above 500 ℃, the formation of hydrogen was limited as a result of reverse water-gas shift reaction ($H_2 + CO_2 \rightarrow CO + H_2O$). Below 400 ℃, methane was the major product obtained. This was attributed to the methanation reaction, which was thermodynamically favorable at lower temperatures as a result of the exothermicity of the reaction. The ethanol/water ratio under equilibrium conditions showed a significant impact on the formation of carbon deposits on the catalyst surface. When the ratio was less than 1:5, no catalyst coking was predicted.

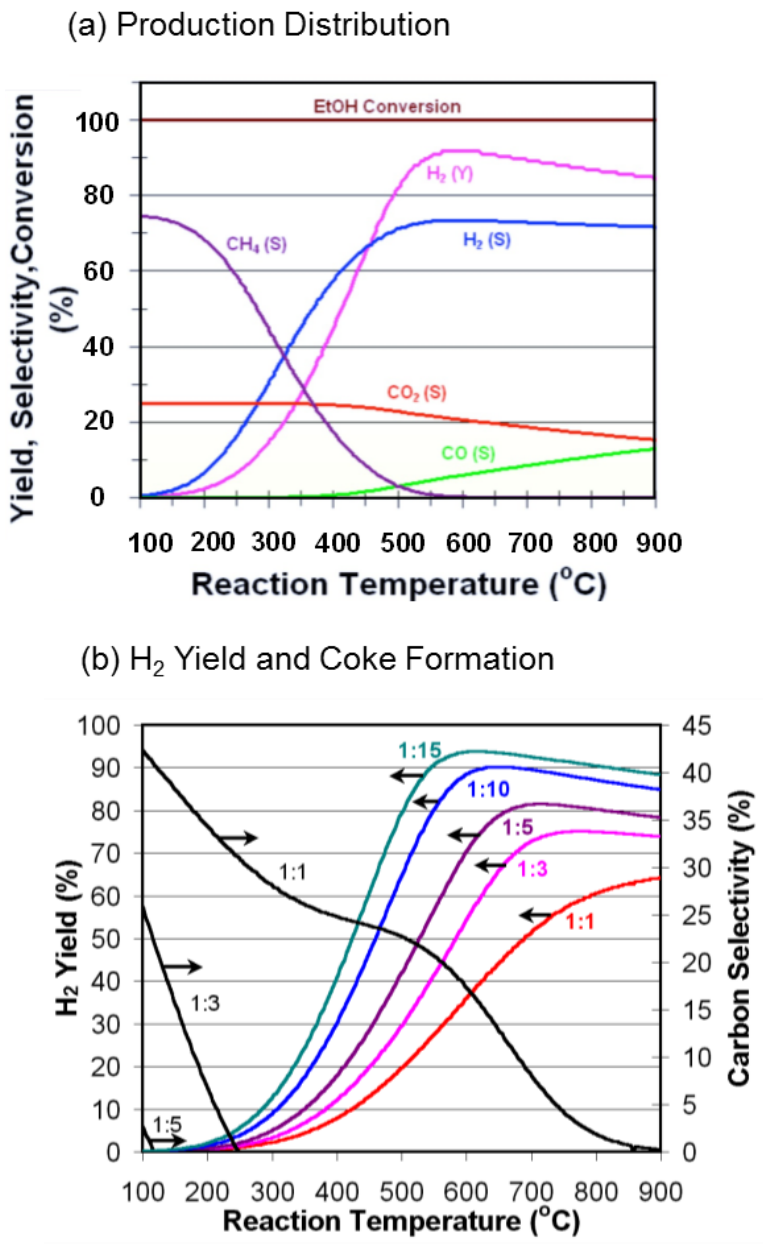

Figure 29. Product distribution in ethanol steam reforming in thermodynamic equilibrium: (a) conversion and yields [EtOH/H_2O = 1:10 (molar), C_{EtOH} = 2.8%] and (b) H_2 yield and C selectivity at different EtOH/water ratios.[122] (*cited from "Song, H.; Zhang, L.; Watson, R.; Braden, D.; Ozkan, U., Investigation of Bio-Ethanol Steam Reforming over Cobalt-Based Catalysts. Catal. Today 2007, 129, 346-354."*)

Although the ethanol steam reforming reaction appears to be quite simple and, under thermodynamic equilibrium conditions, the number of possible products is few, when the reaction is governed by kinetics, there are many side and intermediate reactions that occur simultaneously, hence decreasing the hydrogen yield and forming many byproducts, such as CH_4, CO, acetone, acetaldehyde, ethylene, and coke. The following is a list of possible reactions that can take place during ethanol steam reforming:

$CH_3CH_2OH \rightarrow CH_4 + CO + H_2$	(ethanol decomposition)
$CH_3CH_2OH + H_2O \rightarrow 2CO + 4H_2$	(incomplete reforming)
$CH_3CH_2OH \rightarrow CH_3CHO + H_2$	(dehydrogenation)
$CH_3CH_2OH \rightarrow C_2H_4 + H_2O$	(dehydration)
$C_2H_4 \rightarrow$ Coke	(coke formation)
$2CH_3CH_2OH \rightarrow (C_2H_5)_2O + H_2O$	(diethyl ether formation)
$CO + 3H_2 \rightarrow CH_4 + H_2O$	(methanation)
$CH_4 \rightarrow C + 2H_2$	(methane decomposition)
$CH_4 + 2H_2O \rightarrow 4H_2 + CO_2$	(methane steam reforming)
$CH_3CHO \rightarrow CH_4 + CO$	(acetaldehyde decomposition)
$CH_3CHO + 3H_2O \rightarrow 2CO_2 + 5H_2$	(acetaldehyde steam reforming)
$2CH_3CHO \rightarrow CH_3COCH_3 + CO + H_2$	(acetone formation)
$C_2H_5OH + H_2O \rightarrow CH_3COOH + 2H_2$	(acetic acid formation)
$CO+H_2O \leftrightarrows CO_2+H_2$	(water-gas shift and reverse water-gas shift)
$2\ CO \rightarrow CO_2 + C$	(Boudouard reaction)

Ethanol steam reforming involves a complex reaction network. The adsorption of ethanol and water on the catalyst surface undergoes multiple side reactions, thereby forming different intermediate surface species, which eventually lead to production of hydrogen and carbon dioxide. Figure 30 presents a reaction scheme for ethanol steam reforming.

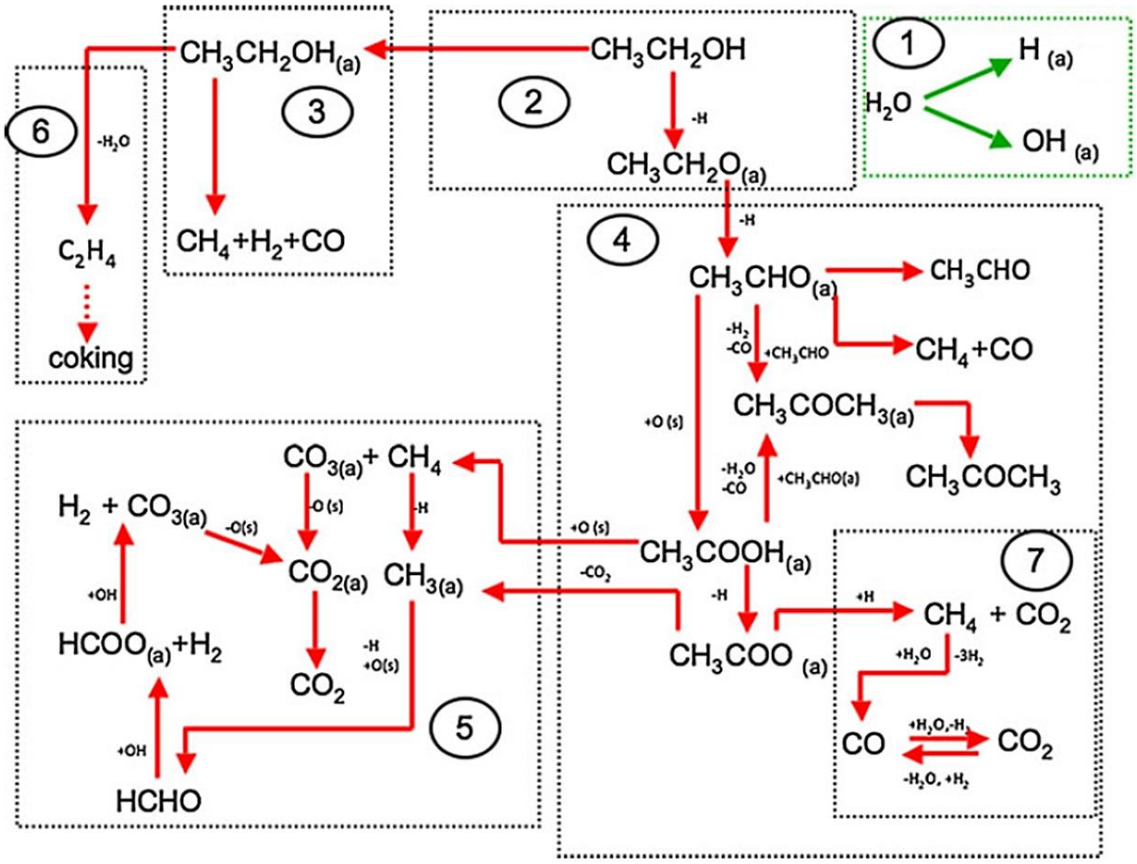

Figure 30. Reaction network of ethanol steam reforming[123] *(cited from "Song, H.; Bao, X.; Hadad, C. M.; Ozkan, U. S., Adsorption/Desorption Behavior of Ethanol Steam Reforming Reactants and Intermediates over Supported Cobalt Catalysts. Catal. Lett. 2011, 141, 43-54.")*

First of all, (1) the dissociation of water occurs on the catalyst surface forming hydroxyl groups (OH*) and H* species. Direct adsorption of water molecules on the surface is also possible at lower temperatures. However, most of them leave the surface when temperature is increased. (2) The adsorption of ethanol on the catalyst surface produces ethoxide species with abstraction of H. The first H radical either combines to O* to produce OH or reacts with surface OH* to form H_2 resulting surface oxygen. (3) When ethanol adsorbs on the surface molecularly, decomposition of ethanol is feasible leading to CH_4, H_2 and CO (ethanol decomposition reaction). (4) The ethoxide species are oxidized to acetaldehyde on the surface involving another abstraction of hydrogen. The adsorbed acetaldehyde species are important intermediates since it goes through multiple reaction pathways. It either decomposes into CH_4 and CO or desorbs directly as acetaldehyde into gases phase. Another route can be oxidation of acetaldehyde to acetic acid and eventually to acetate species. Formation of acetone is possible in two different ways, either by aldol condensation of acetaldehyde releasing H_2 and CO, or reaction between acetaldehyde and produced acetic acid giving H_2O and CO.[124] Once acetone is formed, it desorbs directly to gas phase, or oxidizes to acetate species reacting with OH surface groups. The surface acetate species are the main intermediate for ethanol steam reforming. From the acetate species to all the way to CO_2 production process involves various surface reaction mechanisms. First, (7) the decomposition of acetate species release CH_4 and CO_2 or (5) form surface methyl group and CO_2. (5) But also, formation of CH_4 and carbonate species on the catalyst surface is possible. This process involves surface O*, hence, without a higher oxygen storage capacity of the support, coke formation due to acetate decomposition is significant.[125-126] The carbonate species eventually desorbs as CO_2 gases. Another

pathway is oxidation of methyl groups into formaldehyde which desorb, either as it is, or decompose into formate species while producing hydrogen. The decomposition of formate species to carbonates again releases hydrogen. The carbonate species undergoes a reduction process and converts into CO_2 at the end. (7) The released CH_4 resulting from acetate decomposition can react with H_2O producing hydrogen (methane reforming). The gas molecules of CO, CO_2 and H_2O formed during the reaction can be consumed both in water gas shift reaction, and reverse water gas shift reaction. (6) When the catalyst contains more acidic sites, it facilitates dehydration reaction which produces ethylene. The abundance of ethylene on the catalyst surface leads to sever catalyst coking.

** Information in this chapter is reproduced/adapted from "Sohn, H.; Ozkan, U. S., Cobalt-Based Catalysts for Ethanol Steam Reforming: An Overview. Energy & Fuels 2016. April-Published"*

CHAPTER 6

LITERATURE REVIEW

6.1 Catalysts Used for Ethanol Steam Reforming

To obtain high hydrogen yield and ethanol conversion, precious metals, such as Pd, Pt, Rh, Ru, Re, and Ir,[125-136] have been tested and have shown promising catalytic activity for ethanol steam reforming. Especially over a Rh-based catalyst, many studies have indicated the superior catalytic performance of Rh compared to other metals.[128, 137-140] For example, Breen et al. reported the order of catalytic activity to be Rh > Pd > Ni = Pt, supported on either ceria or zirconia for ethanol steam reforming.[128] Similarly, Aupretre and co-workers compared the catalytic activity of Rh, Pt, Ni, Cu, Zn, and Fe and demonstrated that Rh is the most active catalyst for ethanol steam reforming.[137] Bimetallic systems, such as Rh−Pt,[141-142] Rh−Pd,[131, 143] Rh−Ni,[144-145] and Ru−Co,[146-147] have been widely studied for ethanol steam reforming as well.

Although higher activities can be attained with precious metals, the catalyst cost limits the feasibility of this technology. Hence, non-precious metals, such as Co, Ni, and Cu,[138, 148-153] have also been investigated at much higher metal loadings. Among these metals, cobalt has emerged as an active metal catalyst for C−C bond scission, which is an

important characteristic for ethanol steam reforming.[154] Among the earlier studies performed regarding ethanol steam reforming, Llorca et al. have published studies on the catalytic activity of cobalt metal-based catalysts.[148, 155-158] High ethanol conversions over Co catalysts supported on different supports have also been reported.[159-160]

The choice of support strongly affects the cobalt dispersion, particle size, and reducibility, thereby altering the catalytic activity. Many metal oxide materials have been used as catalyst supports for cobalt, including Al_2O_3,[161] ZrO_2,[162-163] SiO_2,[164] CeO_2,[165-166] MgO,[167], and ZnO.[168-169] On the basis of a comparison study by Haga et al.,[170] Co supported on Al_2O_3 revealed the highest catalytic activity compared to Co supported on SiO_2, MgO, ZrO_2, and carbon supports. They concluded that the change in support greatly influenced the catalytic performance mostly as a result of suppression of methanation and decomposition of ethanol reactions. Another study by Llorca and co-workers[148] demonstrated promising catalytic activity of cobalt over ZnO and CeO_2 supports with high hydrogen selectivity compared to Co supported on MgO, γ-Al_2O_3, SiO_2, TiO_2, V_2O_5, La_2O_3, and Sm_2O_3. More recently, Moura et al. investigated the effect of support for RhCo on Al_2O_3, MgO, and Mg-Al oxide catalysts. They reported the highest hydrogen yield and low ethylene selectivity over the RhCo/Mg-Al oxide catalyst.[171]

6.2 Cerium Oxide (CeO_2)

Over the past few decades, ceria has been used and tested for various catalytic applications as a catalyst, catalyst support, or catalyst promoter. The high oxygen storage capacity and oxygen mobility of ceria make it an attractive material especially for catalytic reactions involving oxygen. For example, in automobile exhaust treatment, where simultaneous oxidation and reduction reactions occur, ceria has been widely employed as a component of the three-way catalysts.[172-173] It has also been reported to enhance the activity for the water-gas shift reaction.[174-175] Other catalytic applications where ceria is used include fluid catalytic cracking,[176] fuel cell electrodes,[177] oxidation of CO and hydrocarbons,[178-179] and dry and wet reforming.[180-181] Furthermore, ceria has also been reported to provide higher stability when used as a support and shows significant catalytic activity when used as a catalyst for ethanol steam reforming.[182-184]

Among the various metal oxides studied, ceria has exhibited a crucial role in reducing coke deposits on the catalyst surface as well as altering/modifying the reaction kinetics.[153, 182, 185-187] In addition, the strong metal−ceria interaction was found to increase the metal dispersion of the catalyst.[130] Several studies have shown a promotion effect of doping cerium into the catalyst supports such as Al_2O_3,[188] ZrO_2,[182, 189] and Al_2O_3-La_2O_3,[190] leading to a better catalytic activity and stability of the metal catalyst under ethanol steam reforming conditions. Even ceria itself has been examined for its catalytic activity for ethanol steam reforming. Laosiripojana and Assabumrungrat[186] have reported that ceria itself with high surface area is active for C−C bond cleavage, showing 90% ethanol conversion at 900 ℃ with 67.5% hydrogen selectivity. Their results indicate that the

catalytic activity of ceria in ethanol steam reforming is greater than Ni/Al_2O_3 but lower than Rh/Al_2O_3 catalyst.[186] Regardless of the activity, ceria shows significantly less carbon deposition.

The superior performance of ceria as a support or even as a catalyst is attributed to the abundant number of oxygen vacancies and/or the rapid change between Ce^{3+} and Ce^{4+} oxidation states in redox reactions.[191] These properties offer high oxygen mobility and storage capacity within its structure. The transportation of the oxygen species from the support to the supported metal alleviates carbon deposition and also provides oxygen for the surface reaction. Significantly improved activities of catalysts with ceria support have been reported in many studies under ethanol steam reforming conditions, including those with even higher oxygen mobility of ceria, by doping a lower-valence element into CeO_2 structure.[183, 192-193]

A variety of methods to synthesize ceria have been reported until now, including precipitation,[194] spray pyrolysis,[195-196] thermal hydrolysis,[197] micro-emulsion,[198] combustion,[199] sonochemical,[200] hydrothermal,[201] solvothermal,[202-203] and sol-gel[204] techniques. It is a well-established fact that changing the synthesis parameters, such as temperature, pressure, pH, and crystallization time, produces different particle sizes and morphologies, which, in turn, alter the physical and chemical properties of ceria, as well as the catalytic performance of the ceria-supported catalysts. For example, an increase in oxygen vacancies with decreased particle size of ceria has been reported in many studies.[205-207] Deshpande et al.[206] obtained 17% to 44% increase in Ce^{3+} concentration as ceria particles size was reduced from 30 nm to 3 nm, which was prepared by micro-emulsion. This was attributed to the generation of oxygen vacancies of ceria. Flytzani-

Stephanopoulos and colleagues synthesized nano-polyhedra, rods and cubic ceria particles using hydrolysis method and examined its catalytic activity for various reactions.[208-212] They demonstrated that different shapes of ceria nanoparticles exposing different crystal planes on the catalyst surface significantly influenced the Au dispersion on the ceria support.

In our previous studies, two different shapes of ceria supports were prepared using the hydrothermal synthesis method.[213] The particle sizes for nanorods were 22 ± 6 nm (length) and 6 ± 1.3 nm (width). The nanocubes were observed as bigger particles, with 21 ± 7 nm particle sizes. It was found that the morphology of the ceria support significantly affected the surface acidity where ceria nanocubes were shown to be more basic compared to ceria nanorods. In addition, higher reducibility of cobalt was found in the case of Co/CeO_2 nanocubes under reducing environment. The significant difference in properties of the Co/CeO_2 nanocubes compared to the Co/CeO_2 nanorods led to a pronounced increase in catalytic performance for ethanol steam reforming. Over the Co/CeO_2 nanocubes, a 4.5 times greater hydrogen yield was achieved in comparison to Co/CeO_2 nanorods.

Similar to the morphology study, two different particle sizes of ceria were prepared, one in nanosize the other in microsize, to examine the effect of the support particle size on the catalytic activity of the Co/CeO_2 catalyst.[214] The particle sizes of nanoceria were in the range of 5−8 nm, whereas the microceria contained 0.1−0.2 μm particles. The Co/CeO_2 nanoceria showed a higher reducibility of in similar reducing environments compared Co/CeO_2 microceria. Also, catalysts supported on nanoceria was seen to contain a higher density of redox sites. As a result, Co/CeO_2 nanoceria was shown to lead to a higher H_2

yield and higher stability. After 13 h of ethanol steam reforming, a significant catalyst coking was observed for Co/CeO_2 microceria.

** Information in this chapter is reproduced/adapted from "(1) Sohn, H.; Ozkan, U. S., Cobalt-Based Catalysts for Ethanol Steam Reforming: An Overview. Energy & Fuels 2016. April-Published (2) Sohn, H.; Soykal, I. I.; Zhang, S.; Shan, J.; Tao, F.; Miller, J. T.; Ozkan, U. S., Effect of Cobalt on Reduction Characteristics of Ceria under Ethanol Steam Reforming Conditions: AP-XPS and XANES Studies. The Journal of Physical Chemistry C 2016. June-Published (3) Soykal, I.; Sohn, H.; Bayram, B.; Gawade, P.; Snyder, M.; Levine, S.; Oz, H.; Ozkan, U., Effect of Microgravity on Synthesis of Nano Ceria. Catalysts 2015, 5 (3), 1306-1320."*

CHAPTER 7

INVESTIGATION OF THE REDUCTION/OXIDATION BEHAVIOR OF COBALT SUPPORTED ON NANO-CERIA

7.1 Summary of Chapter 7

The oxidation and reduction behavior of cobalt catalysts supported on nano-ceria (5-8 nm) was investigated under hydrogen, oxygen and water atmospheres. A novel quantitative isothermal reduction (QIR) technique was introduced to analyze the kinetics and activation barrier of Co reduction. CoO to Co reduction was found to be of first order in the 250-350 °C temperature range. Temperature programmed reduction and oxidation experiments were conducted and the Kissinger method was used to obtain apparent activation energies for reduction and oxidation with O_2. The apparent activation energy for CoO reduction was found to agree with that obtained from the QIR technique. Re-oxidation of Co metal was found to have a slightly lower activation energy barrier than the reduction. The reduction and oxidation behavior was further investigated with *in situ* XANES where the reaction order for reduction was observed to change at 450 °C. The pre-reduced samples were seen to re-oxidize under a water atmosphere, where the oxidation followed first order kinetics. Re-oxidation by water yielded a higher activation energy when compared to re-oxidation under oxygen.

7.2 Experimental Section

7.2.1 Catalyst Preparation

Ceria support with a particle size in the 5-8 nm range was selected and synthesized for this study. 1.5 g $Ce(NO_3)_3 \cdot 6H_2O$ (Sigma Aldrich 99.9 %) was dissolved in 9.4 ml water and mixed with 25 ml of 11 wt% NaOH. The suspension was stirred at room temperature for 15 min during which $Ce(OH)_3$ particles precipitated. Following an aging period of 24 h at room temperature, particles were separated by filtration. Approximately 2 L of deionized and distilled water were used for washing. The particles were dried in air at 90 °C overnight. The dried $Ce(OH)_3$ precursors were calcined at 450 °C for 3 h under air to obtain 5-8 nm CeO_2 support.

The incipient wetness impregnation (IWI) method was used to place 10 % (wt%) cobalt metal on the ceria support. $Co(NO_3)_2$ (Aldrich, 99.999 %) dissolved in 200 proof ethanol (Decon Labs) was applied onto the support drop by drop by a pipette and dried at 110 °C overnight in a drying oven. The whole process was repeated five times consecutively in order to improve the homogeneity of the resulting catalysts. Following the final impregnation and drying step, the catalyst was calcined at 450 °C for 3 h under air flow to obtain the supported catalyst, which will be denoted as Co/CeO_2 in the text, regardless of the oxidation state of Co.

7.2.2 Catalyst Characterization

7.2.2.1 Surface Area, Pore Size Distribution

The BET surface area and pore size distribution of the bare support and supported catalyst were obtained using a Micromeritics ASAP 2020 (accelerated surface area and porosimetry) instrument. Prior to measurement, the catalyst was degassed for 12 h at 130 °C under a vacuum of better than 2 μm Hg, to remove impurities on the catalyst surface. The analysis was performed at liquid nitrogen temperature with nitrogen used as the adsorptive gas. The saturation pressure of nitrogen was measured at regular intervals during the analysis to acquire nitrogen adsorption/desorption isotherms through which the BET surface area was calculated. The desorption isotherm was used to determine the BJH pore size distributions.

7.2.2.2 Metal Dispersion

Metal dispersion of the ceria support was obtained using the N_2O chemisorption technique described by Jensen et al.[215] The measurement was performed using a ¼" fixed bed quartz reactor with a quartz frit, which was located inside a fast-response furnace (Carbolite, MTF 10/15/130). The catalyst sample was packed in the quartz reactor and reduced in situ at 400 °C using 5 % H_2 in He for 2 h. The reactor was then cooled down to room temperature by flushing it with He. The temperature was again increased to 40 °C to conduct N_2O chemisorption. 3 % N_2O/He was introduced to the reactor while mass of m/z 12-46 range were monitored via an MKS-Cirrus II on-line mass spectrometer. As surface Co sites consumed O atoms from N_2O, N_2 was formed and desorbed from the sample

surface. The amount was quantified to calculate Co sites accessible on the surface. The calculation for Co sites was done after the Fickian diffusion correction. The Co:O ratio was assumed to be 1:1. Throughout the experiment, N_2O and N_2 were the only species detected in the reactor effluent. To quantify the N_2 amount, a 250-µl-sample loop, which was connected to an automated six-port valve, was utilized for N_2 calibration. For quantification of N_2, m/z 28 trace was corrected by subtracting the contribution of N_2O fragment to the m/z 28. The mass spectrometer signal was corrected using instrumental sensitivity factors.

7.2.2.3 Transmission Electron Microscopy (TEM)

All TEM images were taken from a Phillips Tecnai F20 instrument equipped with a field emission gun operated at 200 kV. Samples were sonicated with ethanol for 10 min to remove the charging effect as well as to obtain high dispersion. A few drops of the suspension were placed on a Tedpella, Inc 200 mesh copper grid coated with lacey carbon. TEM images were then interpreted and labeled using image processing software ImageJ.

7.2.2.4 *In Situ* X-ray Diffraction

The *in situ* XRD patterns of Co/CeO_2 samples were acquired during reduction using a Bruker D8 Advance X-ray diffractometer with monochromatic Cu Ka radiation (k = 1.5418 Å) through an X-ray tube operated at 40 kV and 50 mA. The instrument was equipped with an Anton Paar HTK1200 controlled-atmosphere chamber. A linear heating rate of 7 °C/min was used and the temperature was held constant at each temperature step for at least 30 min prior to the collection of the diffraction patterns. The sample was reduced

stepwise under 30 cc/min of 5% H_2/He starting from room temperature in 50 °C increments up to 500 °C.

7.2.2.5 Quantitative Isothermal Reduction (QIR)

QIR experiments were conducted with an MKS-Cirrus II on-line mass spectrometer. The measurement was performed in the same reactor system where N_2O dispersion experiments were done. The sample was reduced under 5% H_2 for 60 min at temperatures of 250, 275, 300 and 350 °C and at each temperature a fresh catalyst was used. Throughout the analysis, water, which is the only gas-phase product of reduction, was followed by the mass spectrometer. The m/z 18 peak was integrated and the change of area with respect to time was plotted.

The integral method was used to calculate reaction rate constant (k) at each temperature and, subsequently, the activation energy (E_a) using the Arrhenius equation. Hydrogen was fed continuously and therefore assumed to be in excess. For the reduction of CoO to Co, a 1st order reaction rate in the CoO content (C_{ox}) was assumed

$$-\frac{dC_{ox}}{dt} = kC_{ox}$$

Integration with a boundary condition of $C_{ox} = C_{ox,o}\ at\ t = 0$ gives,

$$ln\frac{C_{ox}}{C_{ox,o}} = -kt$$

Plotting $ln\frac{C_{ox}}{C_{ox,o}}$ versus t allows testing the reaction order assumed, and if a straight line is obtained, the observed rate constant k can be calculated from the slope. The procedure was

repeated for each temperature step. Activation energy was obtained from the Arrhenius equation where ln (k) values were plotted against 1/T to get a straight line, where the slope is equal to $-E_a/R$ with R as the universal gas constant.

7.2.2.6 Temperature Programmed Reduction and Re-oxidation: Kissinger Experiments

The oxidation/reduction characteristics of the samples were examined via temperature programmed studies. 100 mg of the sample was packed in a ¼" OD quartz tube and loaded into a Carbolite MTF 10/15/130 furnace. For temperature programmed reduction, the samples were treated with 5% H_2/He and the reactor effluents during reduction were monitored via a residual gas analyzer (MKS-Cirrus II) operated in selective ion mode. A 100x multiplier detector was used to monitor the m/z signals of 2, 4, 17, 18, 32 and 44. The gas lines from the reactor outlet to the mass spectrometer were heated to prevent condensation in the lines during the procedure. The background mass traces were allowed to stabilize at room temperature for 30 min while the sample was kept under a helium atmosphere. The sample temperature was ramped using a different heating rate of 10, 13, 16 and 19 °C/min for each experiment. For temperature programmed reoxidation, catalyst went through an *in situ* temperature-programmed reduction (TPR) procedure with 5% H_2/He until both of the reduction features, that correspond to Co_3O_4-to-CoO and CoO-to-Co reduction steps[158, 216-219] were observed. Following the reduction step, the samples were kept under helium for water removal at the same temperature for 30 min and then cooled to room temperature. The catalysts then went through the temperature-programmed

oxidation step with 5% O_2/He under varying heating rates of 10, 13, 16 and 19 °C/min for each experiment.

Activation energies for cobalt oxide reduction and reoxidation were calculated through Kissinger's experiments. In this technique, when the reductant (H_2) or oxidant (O_2) consumption is plotted as a function of temperature, the deflection point gives the temperature T_m at which the reductant or oxidant consumption rate is a maximum. The deflection points shift to higher temperatures as the heating rate Φ increases. The activation energy can be calculated by plotting $1/T_m$ versus ln (Φ/T_m^2) and the slope is equal to -Ea/R, where R is the universal gas constant in J/K mol and Φ stands for the heating rate in °C/min.[220]

7.2.2.7 X-ray Absorption Near Edge Spectroscopy (XANES)

Reduction and oxidation behavior of Co catalysts under hydrogen and water, respectively, were examined using a controlled-atmosphere X-ray absorption fine structure (XAFS) technique.

The experiments were conducted at the bending magnet beamline (5BM-D) of the Dow-Northwestern-DuPont Collaborative Access Team (DND-CAT) of the Advanced Photon Source, Argonne National Laboratories. Supported Co catalyst sample was first mixed with SiO2 at a ratio of 1:4 to optimize XAFS signal, then finely ground (<150 mesh) to obtain a homogeneous mixture. 6 mg of sample mixture was then pelletized using a 6-mm polished steel die and transferred inside a 5 cm-long quartz tube (6.5 mm ID) and supported with quartz wool plugs. The X-ray beam was centered as it penetrates the sample

in a 45 x 2 cm controlled-atmosphere XAFS chamber that was fitted with Kapton® windows. The XAFS chamber was isolated from outside atmosphere and placed into a furnace to perform the *in situ* experiment. The experiment consisted of three continuous cycles of reduction and re-oxidation reactions. Each cycle includes hydrogen reduction followed by water re-oxidation. The sample was first reduced using 3.6% H_2 and then water vapor was introduced to the XAFS chamber using a bubbler system. The concentration of water was ~4 %. The *in situ* XANES spectra were collected for the Co K-edge (7709 eV) at 350, 400 and 450 °C during each cycle, except the first oxidation cycle at 350 °C, for which there was no spectral acquisition. For each temperature step, a fresh catalyst was used. The catalyst was maintained for 45 min at each step, and XANES spectra were collected at regular time intervals during each of the cycles. The reduction and oxidation steps were repeated for 3 times at each temperature. The measurements were made in transmission mode with the Si(111) monochromator detuned by 30% to remove the higher order harmonics in the beam. The sample thickness was chosen to give an absorption edge jump of about 0.3 at the Co K-edge. XANES spectra were analyzed by linear combination fitting of the Co_3O_4, CoO and Co foil to obtain oxidation states.

7.3 Results and Discussion

7.3.1 Surface Area, Pore Volume and Dispersion

Surface area and pore volume of bare ceria nanoparticles and Co/CeO_2 are shown in Table 5. The surface area and pore volume both decreased following Co impregnation. Figure 31 shows the distribution of pore size in the ceria support and in the Co/CeO_2

catalyst. Ceria sample shows a similar pore size distribution to the supported catalyst with a highest pore volume around 40 Å for the support and 65 Å for Co/CeO_2. Our previous work on these catalytic systems has shown an average ceria particle size of 5-8 nm.[214] The pores with larger than 80 Å in diameter can be explained by the presence of interstitial pores between two or more particles.

Dispersion of metallic cobalt over the Co/CeO_2 sample was studied with the Jensen's method[215] using N_2O as a probe molecule for chemisorption onto the pre-reduced surface at 40 °C. A relatively low concentration of N_2O (3% in balance helium) was fed to the sample following reduction with 5% H_2 at 400 °C for 1 h. This created a mildly oxidizing atmosphere to minimize the chance of further oxidizing CoO species to Co_3O_4. The metallic cobalt dispersion is calculated as explained in the experimental section and was found to be around 24% for the Co/CeO_2 sample.

Table 5. Surface area and pore volume of the bare support and Co/CeO_2 catalyst measured using N_2 physisorption

	BET surface area (m^2/g)	Pore volume (cm^3/g)
CeO_2	100	0.17
Co/CeO_2	56	0.12

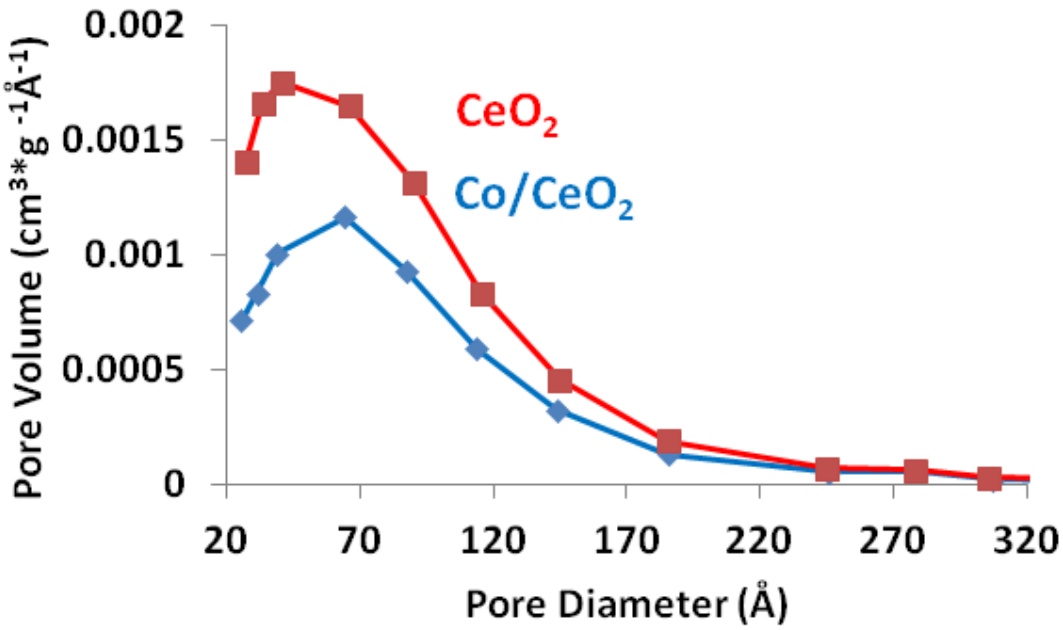

Figure 31. Pore size distribution of bare ceria support and Co/CeO_2

7.3.2 Transmission Electron Spectroscopy (TEM)

Digital micrographs for the bare ceria support and the supported Co/CeO_2 catalyst are shown in Figure 32. The ceria particle size ranges between ~5 and 8 nm and a particle size histogram was reported in our previous work for the nanoparticles.[214] Cobalt species exist in fully oxidized form and a cobalt particle positioned on ceria in Figure 32 b can be identified by lattice fringe identification with 0.29 nm d-spacing associated with the (220) plane of Co_3O_4 (ICDD 42-1467). Cobalt particle size was around 4-5 nm. The ceria particles can also be identified with the lattice fringes, using 0.31 nm d-spacing for the (111) plane of ceria (ICDD 81-792).

7.3.3 *In Situ* X-ray Diffraction (XRD)

Figure 33 shows the *in situ* XRD patterns taken at 100 and 500 °C during reduction with 5% H_2/He. The diffraction line at 33° corresponds to the (200) plane of ceria (ICDD #34-394) in the face-centered cubic cerianite structure and was the most prominent peak during the experiment. Cobalt was in fully oxidized Co_3O_4 form at 100 °C which can be inferred from the diffraction lines at $2\theta = 31°$ and 37°, corresponding to the (220) and (311) planes, respectively (ICDD #42-1467). Reduction of cobalt species was observed in situ as the temperature is increased during *in situ* XRD. At 500 °C, a weak CoO peak was observed at $2\theta = 42.4°$ signifying the (200) plane of CoO (ICDD #43-1004). Metallic cobalt was also present at 500 °C with the peak at $2\theta = 44°$ corresponding to the (111) plane (ICDD #15-806). This feature is more prominent than the diffraction line that corresponding to CoO. Scherrer calculations have shown a ceria particle size around 8.7 nm whereas the particle

sizes for the Co_3O_4 species were found to be around 5 nm. These findings are consistent with the observations from TEM images.

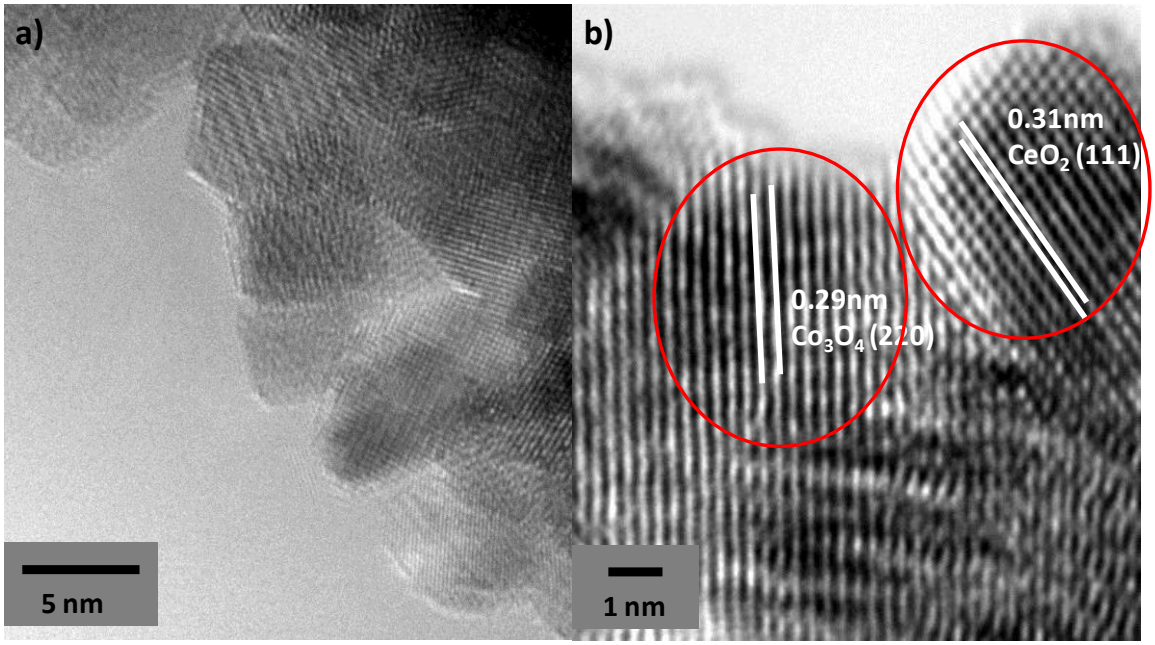

Figure 32. TEM micrographs a) CeO_2 b) Co/CeO_2

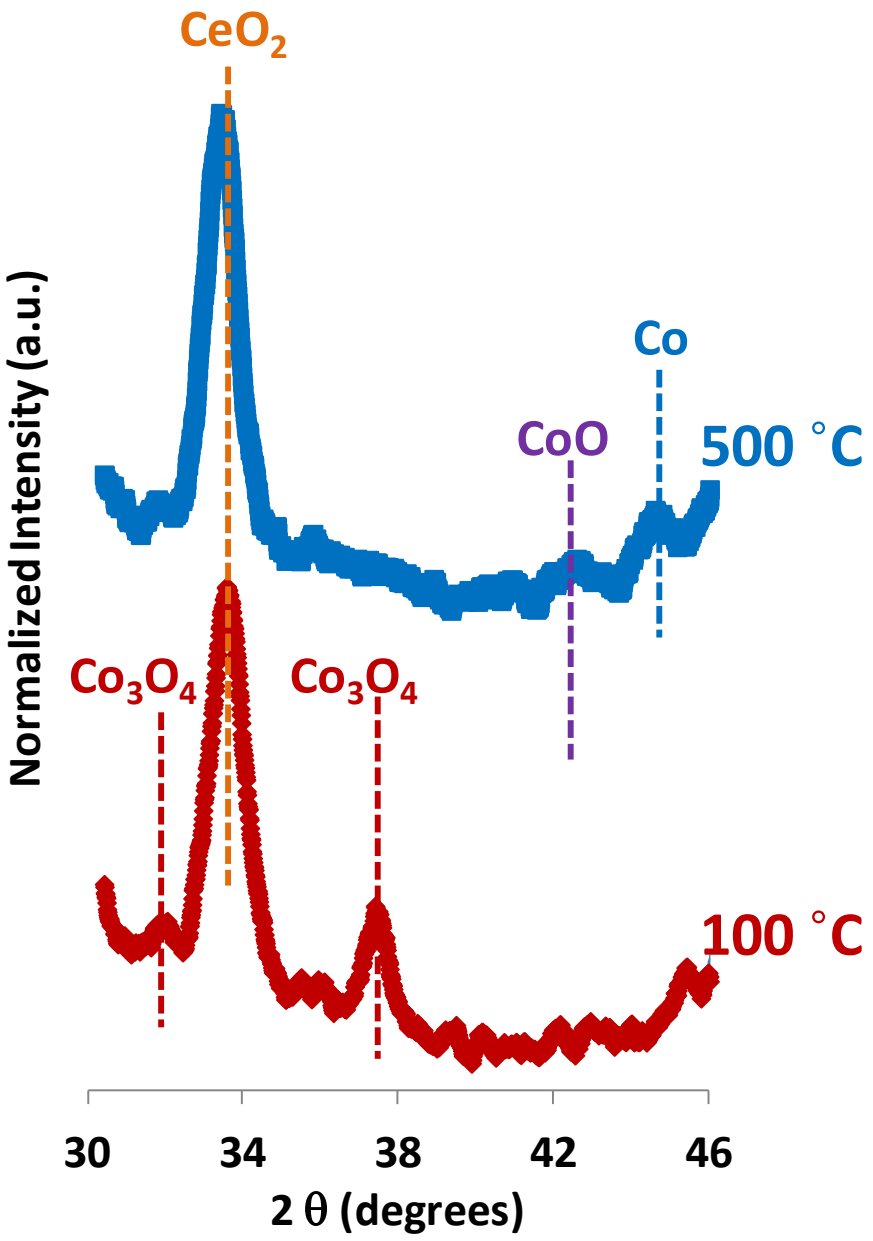

Figure 33. *In situ* X-ray diffraction patterns of Co/CeO2 taken during reduction

7.3.4 Quantitative Isothermal Reduction Experiments

In order to understand the kinetics of Co reduction, QIR experiments were conducted at 250, 275, 300 and 350 °C. Water being the only gas-phase product of reduction of the oxide phase, its signal was monitored as a function of time. Cupric oxide was used as the calibration standard for quantification of the moles of water produced following the reduction of the catalysts. Figure34 illustrates the procedure we used for the quantification. The water signal seen in Figure 34 a was integrated (area under the curve) and plotted as a function of time (Figure 34 b). Using the calibration standard, the area under the curve was converted to the total amount of water produced. The reduction of Co_3O_4 goes through two distinct steps.[218]

$$Co_3O_4 + H_2 \rightarrow 3\,CoO + H_2O \quad 1^{st} \text{ reduction step}$$

$$CoO + H_2 \rightarrow Co + H_2O \quad 2^{nd} \text{ reduction step}$$

The first step is much faster than the second one. Therefore, our focus on these experiments was on the kinetics of the second reduction step from CoO to Co. To achieve this, the amount of water produced during the first step was subtracted and the ‘‘total water formation versus time’’ data were converted to the change in CoO content as a function of time and presented for each temperature in Figure 35 a. This figure also represents the extent of reduction of CoO with respect to time. It should be noted that the experiments were designed not to have fully reduced samples for the analysis to have correct kinetic interpretation.

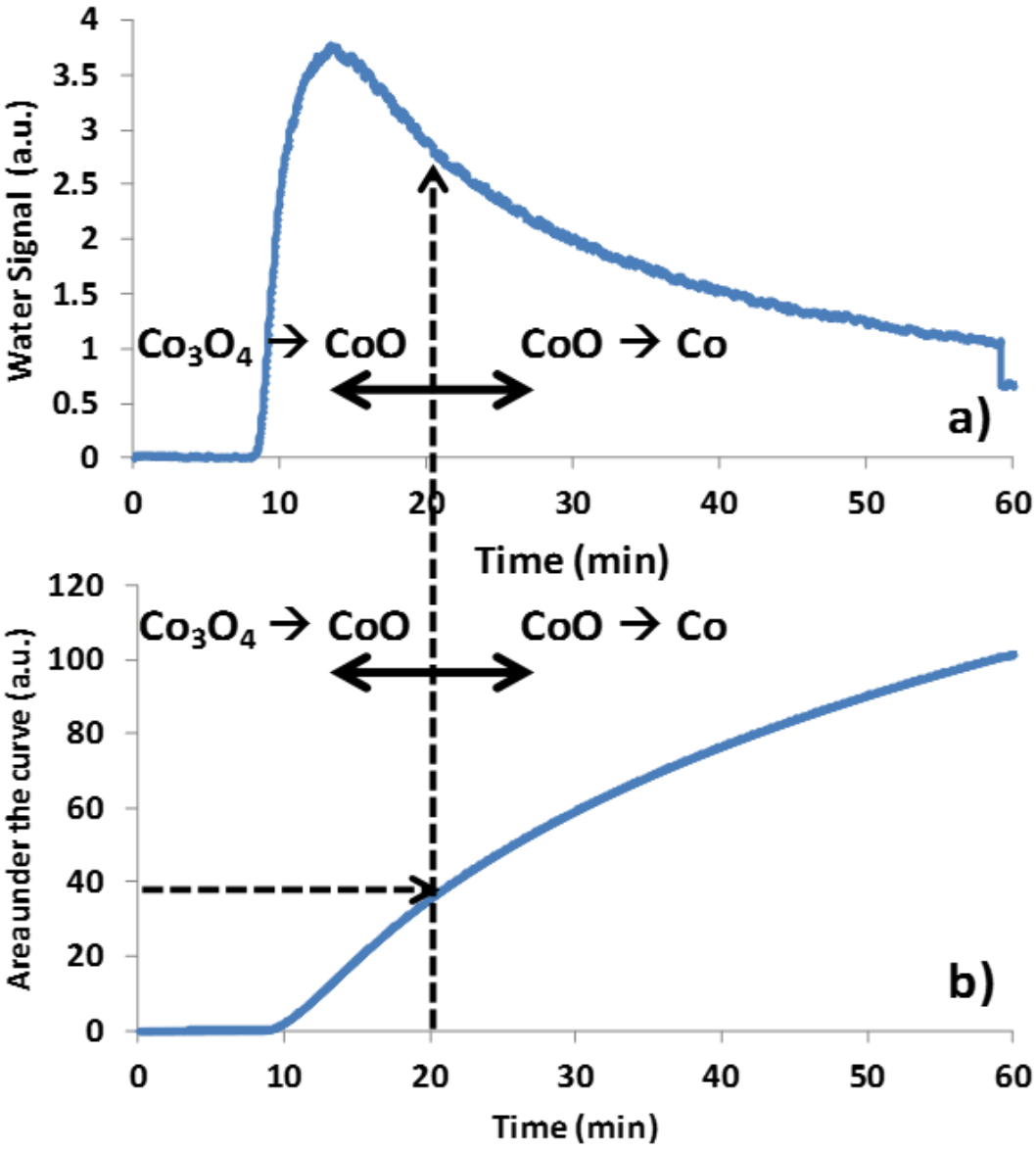

Figure 34. The calculation method for the quantitative isothermal, reduction: a Raw signal for m/z:18 from the mass spectrometer, b The area under the curve calculated from numerical integration

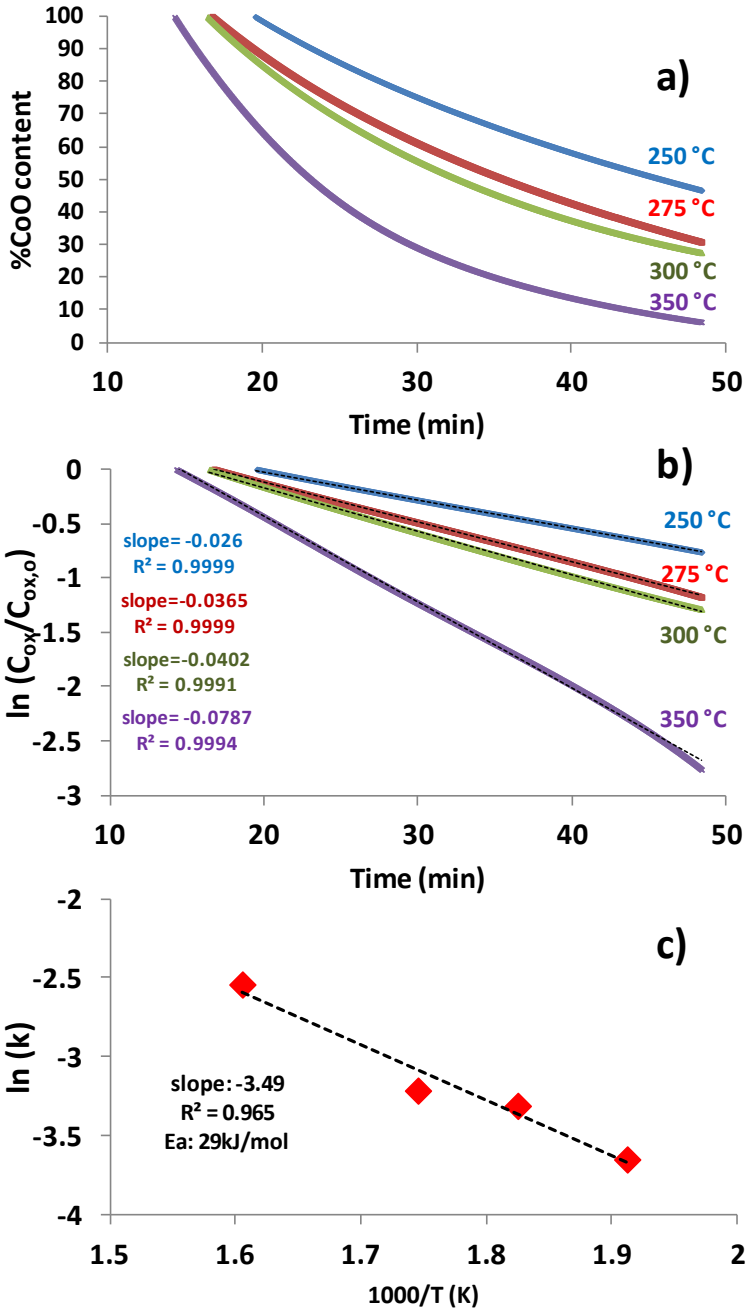

Figure 35. The results of the quantitative isothermal reduction experiments at temperatures 250, 275, 300, 350 °C **a** CoO content with respect to time during reduction with 5% H_2, **b** Integral plots for the 1st order kinetics, **c** Arrhenius plot for determining the activation energy of CoO → Co reduction

As described in the section 7.2.2.5, a first order kinetics with respect to CoO content was assumed. The assumption was tested by plotting ‘‘$\ln(C_{ox}/C_{ox,o})$ versus time’’ data (Figure 35 b). When straight lines were obtained, k values for each temperature were calculated using the slope. These k values were then used to construct an Arrhenius plot (Figure 35 c). The activation energy for CoO to Co reduction was calculated to be ~29 kJ/mol.

It should be noted that a possible reduction of bulk or surface ceria was not considered for the calculation of activation energy. Reduction of ceria below 350 °C was assumed to be negligible for the kinetic studies.

7.3.5 Temperature Programmed Reduction and Re-oxidation: Kissinger Experiments

The reduction and oxidation behavior of the Co/CeO_2 sample was also investigated with temperature programmed reduction (TPR) and re-oxidation (TPO) experiments. Figure 36 shows the TPR profiles obtained for each heating rate. 5% H_2/He was used as the reducing gas and the ramp rates used were 10, 13, 16 and 19 °C/min. The reduction of Co_3O_4 to CoO was observed prior to the main reduction peak around 200 °C and shifted with the heating rate. The analysis was done for the larger reduction peak which is believed to represent the CoO-to-metallic Co reduction. The temperature for the maximum hydrogen consumption rate (T_m) was observed to shift from 283 to 330 °C as the heating rate was increased. The activation energy for reduction was calculated from the local maxima of the hydrogen consumption curve as explained in the experimental section. The inset in Figure 36 shows the Arrhenius plot for reduction of Co/CeO_2 sample with a slope

of -3.44 which corresponds to an apparent activation energy of ~29 kJ/mol. This result agrees closely with the Ea calculated from QIR experiments.

For the temperature programmed re-oxidation experiments, 5% O_2/He was used to re-oxidize a sample which was pre-reduced with 5% H_2/He for at 400 °C. The profiles during pre-reduction were monitored with mass spectrometer until both of the features that correspond to of $Co_3O_4 \rightarrow CoO$ and $CoO \rightarrow Co$ reduction steps were observed to ascertain complete reduction to metallic cobalt. The ramp rates and the calculation procedure were similar to the TPR section. Figure 37 shows a shift in the maximum oxygen consumption from 212 to 261 °C which corresponded to an apparent Ea of ~20 kJ/mol. It should be noted that re-oxidation of the sample takes place in a single step and it was not possible to differentiate between the Co to CoO and CoO to Co_3O_4 oxidation. The sample was slightly easier to oxidize than reduce in the temperature range.

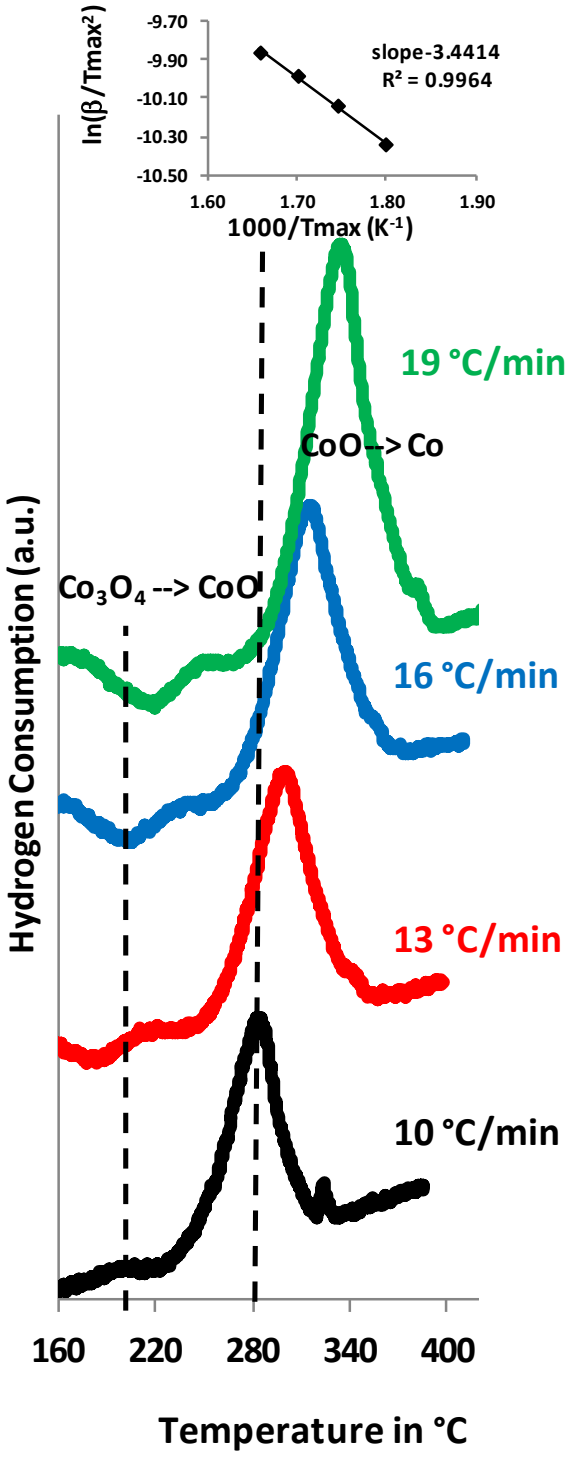

Figure 36. Temperature-programmed reduction of Co/CeO_2 samples at different ramp rates. Inset shows calculation of the activation energy of reduction using the Kissinger method

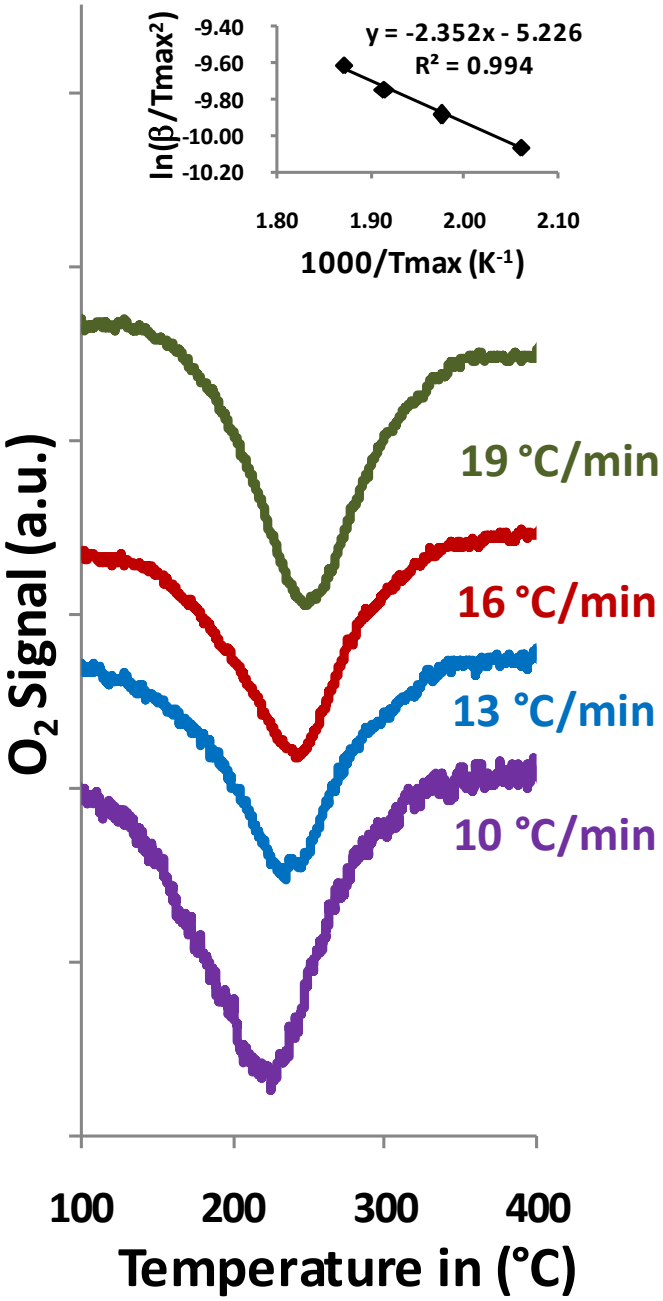

Figure 37. Temperature-programmed re-oxidation of pre-reduced Co/CeO_2 samples at different heating rates. Inset shows calculation of the activation energy re-oxidation using the Kissinger method

7.3.6 *In Situ* X-ray Adsorption Near Edge Spectroscopy (XANES) Reduction/Oxidation

The reduction and oxidation behavior of the Co/CeO_2 catalyst was also investigated via *in situ* XAFS technique. The samples were reduced under 3.6% H_2/He flow and were reoxidized with 4% water in balance helium at 350, 400 and 450 °C. Co_3O_4, CoO and Co were used as reference compounds in linear combination fitting of the XANES region. Figure 38 shows the normalized XANES spectra where the catalyst was cycled 3 times between reduction under hydrogen and re-oxidation under water flow for each temperature. Spectra were collected at regular time intervals except for the first oxidation cycle at 350 °C during which there was no spectral acquisition. A fresh sample was used at each temperature. XANES fitting with the standards provided the Co oxidation state for each spectrum. Figure 39 is a summary of the XANES fittings. The y-axis is defined as the overall oxidation state where the contribution from Co_3O_4 and CoO were calculated to be 2.67 and 2, respectively. Therefore, data points above 2 signify a Co_3O_4 and CoO mixture whereas data points below two indicate CoO and metallic Co presence in the sample. The reduction rate increased significantly with increasing temperature, with average oxidation state approaching zero at the end of the reduction cycles at 450 °C although at 350 °C the average oxidation state was around 1.2, indicating that the metal content at that point in time was ~40%. Cobalt species were found to re-oxidize under water. However, the reoxidation rate appeared to be lower than the reduction rate. Also, the extent of re-oxidation dropped at each cycle, although the starting oxidation level was about the same in each cycle. The data clearly show that water acts as an oxidant for the nano Co/CeO_2 system and is able to oxidize the partially reduced sample.

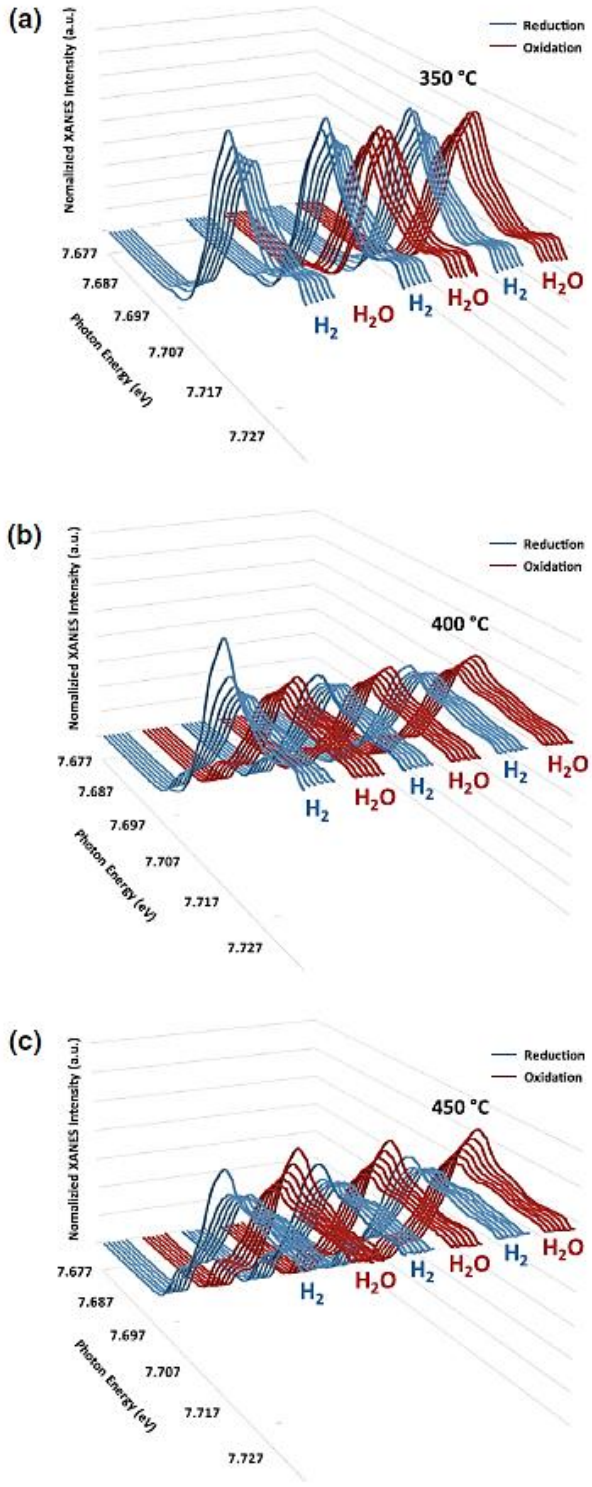

Figure 38. *In situ* XANES spectra taken during reduction and re-oxidation cycles at regular time intervals for Co/CeO2 at **a** 350 ℃, **b** 400 ℃, **c** 450 ℃

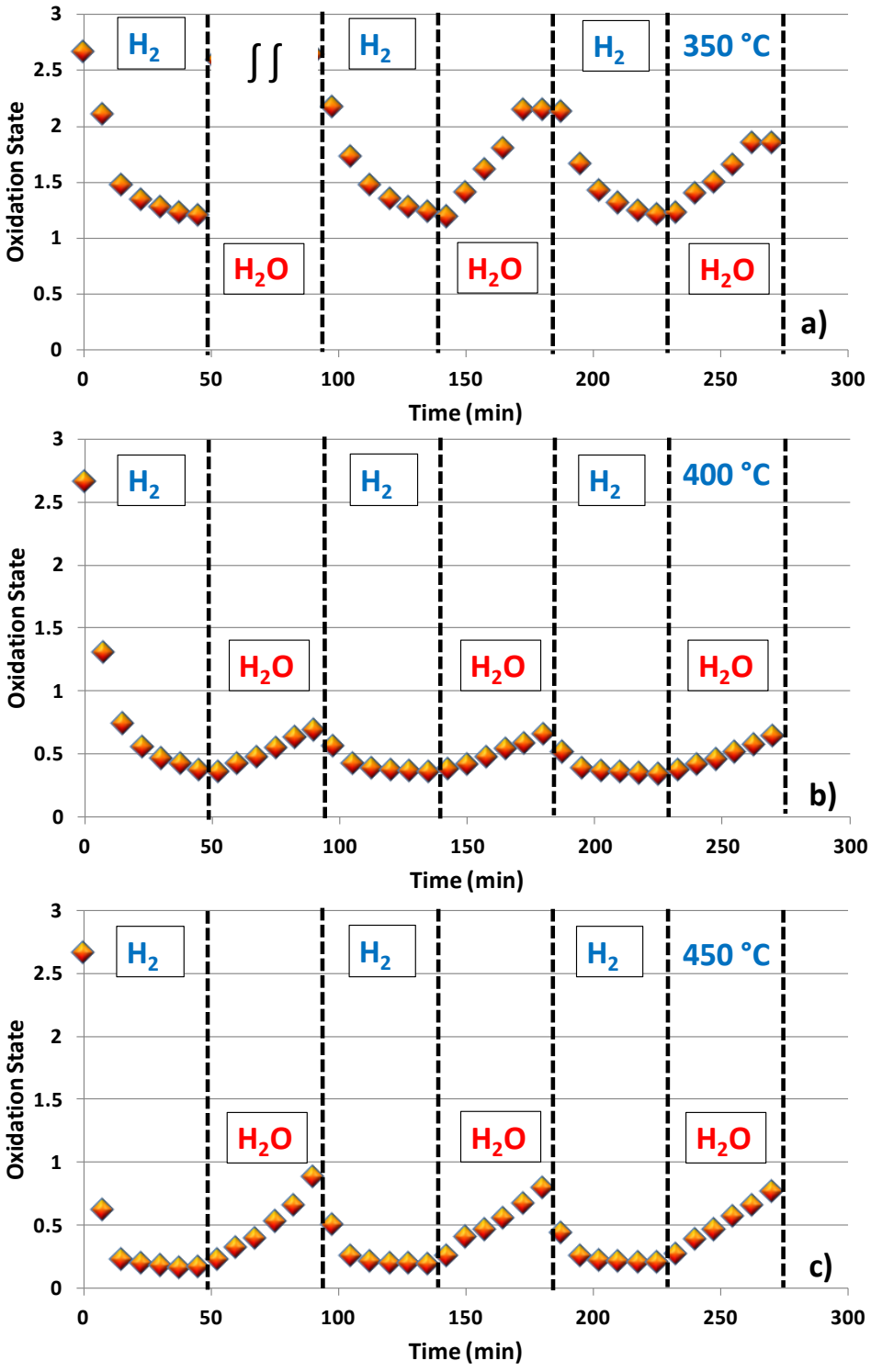

Figure 39. A summary of XANES fittings for time-on-stream cyclic reduction and reoxidation for Co/CeO_2 at **a** 350 ℃, **b** 400 ℃, **c** 450 ℃

The XANES data were also used for kinetic analysis (Figure 40). Again a first order rate expression with respect to the CoO content was assumed. The H_2 content was assumed to be constant since there was a constant flow of H_2 at all times. Only the data points taken after all Co_3O_4 was reduced to CoO were included for this analysis. Although the plots of $\ln(C_{ox}/C_{ox,o})$ versus time agreed with 1st order kinetics assumption for the two lower temperatures, the reduction behavior of CoO at 450 °C was quite different. Therefore, an activation energy could not be calculated from the reduction portion of *in situ* XANES. The data suggest that, at higher temperatures, the kinetics change, possibly due to mass transfer effects becoming more significant.

Figure 41 a shows the calculation of the rate constants for the re-oxidation portion of the spectra with Figure 40 b showing the respective Arrhenius graph in the 350-450 °C temperature range. In this analysis, the reactant was assumed to be the metallic Co, and the initial metal content at each cycle was assumed to be the level observed at the end of the reduction cycle. Similar to reduction experiments, the water concentration was assumed to be constant. The re-oxidation behavior was found to follow 1st order kinetics. The apparent activation energy for the re-oxidation of Co to CoO calculated from the XANES is ~37 kJ/mol for re-oxidation of Co/CeO_2 with 4% water. It is worthwhile to note that oxidation with water had a higher energy barrier when compared to oxidation with 5% O_2/He calculated from the TPO-Kissinger experiments.

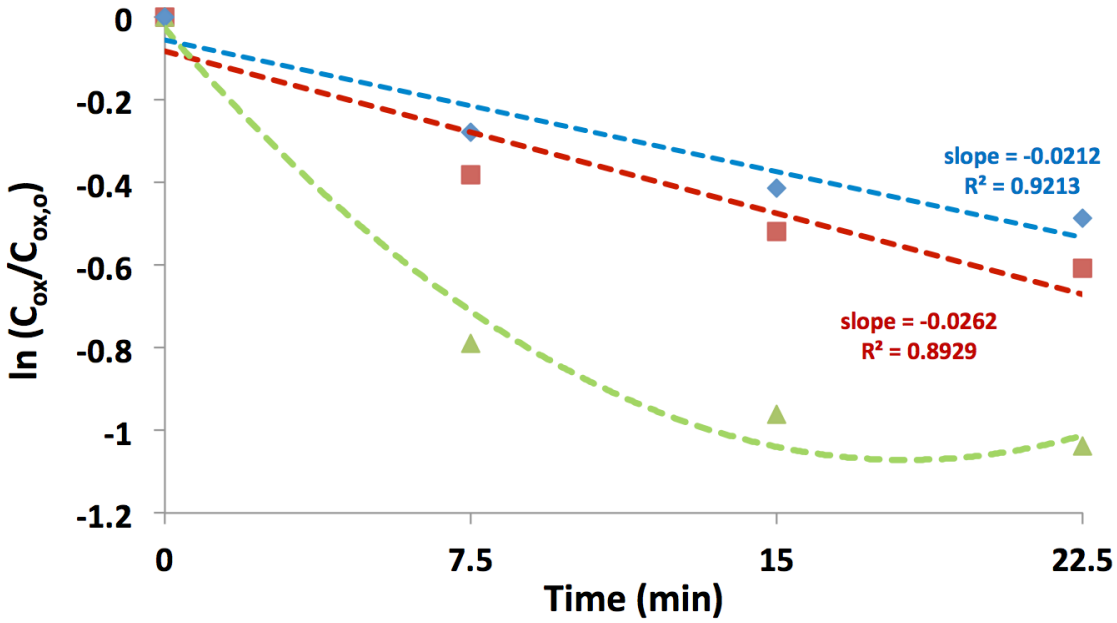

Figure 40. Kinetic analysis of the XANES data for the reduction cycles at 350, 400, 450 ℃. Integral plots were constructed for the reduction rate of CoO assuming 1st order kinetics

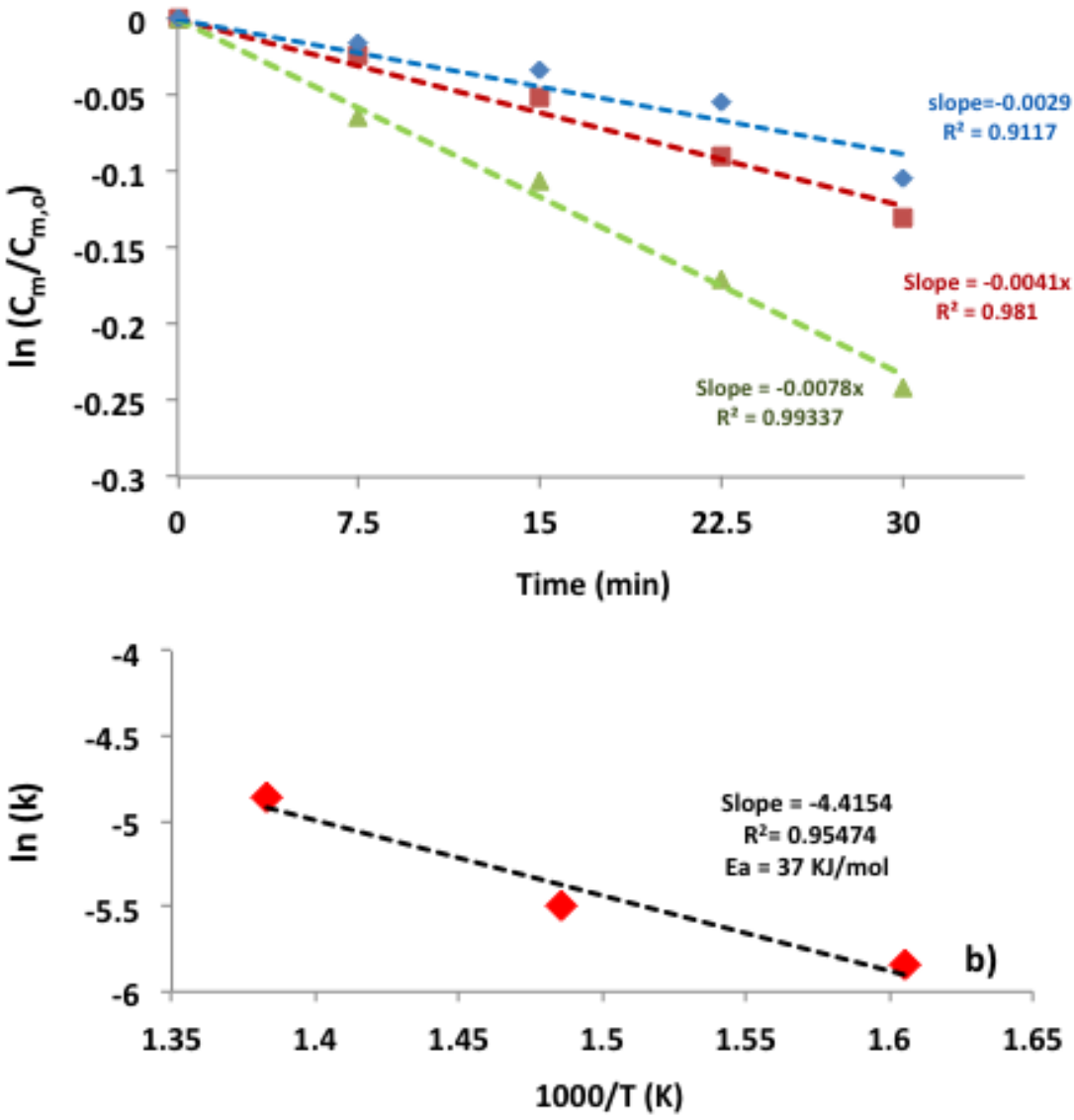

Figure 41. **a** Kinetic analysis of the XANES data for the re-oxidation cycles at 350, 400, 450 ℃. Integral plots were constructed for the reoxidation rate of Co assuming 1st order kinetics, **b** Arrhenius plot for determining the activation energy of Co → CoO oxidation with water

7.4. Conclusion of Chapter 7

Co supported on 5-8 nm nano-ceria was studied in terms of its reduction and oxidation behavior under hydrogen, oxygen and water atmospheres. TPR and oxidation studies showed a slightly higher activation barrier for the reduction of the cobalt species when compared to oxidation with O_2. A novel QIR technique was introduced and used for investigating the kinetics of Co reduction, where the reduction of CoO to metallic Co was found to be first order in the 250-350 °C temperature range. *In situ* XANES studies suggest a change in reaction order at higher temperatures, possibly due to mass transfer effects becoming more significant. *In situ* XANES studies have also shown that re-oxidation of cobalt with water is possible between 350 and 450 °C and follows a first order kinetics. The apparent activation energy of oxidation with water was significantly higher than the Ea of oxidation with 5% O_2. Apparent activation barriers calculated for CoO to Co reduction via TPR-Kissinger and QIR techniques were found to be very similar.

** Information in this chapter is reproduced/adapted from "Ilgaz Soykal, I.; Sohn, H.; Miller, J. T.; Ozkan, U. S., Investigation of the Reduction/Oxidation Behavior of Cobalt Supported on Nano-ceria. Topics in Catalysis 2013, 57 (6-9), 785-795."*

CHAPTER 8

REDUCTION CHARACTERISTICS OF CERIA UNDER ETHANOL STEAM REFORMING CONDITIONS: EFFECT OF THE PARTICLE SIZE

8.1 Summary of Chapter 8

Reducibility of ceria under steam reforming conditions and the effect of particle size on its reducibility was examined using two ceria samples with distinctly different mean particle sizes (3.5 nm versus 120 nm), but with similar polyhedral morphologies. The degree of reduction from Ce^{4+} to Ce^{3+} was characterized by temperature programmed reduction (TPR) and *in situ* X-ray absorption near edge structure spectroscopy (XANES) where the nanopolyhedra were observed to reduce much more readily compared to the larger particle-size sample. There was also significant reduction of the nanopolyhedra under ethanol steam reforming conditions. Ceria nanopolyhedra exhibited significantly more Ce^{3+} sites which contributed to a lower occurrence of surface acidic sites. The acidic/basic sites were probed by probe molecules such as pyridine and CO_2 through *in situ* diffuse reflectance infrared spectroscopy (DRIFTS). The particle size also showed major differences in the steam reforming activity of ceria, with nanopolyhedra with a 3.5-nm mean particle size exhibiting significantly higher carbon cleavage and ethanol dehydration activity than its counterpart of 120 nm mean particle size.

8.2. Experimental Section

8.2.1 Catalyst Preparation

Ceria nanopolyhedra (CeO_2-NP) were prepared via the solvothermal[221] method where 2 g of ceriumisopropoxide precursor (Alfa Aesar, Ce 37−45%) is mixed with 20 mL of benzyl alcohol (Alfa Aesar, 98%). The mixture was rigorously stirred until the ceriumisopropoxide was dissolved. A total of 10 mL of benzyl alcohol was added, and the resulting brownish solution was transferred to a 50-mL stainless steel autoclave, which was heated at 200 ℃ for 24 h in an oven. Following the precipitation, the autoclave was cooled down to room temperature and the suspension was filtered. The remaining solids were washed with water and dried overnight at 90 ℃. The dried sample was tested as uncalcined ceria. The solids were then calcined at 450 ℃ for 3 h under air to yield ceria nanopolyhedra with a light yellow color (denoted as CeO_2-NP). Commercial ceria with a particle size in the 0.1 μm range (denoted as CeO_2-MP) was prepared by calcining Sigma Aldrich 99.999% <5 μm CeO_2 at 450 ℃ for 3 h in the air.

Ten percent (by weight, metallic) cobalt was impregnated on both samples via the incipient wetness impregnation method with $Co(NO_3)_2$ (Aldrich, 99.999%) dissolved in 200 proof ethanol (Decon Labs) and applied onto the ceria in six consecutive steps by drying the impregnated catalyst at 110 ℃ overnight in between each step to improve the homogeneity of the resulting catalyst. Following the final impregnation and drying step, the catalyst was calcined at 50 ℃ for 3 h under air flow.

8.2.2 Catalyst Characterization

8.2.2.1 Surface Area, Pore Volume, and X-Ray Diffraction (XRD).

BET surface area and pore volume were measured by a Micromeritics ASAP 2020 accelerated surface area analyzer and porosimetry instrument, using nitrogen adsorption and desorption isotherms collected at liquid N_2 temperature. BJH pore size distribution was determined by the desorption branch of the isotherm. Before measurement, the catalyst was degassed for 12 h at 130 ℃ under a vacuum better than 2 μm Hg. A Rigaku Xray diffractometer (X-ray source: Cu Kα radiation, λ = 1.5418 Å) operated at 40 kV and 25 mA was used to collect the diffraction patterns of the samples.

8.2.2.2 Transmission Electron Microscopy (TEM)

A Phillips Tecnai F20 instrument equipped with a field emission gun operated at 200 kV was used for obtaining the CeO_2-MP and CeO_2-NP TEM images. Samples were suspended in 200 proof ethanol (Decon Labs) and were sonicated for 10 min. The resulting suspension was deposited on a Tedpella, Inc. 200 mesh copper grid coated with lacey carbon. ImageJ processing software is used for the analysis of the TEM digital micrographs.

8.2.2.3 Temperature-Programmed Reduction (TPR)

The reduction of ceria samples was characterized by TPR. The quantification was done using CuO as a reference. A total of 50 mg of CuO was packed in a 1/4″ OD quartz tube and loaded into a Carbolite MTF 10/15/130 furnace. The sample was reduced under 30 cc/min 5% H_2/He with a temperature ramp of 10 ℃/min. The effluent during reduction

was monitored via a residual gas analyzer (MKS-Cirrus II) operated in scanning ion mode. A 100x multiplier detector was used to monitor the signals for m/z 2, 4, 17, 18. The peak area for m/z 2 was calculated and used as a standard for quantification of hydrogen used during reduction. Fifty milligrams of CeO_2-MP and CeO_2-NP samples was reduced similarly, and the extent of reduction was quantified using copper oxide as a standard.

8.2.2.4 X-Ray Adsorption near Edge Spectroscopy

Catalyst samples were investigated in situ under ethanol steam reforming conditions in terms of their cerium coordination environment using the controlledatmosphere X-ray absorption fine structure (XAFS) technique. The spectra were collected for the Ce LIII-edge at the bending magnetbeamline (5BM-D) of the Dow−Northwestern−DuPont Collaborative Access Team (DND-CAT) of the Advanced Photon Source, Argonne National Laboratories. The measurements were made in transmission mode with the Si(111) monochromator detuned by 30% to eliminate the higher order harmonics in the beam. CeO_2 samples were mixed with SiO_2 at a ratio of 1:8 and finely ground (<150 mesh) to obtain a homogeneous mixture. Approximately 6 mg of the mixture was then pelletized using a 6-mm polished steel die and placed inside a 5-cm-long quartz tube (6.5 mm ID) and supported with quartz wool plugs. The sample was then centered in a 45 x 2 cm controlled atmosphere XAFS chamber that was fitted with Kapton® windows. The XAFS reactor setup allowed continuous flow of the reactants as well as the isolation of the catalyst sample.

The preoxidized catalyst was heated to 400 ℃ and kept under He for the initial spectrum collection. Following that, it was kept under the ethanol steam reforming mixture of 0.3% ethanol and 3% water. *In situ* XANES data on the sample was collected at 400, 450, and 500 ℃. At each temperature step, the catalyst was kept on stream for 60 min and the XANES spectra were collected in the presence of the reaction mixture. The prereduced sample was reduced in situ at 400 ℃ with 3.6% H_2 in the XAFS reactor for the initial spectrum. The gas phase was flushed with He for 1 h, and the *in situ* XANES data were collected following the pretreatment. XANES spectra were obtained by linear combination fitting of CeO_2 (Sigma Aldrich, <25 nm particle size nanopowder) and Cerium nitrate hexahydrate standards for the Ce^{4+} and Ce^{3+} phases, respectively.

8.2.2.5 Diffuse Reflectance Infrared Spectroscopy (DRIFTS)

A Thermo NICOLET 6700 FTIR spectrometer equipped with a liquidnitrogen-cooled MCT detector and a KBr beam splitter was used for *in situ* diffuse reflectance Fourier transform infrared spectroscopy (DRIFTS). The samples were loaded into a Praying Mantis diffuse reflectance controlled atmosphere chamber with ZnSe windows and were pretreated at 400 ℃ under 30 cm^3/min He flow. Samples underwent additional treatment with reduction for 1 h in 5% H_2/He (30 ccm) at the same temperature and purging with He (30 ccm) for 1 h at 450 ℃. Following the pretreatment step, temperature was lowered to 400 ℃ under 5% H_2 balance He flow, and the background spectra were collected every 50 ℃, during cooling. CO_2 and pyridine were used separately as probes for basic and acidic sites, respectively. At room temperature, the selected probe molecule

was introduced with CO_2 in the gas flow and pyridine through bubbling He through liquid pyridine. Following 1 h of adsorption, the sample was flushed 1 h with He to remove the gas phase. Spectra were collected during the temperature ramp at every 50 ℃ step up to 400 ℃.

8.2.3 Catalyst Activity Testing

The steady-state ethanol steam reforming activity data were collected in the 350-450 ℃ range using a fixed bed flow reactor system, which consisted of a feed system capable of delivering reactant mixtures of desired flow rate and composition, a 4-mm-ID quartz reactor with a quartz frit, and an online gas chromatograph. For each run, a 20-150 mg batch of the CeO_2 was packed inside the reactor. The reactor was placed inside a resistively heated furnace (Carbolite, MTF 10/15/130), and the temperature was controlled by an Omega CSC232 PID temperature controller. Helium was used as the carrier gas, and the reactants were introduced to the helium stream using a heated evaporator-syringe pump assembly. The reactants, water and ethanol, at a 10-to-1 molar ratio, were fed to an evaporator maintained at 230 ℃, using pulse-free syringe pumps (Cole-Parmer). The gas lines in contact with the reactant gas stream were heated to 130 ℃ to prevent condensation. The steady-state reaction experiments were run in the kinetically controlled regime by maintaining the reaction conditions away from equilibrium at all temperatures. The reaction experiments were conducted with a feed stream concentration of 1.7% ethanol and 17% water balance helium. The weight hour space velocities (WHSV) ranged between 0.19 and 2.88 g EtOH $(g\ cat)^{-1}\ h^{-1}$ and were varied to allow for equal surface area

comparisons. Prereduced catalyst samples were subjected to the reduction pretreatments at 400 ℃ as described earlier in the section.

The reported reactant conversion and product yield values are representative of the catalytic activity after a steady state was reached at each temperature. Ethanol conversion, hydrogen yield, and selectivity of carbon containing species are defined as follows:

$$\text{ethanol conversion (\%)} = \frac{\text{moles of ethanol converted}}{\text{moles of ethanol fed}} \times 100$$

$$\text{H}_2\text{ yield (\%)} = \frac{\text{moles of H}_2\text{ produced}}{6 \times (\text{moles of ethanol fed})} \times 100$$

$$\text{yield of C-containing product } i \text{ (\%)} = \frac{(\#\text{C atoms}) \times (\text{moles of } i \text{ produced})}{2 \times (\text{moles of EtOH fed})} \times 100$$

For ethylene steam reforming, all reaction parameters were kept identical except feeding 1.7% ethylene instead of 1.7% ethanol.

The quantitative analysis of the reactor effluents was carried out by online gas chromatography (Shimadzu Scientific 2010) equipped with a Carboxen column coupled with a pulsed discharge helium ionization detector (PDHID) which was used to separate and detect H_2, CO, and CO_2 and a Q-Bond column with a flame ionization detector (FID) to separate and detect the hydrocarbon species. The carbon balances were always better than 95%.

8.3 Results and Discussion

8.3.1 Surface Area, Pore Volume, and XRD

The surface areas, pore volumes, and the average pore diameters of the ceria samples, with and without Co loading, are shown in Table 6. The commercial ceria was found to have a significantly lower surface area of 10 m^2/g compared to the 120 m^2/g of the nanopolyhedra prepared by the solvothermal method. The average pore volumes of both samples were also significantly different with a lower average pore volume and larger average pore diameter for the CeO_2-MP sample.

Figure 42 shows the XRD patterns of the ceria samples where the most intense diffraction line is seen at a 2θ value of 28.5°, which indicates cerianite in the cubic phase (ICDD 81-792). The other diffraction lines at 33°, 47.5°, 56°, 59°, and 69.4° were identified as (200), (220), (311), (222), and (400) planes, respectively. Higher intensities and sharper peaks observed in the CeO_2-MP sample as opposed to the broader peaks in the CeO_2-NP pattern indicate higher crystallinity in the sample with the larger particle size. Scherrer calculations around the (111) peak have shown the particle size to be around 90 nm and 5 nm for CeO_2-MP and CeO_2-NP, respectively. The inset of Figure 42 tabulates the peak areas of the diffraction pattern, which are then normalized with respect to the (111) peak. Both samples show very similar distribution of crystal planes, which indicates similar morphologies for the two samples. Both the XRD patterns and the TEM images shown in the following section point to similar morphologies and allow us to assume that any possible effects of different crystal plane exposures or morphological differences, which

are known to affect the catalytic behavior,[209, 213-214] are negligible. This, in turn, allows isolating the effect of ceria particle size.

Table 6. Surface Area and Pore Volume of CeO_2 and Co/CeO_2 Samples Measured Using N_2 Physisorption

	surface area m^2/g	pore volume cm^3/g	average pore diameter (Å)
CeO_2-MP	10	0.04	172
CeO_2-NP	120	0.12	39
Co/CeO_2-MP	8	0.03	170
Co/CeO_2-NP	34	0.04	40

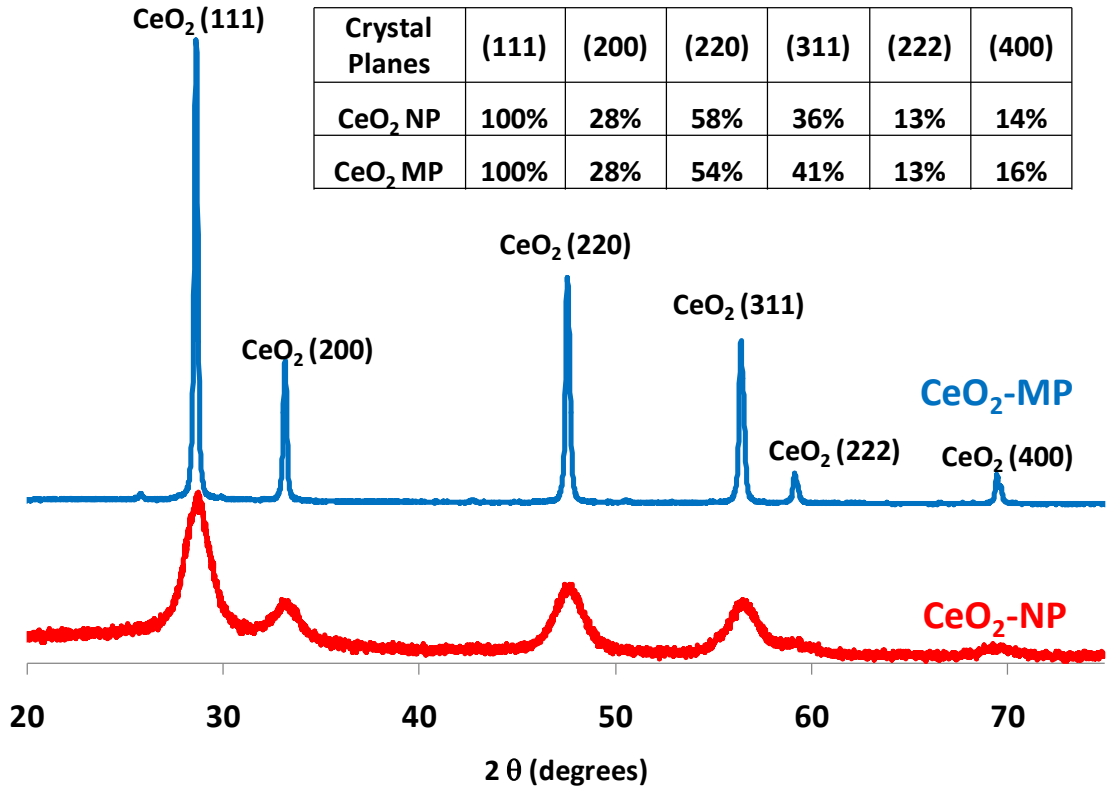

Crystal Planes	(111)	(200)	(220)	(311)	(222)	(400)
CeO_2 NP	100%	28%	58%	36%	13%	14%
CeO_2 MP	100%	28%	54%	41%	13%	16%

Figure 42. X-ray diffraction patterns of CeO_2-MP and CeO_2-NP. The inset shows the peak areas normalized with respect to the (111) diffraction line.

8.3.2 Transmission Electron Microscopy (TEM)

Figure 43 shows digital micrographs of the CeO_2-MP and CeO_2-NP particles. Ceria particles prepared by the solvothermal method exhibited distinctly smaller particle sizes. The polyhedral morphologies of both samples were rather similar. Figure 44 shows the particle size distribution of the samples in a histogram where the average sizes were calculated to have a mean of 120 nm with a standard deviation of 50 nm (120 ± 50 nm) for the CeO_2-MP and 3.5 ± 1 nm for the CeO_2-NP. Analysis was done over a large sample area through multiple histograms to ascertain random sampling. The digital micrographs further establish the morphological similarities of both samples, allowing the focus of the study to be on the effect of particle size.

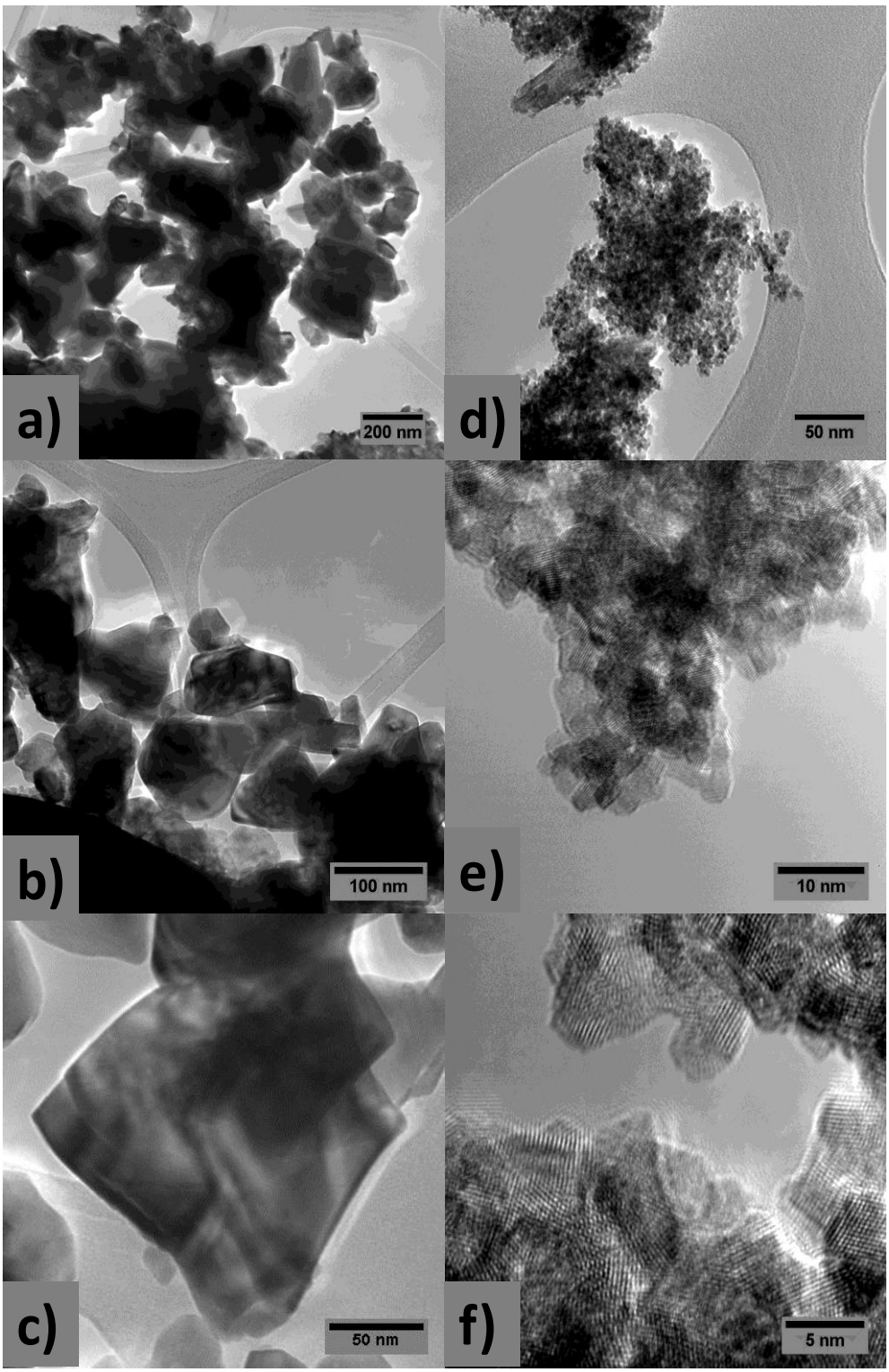

Figure 43. TEM images of (a, b, c) CeO_2-MP and (d, e, f) CeO_2-NP.

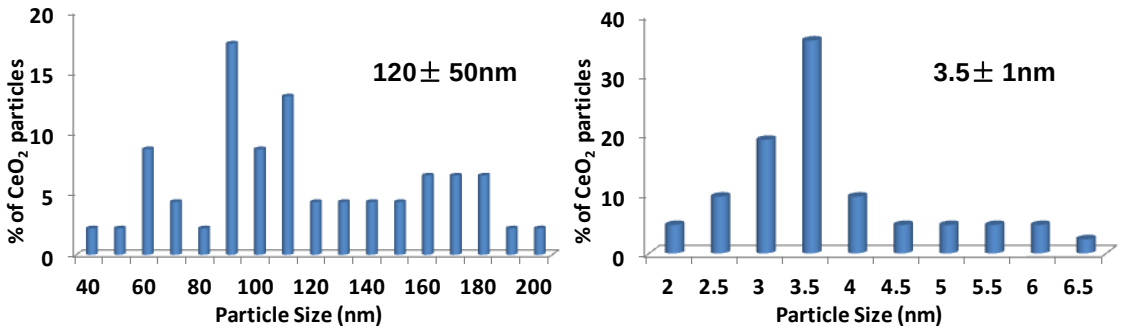

Figure 44. Particle size distribution histograms. (a) CeO_2-MP. (b) CeO_2-NP

8.3.3 Temperature-Programmed Reduction (TPR)

The ease of reducibility of the ceria samples was investigated using temperature programmed reduction. Fifty milligrams of CuO was used as a standard, and hydrogen required to reduce the sample was calculated to be 6.3×10^{-4} moles. Figure 45 shows the reduction profiles of both CeO_2-MP and CeO_2-NP. Although no significant reduction was observed below ~630 ℃ for the CeO_2-MP sample, the nanopolyhedra with a 3.5 nm average size were observed to reduce at much lower temperatures, with the maximum for H_2 consumption being around 390 ℃. Assuming the m/z 2 signal to be linear within the detection range, 50 mg of CeO_2-NP was observed to react with 3.2×10^{-5} moles of hydrogen, which corresponds to a stoichiometry of $CeO_{1.89}$. Laachir et al.[222] report approximately 20% Ce^{3+} and 80% Ce^{4+} at 700 K with a similar TPR analysis, which is consistent with 22% Ce^{3+} and 78% Ce^{4+} observed in our measurements. CeO_2-MP achieved the same degree of reduction at the much higher temperature of 750 ℃. CeO_2-NP was observed to further reduce by reacting with an additional 1.7×10^{-5} moles of hydrogen to $CeO_{1.83}$, which corresponds to 34% Ce^{3+} and 66% Ce^{4+} at 700 ℃. Ceria with the smaller particle size was found to be more readily reducible than the sample with a larger particle size. The oxidation state of the Ce is known to affect its acidic characteristics, with Ce^{3+} sites being significantly less acidic[223] than Ce^{4+}, thereby changing the surface chemistry. Further investigation of the reduction state of the ceria samples was conducted by *in situ* XANES.

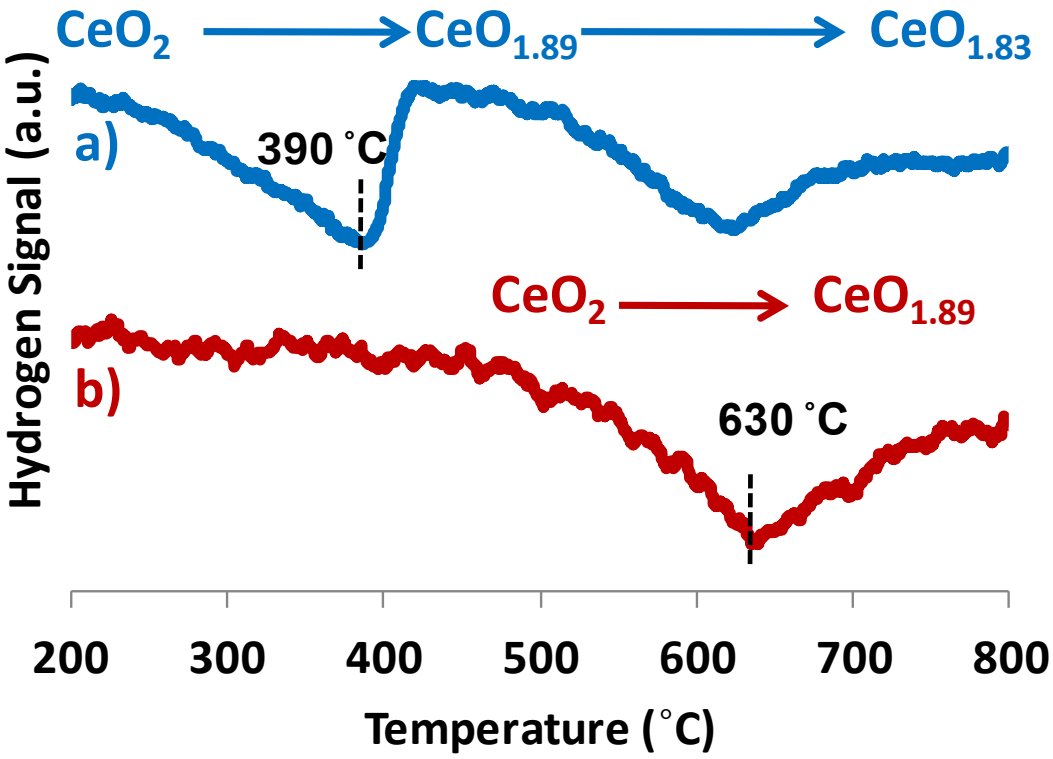

Figure 45. Temperature programmed reduction profiles of (a) CeO_2-NP and (b) CeO_2-MP.

8.3.4 X-Ray Adsorption near Edge Spectroscopy (XANES)

The transformation of the cerium oxidation state during ethanol steam reforming for the preoxidized and prereduced nanopolyhedra was investigated by the XANES technique. Ceria samples with particle sizes larger than 25 nm were not observed to reduce below 600 ℃. *In situ* XANES data for the CeO_2-NP in the 400-500 ℃ range are presented in Figure 46. Reference spectra for Ce^{3+} and Ce^{4+} are also included using $Ce(NO_3)_3$ and CeO_2 as standards, respectively. The insets show the 5.722-5.740 keV regions of the sample spectra only. The respective results of the linear combination fittings are presented in Table 7.

The oxidized sample was found to be in the form of CeO_2, whereas the reduced sample has shown 23% Ce^{3+}, which is in agreement with the TPR data presented in the previous section as well as the results of Laachir et al.[222] for similar reduction parameters. Although the starting oxidation states were quite different, both prereduced and preoxidized CeO_2-NP samples were found to converge to the same oxidation state and have a mixture of Ce^{3+} and Ce^{4+} oxidation states during steady-state ethanol steam reforming. Such behavior was previously reported in cobalt species in the ethanol steam reforming as well.[185, 218, 224] It should be noted that the reduction of cerium species was probed by predominantly bulk characterization techniques, and reported figures represent mainly bulk oxide ratios. Studies are underway to quantify the extent of surface reduction.

Table 7. Results of Linear Combination Fitting with Reference Compounds

	preoxidized		prereduced	
	$\%Ce^{3+}$	$\%Ce^{4+}$	$\%Ce^{3+}$	$\%Ce^{4+}$
after pretreatment		100	23	77
ESR at 400 °C	23	77	23	77
ESR at 450 °C	25	75	26	74
ESR at 500 °C	27	73	27	73

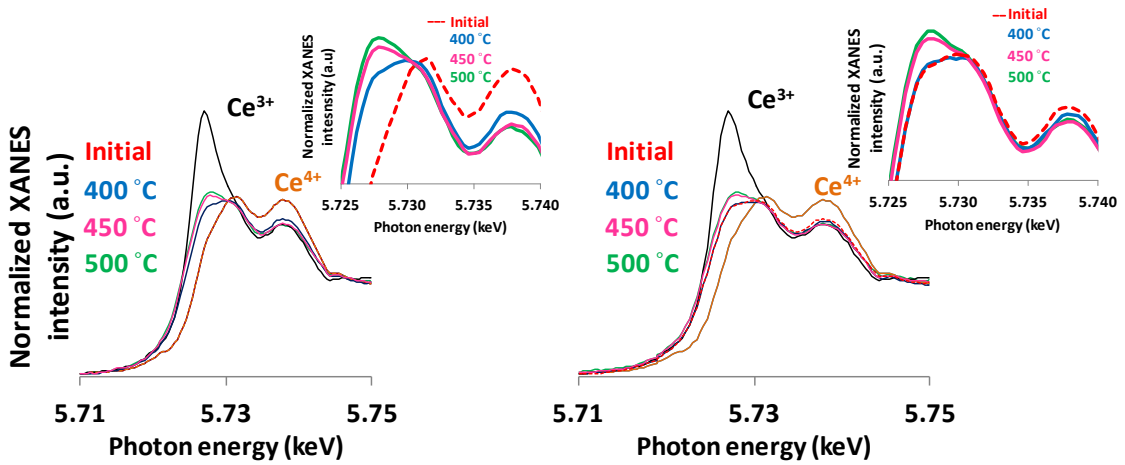

Figure 46. Operando XANES spectra for preoxidized (left) and prereduced (right) CeO_2-NP. Spectra for $Ce(NO_3)_3$ and CeO_2 are included as references for Ce^{3+} and Ce^{4+}, respectively. Insets: Enlarged views of the 5.722-5.740 keV regions for the sample spectra.

8.3.5 Diffuse Reflectance Infrared Spectroscopy (DRIFTS)

DRIFTS studies focused on probing the catalyst surface for surface acidity and basicity. For Figures 47 and 48, the same detector gain and aperture sizes were used for both samples, which enabled comparison of the relative peak intensities.

Pyridine, being a basic molecule, was used to probe the acidic sites on CeO_2 samples. Figure 47 shows DRIFT spectra taken during pyridine temperature programmed desorption (TPD) in the 25-400 ℃ temperature range. The National Institute of Standards and Technology (NIST) chemistry webbook was used along with references 46-49 for identification of the vibrational energies. Upon room-temperature adsorption, bands to due molecularly adsorbed pyridine are apparent (C-C bonds at 1038, 1067, 116, 1147, and 1217 cm^{-1}; N-CH bond at 1284 cm^{-1}).[225] The band at 1441 could be due to molecularly adsorbed pyridine, but it could also represent a pyridinium species over a Bronsted acid site. Over the CeO_2-NP sample, the only other major band seen at room temperature is the one at 1595 cm^{-1}, which can be assigned to H-bonded pyridine. All of the bands grow weaker with increasing temperature. Above 200 ℃, however, three new bands appear, suggesting decomposition of pyridine. The band at 1564 cm^{-1} could be assigned to possibly acetates, and the ones at 1373 and 1354 cm^{-1} could be due to carbonates.[226] The spectra taken over this sample suggest a surface with a very low acidity.

The spectra taken over the CeO_2-MP, on the other hand, present a much different picture. The bands due to molecular pyridine (1067, 1117, 1217, 1284 cm^{-1}) are also present in this sample. There are many more bands in the 1460−1420 range, suggesting pyridinium ions. The group of bands that is not well resolved in the 1560-1480 cm^{-1} region

may be due to pyridine adsorbed on Lewis acid sites. A band at 1595 cm^{-1} indicates the presence of H-bonded pyridine. Even at 400 ℃, the bands at the Bronsted acid and Lewis acid regions are still very strong, although there is evidence of pyridine decomposition and conversion to acetates and carbonates as well, as seen through the bands at 1564, 1373, 1354, and 1313 cm^{-1}. The high intensity of these bands all indicates a highly acidic surface where pyridine adsorbs quite strongly.

CO_2, an acidic molecule, was used to probe for the basic sites by acquiring DRIFT spectra during CO_2 TPD. Figure 48 shows spectra collected for both samples, which have some bands in common, but diverge greatly in the relative intensities of the said bands. Moreover, the adsorbed species on CeO_2-MP do not persist beyond 150-200 ℃. The major bands observed are at 1639, 1576, 1386, 1296, and 1049 cm^{-1}. The 1386 and 1049 cm^{-1} bands can be attributed to surface formates, which reform to carbonates as the temperature increases. The large bands around 1576 and 1290 cm^{-1} indicate ν_{as} (OCO) and ν_s (OCO), which can signal the presence of surface carbonates.[227-228] The band at 1639 cm^{-1} is likely due to adsorbed water. The CeO_2-NP sample has shown strong interaction with the adsorbed CO_2 throughout the temperature range, which can be explained by the presence of relatively more basic Ce^{3+} sites. The acidic probe persists even at 400 ℃ with the nanopolyhedra, whereas it was absent after 200 ℃ with the CeO_2-MP sample.

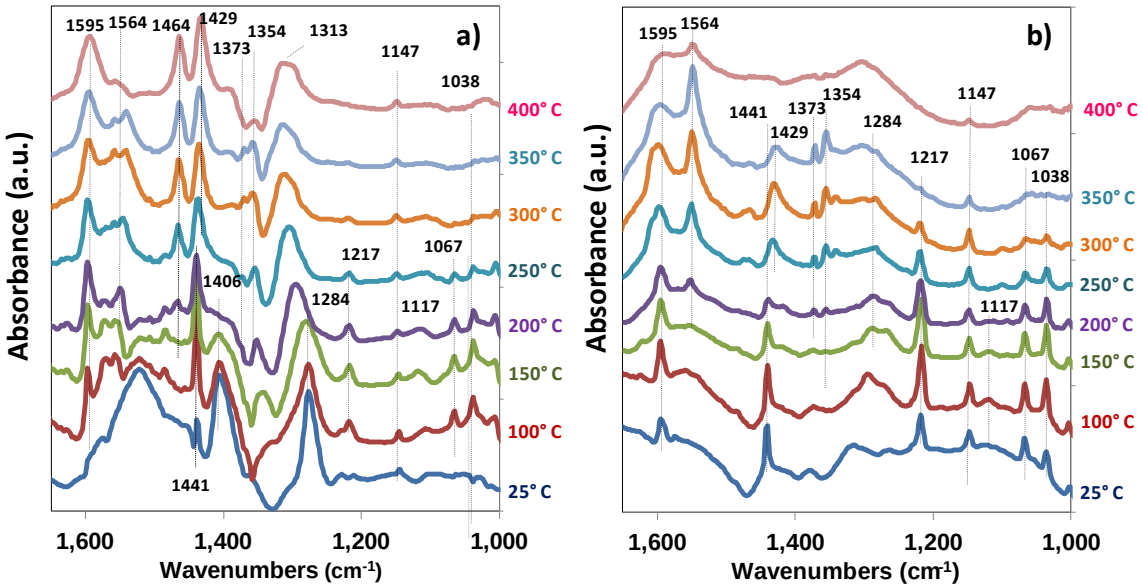

Figure 47. *In situ* DRIFT spectra during pyridine TPD. (a) CeO_2-MP. (b) CeO_2-NP. Samples were prereduced with H_2 prior to pyridine adsorption.

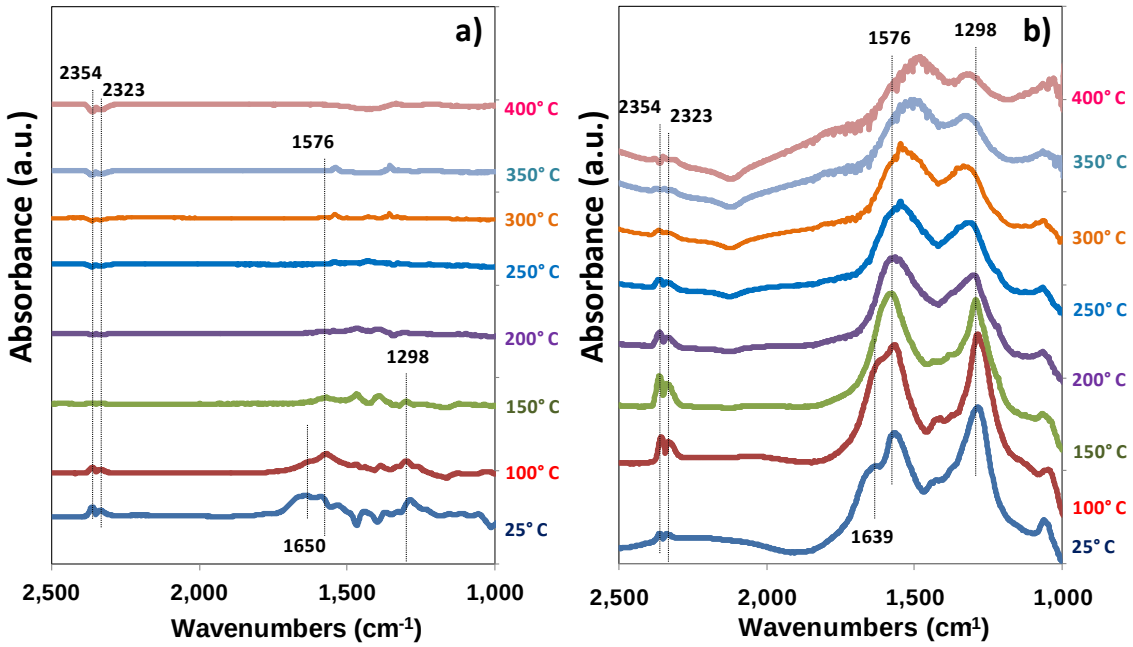

Figure 48. *In situ* DRIFT spectra during CO_2 TPD. (a) CeO_2-MP. (b) CeO_2-NP. Samples were prereduced with H_2 prior to CO_2 adsorption.

8.3.6 Steady-State Catalyst Activity Testing

Steady-state activity testing over preoxidized (O) and prereduced (R) CeO_2-MP and CeO_2-NP catalysts was performed to investigate the effect of ceria particle size and the extent of reduction on steam reforming activity. Blank experiments with the same feed conditions showed no ethanol conversion within the temperature range of 350-450 ℃, which indicated negligible gas phase reforming. The products formed over both samples consisted of H_2, CO_2, CO, CH_4, C_2H_4, and C_2H_6 and the liquid products CH_3CHO and CH_3COCH_3. Equal surface area basis was used for the experiments where the catalyst loadings were varied to achieve 1 m^2 surface areas. Table 8 presents a comparison for ethanol conversion levels of hydrogen and carbon containing product yields between the two samples at 350, 400, and 450 ℃. For each catalyst, two different pretreatment procedures are used. i.e., preoxidation or prereduction, as described earlier. The samples are not particularly active at 350 ℃. At lower temperatures, the CeO_2-NP sample shows higher activity if it is prereduced. At 450 ℃, the conversion and product distributions over this sample become very similar, regardless of the pretreatment used. As shown by the XANES data collected under steam reforming conditions (Figure 46), CeO_2-NP samples converge to the same cerium oxidation state under ethanol steam reforming conditions, hence leading to identical performances at higher temperatures.

CeO_2-MP samples, on the other hand, show very similar performances whether they were prereduced or not. These samples are never as active as the prereduced nanopolyhedra. This difference can be explained by the higher reducibility of the CeO_2-NP, and the higher activity of the Ce^{3+} sites. The sample with the larger particle size does not reduce during

H_2-prereduction or under ethanol steam reforming conditions. Therefore, the pretreatment does not make any difference in the performance, leading to similar product distributions. The prereduced CeO_2-NP samples outperform CeO_2-MP at every temperature.

The most prominent C-containing product over these catalysts is ethylene, reaching selectivity levels of ~50% for CeO_2-MP and ~60% for CeO_2-NP at 450 ℃, suggesting that dehydration is a primary reaction pathway over ceria. Compared to ethylene, the other products, such as CH_4, CO and CH_3CHO are observed in much lesser quantities. However, over the CeO_2-MP sample, acetone is observed in substantial amounts, suggesting that ceria in its fully oxidized form can lead C-C bond formation, through ketonization reactions.[229-230]

Since ethylene was the primary product over these samples, they were further tested for ethylene steam reforming with C_2H_4 and H_2O in the reactant stream under the same feed conditions. Ceria, without any metal, did not show any catalytic activity for C-C bond cleavage. There was no detectable evidence of ethylene reforming or cracking, confirming that any ethylene that is formed from the dehydration of ethanol does not go through any further transformation over the ceria surfaces and is observed as a major product under steady-state conditions.

.

Table 8. Steady State Catalytic Activity Data for Steam Reforming of Ethanol over Oxidized and Pre-reduced CeO_2-MP CeO_2-NP Catalysts

Products	350 ˚C				400 ˚C				450 ˚C			
	MP(Ox)	MP(Red)	NP(Ox)	NP(Red)	MP(Ox)	MP(Red)	NP(Ox)	NP(Red)	MP(Ox)	MP(Red)	NP(Ox)	NP(Red)
% C_2H_5OH conversion	1.0	1.2	0.0	1.4	5.0	5.0	5.1	9.1	40.8	40.3	55.4	55.3
% H2 Yield	0.4	0.5	0.0	1.0	2.0	2.2	1.6	2.9	12.0	12.6	15.3	15.3
% Yield												
CO_2	0.5	0.6	0.0	1.1	2.4	2.3	1.8	2.7	12.1	12.8	14.9	15.0
CO	0.0	0.0	0.0	0.0	0.0	0.0	0.0	0.0	0.3	0.3	0.5	0.5
CH_4	0.0	0.0	0.0	0.0	0.0	0.0	0.1	0.1	0.4	0.4	0.9	1.1
C_2H_4	0.5	0.5	0.0	0.3	2.5	2.5	2.8	5.7	19.9	20.2	31.8	33.4
C_2H_6	0.0	0.0	0.0	0.0	0.0	0.0	0.2	0.1	0.1	0.1	1.5	1.5
CH_3COCH_3	0.0	0.0	0.0	0.0	0.0	0.0	0.0	0.0	6.6	6.7	2.0	3.1
CH_3CHO	0.0	0.0	0.0	0.0	0.0	0.0	0.0	0.0	0.0	0.0	0.8	0.8

C_{EtOH}= 1.7% and H_2O:EtOH = 10:1 (molar ratio) 1 m^2 total surface area

To test this assertion, the same ceria materials were impregnated with Co and used as catalysts in ethanol steam reforming, following a prereduction step. As expected, much higher conversions and H_2 yields were obtained as well as much higher CO_2 yields (Table 9). Some trends that were observed nanopolyhedra with a mean particle size of 3.5 nm were found to reduce much more easily both with H_2 as well as during steady-state ethanol steam reforming, at temperatures as low as 400 ℃. The presence of Ce^{3+} sites led to a less acidic surface over the 3.5 nm polyhedral sample. The differences in acidity manifested major differences in *in situ* DRIFTS spectra acquired during temperature-programmed desorption of probe molecules. In steady-state reaction experiments, ceria samples showed significant ethanol dehydration and steam reforming activity, with the more reduced samples exhibiting higher activity. No significant ethylene reforming was observed with either sample. Smaller particle size, increased reducibility and a higher surface density of the basic sites are thought to lead to higher activity for steam reforming. An important finding of the study is that ceria, which is commonly used as a support in many catalyst systems, has significant reducibility as well as catalytic activity in its own right and is likely to contribute to the observed activities of many catalysts supported on ceria.

Table 9. Steady State Catalytic Activity Data for Steam Reforming of Ethanol over Oxidized and Pre-reduced Co/CeO_2-MP Co/CeO_2-NP Catalysts

Products	350 ˚C		400 ˚C		450 ˚C	
	Co-MP	Co-NP	Co-MP	Co-NP	Co-MP	Co-NP
% C_2H_5OH conversion	16.4	20.9	44.0	40.2	81.3	97.1
% H2 Yield	6.5	11.2	26.4	35.6	49.2	93.3
% Yield						
CO_2	4.6	9.5	21.0	26.7	45.5	81.4
CO	0.0	0.0	0.3	0.0	0.6	0.0
CH_4	0.0	0.5	0.3	1.3	0.5	2.8
C_2H_4	0.2	0.2	2.5	2.1	8.4	4.7
C_2H_6	0.0	0.0	0.0	1.3	0.0	0.1
CH_3COCH_3	0.0	0.0	6.5	1.3	20.1	5.0
CH_3CHO	11.5	10.4	13.2	7.9	6.1	3.1

C_{EtOH}= 1.7% and H_2O:EtOH = 10:1 (molar ratio) 1 m^2 total surface area

8.4 Conclusion of Chapter 8

Ceria samples with similar polyhedral morphologies but different particle sizes were investigated for their reducibility, surface acidity/basicity, and performance for ethanol and ethylene steam reforming in the absence of another metal or metal oxide. The ceria sample with the larger mean particle size of 120 nm had negligible reducibility below 600 ℃. The nanopolyhedra with a mean particle size of 3.5 nm were found to reduce much more easily both with H_2 as well as during steady-state ethanol steam reforming, at temperatures as low as 400 ℃. The presence of Ce^{3+} sites led to a less acidic surface over the 3.5 nm polyhedral sample. The differences in acidity manifested major differences in *in situ* DRIFTS spectra acquired during temperature-programmed desorption of probe molecules. In steady-state reaction experiments, ceria samples showed significant ethanol dehydration and steam reforming activity, with the more reduced samples exhibiting higher activity. No significant ethylene reforming was observed with either sample. Smaller particle size, increased reducibility and a higher surface density of the basic sites are thought to lead to higher activity for steam reforming. An important finding of the study is that ceria, which is commonly used as a support in many catalyst systems, has significant reducibility as well as catalytic activity in its own right and is likely to contribute to the observed activities of many catalysts supported on ceria.

** Information in this chapter is reproduced/adapted from "Soykal, I. I.; Sohn, H.; Singh, D.; Miller, J. T.; Ozkan, U. S., Reduction Characteristics of Ceria under Ethanol Steam Reforming Conditions: Effect of the Particle Size. ACS Catalysis 2014, 4 (2), 585-592."*

CHAPTER 9

EFFECT OF COBALT ON REDUCTION CHARACTERISTICS OF CERIA UNDER ETHANOL STEAM REFORMING CONDITIONS: AP-XPS AND XANES STUDIES

9.1 Summary of Chapter 9

The surface and bulk reduction characteristics of bare ceria and ceria with supported cobalt nanoparticles were investigated under ethanol steam reforming conditions using AP-XPS and XANES techniques. Ceria particles were prepared in two different particle sizes, one in nano and the other in micro size (termed CeO_2-NP and CeO_2-MP), with average particle sizes of 4 and 120 nm, respectively. It was found that particle size affects surface reducibility of ceria particles; smaller particle size leads to a higher extent of surface reduction. Supported cobalt nanoparticles have a significant effect on the surface reducibility of both CeO_2-NP and CeO_2-MP. Compared to bare ceria particles, the presence of fully oxidized cobalt nanoparticles on the surface of ceria support retards surface reducibility of ceria since reduction of the cobalt oxide phases (Co_3O_4 and CoO) takes precedence over that of ceria. The degree of reduction of the cobalt phase during ethanol steam reforming determines the effect of cobalt on the reduction process of ceria, i.e., whether it retards or facilitates the reduction of ceria support. AP-XPS studies show

that the surface of cobalt nanoparticles consists of both metallic Co and CoOx. The reduction of the surface region of CoOx to metallic Co forms a metallic Co-based shell and CoOx-based core. The anchor of metallic Co on CoOx make metallic Co shell well dispersed on CeO_2 without sintering. In addition, the reforming reaction takes place primarily at the interface of metallic Co and CeO_2. The much larger difference between Co/CeO_2-NP and Co/CeO_2-MP than the difference between CeO_2-NP and CeO_2-MP suggests the significance of metallic Co in catalyzing the reforming reaction, although bare ceria support shows some dehydration activity in its own right.

9.2 Experimental Section

9.2.1 Catalyst Preparation

Two different particle sizes of ceria samples were used for this study. The ceria in the nano-sized sample was synthesized using the solvothermal protocol where 2 g of cerium isopropoxide (Alfa Aesar, Ce 37-45%) and 20 mL of benzyl alcohol (Alfa Aesar, 98%) were mixed rigorously until a homogeneous solution was obtained. A detailed synthesis procedure has been reported earlier.[231] The nano-sized ceria is referred to as CeO_2-NP throughout the text. The micro-sized ceria sample was purchased from Sigma-Aldrich (99.999%, <5 μm). The as-received sample was treated at identical calcination conditions as those used for CeO_2-NP. The resulting solids were considered as microparticles and denoted as CeO_2-MP.

The 10 wt % cobalt supported on ceria samples were prepared using incipient wetness impregnation method with an organic solvent, as reported before.[217] After the

impregnation step, the samples were dried and calcined at 450 ℃ for 3 h under air flow to acquire a fully oxidized catalyst (10% Co/CeO_2-NP and 10% Co/CeO_2-MP).

9.2.2 Catalyst Characterization

9.2.2.1 Surface Analysis

A Micromeritics accelerated surface area analyzer and porosimetry instrument (ASAP 2020) was used to measure the Brunauer, Emmett, and Teller (BET) surface area, pore diameter, and pore volume. The average pore diameter and pore volume were obtained by Barrett-Joyner-Halenda (BJH) analysis using the desorption branch of the isotherm.

9.2.2.2 Transmission Electron Microscopy (TEM)

FEI Image Corrected Titan3 G2 60-300 S/TEM with a high brightness field emission electron gun (X-FEG) operated in the range of 60-300 kV and an S-TWIN lens was utilized for TEM imaging. To obtain higher dispersion of the sample on the grid holder, the samples were first sonicated in ethanol solution for 5 min. A drop of the resulting suspension was then placed on a 200-mesh copper grid (Tedpella, Inc.) coated with lacey carbon. The TEM images were analyzed using an open-source image processing software (ImageJ). Identification of the exposed surface planes was carried out by measuring the distances between the lattice fringes.

9.2.2.3 *In Situ* X-ray Adsorption Near-Edge Spectroscopy (XANES)

The Ce L3 edge *in situ* XANES spectra were collected at the bending magnet beamline (5BM-D) of the DND-CAT synchrotron research center located in Sector 5 of the Advanced Photon Source (APS) at Argonne National Laboratory (ANL). The XANES setup includes a Si (111) monochromator and three spectroscopy-grade ionization chambers which are used as detectors. For sample preparation, all the samples were first finely ground using silica as a diluent to improve the homogeneity of the sample. The ratio between the sample and silica was determined accordingly to achieve a proper edge jump of the spectra. The prepared sample was pelletized to a 6 mm diameter pellet and placed inside a small quartz tube (6.5 mm i.d. x 5 cm) using quartz wool for support. The sample tube was then placed horizontally into a reaction chamber which is composed of Swagelok gas connections and Kapton windows. Thus, the reactor system is capable of performing *in situ* XANES experiments by flowing different gases while the X-ray penetrates the sample pellet in transmission mode.

Following the preparation steps, *in situ* XANES spectra were collected at room temperature under helium to ensure that the ceria samples are fully oxidized showing 100% Ce^{4+}. The temperature of the reaction chamber was then increased to 350 ℃ under helium flow. Helium was utilized as a carrier gas to introduce 0.3 % ethanol and 3 % water in a total volume of 30 mL/min to the reaction chamber. The *in situ* XANES spectra were acquired continuously for 1 h under ethanol steam reforming condition. The reaction chamber was then flushed with helium while the temperature was increased to 400 ℃. These steps were repeated at 400 and 450 ℃.

9.2.2.4 Ambient-Pressure X-ray Photoelectron Spectroscopy (AP-XPS)

The surface properties of the ceria-based samples were investigated under ethanol steam reforming conditions utilizing an AP-XPS instrument described previously.[232-235] The instrument consists of a benchtop monochromated Al Kα X-ray source and a reaction cell with a Si_3N_4 window, allowing X-ray to penetrate into the cell and reach the sample stage. Reactant gases flow into the cell from the gas inlet. The flow rates of the reactants are controlled by leak valves and measured using a mass flow meter. The typical flow rates used are 3-5 mL/min.[232] Gas pressure is measured at two different locations: reactor inlet and outlet. The measured pressures are averaged to determine the actual pressure inside the reaction cell.[232] For ethanol steam reforming, ethanol and water are placed in two separate sealed containers. Both reagents were degassed for several times before their vapors were introduced into the reaction cell controlled by separate leak valves. The pressure was controlled at 0.1 and 1 Torr, for ethanol and water, respectively, to achieve an ethanol and water mixture at a molar ratio of 1:10, which is similar to the composition of the ethanol-water mixture from biomass fermentation. *In situ* AP-XPS spectra for fully oxidized ceria samples were first collected under helium environment at RT. The quantification of the AP-XPS spectra was performed using CasaXPS software.

9.2.3 Catalyst Activity Testing

The catalytic activity data for ethanol steam reforming over the four samples CeO_2-MP, CeO_2-NP, 10% Co/CeO_2-NP, and 10% Co/CeO_2-MP were collected using a continuous flow fixed bed reactor system. Ethanol and water liquid mixture at 1-to-10

molar ratio was introduced to a heated evaporator, which was held at 230 ℃ utilizing a pulse-free syringe pumps (Cole-Parmer). Helium was used as a carrier gas to flush the evaporator, sending the reactants, i.e., ethanol and water vapor, to a 4-mm-i.d. quartz reactor with a quartz frit. The reactor was located and centered inside a furnace (Carbolite, MTF 10/15/130), which was heated at reaction temperatures of 350, 400 and 450 ℃. The reaction temperature was managed by a mega CSC232 PID temperature controller. All the gas lines were heated up to 130 ℃ to prevent condensation of the reactant mixture. The effluent stream of the reactor was connected to an online gas chromatograph (GC-Shimadzu Scientific 2010) in order to separate, identify and quantify the product mixture. For H_2, CO and CO_2, a Carboxen column and a pulsed discharge helium ionization detector (PDHID) were used. All the hydrocarbon products were analyzed using a Q-Bond column with a flame ionization detector (FID). The feed stream of the reactant mixture included 1.4% ethanol and 14% water balanced with helium. The reaction was performed at equal gas hourly space velocity (GHSV) of 71600 h^{-1}. It should be noted that the samples tested for catalytic activity testing did not go through a prereduction step; i.e., they were fully oxidized at the outset of each reaction experiment.

9.3 Results and Discussion

9.3.1 BET Surface area, Pore Volume, Pore Size, and Particle Size

BET surface areas, pore volumes, and particle sizes of CeO_2 bare support and Co/CeO_2 catalysts were reported previously.[231] CeO_2-NP (120 m^2/g, 0.12 cm^3/g, 39 Å) has higher surface area and pore volume with a lower average pore diameter than CeO_2-MP

(10 m^2/g, 0.04 cm^3/g, 172 Å). This is attributed to the significant difference in their particle size. Impregnation of cobalt on both NP (34 m^2/g, 0.04 cm^3/g, 40 Å) and MP (8 m^2/g, 0.03 cm^3/g, 170 Å) ceria samples results in a decrease in surface area and pore volume of bare CeO_2, especially for CeO_2-NP, as evidenced by a significant decrease in surface area from 120 m^2/g of bare CeO_2-NP to 34 m^2/g of Co/CeO_2-NP.

9.3.2 Transmission Electron Microscopy (TEM) Imaging

Particle size and morphology of the CeO_2 support were examined using TEM images. Figures 49 a and 49 b show images of CeO_2-NP. Most nanoparticles are polyhedral with a narrower size distribution compared to CeO_2-MP. The particle sizes were varied from 2 to 10 nm where the average was found to be 4 nm. The identification of the exposed plane shown in Figure 49 b, was based on the d-spacing of 0.31 nm. This indicates the lattice fringes for a single ceria nanoparticle showing (111) plane. Figures 49 c and 49 d present the TEM images of CeO_2-MP. They exhibit much larger particle sizes, which, unlike CeO_2-NP, vary significantly from 40 to 200 nm with an average particle size of 120 nm. The cobalt particle sizes were different between the two Co/CeO_2 samples where bigger cobalt particles were observed over the Co/CeO_2-MP. The cobalt particle sizes for the Co/CeO_2-NP and Co/CeO_2-MP were found around 5 ± 2 and 10 ± 7 nm, respectively. The surface planes such as (220) and (400) of Co_3O_4 were observed, which are shown in Figure 50. As it can be expected, the cobalt dispersion was higher in the case of Co/CeO_2-NP (24%) compared to Co/CeO_2-MP (2%) sample.[214]

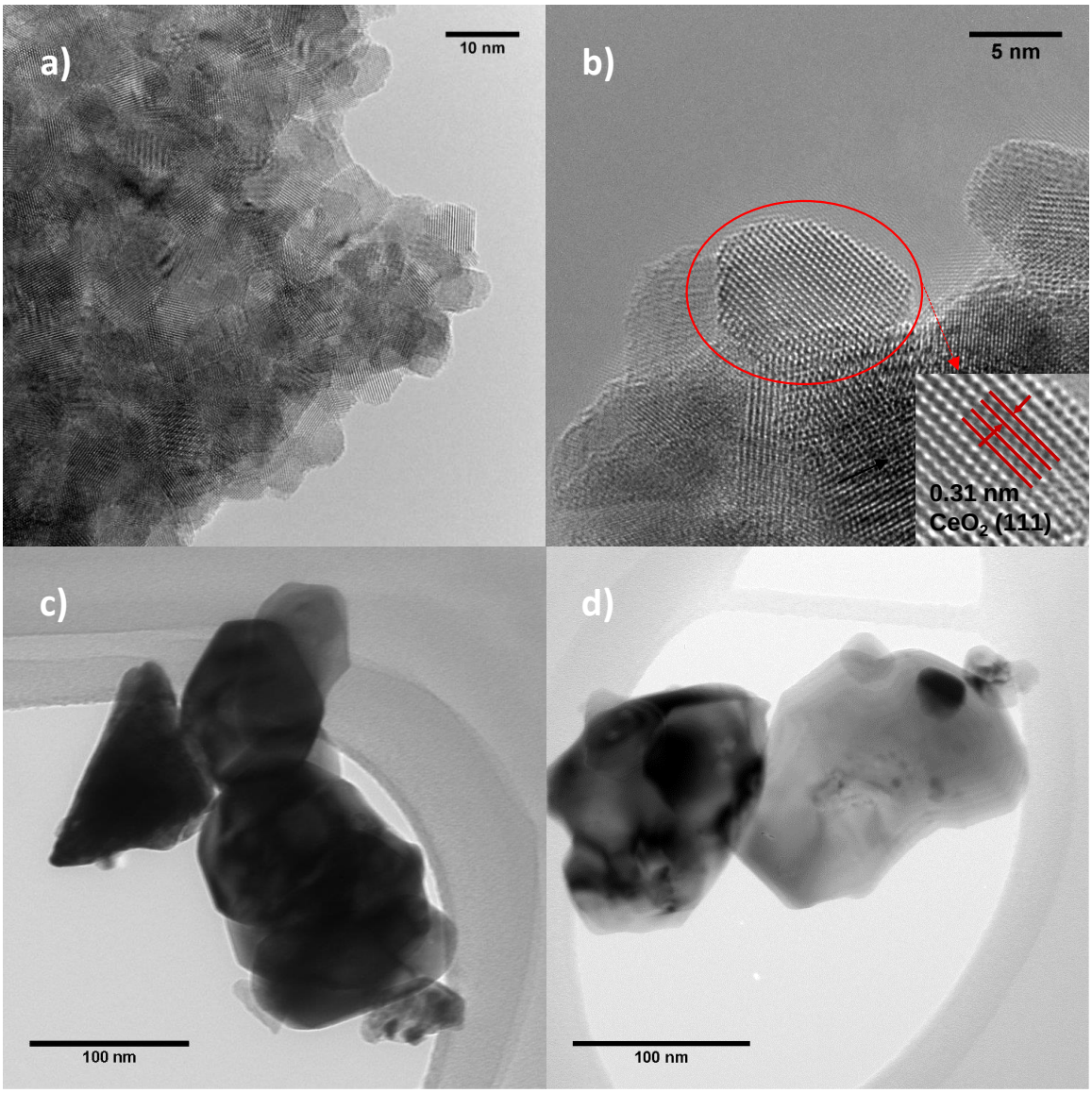

Figure 49. TEM images of CeO2-NP (a, b) and CeO2-MP (c, d).

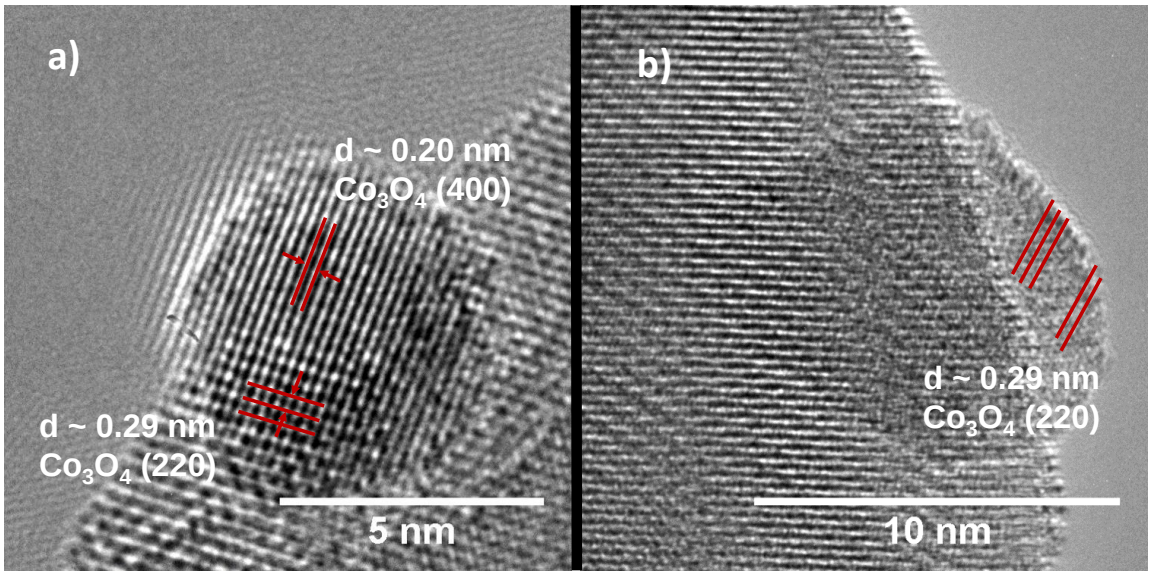

Figure 50. TEM images of cobalt particle supported on (a) CeO2-NP and (b) CeO2-MP.

9.3.3 *In Situ* X-ray Adsorption Near Edge Spectroscopy (XANES)

9.3.3.1 CeO_2-NP and CeO_2-MP

The change in oxidation state of the ceria based samples were examined using *in situ* XANES technique under ethanol steam reforming at 350, 400, and 450 ℃. The *in situ* spectra were collected continuously for 1 h at each temperature over bare ceria samples (CeO_2-NP and -MP) and cobalt-impregnated samples (Co/CeO_2-NP and -MP). The quantification of the data was performed by fitting the sample spectra with two different standards: cerium(III) nitrate hexahydrate for Ce^{3+} and cerium oxide for Ce^{4+}. The fitting was based on the linear combination of the two reference spectra. It should be noted that all the ceria samples tested for this study were fully oxidized before ethanol and water vapor were introduced to the reactor.

Figure 51 shows the Ce L3 edge XANES spectra for CeO_2-NP and -MP. A comparison of Figures 51 a and 51 b shows a clear difference between the two samples. Over the CeO_2-NP, part of the cerium ions are in +3 oxidation state, and the percentage of Ce^{3+} is increasing with increased temperature, reaching 33% at 450 ℃. CeO_2-MP, on the other hand, does not show any reduction.

As seen in Figure 51 b, no reduction of ceria was observed in CeO_2-MP under ethanol steam reforming conditions. However, our previous results[214, 231] showed that the CeO_2-MP sample is active for ethanol steam reforming, especially at higher temperatures. Based on prior observations of chemisorption and dissociation of ethanol on CeO_2, it is deduced that the surface of CeO_2-MP was reduced to some extent while most of the bulk remained unreduced. Compared to CeO_2 nanoparticles, the surface area of CeO_2

microparticles is much smaller. It is expected that the surface contribution is negligible in comparison to the bulk for large ceria particle, and the oxidation state of ceria at surface region could not be reflected in XAS. Therefore, *in situ* AP-XPS technique was used to characterize oxidation states of cerium at the surface region under reaction conditions, as presented in Section 9.3.4.

9.3.3.2 Co/CeO_2-NP and Co/CeO_2-MP

The extent of the reduction of ceria was also examined over samples that had the metal (Co) loading. The XANES spectra for Co/CeO_2-NP and -MP are shown in Figure 52. Similar to the bare ceria, Co/CeO_2-MP showed no bulk reduction. This is expected since the fraction of surface region is quite small. The change of oxidation state of Ce cations in surface region such as 1-3 nm cannot be reflected by the XANES technique.

In terms of Co/CeO_2-NP, there was quantifiable reduction of Ce. However, the degree of reduction of CeO_2-NP in the presence of Co was lower than that of bare CeO_2-NP. The percentage of Ce^{3+} of Co/CeO_2-NP reaches only 10% at 450℃. This is somewhat counterintuitive as one would expect a higher rate of H_2 production in the presence of Co, and hence a more reducing atmosphere, which would lead to a higher extent of reduction for ceria. In addition, during the ethanol steam reforming reaction, adsorbed ethanol can also be partially oxidized, even in the absence of H_2O, by surface lattice oxygen.[123, 236] Thus, surface reduction could also stem from the removal of surface lattice oxygen atoms by ethanol.

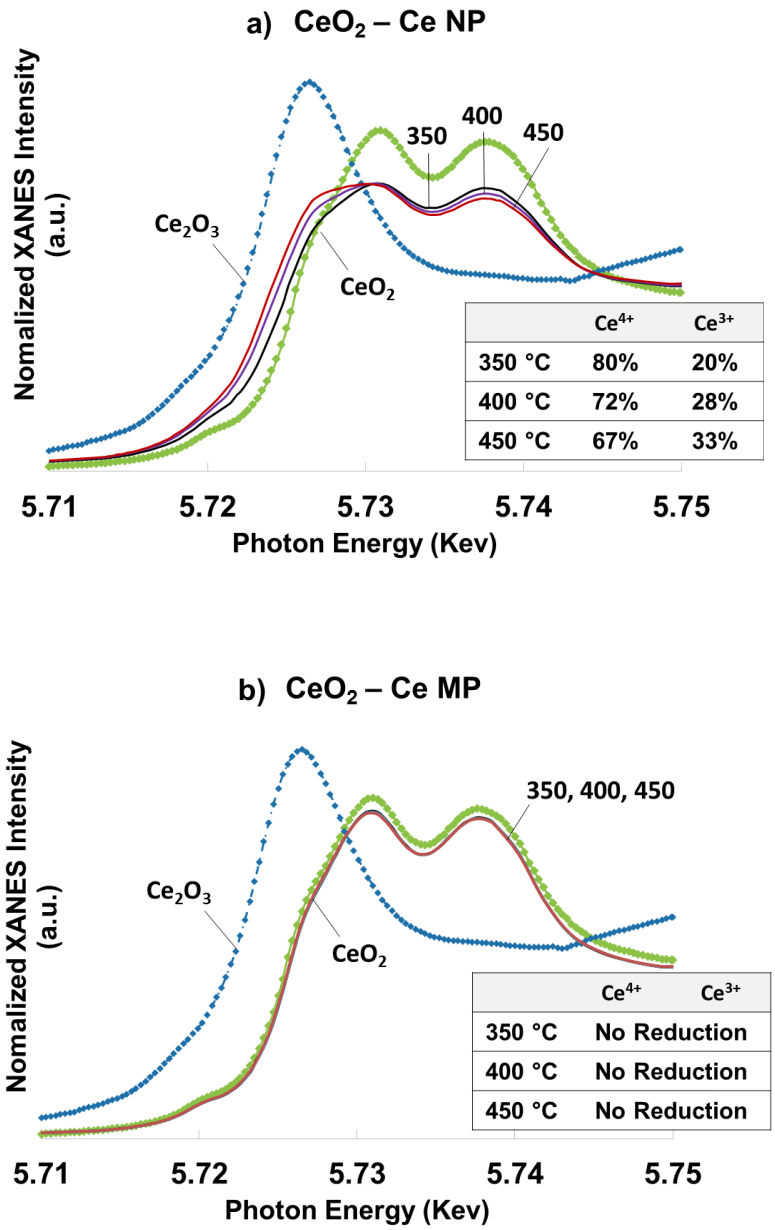

Figure 51. Ce L3 edge *in situ* XANES spectra during ESR at 350, 400, and 450 ℃: (a) CeO_2-NP; (b) CeO_2-MP.

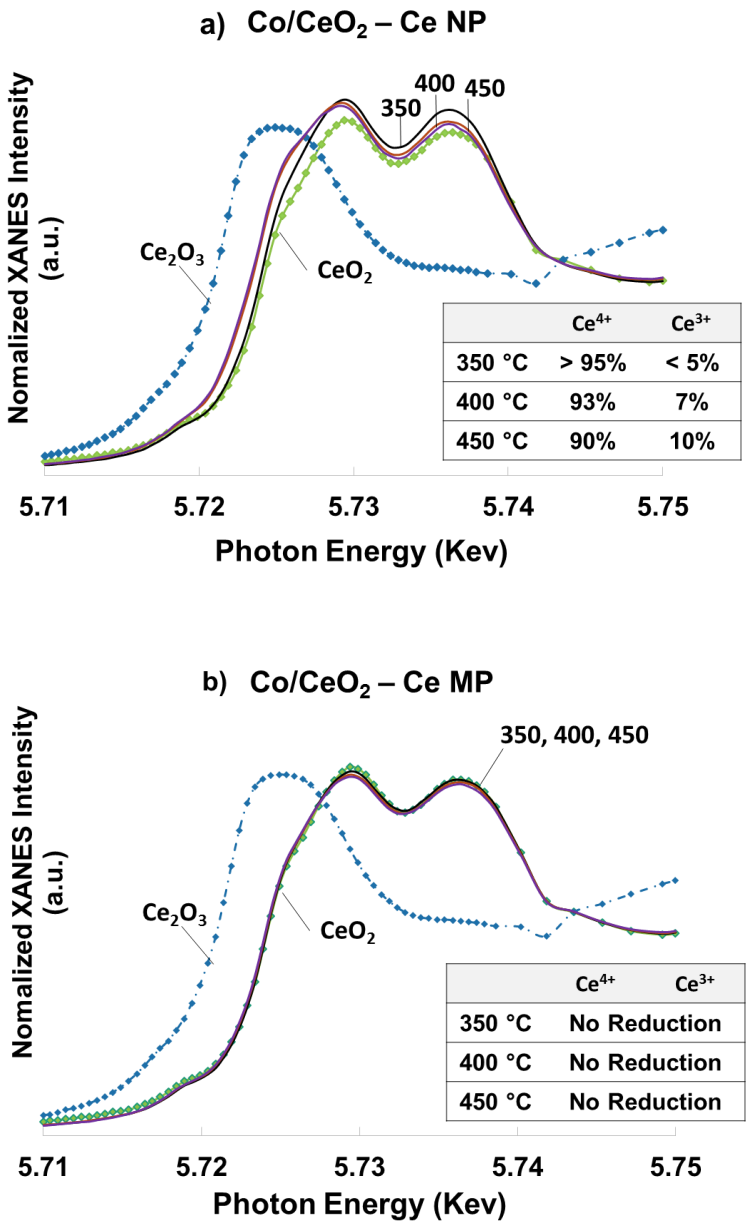

Figure 52. Ce L3 edge *in situ* XANES spectra during ESR at 350, 400, and 450 ℃: (a) Co/CeO_2-NP; (b) Co/CeO_2-MP.

There may be several explanations why ceria support becomes less reduced in the presence of Co. Since the starting point for both catalysts is a fully oxidized sample, one would expect Co sites which are in a Co_3O_4 or CoO matrix, to "compete" with Ce^{4+} sites for interaction with ethanol and hydrogen. Our earlier studies using *in situ* XANES experiments showed reduction of cobalt species during ethanol steam reforming, from Co_3O_4 to CoO and consecutively to metallic Co at elevated temperatures.[213, 217-218] However, at a specific temperature, the catalyst could reach a steady-state composition where Co^{2+} and Co^o oxidation states coexist. The coexistence of Co^o and Co^{2+} was also demonstrated by Llorca et al.[237] using the *in situ* DRIFTS technique for ethanol steam reforming. The authors observed η^2-acetaldehyde species that was formed over metallic Co and hydroxyl groups on the CoO phase. Similar observations were reported by Pena O'Shea and co-workers.[219] Their *in situ* XRD results show that only Co_3O_4 phase was observed at 548 K, while both CoO and Co phases were shown at 623 K under ethanol steam reforming. The reason that ceria is less reduced in the presence of Co may be due to the fact that reduction of the cobalt oxide phases (Co_3O_4 and CoO) takes precedence over that of the ceria support.

An alternative explanation is that the activation of water occurs on cobalt nanoparticles, and the resultant OH^- or O^{2-} intermediates dissociated from water spill over to the ceria support. Although general consensus in the literature is that water activation takes place predominantly on the ceria support involving Ce^{3+} ions and oxygen vacancies[181, 186, 238] where the OH^- species formed by the dissociation of H_2O on the ceria surface migrates to the cobalt metal to suppress catalyst coking or to provide oxygen to form products such as CO and CO_2, the water spillover from the cobalt metal to the support maybe also be possible. Saib et al.[239] conducted a molecular modeling study to estimate

the activation energy of water dissociation on the cobalt surface. It was found that the activation of water on a Co(100) and (111) is exothermic when 25% oxygen coverage of the surface was considered. However, as the oxygen coverage value reaches 100%, water dissociation becomes endothermic with 80 kJ/mol activation energy. Another study from Petitto and co-workers[240] suggests that dissociation of water is possible even under UHV conditions on CoO(100), Co_3O_4(110), and Co_3O_4(111) single crystal substrates if adequate activation energy is provided. According to these studies, it is believed that at temperatures of 350-450 ℃ dissociation of water molecule on a cobalt surface is favorable. This possibility would also explain the higher concentration of Ce^{4+} observed on the ceria surface in the presence of Co.

9.3.4 Ambient Pressure X-ray Photoelectron Spectroscopy (AP-XPS)

Since the XANES technique examines both the bulk and the surface, it is challenging to differentiate the small contribution of surface to the overall signal from that of the bulk. Hence, AP-XPS was implemented to track the surface reduction characteristics of ceria in a reactive environment. For quantification of the data, all the collected Ce 3d spectra were curve fitted to determine the concentration of the Ce^{3+} on the ceria surface. The peak position, fwhm and peak area were constrained to perform an accurate comparison among the spectra collected at different temperatures. The fitting parameters that were employed were in good agreement with the literature values.[241-245] All the peak areas were integrated and used in the following equation to calculate the concentration of Ce^{3+}.

$$\frac{\sum Peak\ area\ of\ Ce^{3+}}{\sum Peak\ area\ of\ (Ce^{3+}+Ce^{4+})} = concentration\ of\ Ce^{3+}$$

Figures 53, 54, 55 and 56 show the AP-XPS spectra collected over CeO_2-NP and -MP, and Co/CeO_2-NP and -MP samples at identical reaction conditions to those used *in situ* XANES. The scans were made every 7 min, but only the last spectrum is shown after 1 h of reaction time at each temperatures.

The Ce^{3+} fraction under helium at RT was obtained as 9% for CeO_2-NP and -MP and 12 and 13% for Co/CeO_2-NP and –MP, respectively. This is in contrast to the fully oxidized ceria observed in XANES for all samples. Additionally, as expected, the surface reduction of ceria was more pronounced compared to bulk reduction for all samples.

Over the CeO_2-NP (Figure 53), the ceria surface reduces readily under ethanol steam reforming conditions, even at 350℃. It was also observed the oxidation state of Ce reached a plateau at 350℃ as opposed to the XANES data where gradual reduction of Ce was seen with increasing temperature. It is conceivable that above 350℃ the surface chemistry is dictated by the competing rates of reduction of Ce^{4+} in the bulk of CeO_2 by the reducing environment and its oxidation by diffusion from the ceria lattice.

Contrary to the information suggested by XANES data that no reduction was seen, a significant reduction of CeO_2-MP was revealed on the catalyst surface using AP-XPS. This difference clearly illustrates the sensitivity of the technique for surface analysis. In Figure 54 all the concentrations of Ce^{3+} ions for CeO_2-MP under ethanol steam reforming are shown. It is also noted that the surface of the nano-ceria is more reduced than the sample with the larger particle size, especially at lower temperatures. In the literature, studies have

shown increasing oxygen vacancies and Ce^{3+} ions in the ceria lattice with decreasing particle size.[205-206] Deshpande and co-workers[206] have presented a correlation between the lattice parameters and particle size of 3-30 nm ceria particles. Based on the XPS results, it was concluded that the increase in oxygen vacancies and Ce^{3+} concentration on the surface was due to the higher lattice strain in smaller particles. As observed here, under ethanol steam reforming, the faster bulk to surface oxygen diffusion in CeO_2-NP particles results in higher extent of reduction of both bulk and surface. On the other hand, as the particle size increases the concentration of Ce^{4+} increases in the bulk phase along with lower oxygen diffusion from the bulk to the surface.

For the Co/CeO_2 catalysts (Figures 55 and 56), a higher oxidation state of ceria was observed in the presence of cobalt, similar to what was previously seen from the XANES results. Because of the same reason, the extent of surface reduction over the $Co\text{-}CeO_2$-NP was higher than that of $Co\text{-}CeO_2$-MP. In all cases, the surface is more reduced than the bulk of the catalyst.

Table 10 summarizes the X values in CeO_x for all samples tested. As indicated before, as temperature increases, the X value decreases. Nano-ceria based samples are always more reduced than their micro-ceria counterparts. When cobalt is present on the ceria support, ceria is more oxidized compared to its bare support for both MP and NP particles under ethanol steam reforming condition. In all cases, surface is more reduced than the bulk.

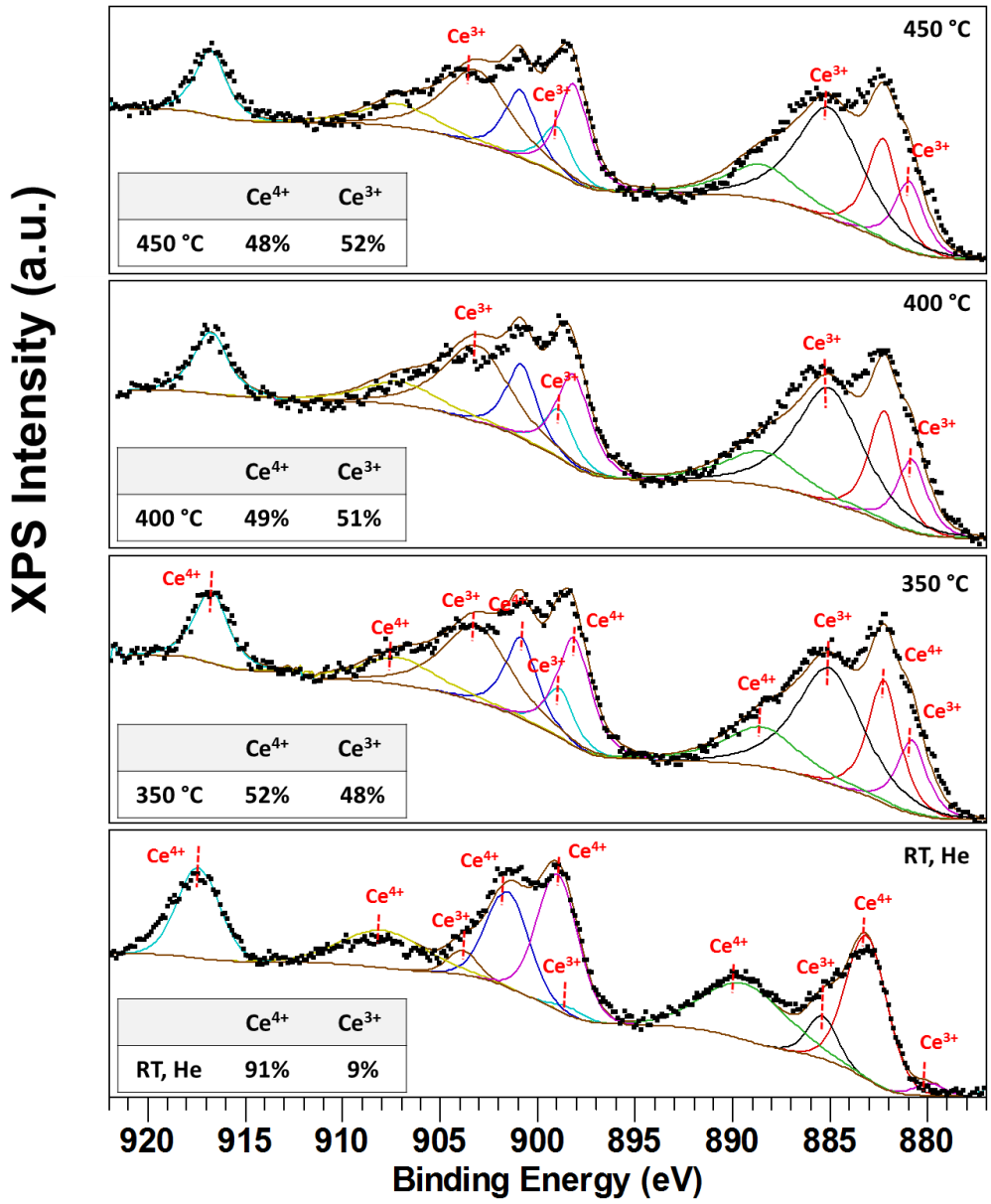

Figure 53. Ce 3d *in situ* ambient pressure AP-XPS spectra for CeO_2-NP during ESR at 350, 400, and 450 ℃.

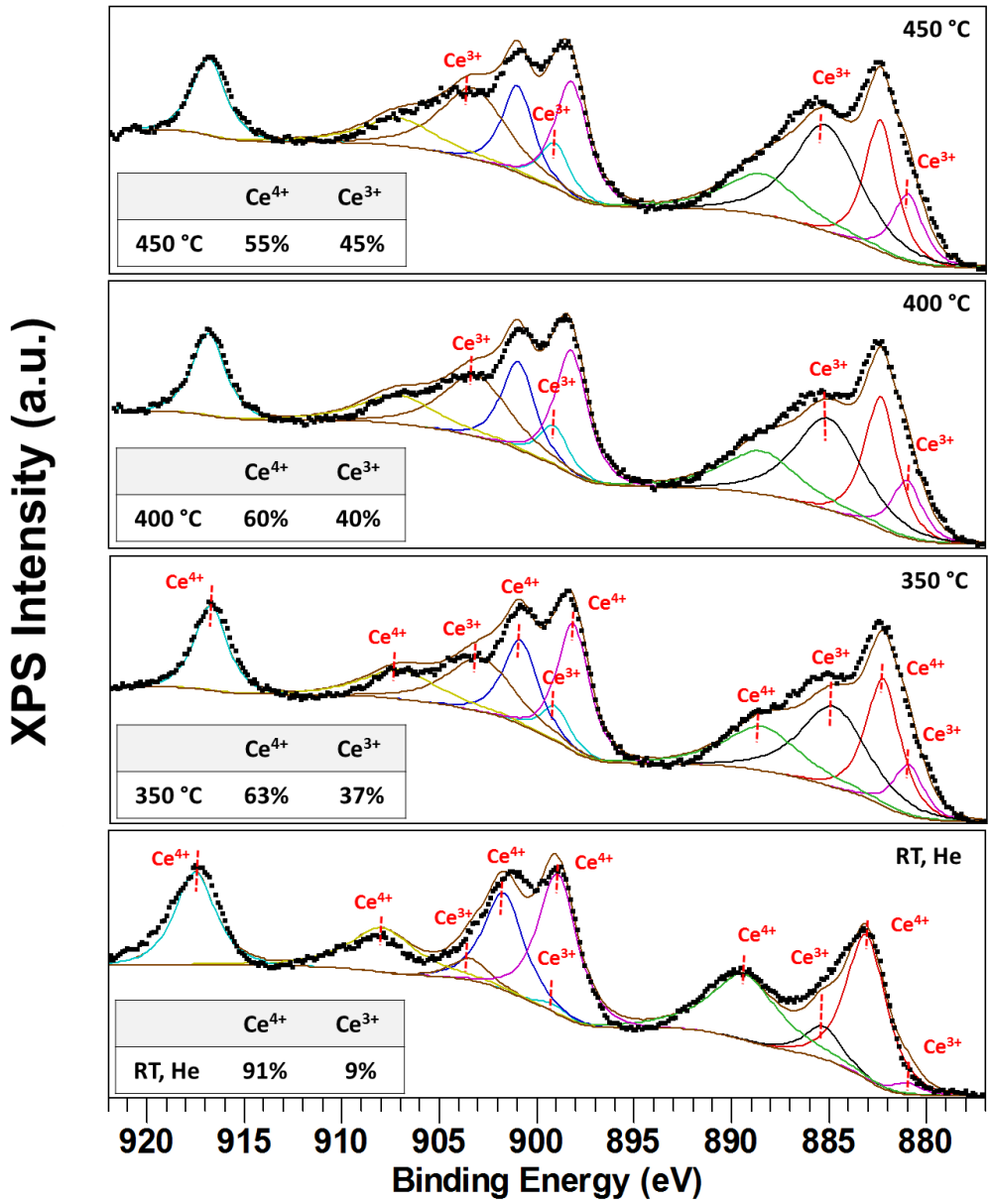

Figure 54. Ce 3d *in situ* ambient pressure AP-XPS spectra for CeO_2-MP during ESR at 350, 400, and 450 ℃.

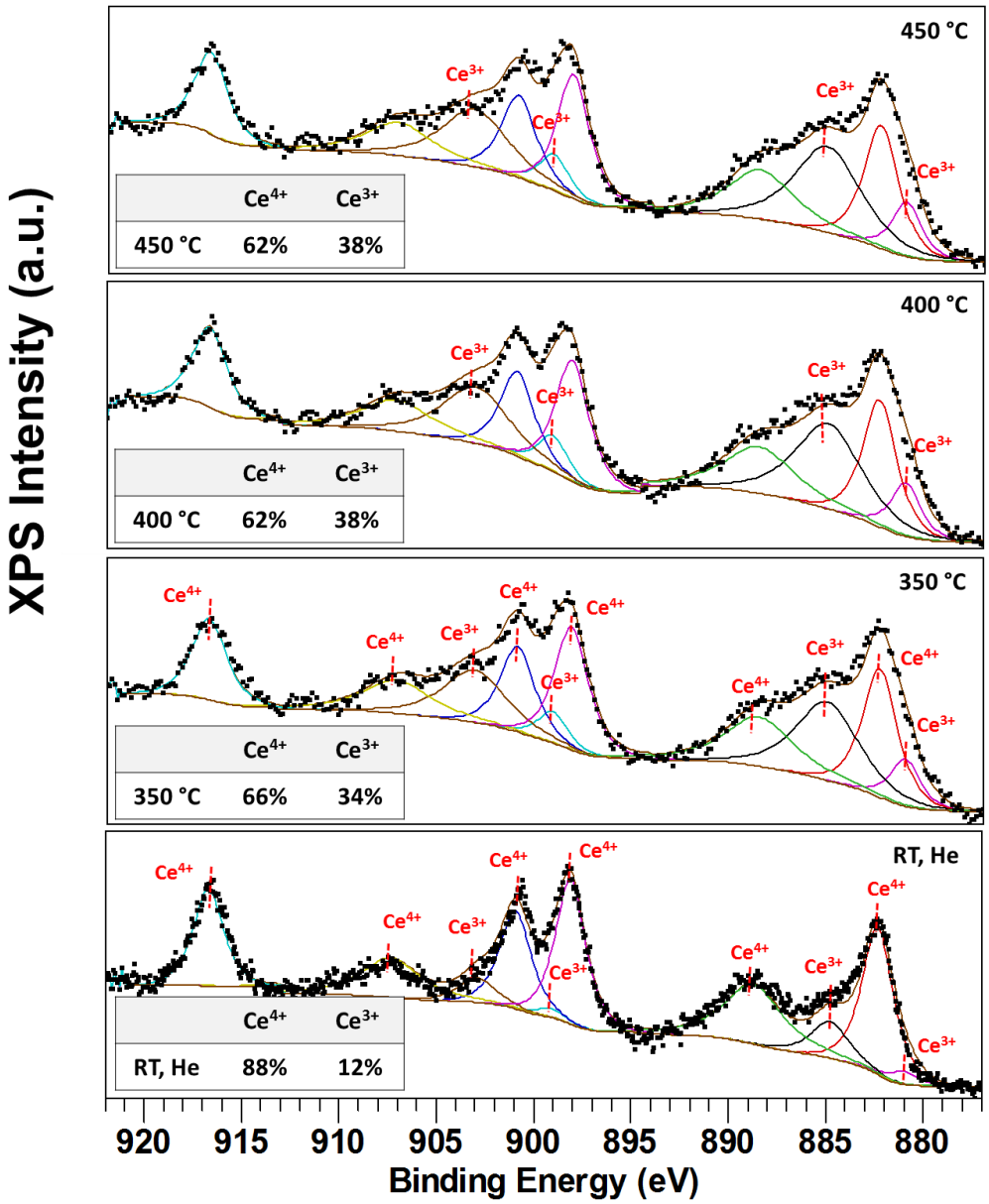

Figure 55. Ce 3d *in situ* ambient pressure AP-XPS spectra for Co/CeO_2-NP during ESR at 350, 400, and 450 ℃.

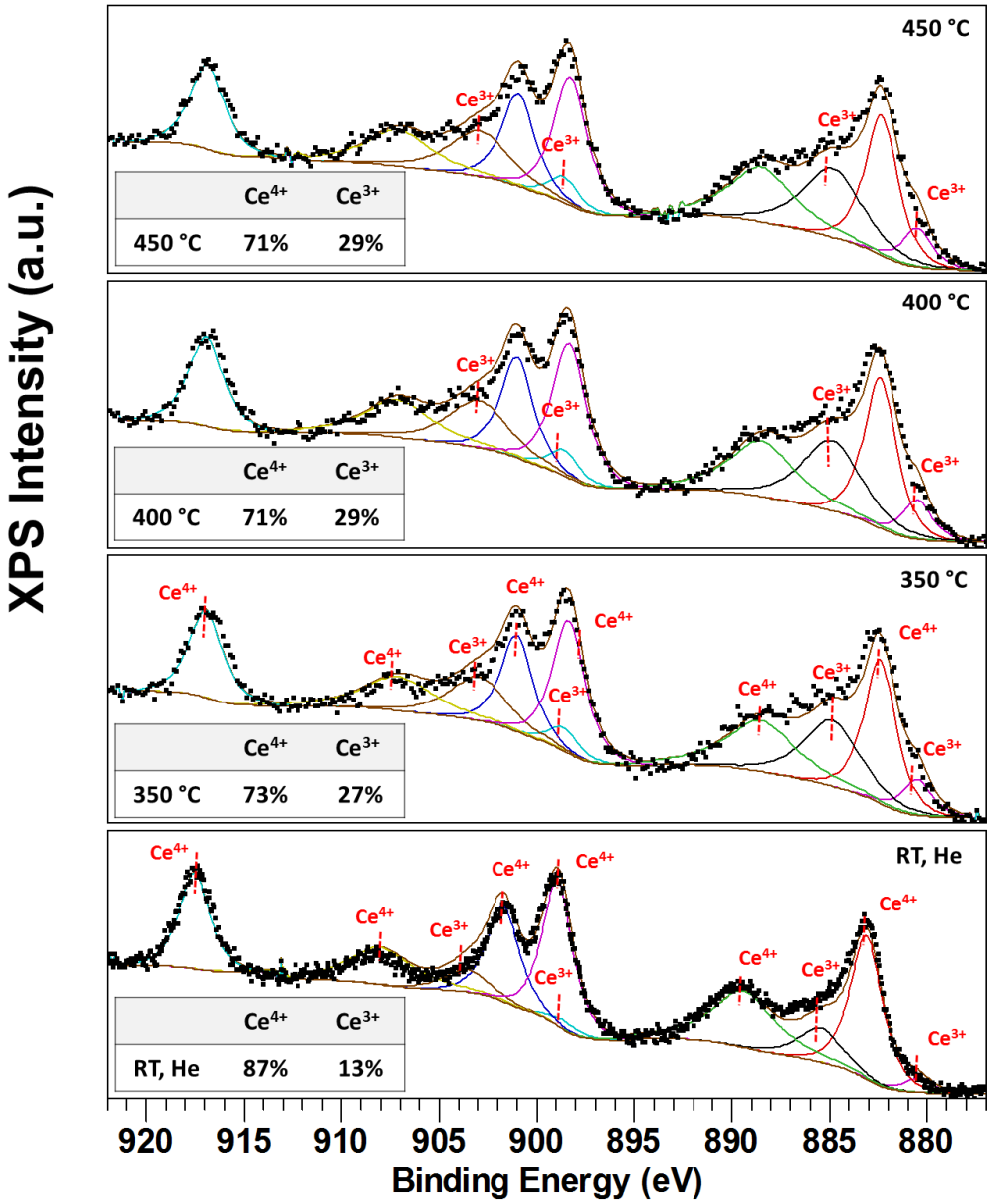

Figure 56. Ce 3d *in situ* ambient pressure AP-XPS spectra for Co/CeO_2-MP during ESR at 350, 400, and 450 ℃.

Table 10. Comparison of X Values in CeO_x for XANES and AP-XPS

XANES				
	CeO_2 - NP	**Co/CeO_2 - NP**	**CeO_2 - MP**	**Co/CeO_2 - MP**
RT	2	2	2	2
350 °C	1.90	1.98	2	2
400 °C	1.86	1.97	2	2
450 °C	1.84	1.95	2	2

AP-XPS				
	CeO_2 - NP	**Co/CeO_2 - NP**	**CeO_2 - MP**	**Co/CeO_2 - MP**
RT	1.96	1.94	1.96	1.94
350 °C	1.76	1.83	1.82	1.87
400 °C	1.75	1.81	1.80	1.86
450 °C	1.74	1.81	1.78	1.86

Along with the ceria, Co 2p AP-XPS spectra for Co/CeO_2-NP and -MP samples were collected in order to determine the extent of reduction of cobalt particles. As is shown in Figure 57, the two main spin-orbit peaks were observed which were assigned to Co $2p_{1/2}$ and $2p_{3/2}$.[246] The Co $2p_{3/2}$ peak was deconvoluted into five different components of Co^o, Co^{3+} (octahedral), Co^{2+} (tetrahedral), Co^{2+} (octahedral), and a satellite peak associated with Co^{2+} (octahedral).[247-250] Based on the literature findings, the Co^{3+} (octahedral) and Co^{2+} (tetrahedral) peaks were associated with the Co_3O_4 phase.[251-252] The Co^{2+} (octahedral) and Co^{2+} (satellite) peaks were linked to CoO. With respect to both Co/CeO_2-NP and -MP samples, cobalt was completely oxidized at room temperature under helium environment as there were no contribution of the Co^{2+} (satellite) peak. However, at higher temperatures, a similar trend was observed for both samples under ethanol steam reforming conditions. The cobalt species were found to be a mixture of CoO and metallic Co. This can be attributed to the relatively lower bond strength of Co-O of Co_3O_4 compared to other metal -oxygen bonds, which allows the surface of Co_3O_4 nanoparticles to be reduced readily even at lower temperatures; the resulting metallic Co foil could cover the whole surface of Co_3O_4 and/or CoO and thus prevent further reduction of Co oxides. A complete reduction of Co_3O_4 nanoparticles requires a higher temperature so that oxygen inside could overcome the diffusion barrier and migrate to the surface. As a consequence, the lower reducibility of ceria in Co/CeO_2-NP compared to CeO_2-NP could result from the formation of metal/oxide core-shell structure of cobalt oxide. Although XPS using Al Kα is a surface-sensitive technique, its analytical depth is not only superficial atoms with certain depth subsurface under the topmost layer. Photoelectron spectra show that Co exists in Co^{3+} and Co^{2+} states at room temperature, corresponding to the Co_3O_4 phase. After exposing to

reactive environment, it was reduced to Co^{2+} and metallic Co. As catalysis occurs on surface of catalysts, it is reasonable to deduce that catalyst surface, i.e., supported Co_3O_4 nanoparticle, is more reduced at the surface than those deeper layers under the surface, which corresponds to a metallic Co foil covering the CoO_x core. The extent of reduction of cobalt was higher over the Co/CeO_2-MP compared to Co/CeO_2-NP (Table 11).

The atomic ratio of Co/Ce was calculated to understand the dispersion of cobalt on the catalyst surface. The resulting values are shown in Table 12. It was observed that the Co/Ce ratio was decreased with increasing temperature from RT to 450 ℃ for both Co/CeO_2-NP and -MP catalysts. This is likely due to the migration and agglomeration of cobalt particles on the catalyst surface forming larger particles.

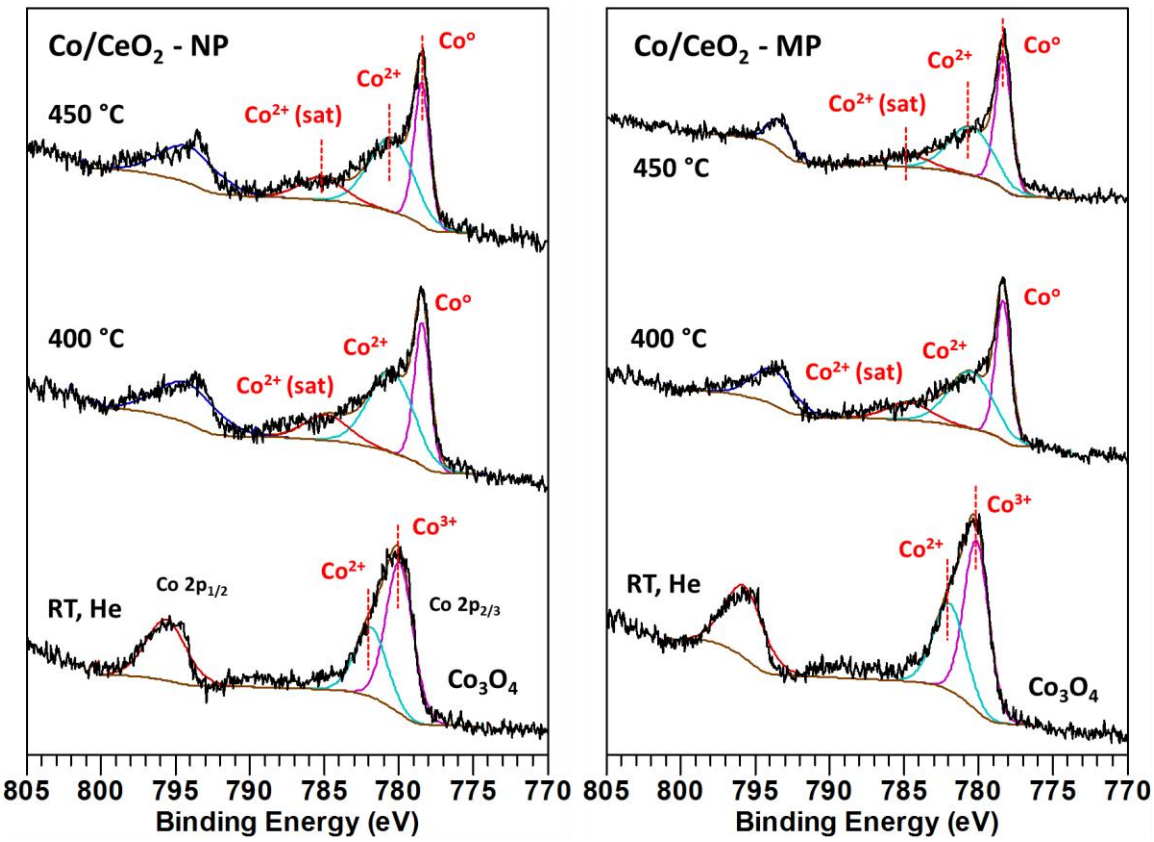

Figure 57. Co 2p *in situ* ambient pressure AP-XPS spectra for Co/CeO_2-NP and -MP during ESR at 400 and 450 ℃.

Table 11. % of Cobalt Species Over Co/CeO_2-NP and -MP during ESR at 400 and 450 ℃

AP-XPS	Co/CeO_2 - NP			Co/CeO_2 - MP		
	% Co_3O_4	% CoO	% Co	% Co_3O_4	% CoO	% Co
RT, He	100	0	0	100	0	0
400 °C	0	68	32	0	61	39
450 °C	0	66	34	0	56	44

Table 12. Co/Ce Atomic Ratios for Co/CeO_2-NP and -MP during ESR at 400 and 450 ℃

AP-XPS	atomic ratios (Co/Ce)	
	Co/CeO_2 - NP	Co/CeO_2 - MP
RT, He	0.37	0.31
400 °C	0.20	0.18
450 °C	0.17	0.13

In the literature, several studies have been conducted using AP-XPS technique during ethanol steam reforming.[253-255] Divins and co-workers performed ethanol steam reforming over $Rh_{0.5}Pd_{0.5}$ nanoparticles (NPs) and $Rh_{0.5}Pd_{0.5}$ NPs supported on CeO_2 powder using AP-XPS.[253] The authors incorporated three photon energies of 670, 875, and 1150 eV in order to understand the catalyst composition and metal oxidation states in the outer shell, intermediate shell, and inner shell, respectively. The results indicated that the CeO_2 support was important in determining the oxidation states of metals by providing oxygen sources. Moreover, it was found that the CeO_2 support prevented the rearrangement of the RhPd alloy NPs under reaction conditions, referred as the quenching effect. The difference in metal oxidation state between in the outer shell and inner shell under ethanol steam reforming conditions was significant.

Another AP-XPS study was carried out by Liu et al. using Ni-CeO_2 (111) model catalysts for ethanol steam reforming.[254] The major finding of this study was the coexistence of Ni^0 and ceria hydroxide ($Ce^{3+}(OH)_x$) species on the catalyst surface. The Ni^0 sites were found to have C-C and C-H bond cleavage as an active site for ethanol steam reforming. It was concluded that the combination of Ni^0 particles and $Ce^{3+}(OH)_x$ surface sites play an important role in transportation of hydroxyl and oxygen which reduces the coke formation. The authors also quantified and compared the Ce^{3+} concentrations in CeO_2 (111) and Ni-CeO_2 (111) catalysts under ethanol steam reforming conditions. The results obtained at lower temperatures (below 500 K) were in good agreement with the present study where extent of reduction for ceria was lower in the presence of Ni particles than it was for the bare ceria support. However, as the temperature increased above 500 K, an opposite trend was observed having significantly more reduced ceria in Ni-CeO_2 (111)

compared to CeO_2 (111). This result suggests that whether Ni facilitates the reduction of the ceria from Ce^{4+} to Ce^{3+} is dependent on the temperature and is closely related to the oxidation state of Ni under ethanol steam reforming conditions.

Ó vári et al. studied the interaction of ethanol with CeO_2 (111) and Co/CeO_2 (111) model catalysts using NAP-XPS[255]. A higher extent of reduction of ceria was demonstrated with increasing reaction temperature and ethanol pressure. For Co/CeO_2 (111) catalyst, a decrease in Co^{2+} was observed as temperature was increased, leading to metallic Co. The authors also presented the [Ce(III)/Ce(III)+Ce(IV)] values obtained under 0.1 mbar of ethanol environment for both CeO_2 (111) and Co/CeO_2 (111) catalysts. Interestingly, at temperatures of 500 K and below, ceria was shown to be in a more oxidized state in the presence of cobalt compared to the bare ceria support. However, at 600 K, this trend was reversed, with the presence of Co leading to a higher extent of reduction for ceria.

The results reported in these studies agree with our findings in the present study in showing that the presence of metal may impede or facilitate the reduction of the ceria support and this effect is dictated by the temperature. It is conceivable that at lower temperatures the reduction of the metal oxide (Co or Ni oxide) takes precedence over the reduction of ceria, leaving the support in a more oxidized state. On the other hand, at higher temperatures, the catalyst (Ni or Co) is likely to be in a more reduced state, thus facilitating the reduction of ceria through hydrogen spillover. Although these studies are not contradicting our findings, a direct comparison is not possible due to different experimental parameters used. For example, in the study by Liu et al.,[254] the active metal is Ni, which has a different reduction behavior compare to Co. In the study performed by Ó vári et al.,[255] water was absent in the reaction; thus the results are not directly comparable.

Not only increasing the reaction temperature for ethanol but also starting with a prereduced Co/CeO_2 sample would increase the hydrogen yield and change the reduction behavior of ceria in the presence of a reduced cobalt phase. Studies where AP- XPS and *in situ* XANES techniques are used over the prereduced CeO_2 and Co/CeO_2 under ethanol steam reforming conditions are in progress.

9.3.5 Correlation of Surface Chemistry and Structure with Catalytic Performance

In addition to the significant differences in surface and bulk reducibility, ceria particle size affects the catalytic behavior in ethanol steam reforming (Table 13 and 14). When the catalysts are compared on an equal gas hour space velocity basis, CeO_2-NP and Co/CeO_2-NP gave higher ethanol conversions and H_2 yields than CeO_2-MP and Co/CeO_2-MP, respectively. For CeO_2-MP sample, extremely low ethanol conversions were observed in the entire temperature range used. Similarly, CeO_2-NP was not very active for ethanol steam reforming at 350 and 400 ℃. When the temperature was increased to 450 ℃, a significantly higher ethanol conversion was obtained compared to CeO_2-MP, although hydrogen yield was relatively low due to formation of byproducts, especially ethylene.

The formation of ethylene through ethanol dehydration is favored over the Ce^{4+} sites, which are more acidic. On the other hand, hydrogen production from ethanol dehydrogenation mainly takes place on the reduced surface having more Ce^{3+} sites, which are more basic.[231, 256-257] The larger particle size was also seen to lead to coking during ethylene steam reforming.[214] This observation is consistent with the assertion that the

nanoparticle size leads to higher oxygen accessibility, which, in turn, may help with the gasification/oxidation of coke deposits.

In the presence of cobalt particles, the Co/CeO_2-NP and -MP samples showed superior catalytic activity compared to bare ceria support for ethanol steam reforming. This is due to formation of metallic Co coated on CoOx under reducing conditions, which are known as active sites for ethanol steam reforming. Obviously, metallic Co significantly promotes the production of H_2. Also, the difference in hydrogen and CO_2 yields between Co/CeO_2-NP and Co/CeO_2-MP is more prominent compared to bare CeO_2-NP and bare CeO_2-MP, which suggests that the size effect of CeO_2 is not the major diving force for the large difference between Co/CeO_2-NP and Co/CeO_2-MP. In fact, the much larger difference in catalytic activity in ethanol reforming between Co/CeO_2-NP and Co/CeO_2-MP than that between bare CeO_2-NP and bare CeO_2-MP is consistent with the previous conclusions that the metallic Co atoms are the sites for a rate-determining step and the reaction is primarily performed at the interface of metallic Co nanoparticles and CeO_2.

Table 13. Catalytic Activity Data of Preoxidized CeO_2-NP and -MP for ESR at 350, 400, and 450 ℃ (C_{EtOH} = 1.4% and H_2O:EtOH = 10:1 (Molar Ratio), GHSV = 71 600 h^{-1})

Unit: %	350 ˚C		400 ˚C		450 ˚C	
	CeO_2-MP	CeO_2-NP	CeO_2-MP	CeO_2-NP	CeO_2-MP	CeO_2-NP
Ethanol conversion	0.0	1.2	1.1	5.6	3.6	33.2
Hydrogen Yield	0.0	0.4	0.4	2.2	1.5	10.7
Product Yield						
CO_2	0.0	0.3	0.3	3.3	2.3	13.6
CO	0.0	0.1	0.0	0.1	0.0	0.4
CH_4	0.0	0.1	0.0	0.2	0.0	1.8
C_2H_4	0.0	0.1	0.1	1.4	0.3	10.9
C_2H_6	0.0	0.0	0.0	0.1	0.2	0.7
CH_3COCH_3	0.0	0.0	0.0	0.0	0.0	5.2
CH_3CHO	0.0	0.6	0.7	0.5	0.8	0.6

Table 14. Catalytic Activity Data of Preoxidized Co/CeO_2-NP and -MP for ESR at 350, 400, and 450 ℃ (C_{EtOH} = 1.4% and H_2O:EtOH = 10:1 (Molar Ratio), GHSV = 71 600 h^{-1})

Unit: %	350 ˚C		400 ˚C		450 ˚C	
	Co-MP	Co-NP	Co-MP	Co-NP	Co-MP	Co-NP
Ethanol conversion	18.4	10.8	29.6	56.0	79.4	99.7
Hydrogen Yield	10	6.4	16.2	34.1	40.2	63.9
Product Yield						
CO_2	1.3	7.6	5.4	34.2	25.9	67.5
CO	2.1	0.2	4.7	4.9	22.5	10.6
CH_4	0.6	0.2	1.1	1.2	6.0	4.1
C_2H_4	0.0	0.2	0.1	0.9	0.2	3.9
C_2H_6	0.0	0.0	0.0	0.0	0.1	0.1
CH_3COCH_3	0.0	1.5	0.0	12.4	9	12.6
CH_3CHO	14.4	1.1	18.3	2.4	24.7	0.9

9.4 Conclusion of Chapter 9

In this study, the reduction characteristics of ceria with two distinctly different particle sizes were explored in parallel for the two pairs of catalysts, including the pair of bare CeO_2-NP and CeO_2-MP and the pair of Co/CeO_2-NP and Co/CeO_2-MP. *In situ* XANES and AP-XPS techniques were employed to examine both the bulk and surface properties of the samples, respectively. For all samples, higher extents of ceria reduction were observed as temperature was increased under ethanol steam reforming conditions. Also, surface reduction was more prominent than bulk reduction with faster kinetics. Regarding the particle size effect, the NP based samples showed higher surface and bulk reduction of the ceria compared to its MP based counterparts. This indicates that the particle size is significant in determining of the reducibility of the material.

Lastly, the extent of reduction of ceria in Co/CeO_2 catalyst was smaller than that of the CeO_2 bare support. It is conceivable that the reducing agents (such as ethanol and produced hydrogen), may primarily be consumed first to reduce the cobalt species, which are in a fully oxidized form at the start of the experiments, resulting in higher oxidation state of the ceria support compared to bare ceria. Another explanation can be that additional dissociation of H_2O molecules on the cobalt surface may spillover to the ceria support, thereby resulting in a more oxidized ceria surface.

** Information in this chapter is reproduced/adapted from "Sohn, H.; Soykal, I. I.; Zhang, S.; Shan, J.; Tao, F.; Miller, J. T.; Ozkan, U. S., Effect of Cobalt on Reduction Characteristics of Ceria under Ethanol Steam Reforming Conditions: AP-XPS and XANES Studies. The Journal of Physical Chemistry C 2016. June-Published"*

CHAPTER 10

EFFECT OF MICROGRAVITY ON SYNTHESIS OF NANO-CERIA

10.1 Summary of Chapter 10

Cerium oxide (CeO_2) was prepared using a controlled-precipitation method under microgravity at the International Space Station (ISS). For comparison, ceria was also synthesized under normal-gravity conditions (referred as control). The Brunauer-Emmett-Teller (BET) surface area, pore volume and pore size analysis results indicated that the ceria particles grown in space had lower surface area and pore volume compared to the control samples. Furthermore, the space samples had a broader pore size distribution ranging from 30-600 Å , whereas the control samples consisted of pore sizes from 30-50 Å range. Structural information of the ceria particles were obtained using TEM and XRD. Based on the TEM images, it was confirmed that the space samples were predominantly nano-rods, on the other hand, only nano-polyhedra particles were seen in the control ceria samples. The average particle size was larger for ceria samples synthesized in space. XRD results showed higher crystallinity as well as larger mean crystal size for the space samples. The effect of sodium hydroxide concentration on synthesis of ceria was also examined using 1 M and 3 M solutions. It was found that the control samples, prepared in 1 M and 3

M sodium hydroxide solutions, did not show a significant difference between the two. However, when the ceria samples were prepared in a more basic medium (3 M) under microgravity, a decrease in the particle size of the nano-rods and appearances of nano-polyhedra and spheres were observed.

10.2 Experimental Section

10.2.1 Catalyst Preparation

A CubeLab container (Nanoracks, Houston, TX, USA), shown in Figure 58, with the dimensions of 10 cm × 10 cm × 20 cm was utilized to protect the experimental containers during take-off and landing on route to and back from the International Space Station (ISS). Therefore, the catalyst preparation apparatus had to fit into a single CubeLab container.

Ceria nanoparticles were prepared by precipitation method, where 2.1 g $Ce(NO_3)_3 \cdot 6H_2O$ (Sigma-Aldrich, 99.999%, St. Louis, MO, USA) was dissolved in 13.5 mL water. In separate containers, caustic solutions with 66.5 mL of 1 M and 3 M NaOH were prepared. The solutions were loaded into concentric cylindrical rods. The innermost tube contained the cerium nitrate solution. Surrounding the inner glass tube was the sodium hydroxide solution. The astronauts were instructed to bend the assembly and thereby break the innermost glass tubing, allowing the solutions to mix. The assembly was then shaken to allow for a more thorough mixing. It should be noted that the liquid stays spread out through the length of the tube in microgravity, thereby showing different precipitation

behavior. The concentric tubes and the protective cover layers around the catalyst preparation assembly are shown in Figure 59.

Twenty-four rods containing different molarities of NaOH solutions were loaded into the Cubelab. Another batch of 24 rods were prepared and kept in our laboratories as control. The CubeLab sample holder was then tested for vibration, vacuum, and off-gassing,[258] verification as per the NASA space-flight qualification requirements and flight safety regulations, and was sent to the International Space Station (ISS). The samples were not exposed to air during this process. It should be noted that ISS was kept at 25 ℃ and 1 atm.[258] On approximately the same day, the control samples were treated under similar reaction conditions and the solutions were mixed in our laboratories. No further treatment was done until the samples prepared at ISS were delivered to our laboratories.

Following the delivery of the ISS samples, the samples were tested for ruptures. No serious containment breaches were found. Following the inspection, all samples including the control were filtered and washed with deionized and distilled water until a pH of 7 is reached. The samples were then dried in an oven at 90 ℃ overnight and were ready for characterization. Throughout the text, the ceria samples prepared in normal-gravity and microgravity are referred to as control and space samples, respectively.

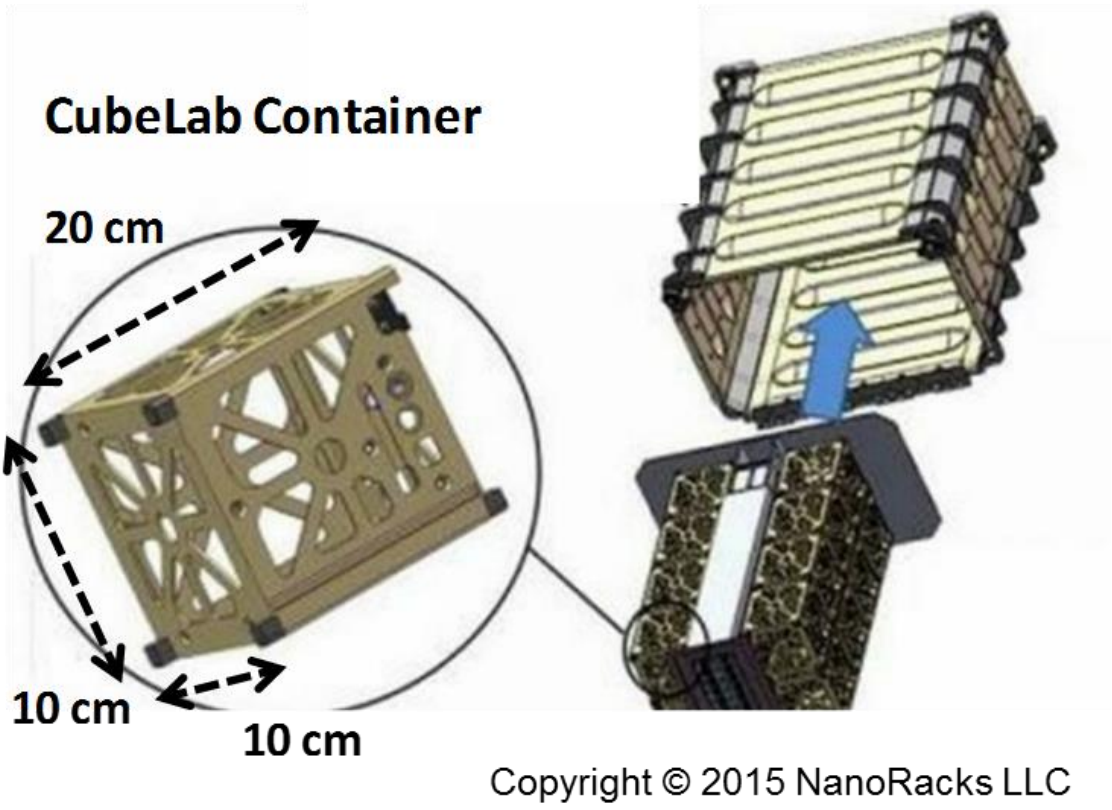

Figure 58. Schematic and dimensions of CubeLab and NanoRack Modules

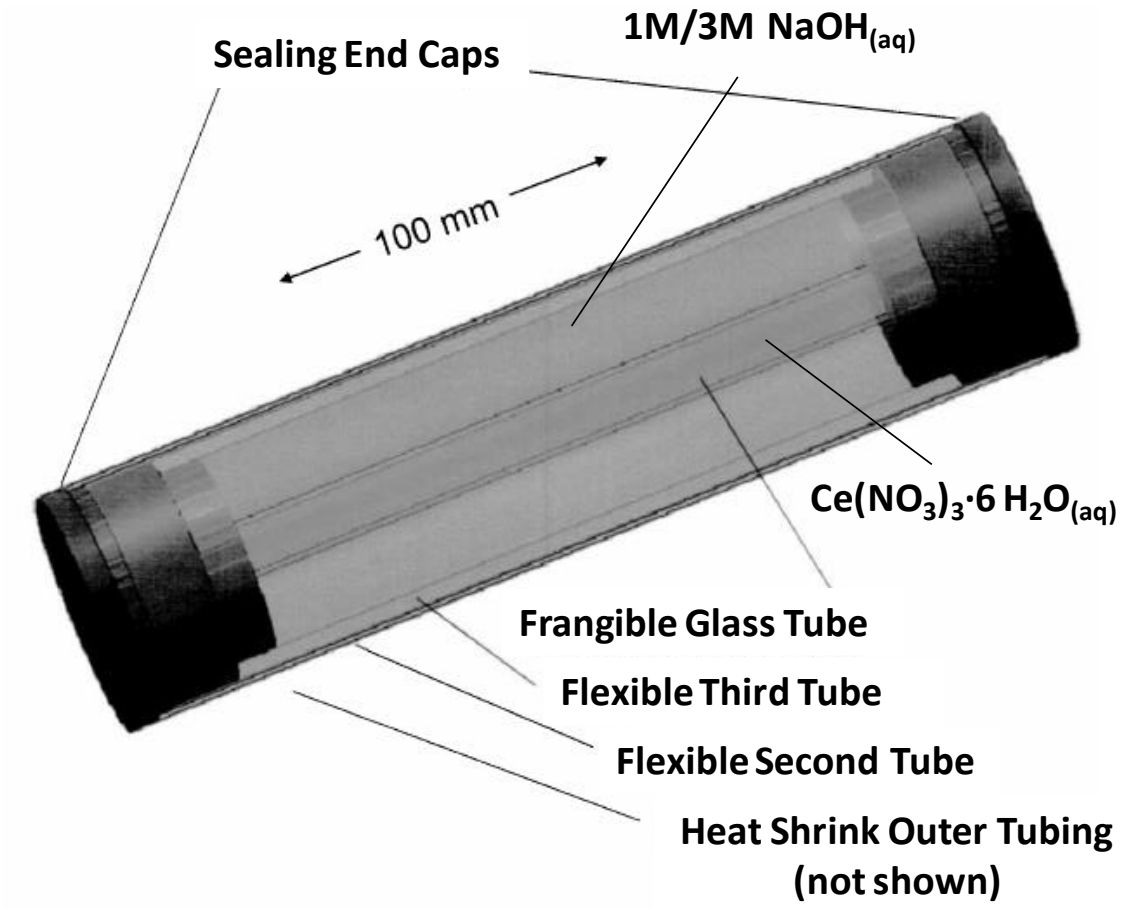

Figure 59. Schematic for the catalyst preparation assembly

10.2.2 Surface Analysis

BET surface area and pore volume measurements were carried out on a Micromeritics ASAP 2020 (Norcross, GA, USA) accelerated surface area and porosimetry instrument. The samples were degassed at 130 ℃ for 12 h prior to analysis under vacuum (<2 μm·Hg). Adsorption/desorption isotherms were collected at liquid nitrogen temperature where the desorption branch of the isotherm was used to calculate Barrett-Joyner-Halenda (BJH) pore size distributions.

10.2.3 Transmission Electron Microscopy (TEM)

A Phillips Tecnai F20 TEM (Hillsboro, OR, USA) equipped with a Field Emission Gun (FEG) and operated at 200 kV was used for imaging the particles. All exposures were collected in the bright field. The samples were suspended in ethanol and were sonicated for ~10 min to improve dispersion. Following sonication, the resulting mixture was immediately deposited on a 200-mesh copper grid coated with lacey carbon in order to prevent agglomeration of the particles. Image J open-source processing and analysis software was used to estimate the particle sizes.

10.2.4 X-ray Diffraction (XRD)

XRD powder patterns were collected using a Rigaku diffractometer (Tokyo, Japan) with Cu Kα radiation with $\lambda = 1.5418$ Å operated at 40 kV and 25 mA. The patterns were collected in the 2θ range of 20°-75°. International Center for Diffraction Data (ICDD) database was used for identification of the crystalline phases. The crystal size of the

samples were calculated by Scherrer equation $L = K\lambda/\beta\cos\theta$ where K is the Scherrer constant, λ is the wavelength of the X-ray, β is the full width half maximum (FWHM), and θ is the diffraction angle.

10.3 Results and Discussion

10.3.1 BET Surface Area, Pore Size and Pore Volume

BET surface analysis was conducted on the ceria samples to determine the effect of microgravity on their surface characteristics. Table 15 compares the surface areas and pore volumes of the various samples tested. The control samples exhibited higher surface area and higher pore volume than the space samples. Regarding the effect of pH on the pore volume and surface area, higher surface areas and pore volumes were observed with increase in basicity of the medium for space samples whereas the opposite trend was exhibited by the control samples.

There was a considerable difference between control and space ceria in terms of the pore size distribution, as observed in Figure 60. The control ceria had a narrower pore size distribution with most of the pores being the 50-100 Å range and no pores larger than ~200 Å. On the other hand, for the space samples, a wide range of pore diameters ranging from 30-600 Å were observed. The lower pore volume and surface area can be due to larger particles size of the space samples compared to control samples. This was further confirmed in the TEM section. With respect to the effect of NaOH concentration, broader pore size distribution was obtained in case of 1 M control ceria than 3 M. The highest pore

volume was obtained at a pore diameter of 83 Å and 62 Å for 1 M and 3 M, respectively. For space-grown ceria, there were no significant changes in the pore size distribution.

Table 15. Surface area and pore volume of CeO_2 sample measured using N_2 physisorption.

	BET Surface Area (m^2/g)	**Pore volume (cm^3/g)**
Control 1M	138	0.3
Control 3M	118	0.23
Space 1M	47	0.18
Space 3M	69	0.19

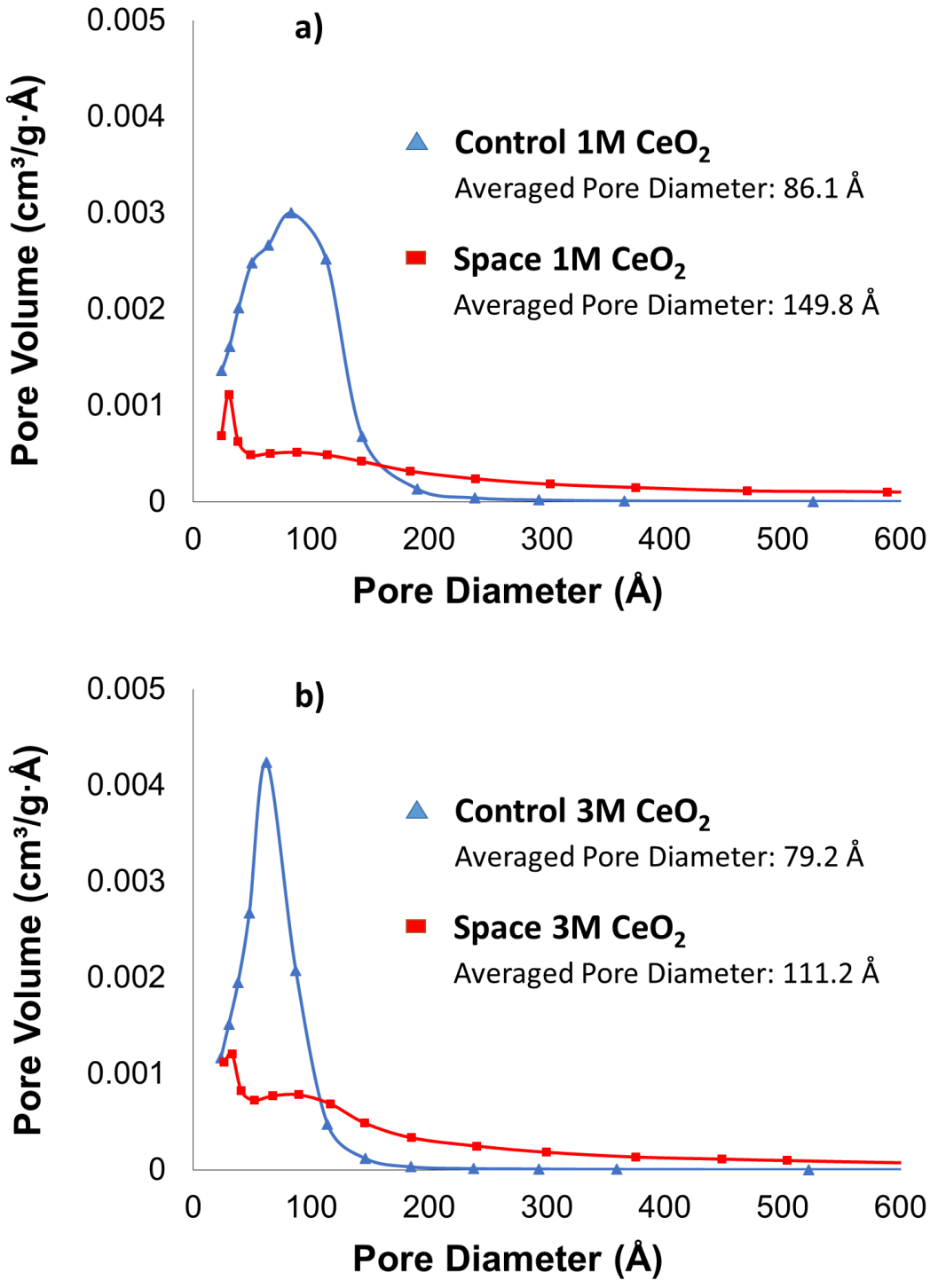

Figure 60. Barrett-Joyner-Halenda (BJH) Pore size distribution of CeO_2 sample measured using N_2 physisorptionprepared (a) with 1M NaOH (b) with 3M NaOH.

10.3.2 Transmission Electron Microscopy (TEM)

TEM images were obtained to confirm the ceria morphology and particle size (Figures 61 and 62). The particle size measurement was done by random sampling using multiple micrographs. Additionally, different batches of space and control samples are used for analysis.

In Figure 61 a–c, TEM images of control ceria prepared with 1 M NaOH solution are shown. These samples consisted of polyhedron-shaped particles with an average particle size of 3.8 nm, fairly uniform particle size and shape throughout the sample. Similarly, control samples prepared at more basic conditions (Figure 61 d–f) contained smaller nanopolyhedra with an average particle size of 2.9 nm.

TEM images of the space samples are presented in Figure 62. The samples had mostly nano-rods, with 2-13 nm in width and 10-50 nm in length. Samples prepared with 1 M-solution were seen to give larger and more uniform particles on the average. The 3 M-space samples had some nano-spheres as well as rods. The particle size distributions for all four ceria samples are shown in Figures 63 and 64.

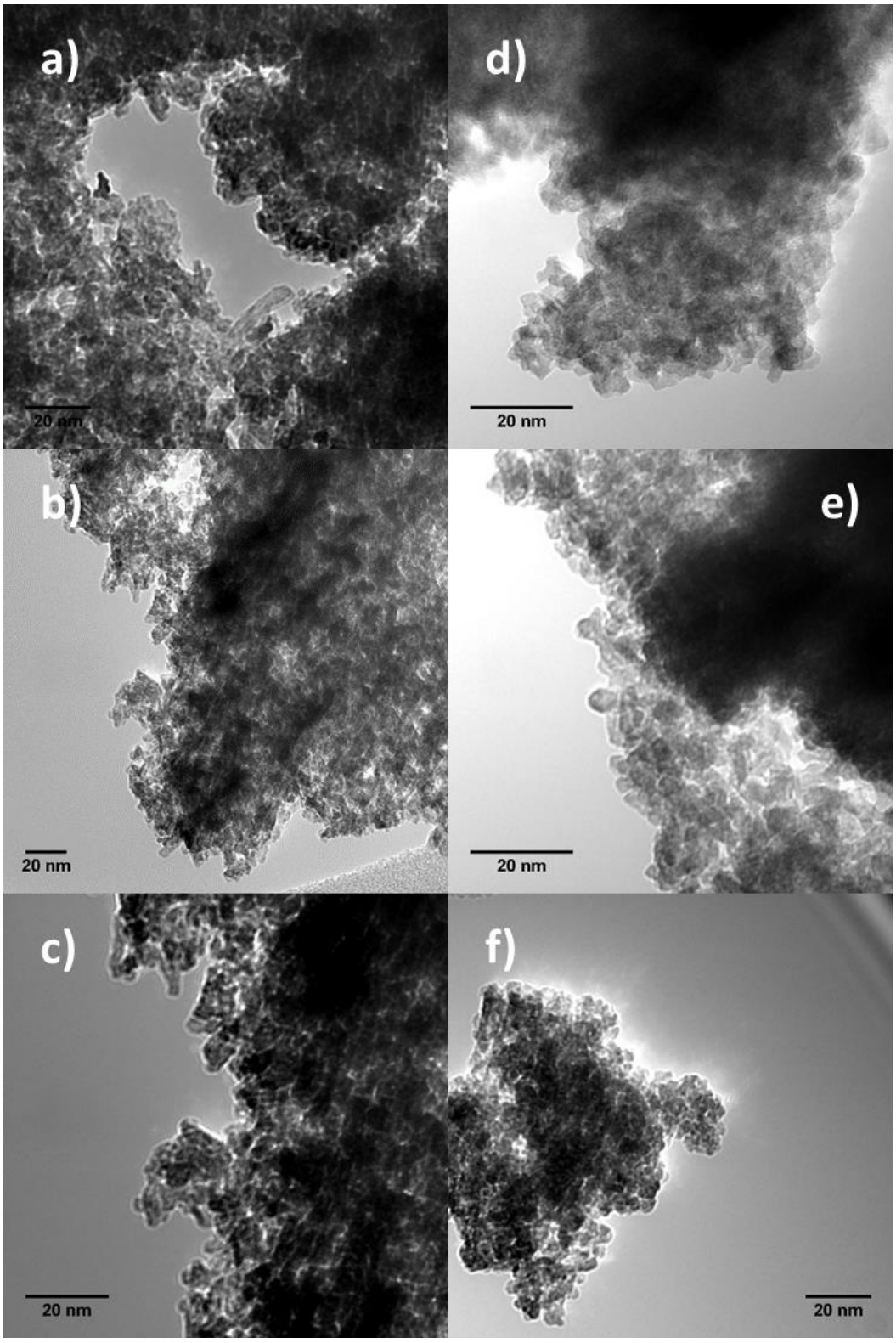

Figure 61. TEM image of control CeO_2 sample: 1 M (a–c) and 3 M (d–f)

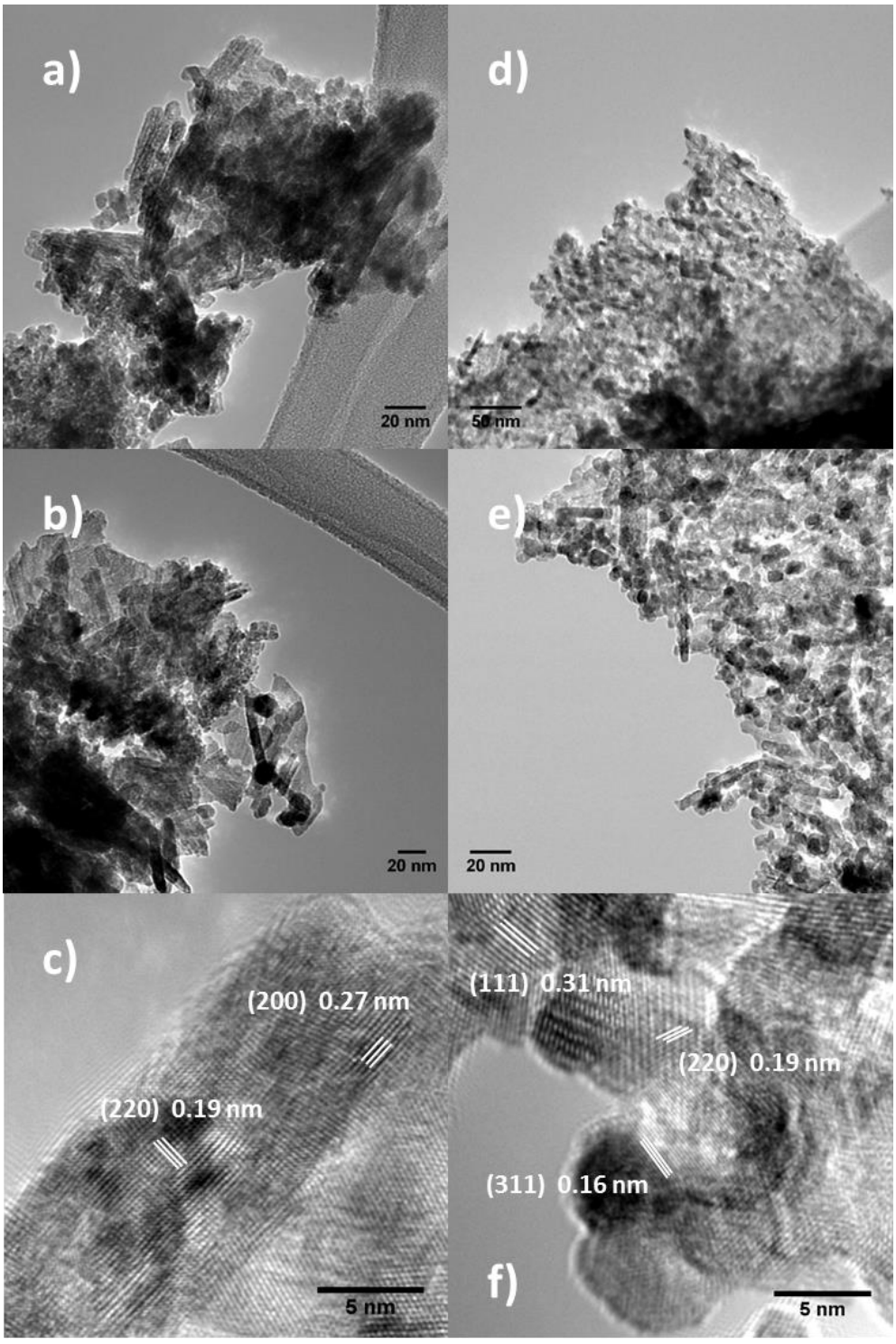

Figure 62. TEM image of space CeO_2 sample: 1 M (a–c) and 3 M (d–f)

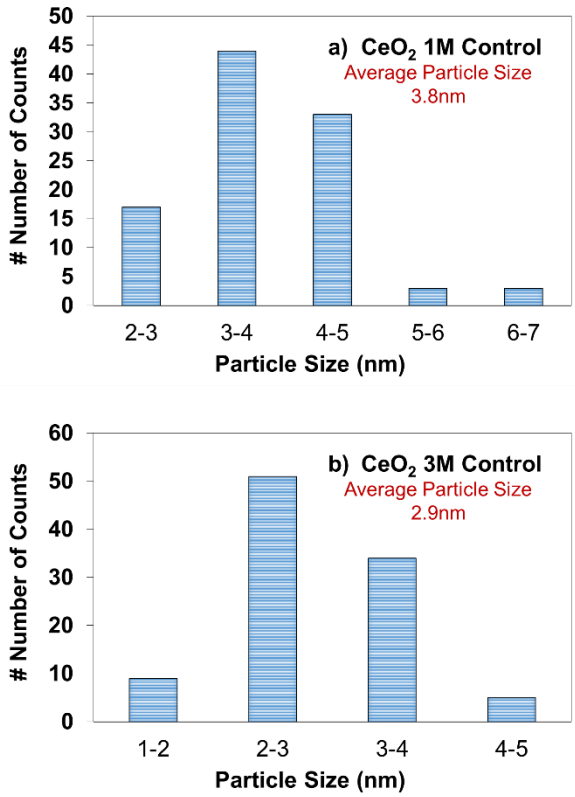

Figure 63. Particle size distribution histogram of Control CeO_2 sample: (a) 1 M; (b) 3 M.

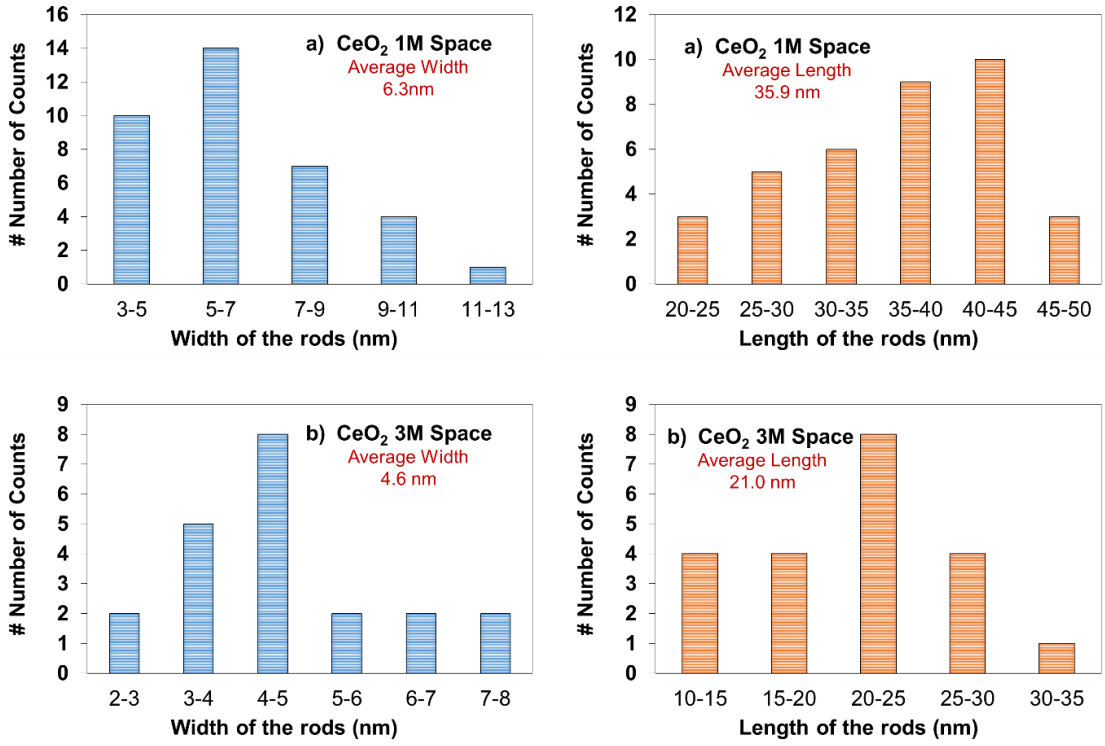

Figure 64. Width and length distribution histogram of Space CeO_2 sample: (a) 1 M and (b) 3 M

These results are significant in showing that ceria nanorods can be synthesized at room temperature and atmospheric pressure. To the best of our knowledge, there have not been any publications for the synthesis of nanorods under such conditions. In most cases, studies have concluded that ceria nanorods are formed at much higher temperatures and pressures.[201, 213, 259-261] In order to understand the formation of ceria nanorods under micrograviti condition, two crystal growth processes, Oswald ripening and oriented attachment, can be considered. These crystal growth mechanisms have been utilized to demonstrate the increase in particle size and change in morphology of the ceria particles.[262-264] The Ostwald ripening process follows the dissolution and reprecipitation of solution ions (Ce^{4+}, OH^-) from the ceria nuclei minimizing the surface energy state.[265] On the other hand, the oriented attachment mechanism predominantly depends on the collision between nuclei during reaction. This process allows ceria nano-crystal to grow into a certain direction.[265] Under microgravity condition, the lack of sedimentation of ceria particles in the solution may increase the residence time for nucleation of ceria crystals.[266] Additionally, the diffusion and/or natural convection of ceria particles can be somewhat enhanced. These factors can significantly affect the crystal growth through oriented attachment, which results in more frequent collision between nuclei, thus forming larger particles and nanorods. There have been several articles showing evidence that oriented attachment crystal growth is the main route for the formation of nanorods of ceria,[262] as well as various metal oxides.[267]

In the literature, numerous studies on understanding the effect of pH on ceria particles size and shape have been conducted, however, depending on the synthesis method and choice of ceria precursor, different results have been reported. Tok et al.[263] observed

similar behavior where smaller grains were seen in a more basic environment. This was because the $Ce(OH)_4$ precipitate is basic; thus, the solubility of $Ce(OH)_4$ in a more basic medium limits further agglomeration to form larger particles.[263] However, an opposite trend was reported by Yang and coworkers,[262] where changing the concentration of NaOH from 1 M to 5 M, increased the particle size of the ceria cubes from 20 nm to 25-40 nm. Mai et al.[264] prepared ceria using cerium nitrate precursor at different NaOH concentrations of 1, 3, 6 and 9 M, at a fixed reaction temperature of 100 ℃ and reaction time of 24 h. It was observed that polyhedra particles were formed using 1 M NaOH, but as the solution became more basic, only rods were obtained.

In this study, the effect of pH on the ceria morphology and particle size was more apparent in the case of the space samples. It was found that the length of the nanorods were longer for the 1 M-space samples whereas smaller dimensions were observed for the 3 M-space samples. Moreover, the rods were prominent the former, while the number of rods were smaller in the 3 M-space samples, with nano-polyhedra and spheres also being observed. It should also be noted that the control ceria samples were under reaction condition of 25 ℃ and 1 atm. For example, Wu et al.[268] prepared ceria powders in acidic, basic and neutral reaction mediums indicating that the effect of pH on particles size was insignificant at room temperature. The similarities between the particles size and shape in the 1 M and 3 M-control samples are in good agreement with their results. Therefore, it can be concluded that under microgravity, the pH affects the ceria morphology and particle size, whereas the effect is less prominent under normal gravity at room temperature.

Lastly, identification of the diffracted planes was conducted. D-spacing was measured using Image J software. Figure 62 c shows a ceria rod including (220) and (200)

planes with 0.19 and 0.27 nm d-spacing [34,46,52]. Figure 62 f indicates ceria nanopolyhedra and spheres with (311) and (220) planes.[267]

10.3.3 X-ray Diffraction (XRD) Analysis

The XRD patterns of the ceria samples are shown in Figure 65. All patterns exhibited five distinct peaks which ensured that pure ceria was formed. Each peak was assigned to a particular crystal plane. The peak at a 2θ value of 28.5°, which showed the highest intensity, was identified as (111) plane of the cubic cerianite phase (ICDD 81-792). Others at 2θ values of 33°, 47.5°, 56°, and 69.4° were identified as (200), (220), (311), and (400) planes of ceria. For comparison, sharper diffraction lines were obtained for space samples, which suggest higher crystallinity of the structure.

The full width at half maximum (FWHM) values are shown in Figure 66. These values were used to calculate the mean crystal size which is listed in Table 16. It appears that the (111) peak is broader for control samples, resulting smaller crystal size than those that were prepared in space. Generally, the crystal size estimated from XRD is in good agreement with the particle size observed in TEM. In the control samples, however, an increase of crystal size from 31.6 to 39.6 Å was obtained with an increasing NaOH concentration, whereas almost no change in terms of particle size was concluded from TEM results. In contrast, the effect of pH on the crystal size was clear for space samples, where a significant decrease of crystal size from 67.9 to 53.5 Å was seen, which follows the same trend as that of the TEM results.

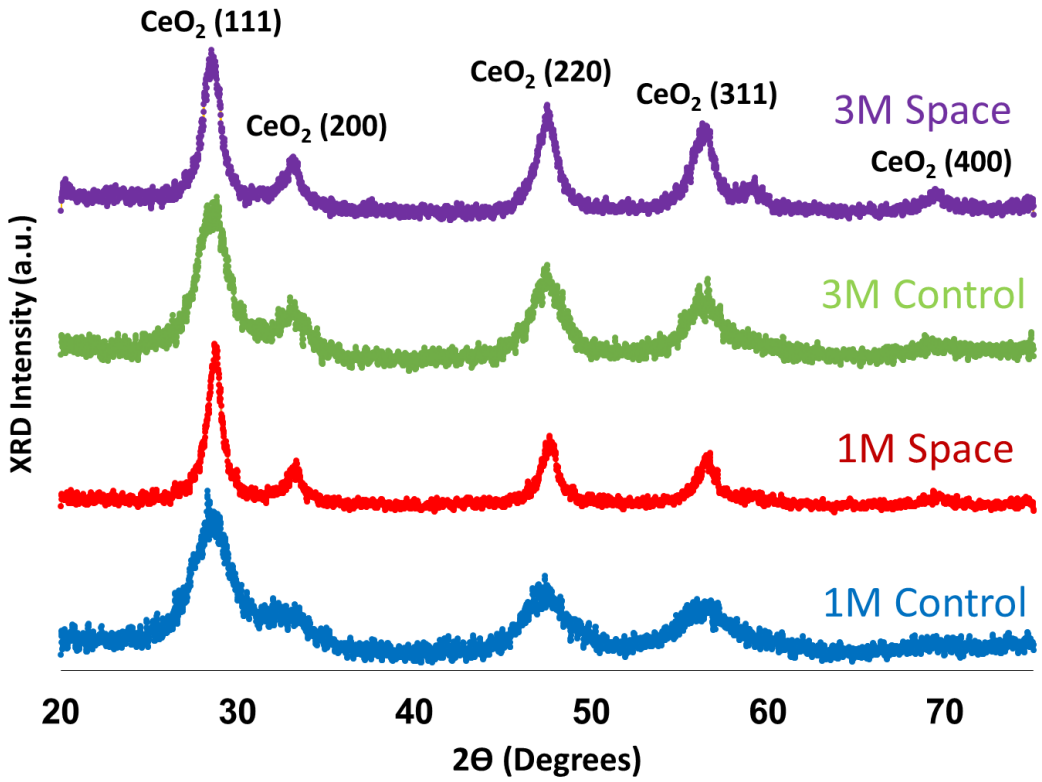

Figure 65. XRD pattern of the CeO_2 sample.

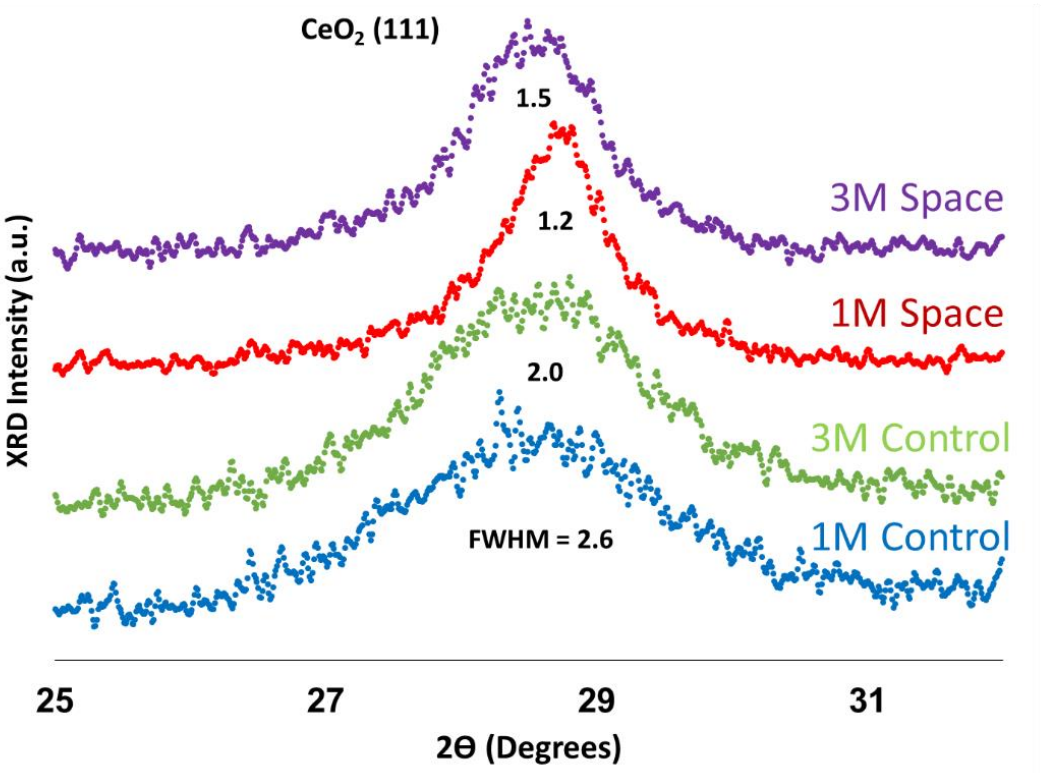

Figure 66. Comparison of FWHM of (111) plane for CeO_2 sample.

Table 16. Mean crystal sizes of CeO_2 sample

Mean Crystal Size (nm)	
1M Control	3.2
3M Control	4.0
1M Space	6.8
3M Space	5.3

10.4 Conclusion of Chapter 10

The effect of microgravity on ceria synthesis was investigated. Ceria was synthesized by mixing cerium nitrate and sodium hydroxide solutions at room temperature, under both microgravity (space) and normal-gravity (control) for comparison. The ceria samples that were prepared in space showed lower surface area and pore volume compared to the Earth samples. BJH pore size analysis indicated that the space ceria samples consisted of larger pores with a broader pore size distribution. The morphology of the ceria particles were observed from TEM images. It was concluded that the space samples were mostly nano-rods, whereas control samples contained nano-polyhedra. The average particle size observed was larger for space ceria. From XRD results, space ceria samples were more crystalline than the control samples. The mean crystal size obtained using Scherer equation was larger in case of space samples than control. The difference in particle size and shape between space and control ceria is thought to be due to improved oriented attachment crystal growth process where more collision of ceria particle occurs. This can be attributed to lack of sedimentation of the ceria particles under microgravity condition. Lastly, the effect of pH was examined by changing the concentration of sodium hydroxide solution (1 M and 3 M). The ceria samples synthesized under normal-gravity at room temperature showed minimal differences between 1 M and 3 M. However, a significant decrease in particle size was observed for space samples which were prepared in a more basic medium, with a number of nano-polyhedra and spheres also being present.

** Information in this chapter is reproduced/adapted from " Soykal, I.; Sohn, H.; Bayram, B.; Gawade, P.; Snyder, M.; Levine, S.; Oz, H.; Ozkan, U., Effect of Microgravity on Synthesis of Nano Ceria. Catalysts 2015, 5 (3), 1306-1320."*

APPENDIX A

LIST OF ACRONYMS

AC	Activated Carbon
ANL	Argonne National Laboratory
APS	Advanced Photon Source
AP-XPS	Ambient-Pressure X-ray Photoelectron Spectroscopy
ASAP	Accelerated Surface Area and Porosimetry
BET	Brunauer-Emmett-Teller
BTEB	Bis(trimethoxysilylethyl)benzene
BJH	Brunauer-Joyner-Helena
BM-D	Bending Magnet Beamline
CFC	Chlorofluorocarbon
CHC	Chlorinated Hydrocarbon
CLF	Chloroform
CMC	Carboxymethyl Cellulose
CRD	Catalytic Reductive Dechlorination
CTC	Tetrachloride
DCE	Dichloroethylene
DCM	Dichloromethane
DRIFTS	Diffuse Reflectance Fourier Transform Infrared Spectroscopy
DSC	Differential Scanning Calorimetry

DTA	Differential Thermal Analysis
EDAX	Energy-Dispersive X-ray Analysis
EPA	Environmental Protection Agency
ESR	Ethanol Steam Reforming
FID	Flame Ionization Detector
GC-MS	Gas Chromatography-Mass Spectrometry
GHSV	Gas Hour Space Velocity
HADDF	High Angle Annular Dark Field
HDC	Hydrodechlorination
H-SOMS	High-temperature-treated Swellable Organically-Modified Silica
ICP-OES	Inductively Coupled Plasma Optical Emission Spectrometry
IR	Infrared
IWI	Incipient Wetness Impregnation
LHSV	Liquid Hour Space Velocity
LO-TO	Longitudinal Optic-Transverse Optical
MRCAT	Materials Research Collaborative Access
MTBE	Methyl tert-butyl Ether
NMR	Nuclear Magnetic Resonance
PCB	Polychlorinated Biphenyl
PCE	Perchloroethylene
PDHID	Pulsed Discharge Helium Ionization Detector
PEM	Proton Exchange Membrane
PSD	Pore Size Distribution
QIR	Quantitative Isothermal Reduction

SAXS	Small-angle X-Ray Scattering
SOMS	Swellable Organically-Modified Silica
STEM	Scanning Transmission Electron Microscopy
TCA	Trichloroethane
TCE	Trichloroethylene
TEM	Transmission Electron Microscopy
TEOS	Tetrarthyl Orthodilicate
TGA	Thermogravimetric Analyzer
TPA	Temperature Programmed Analysis
TPD	Temperature Programmed Desorption
TPO	Temperature Programmed Oxidation
TTCE	Tetrachloroethylene
VC	Vinyl Chloride
VOC	Volatile Organic Compounds
XAFS	X-ray Absorption Fine Structure
XANES	X-ray Absorption Near Edge Structure
XPS	X-ray Photoelectron Spectroscopy
XRD	X-ray Diffraction
ZVI	Zerovalent Iron

APPENDIX B

GAS-PHASE FIXED BED FLOW REACTOR SYSTEM

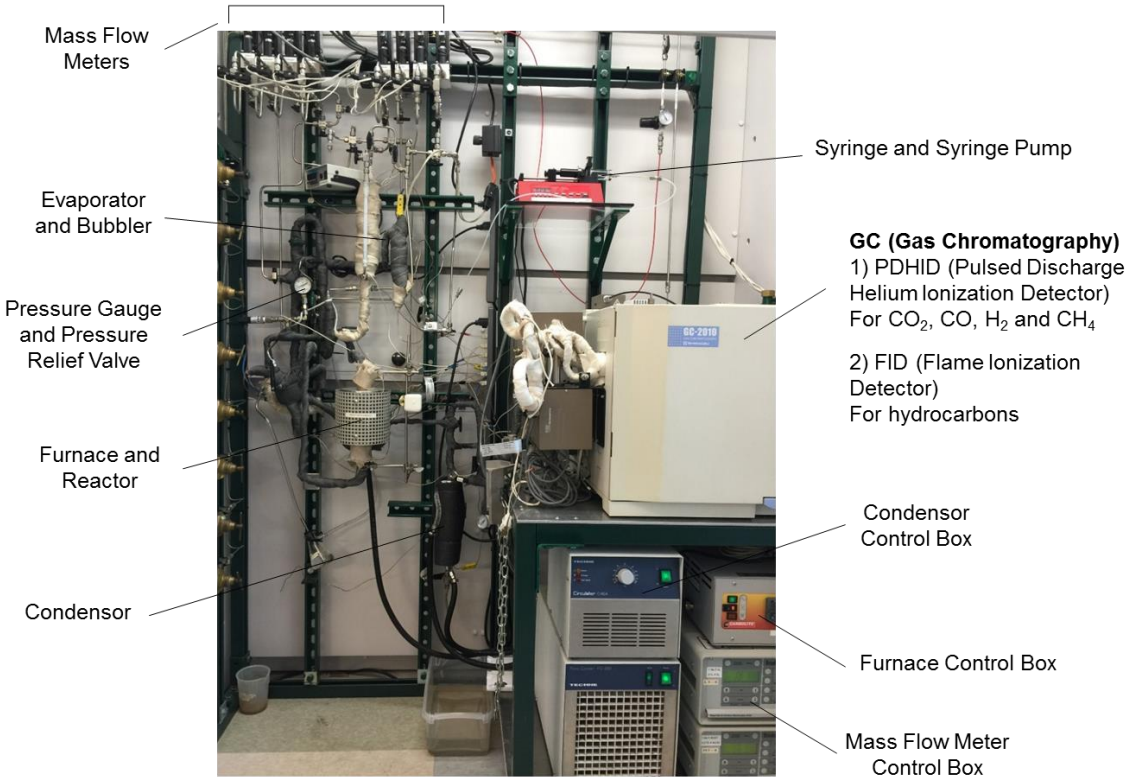

Figure 67. Picture of the Reactor System

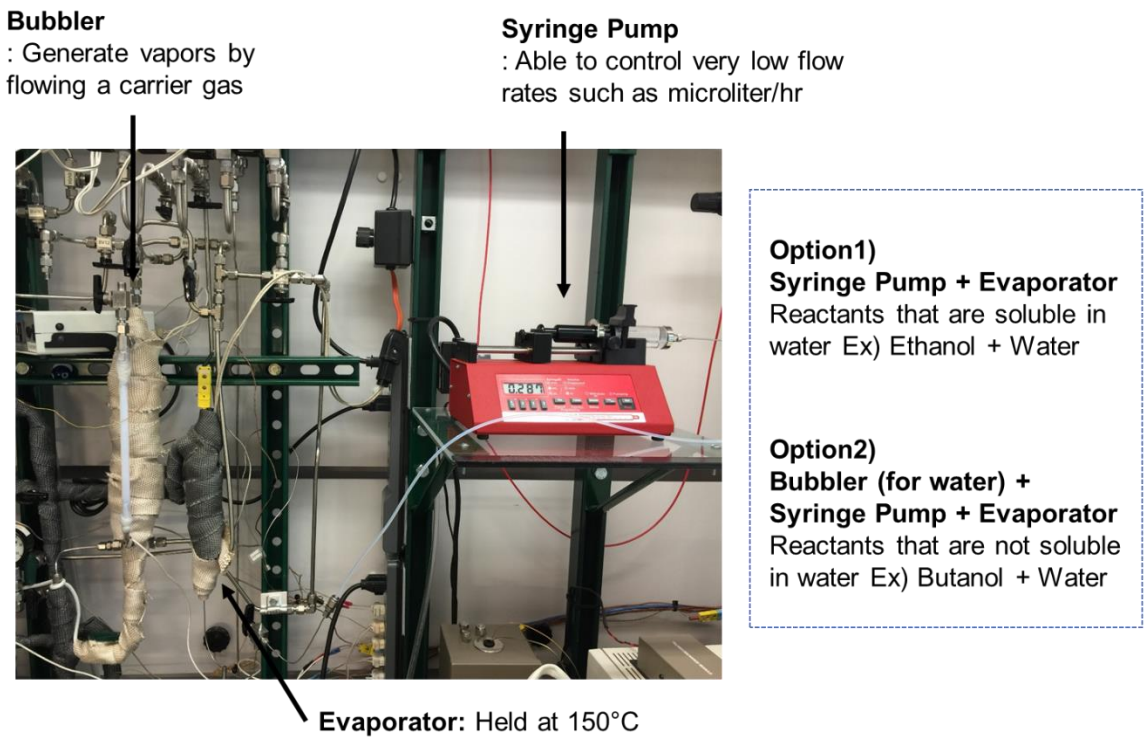

Figure 68. Picture of two bubblers and a syringe pump

APPENDIX C

CATALYST CHARACTERIZATION AND PRINCIPLES BEHIND THE TECHNIQUES

C.1 Surface area, Pore volume and Pore Size Distribution

If a chemical reaction is a surface-mediated reaction over heterogeneous metal catalysts the kinetic reaction rate fairly depends on the amount of surface area that can be utilized. As more surface area is employed, the availability of active sites on the catalyst surface to the reactants increases, thereby enhancing the reaction. Therefore, it is a reasonable statement that the more the surface area the faster the reaction and the better the catalytic activity is.

There are few parameters that increase the available surface area of the catalyst. One can be the pore size. Porous materials serve a crucial role in the catalysts field as catalyst supports. This is because the existence of pores allows the utilization of inner-particle surfaces, which escalates the overall amount of surface area significantly. The increase in surface area directly has an effect on the increase in number of adsorption sites where more reactants can be adsorbed on the catalyst surface. The inner surface area is considerably larger compared to the outer surface area of the catalyst.[269] At a fixed particle diameter, a decrease in pore diameter and the associated increase in number of pores, leads to a larger surface area of the particle.

Another effect of the pore size to the catalytic activity is associated with the diffusion of reactant through the pores. For example, if the pore diameter is significantly

small, it is possible that the reactants may not able to diffuse into the pores to reach the internal surface area. The mass transfer limitation by pore diffusion can change the overall reaction rate to be controlled by the internal diffusion of reactant in the pores thus degrading the catalytic activity. Therefore, understanding the pore size distribution indirectly provides valuable information about the surface area and the degree of diffusion limitation.

Pore size distribution (PSD) comprises a wide range of pore diameter from micropores to macropores. The range of pore diameters are as follow:[270]

Ultramicropores: pore size of less than 0.7nm (X< 0.7nm)

Micropores: pore size of less than 2nm (X< 2nm)

Mesopores: pore size of between 2nm and 50nm (2< X< 50nm)

Macropores: pore size of greater than 50nm (X>50nm)

A typical methodology to obtain PDS is using physical adsorption and desorption of gas probe molecules on the catalyst surface at liquid nitrogen temperature. The analysis of PDS is usually qualitative to estimate the structural characteristics of the catalyst. A detailed demonstration of the experimental procedures to obtain surface area, pore volume and pore size distribution are as follow:

"Brunauer-Emmett-Teller (BET) surface analysis provides surface area and pore volume of the materials by using nitrogen adsorption/desorption isotherms which can be collected by a Micromeritics ASAP 2020 (accelerated surface area and porosimetry) instrument. The principle of this technique encompasses physical adsorption of nitrogen molecules in multilayers on the catalysts surface. First, the sample is degassed for 12h at

130 ℃ under vacuum conditions in order to remove any impurities on the surface. The pre-treated sample is then transferred to the analysis port where the analysis is performed at liquid nitrogen temperature. The Brunauer-Joyner-Helena (BJH) pore size distribution of the sample is acquired from desorption branch of the isotherm after saturation pressure of nitrogen is reached."

As mentioned early, technically, a catalyst containing more number of micropores exhibit higher surface area, which can be expected to increase the catalytic activity. However, this is a very ambiguous argument to make because other various parameters such as pore acidity/basicity, shape and tortuosity of the catalyst can significantly influence the extent of diffusion limitation of the reactants to the pores, which degrades the catalytic performance. Therefore, the effect of pore size to the catalytic activity should not be considered alone without including the effect of morphological and geological aspects of the pores as well as how the active sites are well dispersed inside the pores.

C.2 High-Angle Annular Dark-Field Imaging (HAADF) in Scanning Transmission Electron Microscope (STEM)

STEM holds the same fundamentals as TEM does. The basic principle of electron microscopy is that the electron beam emitted from the electron source travel through several condenser lenses and penetrates the specimen. The electron bombardment on the sample produces scattered (bright field), diffracted (dark field) and secondary electrons. The electrons that were transmitted throughout the specimen crates an image focused by the objective lens. STEM utilizes the secondary electrons to conduct another type of imaging. Since the electrons are collected using a detector, identification of metals can be performed. Also, oxidation states

of the metal can be obtained. HDDAF STEM is a dark field imaging method where metals are shown in bright contrasting the background which is dark.

C.3 Metal Dispersion

Most commercial catalysts consist of noble transition metals, which acts as active sites, and metal oxides as supports.[271] It is feasible that pure metal powders can be used as heterogeneous catalysts without the support. However, it is not a practical method because the cost of noble metals such as Pd, Pt, Ru and Rd is very expensive. Also, the agglomeration of these metal particles decreases the efficiency of employing the metal surface area as active sites.[42] Therefore, a typical way to increase the utilization of metal particles and lower the cost of catalyst is to impregnate them on a catalyst support. However, most impregnation process leads to losses of metal particles in the bulk phase of the support, thus becoming not accessible to the reactants. The ratio between the accessible metal sites (surface) and the inaccessible sites (bulk) is called as metal dispersion.

Metal dispersion is conventionally defined as,

$$Metal\ dispersion\ (\%) = \frac{Number\ of\ moles\ of\ metal\ on\ the\ suface}{Number\ of\ moles\ metal\ in\ bulk\ phase}$$

It is not enough to stress the substantial contribution of metal dispersion on the catalytic activity. Catalysts with higher metal dispersion indicate that there are more active metal particles on the surface, which enhances the reaction rate and improves the catalytic performance.

Among many different techniques, metal dispersion of the sample can be investigated by N_2O chemisorption technique described by Jensen et al.[215] A detailed explanation of the experiment procedures are as follow:

"A ¼" OD fixed bed quartz reactor packed with catalysts is located inside fast-response furnace (Carbolite, MTF 10/15/130). The sample is first pre-treated under 5% H_2 in He for 2 hours at 400 ℃ to make sure that all the metals on the catalysts surface are in their reduced form. Then, the sample is cooled down to 40 ℃ under a flow of He to perform N_2O chemisorption. When the analysis temperature is reached, 3% N_2O/He is introduced to the fixed bed reactor. The analysis is based on the number of oxygen atoms from N_2O adsorbed on the reduced metal sites on the surface. As the reaction proceeds, unreacted N_2O and N_2 will be the only species contained in the exhausted stream of the reactor. The amount of produced N_2 will be calibrated to quantify the number of moles of N_2, and this will be correlated to the number of moles of oxygen adsorbed on the surface. Assuming Pd:O ratio as 1:1, the number of Pd sites formed on the catalysts surface will be calculated. The experiment will be done via an MKS – Cirrus II on-line mass spectrometer."

C.4 Temperature Programmed Analysis (TPA)

Temperature programmed analysis encompasses chemical adsorption of probe molecules on the catalyst surface to investigate its characteristics. As temperature increases, the chemisorbed species desorb as different products which is typically detected by an on-line mass spectrometer. Over the past few decades, TPA has been the most frequently used technique in the catalysis area. Temperature Programmed Reduction (TPR) is a method, in which hydrogen is introduced to the sample and temperature is increase at a constant

heating rate. This is to inspect how much the surface sites are in its reduced form, qualitatively and quantitatively. Temperature Programmed Oxidation (TPO) incorporates oxygen instead of hydrogen. This is a common way especially for post-reaction analysis in order to examine catalyst coking by oxidizing carbonaceous species into CO and CO_2. Lastly, Temperature Programmed Desorption (TPD) is a technique to understand how strong the probe molecules are bonded to the surface active sites, for example, either acid or basic probe molecules can be used to explore the acidity or basicity of the surface.

C.5 Small-Angle X-Ray Scattering (SAXS)

SAXS technique is a convenient way to obtain structural ordering, sizes and shapes of nanoscale particles. A scattered X-ray beam hits the sample and a detector collects the difference in intensities of the beam. Since the method does not require crystallinity of the sample, it can be used for non-crystalline materials that do not exhibit long-range order, which is appropriate for SOMS. Therefore, SAXS experiments on SOMS will be carried out to possibly gain crucial information of the swelling process of SOMS.

C.6 Differential Scanning Calorimetry (DSC) and Differential Thermal Analysis (DTA)

When a material changes its phase or undergoes a reaction, it always accompanies with a heat or energy change. Thermal analysis is a promising methodology that allows to calculate the amount of heat change of a particular material under various reaction environments at different temperatures.[272-273] Among many different techniques, differential scanning calorimetry (DSC) is a commonly used method, which provides

valuable information about chemical properties such as meliting point, crystallization point, evaporation temperature as well as heat capacity.[272] In field of heterogeneous catalysis, DSC is typically used in combination with thermogravimetric analysis (TGA) to determine the enthalpy change during adsorption/desorption of different gas molecules on the catalyst surface. Furthermore, the phase equilibrium for gas mixtures in the presence of catalysts can be obtained to understand the heterogeneously catalyzed reactions.

The principal of the DSC technique is very similar to differential thermal analysis (DTA) which has been extensively utilized in the early 1900s.[274] DTA analysis is based on the temperature difference between the sample and an inert reference. A shared heating source is utilized to introduce an identical heat flux to both sample and reference to increase or decrease the temperature.[272, 274] First of all, the temperature is set to a certain value with a fixed heating rate. During operation, any heat exchange activity of the sample, influences the sample temperature. The change in temperature is monitored as a function of time.

DSC system also measures the temperature difference between sample and reference but the measurement is based on the heat flux.[274] There are two types of DSC system, one is heat flux DSC and the other is power compensating DSC. Heat flux DSC technique exploits a single heater to control the temperature of both sample and reference. However, for power compensating, two individual heating sources are utilized to increase the temperature separately.[274] While the temperature is increasing at a known heating rate, the heating rate of the reference cell maintains constant since there is no heat exchange. However, in case of the sample, either higher or lower energy flux (J/s or W) is required to maintain the same heating rate (power compensating DSC) due to change in chemical properties. The change in heat flux of the sample heater is then collected and analyzed.

Another way is to build a connection between the sample and reference to exchange the heat energy (heat flux DSC). The transported heat flux can be recorded by the difference in thermocouples voltages.[273-274] A typical DSC scan contains 'heat flow' on the y-axis with a unit of mJ/sec and x-axis for 'temperatures'.[275] Using DSC technique, comparative studies are possible by looking at the difference in heat capacity and enthalpy, which can be calculated per sample mass basis.

C.7 *In Situ* Catalyst Characterization

In recent decades, the use of *in situ* characterization techniques has been a forthcoming trend in catalysis research. Due to the rapid development of analysis equipment, it is possible now to monitor real time data under reaction conditions where gases are flowing and temperatures and pressures are changing. Any kinds of analysis that was limited to ex-situ studies are now mostly available for *in situ* studies.

C.7.1 *In Situ* X-Ray Diffraction (XRD) - bulk analysis

Conducting XRD experiments can identify the crystal structure of a catalyst. A certain wavelength of X-ray is diffracted from the regularly repeated layers of atoms with a specific angle. The theta value of that angle can be plugged into the Bragg's law equation to obtain spacing between atomic layers, called d-spacing. From the d-spacing and with the support of references, dominant planes in the structure can be found. *In situ* XRD will be used to examine how Pd acts under TCE reaction conditions. A bubbler will be employed

to deliver the reactant vapors where the catalysts are placed. Whether Pd atoms oxidize or reduce will be ascertained by the differences in planes between Pd or PdO.

C.7.2 *In Situ* X-ray Photoelectron Spectroscopy (XPS) - surface analysis

When the energy of X-ray is greater than the binding energy of an electron in an atom, the electron gets excited and leaves the surface with a certain kinetic energy. The ejected electron is called a photoelectron and collected using a detector. XPS spectrum is a plot where the numbers of these electrons detected are associated with a wide range of binding energy. Therefore, XPS provides electronic states of any metal that are of interest. Because the electrons may interfere with gas molecules, XPS analysis is typically conducted under ultra-high vacuum. However, a special design of XPS chamber was built by Professor Tao's group at University of Notre Dame, which is capable of introducing reactant gases and collecting photoelectrons simultaneously at ambient pressure. As we are in collaboration with them, samples will be sent to investigate the oxidation state variations of Pd metal on the surface under HDC of TCE reaction.

C.7.3 *In Situ* X-ray Absorption Spectroscopy (XAS) - bulk analysis

Similar to XPS, XAS is a tool that utilizes source of X-ray to emit photoelectrons. However, contrary to XPS, where numbers of electrons are detected, XAS targets the core electron in 1s orbital thus requires high flux of X-rays. These sort of X-rays can be only acquired from synchrotron facility. Since the XAS studies are core electron related, it is element specific. In other words, the ejected 1s electron wave interacts with neighboring

atoms either constructively or destructively hence the intensity of the initial X-ray changes. This allows us to calculate the bond distance and coordination number. Oxidation states of metal can be also obtained. The XAS experiment on Pd/SOMS will take place in Argonne National Lab, IL where one of the highest energy of X-ray is produced in the country.

C.7.4 *In Situ* Diffuse Reflectance Infrared Fourier Transform (DRITFS) - surface analysis

Infrared (IR) spectroscopy is a widely known technique to probe various types of functional groups and characteristics of an unknown structure. The adsorption of specific frequencies of IR initiates vibration of atoms, which can then be used to identify different chemical bonds. DRIFTS operate on the same principle as motioned above; however, it is a surface technique where the IR beam is reflected from the surface. In our lab, we are capable of running DRIFTS reactions at different temperatures while gases are present. Therefore, TCE HDC reaction will be conducted in the DRIFTS *in situ* cell to understand the intermediate steps of how TCE adsorbs on the surface and desorbs as products.

APPENDIX D

SWELLING OF SOMS AND ITS SYNTHESIS METHOD

This section includes a brief review of the three papers listed below.

(1) Burkett, C. M.; Edmiston, P. L., Highly Swellable Sol–Gels Prepared by Chemical Modification of Silanol Groups Prior to Drying. J. Non-Cryst. Solids 2005, 351, 3174-3178.

(2) Burkett, C. M.; Underwood, L. A.; Volzer, R. S.; Baughman, J. A.; Edmiston, P. L., Organic–Inorganic Hybrid Materials That Rapidly Swell in Non-Polar Liquids: Nanoscale Morphology and Swelling Mechanism. Chem. Mater. 2008, 20, 1312-1321.

(3) Edmiston, P. L.; Underwood, L. A., Absorption of Dissolved Organic Species from Water Using Organically Modified Silica That Swells. Sep. Purif. Technol. 2009, 66, 532-540.

In one of the papers published in 2009 which illustrates the chemical properties of the organically modified silica (SOMS), authors claim, "the swelling process is ascribed to the tensile forces generated and stored by the capillary-induced collapse of the nanoporous matrix upon drying during sol-gel synthesis".[17] According to the statement, it can be speculated that the SOMS is closely associated with its synthesis method. Therefore, to obtain better understanding of the swelling process, one should first be aware of how conventional silica is synthesized.

There are several different methods to prepare silica powder, among them, sol-gel synthesis technique including hydrolysis and co-condensation processes has been widely used.[276-280] The reaction involves a mixture of alkoxysilanes, water and organic solvents. To enhance the reaction rate, acidic, basic and fluoride-based catalysts are implemented. The modification of sol-gel synthesis results in different types of silica. For example, addition of surfactant or change in precursor leads to surface functionalization of silica.[281-282] Different silica morphology and particles sizes are obtained as well.[283-284]

Sol-gel synthesis is basically a process that forms a complex inorganic matrix through gelation of the sol (colloidal suspension) in liquid phase under homogenous catalysts. The initial step is hydrolysis of alkoxysilane, reacting readily with water to generate silanol species. Since most alkoxysilance precursors such as tetraethoxysilane (TEOS) are not miscible in water, alcohol is often exploited to obtain a homogeneous solution.[277] After hydrolysis, the silanol groups either undergo water condensation or alcohol condensation, reacting with either each other or with alkoxysilane groups, respectively. Co-condensation of silanol species then start to form Si-O-Si bonds resulting a three-dimensional porous siloxane network consists of numerous siloxane bridges.

As more bridging process proceeds, the network grows significantly until a point where silica nanoparticles are observed. These nanoparticles are then agglomerates to each other and constitutes a gel in the liquid solution. The remaining solvent containing unreacted alkoxide and hydroxyl groups exists in the vacant spaces of the silica gel. Following this stage, the gel is rinsed and dried through evaporation to remove the solvent. Afterwards, the obtained material is grinded to obtain amorphous silica.

First of all, the uniqueness in the synthetic process of SOMS is using a different silane monomer precursor such as bis(trimethoxysilylethyl)benzene (BTEB), compared to regular silica synthesis method.[16-18] BTEB contains a benzene ring directly connected to a silicon whereas TEOS includes four methoxy functional groups. The implementation of BTEB allows polymerization of the precursors in the presence of fluoride catalysts of the precursor solution. Therefore, following the same procedures mentioned above, poly-condensation of BTEB creates a highly cross-linked polymer matrix including covalent linkages between the aryl group and silicon. At this point, particles with 10-20 nm size is formed, which then further agglomerates to a colloidal gel. Since the degree of crosslinking is substantial compared to the case where TEOS is used, the generated gel network is a more tightly connected than regular silica gel.[17-18]

Once the gelation is complete, the gel should be aged for a specific time period and rinsed by organic solvents such as acetone. It should be noted that, prior to drying, derivatization of silanol groups are necessarily for SOMS synthesis. This is because the residual silanols may lead to formation of Si-O-Si bonds during evaporation which may decrease the extent of swelling process.[17-18]

Edmiston and coworkers have examined the influence of various parameters such as choice of precursor, solvent, catalysts, aging time and siliane concentration to invesitgate the principle behind the swelling behavior.[18]

In summary,[18] (1) Fluoride based or strongly concentrated base catalysts must be used. (2) Solvent should be closely to non-polar. (3) Gel should be aged until syneresis is observed. (4) Concentration of precursor solution should be between 0.5 ± 0.25 M.

Interestingly, considering the effect of precursor, the swelling behavior of SOMS is only obtained by the two precursors that include covalent bond between the aryl groups connected to the silicon center. Thus, it can be speculated the stretchiness of SOMS while expanding can be correlated to the flexibility of S-C-aryl bonds.[18]

Through gelation and polymerization of the BTEB monomers, these flexible connections between the aryl group and silcon plays a key role for generating flexibility in between the non-covalently bonded nanoparticles. These interactions allow to maintain the rigidity of the heavily cross-linked network during solvent removal step without resulting any breakages of the chemical bonds. Unlike SOMS, the physical volume expansion is not observed for typical silica powders. Thus, it can be considered that there might be some fractures of inter-particle bonds during the solvent removal step.[18] As the solvent evaporates, the matrix begins to collapse but the interparticle bonds of the network tend to retain its structure thererby producing capillary attraction forces. The attraction forces are then converted to tensile forces because of the high degree of polymer crosslinking that holds the network rigidly linked to each other. When drying is complete, although the structure is in its dry collapsed state but the tensile forces are still stored in the polymeric matrix.[18]

The energy due to tensile forces is released as physical volume expansion of the Osorb when organic liquid and gas molecules are introduced to the matrix. The process is referred as “swelling”. However, energy stored in the network (as tensile forces) produces significant amount of forces in all directions during swelling of organic materials. These forces were measured and are shown in Figure 69.[18]

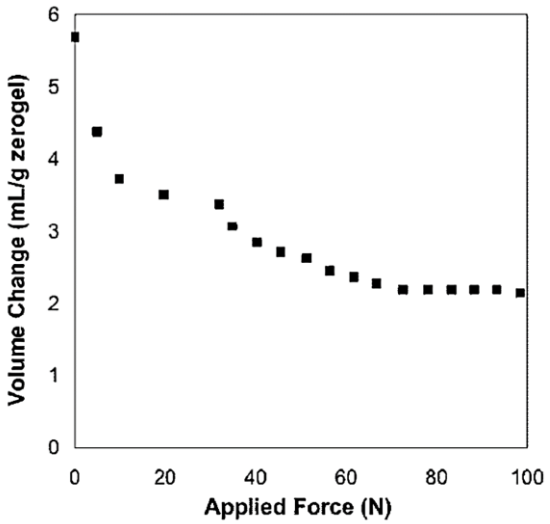

Figure 69. Volume change of SOMS as a function of applied force[18] *(cited from "Burkett, C. M.; Underwood, L. A.; Volzer, R. S.; Baughman, J. A.; Edmiston, P. L., Organic–Inorganic Hybrid Materials That Rapidly Swell in Non-Polar Liquids: Nanoscale Morphology and Swelling Mechanism. Chem. Mater. 2008, 20, 1312-1321.")*

Figure 69 was graphed based on an experiment where a known amount of SOMS was located on a porous frit in a sealed tube equipped with a piston.[18] Organic solvents were introduced to the SOMS through the porous frit resulting a volume expansion, subsequently pushing the piston in the upward direction whose weight was calculated and converted to force (N). Authors demonstrate that 2g of SOMS was able to lift up the piston of 20N (2kg) with a significant volume change of three times its original volume.[18] As more forces were applied to the SOMS, the degree of the volume change reached to a constant value, but the expansion phenomena was still observable. It is a very striking fact that the experiment system was not able to cease the mechanical volume expansion due to swelling, even applying 100 N of forces.[18]

In conclusion, due to the fact that the volume change reaches to a plateau regardless of amount forced being applied, it can be hypothesized that the morphological change for the initial step to open up the matrix is not limited to any static pressure. Once the pore is in its open stage the volume expansion depends on what kind of solvent was used. The mechanism of the swelling process of SOMS is described in Figure 70.

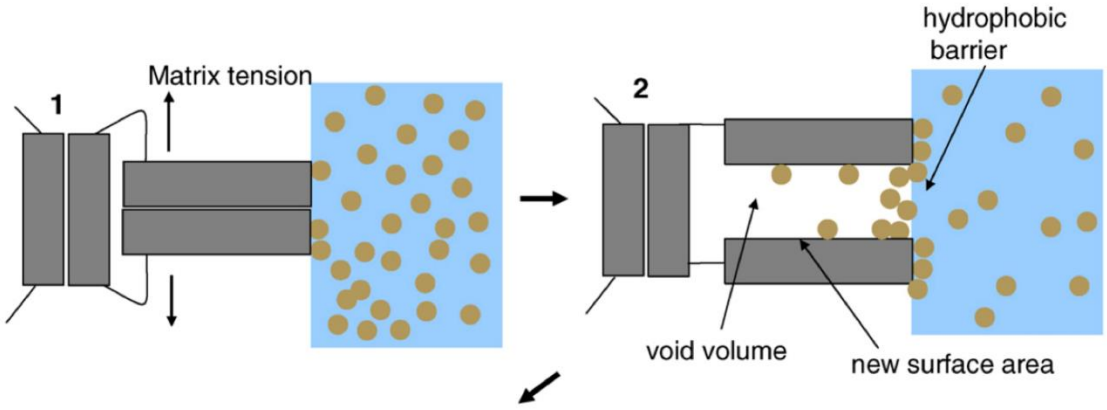

Figure 70. Mechanism of swelling process[17] *(cited from "Edmiston, P. L.; Underwood, L. A., Absorption of Dissolved Organic Species from Water Using Organically Modified Silica That Swells. Sep. Purif. Technol. 2009, 66, 532-540.")*

APPENDIX E

DERIVATION OF THE RATE LAW FOR HYDRODECHLORINATION OF TRICHLOROETHYLENE

Several rate law expressions for hydrodechlorination of trichloroethylene have been established in the literature depending on the reactor types and reaction conditions. In here, two the most commonly used ones are derived.

Hydrodechlorination of Trichloroethylene

$$C_2HCl_3 + 4H_2 \longrightarrow 3HCl + C_2H_6$$

E.1 Batch reactor, liquid phase, pseudo-first-order kinetic model

The derived rate law in here is in good agreement with the references.[35, 38-39, 42, 78, 285-289]

Starting from general mole balance equation,

$$F_{AO} - F_A + \int_0^V r_A \, dV = \frac{dN_A}{dt}$$

Assumptions for batch reactor

1. No input or output (F_{AO} and $F_A = 0$)
2. Well mixed ($\int_0^V r_A \, dV = r_A V$)
3. No volume change, V = constant

Therefore,

$$r_A V = \frac{dN_A}{dt} \qquad r_A = \frac{d(N_A/V)}{dt}$$

For batch reactor,

$$\boldsymbol{\frac{dC_A}{dt} = r_A}$$

Based on the TCE HDC reaction equation above,

$$-r_{TCE} = kC_{H_2}^4 C_{TCE}$$

However, H_2 is usually in excess in most HDC experiments, thus H_2 concentration can be considered as a constant. This allows to assume **pseudo-first-order** reaction.

$$-r_{TCE} = k_{app} C_{TCE} \qquad k_{app} = apparent\ rate\ constant\ (min^{-1})$$

Overall rate expression is,

$$\boldsymbol{-\frac{dC_{TCE}}{dt} = k_{app} C_{TCE}}$$

To obtain a catalyst surface area based rate equation (for Pd metal),

$$-\frac{dC_{TCE}}{dt} = k_{app} C_{TCE} = k_{obs} C_{Pd} C_{TCE} = k_{SA} a_s C_{Pd} C_{TCE}$$

$$k_{SA} = surface\ area\ based\ rate\ constant\ \left(\frac{L}{min * m^3}\right)$$

$$a_s = specific\ surface\ area\ \left(\frac{m^3}{g}\right)\ or\ \left(\frac{m^3}{mol}\right)$$

$$C_{Pd} = concentration\ of\ Pd\ \left(\frac{g}{L}\right)\ or\ \left(\frac{mol}{L}\right)$$

Again,

$$\boldsymbol{-\frac{dC_{TCE}}{dt} = k_{app}C_{TCE} = k_{SA}a_sC_{Pd}C_{TCE}}$$

$$\boldsymbol{k_{app} = k_{SA}a_sC_{Pd}}$$

To calculate the specific surface area based on Pd particle size,

$$r = \frac{3}{\rho a_s} \quad where\ r = particle\ radius$$

$$\rho = particle\ density$$

To obtain the rate constant k_{app},

$$-\frac{dC_{TCE}}{dt} = k_{app}C_{TCE}$$

$$\int_{C_{TCE,o}}^{C_{TCE,t}} \frac{1}{C_{TCE}} dC_{TCE} = -k_{app}\mathrm{t}$$

$$\boldsymbol{ln\frac{C_{TCE,t}}{C_{TCE,o}} == -k_{app}t}$$

$$\boldsymbol{where\ \ k_{app}\ \ is\ the\ slope\ of\ \ ln\frac{C_{TCE,t}}{C_{TCE,o}}\ \ vs\ \ t}$$

Finally, k_{SA} can be obtained by equation,

$$k_{app} = k_{SA}a_sC_{Pd}$$

To obtain k_{obs} ,

$$-\frac{dC_{TCE}}{dt} = k_{app}C_{TCE} = k_{obs}C_{Pd}C_{TCE}$$

$$k_{app} = k_{obs}C_{Pd}$$

$$k_{obs} = observed\ reaction\ rate\ constant\ \left(\frac{L}{min * mol}\right)$$

$$C_{Pd} = concentration\ of\ Pd\ \left(\frac{mol}{L}\right)$$

This kinetic model provides a good estimate of how fast the reaction proceeds, especially when comparing multiple catalysts in terms of their activity. However, the influence from deactivation is not taken into account, which results in a poor curve fitting.

E.2 Fixed-bed reactor, gas phase, Langmuir–Hinshelwood (LH) kinetic model

The derived rate law in here is in good agreement with the references.[26, 71, 290-292]

Hydrodechlorination of trichloroethylene is a surface-mediated reaction, therefore, the Langmuir-Hinshelwood kinetic model is the most appropriate method to derive the rate law equation. Several studies have shown a successful kinetic analysis based on Langmuir-Hinshelwood mechanism. The assumptions of the mechanism as follows:

1. Surface is homogeneous
2. Rate is a function of partial pressure of gases and fraction of vacant sites
3. Only monolayer coverage is considered
4. No interaction between adsorbates

To start with, several assumptions should be made specifically for hydrodechlorination of trichloroethylene.

1. Adsorption of H_2 on catalyst surface is dissociative surface and very strong
2. H_2 partial pressure is constant (excess H_2)
3. Adsorption of H_2 and TCE on the same active sites
4. HCl and ethane is weakly adsorbed
5. Surface reaction is irreversible

Langmuir-Hinshelwood proposed mechanism

$$1)\ H_2 + 2v \ \leftrightarrow\ 2H_{ads}$$

$$2)\ A + v \ \leftrightarrow\ A_{ads} \quad (A = TCE)$$

$$3)\ A_{ads} + H_{ads} \ \rightarrow\ B_{ads} + C_{ads} + v \quad (B = HCl\ \ C = ethane)$$

Step 3) is the surface reaction, therefore,

$$-r_{TCE} = k_{rxn}\theta_A\theta_H$$

From 1) and 2),

$$1)\ k_{H_2}P_{H_2}\theta_v^2 = k_{H_2}{}^{*}\theta_H^2$$

$$\theta_H = \sqrt{K_{H_2}P_{H_2}}\ \theta_v \quad where\ K_{H_2} = \frac{k_{H_2}}{k_{H_2}{}^{*}}$$

$$2)\ k_AP_A\theta_v = k_A{}^{*}\theta_A$$

$$\theta_A = K_AP_A\theta_v \quad where\ K_{H_2} = \frac{k_A}{k_A{}^{*}}$$

Since,

$$1 = \theta_H + \theta_A + \theta_v$$

$$\sqrt{K_{H_2}P_{H_2}}\ \theta_v + K_A P_A \theta_v + \theta_v = 1$$

$$\theta_v\left(\sqrt{K_{H_2}P_{H_2}} + K_A P_A + 1\right) = 1 \qquad \theta_v = \frac{1}{\sqrt{K_{H_2}P_{H_2}} + K_A P_A + 1}$$

$$\theta_H = \sqrt{K_{H_2}P_{H_2}} * \frac{1}{\sqrt{K_{H_2}P_{H_2}} + K_A P_A + 1} \qquad \theta_A = K_A P_A * \frac{1}{\sqrt{K_{H_2}P_{H_2}} + K_A P_A + 1}$$

Therefore, overall rate expression is,

$$-r_{TCE} = k_{rxn}\theta_A\theta_H$$

$$\boldsymbol{-r_{TCE} = k_{rxn}\frac{\sqrt{K_{H_2}P_{H_2}}K_{TCE}P_{TCE}}{\left(\sqrt{K_{H_2}P_{H_2}} + K_{TCE}P_{TCE} + 1\right)^2}}$$

Assuming P_{H_2} is extremely large, the above equation can be simplified to,

$$-r_{TCE} = k_{rxn}\frac{\sqrt{K_{H_2}P_{H_2}}K_{TCE}P_{TCE}}{\left(\sqrt{K_{H_2}P_{H_2}} + 1\right)^2}$$

$$where \quad k_{rxn} = intrinsic\ rate\ constant$$

$$K_{H_2}, K_{TCE} = adsorption\ rate\ constant$$

The overall observed reaction constant is,

$$\boldsymbol{k_{obs} = k_{rxn}\frac{\sqrt{K_{H_2}P_{H_2}}K_{TCE}}{\left(\sqrt{K_{H_2}P_{H_2}} + 1\right)^2}}$$

This can be more simplified to,

$$k_{obs} = k_{rxn}\sqrt{K_{H_2}P_{H_2}}K_{TCE}^{\surd}$$

$$where\ a\ constant\ \ K_{TCE}^{\surd}\ \ is\ defined\ as\ \ \frac{K_{TCE}}{\left(\sqrt{K_{H_2}P_{H_2}}+1\right)^2}$$

To obtain all the rate constants, experiment data should be fitted. Therefore, the fixed-bed reactor is assumed to behave as a PFR reactor under **steady state** condition.

Starting from general mole balance equation,

$$F_{AO} - F_A + \int_0^V r_A\,dV = \cancel{\frac{dN_A}{dt}}$$

Taking the derivative,

$$\frac{dF_A}{dV} = r_A$$

$$X = \frac{F_{A0} - F_A}{F_{A0}} = 1 - \frac{F_A}{F_{A0}} \qquad dX = -\frac{dF_A}{F_{A0}}$$

$$\boldsymbol{F_{A0}\frac{dX}{dV} = -r_A}$$

When integrated with Langmuir-Hinshelwood,

$$F_{A0}\frac{dX}{dV} = k_{rxn}\frac{\sqrt{K_{H_2}P_{H_2}}K_{TCE}P_{TCE}}{\left(\sqrt{K_{H_2}P_{H_2}} + K_{TCE}P_{TCE} + 1\right)^2}$$

When integrated with pseudo-first-order kinetic model,

$$F_{A0}\frac{dX}{dV} = k_{rxn}C_A$$

$$C_A = \frac{F_A}{v_0} \qquad X = 1 - \frac{F_A}{F_{A0}}$$

$$F_{A0}\frac{dX}{dV} = k_{rxn}\frac{F_A}{v_0} \qquad \frac{dX}{dV} = \frac{k_{rxn}}{v_0}\frac{F_A}{F_{A0}} \qquad \frac{dX}{dV} = \frac{k_{rxn}}{v_0}(1-X)$$

$$\frac{1}{(1-X)}dX = \frac{k_{rxn}}{v_0}dV \qquad \int_0^X \frac{1}{(1-X)}dX = \int_0^V \frac{k_{rxn}}{v_0}dV$$

$$-\ln[1-X]_0^X = \frac{k_{rxn}}{v_0}V \qquad -ln(1-X) = \frac{k_{rxn}}{v_0}V$$

$$ln(1-X) = -\frac{k_{rxn}}{v_0}V$$

$$e^{-\frac{k_{rxn}}{v_0}V} = 1 - X$$

$$\boldsymbol{X = 1 - e^{-\frac{k_{rxn}}{v_0}V}}$$

From here, activation energies can be calculated using Arrhenius equations.

REFERENCES

1. Doherty, R. E., A History of the Production and Use of Carbon Tetrachloride, Tetrachloroethylene, Trichloroethylene and 1,1,1-Trichloroethane in the United States: Part 1-Historical Background; Carbon Tetrachloride and Tetrachloroethylene. *Environ. Forensics* **2000**, *1*, 69-81.
2. U.S, E. P. A., Toxicological Review of Trichloroethylene "In Support of Summary Information on the Integrated Risk Information System (IRIS)". U.S. Environmental Protection Agency: Washington, DC, 2011.
3. U.S, E. P. A., IRIS Toxicological Review of Tetrachloroethylene (Perchloroethylene) (External Review Draft). U.S. Environmental Protection Agency: Washington, DC, 2008.
4. Kleijn, R.; Tukker, A.; van der Voet, E., Chlorine in the Netherlands, Part I, An Overview. *J. Ind. Ecol.* **1997**, *1*, 95-116.
5. Tsang, W., Mechanisms for the Formation and Destruction of Chlorinated Organic Products of Incomplete Combustion. *Combust. Sci. Technol.* **1990**, *74*, 99-116.
6. Martino, M.; Rosal, R.; Sastre, H.; Díez, F. V., Hydrodechlorination of dichloromethane, trichloroethane, trichloroethylene and tetrachloroethylene over a sulfided Ni/Mo–γ-alumina catalyst. *Appl. Catal., B* **1999**, *20*, 301-307.
7. Van der Avert, P.; Weckhuysen, B. M., Low-Temperature Destruction of Chlorinated Hydrocarbons over Lanthanide Oxide Based Catalysts. *Angew. Chem.* **2002**, *114*, 4924-4926.
8. Finocchio, E.; Sapienza, G.; Baldi, M.; Busca, G., Trichloroethylene catalytic conversion over acidic solid catalysts. *Appl. Catal., B* **2004**, *51*, 143-148.
9. Den, W.; Ravindran, V.; Pirbazari, M. In *Biofiltration of chlorinated volatile organic compounds: Laboratory-scale and pilot-scale studies*, Proceedings of the AIChE Annual Meeting, 2005.
10. Johnson, R. L.; Pankow, J. F., Dissolution of dense chlorinated solvents into groundwater. 2. Source functions for pools of solvent. *Environ. Sci. Technol.* **1992**, *26*, 896-901.
11. Moran, M. J.; Zogorski, J. S.; Squillace, P. J., Chlorinated Solvents in Groundwater of the United States. *Environ. Sci. Technol.* **2006**, *41*, 74-81.
12. Russell, H. H.; Matthews, J. E.; Guy, W. S., TCE removal from contaminated soil and groundwater. *EPA Environmental Engineering Sourcebook* **1992**, 87-100.

13. Miyake, Y.; Sakoda, A.; Yamanashi, H.; Kaneda, H.; Suzuki, M., Activated carbon adsorption of trichloroethylene (TCE) vapor stripped from TCE-contaminated water. *Water Res.* **2003**, *37*, 1852-1858.
14. Blanford, W. J.; Klingel, E. J.; Johnson, G. R.; Cain, R. B.; Enfield, C.; Brusseau, M. L., Performance Assessment of In-Well Aeration for the Remediation of an Aquifer Contaminated by a Multicomponent Immiscible Liquid. **1999**, *725*, 167-181.
15. Zouboulis, A. I.; Moussas, P. A., Groundwater and Soil Pollution: Bioremediation. In *Encyclopedia of Environmental Health*, Nriagu, J. O., Ed. Elsevier: Burlington, 2011; pp 1037-1044.
16. Burkett, C. M.; Edmiston, P. L., Highly swellable sol–gels prepared by chemical modification of silanol groups prior to drying. *J. Non-Cryst. Solids* **2005**, *351*, 3174-3178.
17. Edmiston, P. L.; Underwood, L. A., Absorption of dissolved organic species from water using organically modified silica that swells. *Sep. Purif. Technol.* **2009**, *66*, 532-540.
18. Burkett, C. M.; Underwood, L. A.; Volzer, R. S.; Baughman, J. A.; Edmiston, P. L., Organic–Inorganic Hybrid Materials that Rapidly Swell in Non-Polar Liquids: Nanoscale Morphology and Swelling Mechanism. *Chem. Mater.* **2008**, *20*, 1312-1321.
19. Edmiston, P. L.; Osborne, C.; Reinbold, K. P.; Pickett, D. C.; Underwood, L. A., Pilot scale testing composite swellable organosilica nanoscale zero-valent iron-Iron-Osorb® -for *in situ* remediation of trichloroethylene. *Remediation Journal* **2011**, *22*, 105-123.
20. Ordóñez, S.; Vivas, B. P.; Diez, F. V., Minimization of the deactivation of palladium catalysts in the hydrodechlorination of trichloroethylene in wastewaters. *Appl. Catal., B* **2010**, *95*, 288-296.
21. Urbano, F. J.; Marinas, J. M., Hydrogenolysis of organohalogen compounds over palladium supported catalysts. *J. Mol. Catal. A: Chem.* **2001**, *173*, 329-345.
22. López, E.; Díez, F. V.; Ordóñez, S., Effect of organosulphur, organonitrogen and organooxygen compounds on the hydrodechlorination of tetrachloroethylene over Pd/Al_2O_3. *Appl. Catal., B* **2008**, *82*, 264-272.
23. Ordóñez, S.; Sastre, H.; Díez, F. V., Hydrodechlorination of aliphatic organochlorinated compounds over commercial hydrogenation catalysts. *Appl. Catal., B* **2000**, *25*, 49-58.
24. Ordóñez, S.; Díez, F. V.; Sastre, H., Characterisation of the deactivation of platinum and palladium supported on activated carbon used as hydrodechlorination catalysts. *Appl. Catal., B* **2001**, *31*, 113-122.
25. Elola, A.; Díaz, E.; Ordoñez, S., A new procedure for the treatment of organochlorinated off-gases combining adsorption and catalytic hydrodechlorination. *Environ. Sci. Technol.* **2009**, *43*, 1999-2004.

26. López, E.; Ordóñez, S.; Díez, F. V., Inhibition effects of organosulphur compounds on the hydrodechlorination of tetrachloroethylene over Pd/Al_2O_3 catalysts. *Catal. Today* **2003**, *84*, 121-127.
27. Ordóñez, S.; Sastre, H.; Díez, F. V., Hydrodechlorination of tetrachloroethene over Pd/Al_2O_3: influence of process conditions on catalyst performance and stability. *Appl. Catal., B* **2003**, *40*, 119-130.
28. Ordóñez, S.; Sastre, H.; Díez, F. V., Thermogravimetric determination of coke deposits on alumina-supported noble metal catalysts used as hydrodechlorination catalysts. *Thermochim. Acta* **2001**, *379*, 25-34.
29. Lowry, G. V.; Reinhard, M., Hydrodehalogenation of 1-to 3-carbon halogenated organic compounds in water using a palladium catalyst and hydrogen gas. *Environ. Sci. Technol.* **1999**, *33*, 1905-1910.
30. Lowry, G. V.; Reinhard, M., Pd-catalyzed TCE dechlorination in groundwater: Solute effects, biological control, and oxidative catalyst regeneration. *Environ. Sci. Technol.* **2000**, *34*, 3217-3223.
31. Lowry, G. V.; Reinhard, M., Pd-Catalyzed TCE Dechlorination in Water: Effect of $[H_2](aq)$ H_2-Utilizing Competitive Solutes on the TCE Dechlorination Rate and Product Distribution. *Environ. Sci. Technol.* **2001**, *35*, 696-702.
32. Munakata, N.; Reinhard, M., Palladium-catalyzed aqueous hydrodehalogenation in column reactors: Modeling of deactivation kinetics with sulfide and comparison of regenerants. *Appl. Catal., B* **2007**, *75*, 1-10.
33. Davie, M. G.; Cheng, H.; Hopkins, G. D.; LeBron, C. A.; Reinhard, M., Implementing heterogeneous catalytic dechlorination technology for remediating TCE-contaminated groundwater. *Environ. Sci. Technol.* **2008**, *42*, 8908-8915.
34. Liu; He, F.; Durham, E.; Zhao, D.; Roberts, C. B., Polysugar-Stabilized Pd Nanoparticles Exhibiting High Catalytic Activities for Hydrodechlorination of Environmentally Deleterious Trichloroethylene. *Langmuir* **2007**, *24*, 328-336.
35. Zhang, M.; Bacik, D. B.; Roberts, C. B.; Zhao, D., Catalytic hydrodechlorination of trichloroethylene in water with supported CMC-stabilized palladium nanoparticles. *Water Res.* **2013**, *47*, 3706-3715.
36. He, F.; Liu, J.; Roberts, C. B.; Zhao, D., One-Step "Green" Synthesis of Pd Nanoparticles of Controlled Size and Their Catalytic Activity for Trichloroethene Hydrodechlorination. *Ind. Eng. Chem. Res.* **2009**, *48*, 6550-6557.
37. He, F.; Zhao, D.; Paul, C., Field assessment of carboxymethyl cellulose stabilized iron nanoparticles for *in situ* destruction of chlorinated solvents in source zones. *Water Res.* **2010**, *44*, 2360-2370.
38. Nutt, M. O.; Hughes, J. B.; Wong, M. S., Designing Pd-on-Au Bimetallic Nanoparticle Catalysts for Trichloroethene Hydrodechlorination. *Environ. Sci. Technol.* **2005**, *39*, 1346-1353.

39. Nutt, M. O.; Heck, K. N.; Alvarez, P.; Wong, M. S., Improved Pd-on-Au bimetallic nanoparticle catalysts for aqueous-phase trichloroethene hydrodechlorination. *Appl. Catal., B* **2006**, *69*, 115-125.
40. Andersin, J.; Honkala, K., First principles investigations of Pd-on-Au nanostructures for trichloroethene catalytic removal from groundwater. *Phys. Chem. Chem. Phys.* **2011**, *13*, 1386-1394.
41. De Corte, S.; Hennebel, T.; Fitts, J. P.; Sabbe, T.; Bliznuk, V.; Verschuere, S.; van der Lelie, D.; Verstraete, W.; Boon, N., Biosupported Bimetallic Pd–Au Nanocatalysts for Dechlorination of Environmental Contaminants. *Environ. Sci. Technol.* **2011**, *45*, 8506-8513.
42. Hildebrand, H.; Mackenzie, K.; Kopinke, F.-D., Highly Active Pd-on-Magnetite Nanocatalysts for Aqueous Phase Hydrodechlorination Reactions. *Environ. Sci. Technol.* **2009**, *43*, 3254-3259.
43. Li, X.-q.; Elliott, D. W.; Zhang, W.-x., Zero-Valent Iron Nanoparticles for Abatement of Environmental Pollutants: Materials and Engineering Aspects. *Crit. Rev. Solid State Mater. Sci.* **2006**, *31*, 111-122.
44. Lo, I. M.; Surampalli, R. Y.; Lai, K. C., *Zero-valent iron reactive materials for hazardous waste and inorganics removal*; ASCE Publications, 2007.
45. Lien, H.-L.; Zhang, W.-X., Nanoscale Pd/Fe bimetallic particles: Catalytic effects of palladium on hydrodechlorination. *Appl. Catal., B* **2007**, *77*, 110-116.
46. Lin, C. J.; Lo, S. L.; Liou, Y. H., Dechlorination of trichloroethylene in aqueous solution by noble metal-modified iron. *J. Hazard. Mater.* **2004**, *116*, 219-228.
47. Grittini, C.; Malcomson, M.; Fernando, Q.; Korte, N., Rapid Dechlorination of Polychlorinated Biphenyls on the Surface of a Pd/Fe Bimetallic System. *Environ. Sci. Technol.* **1995**, *29*, 2898-2900.
48. Wei, J.; Xu, X.; Liu, Y.; Wang, D., Catalytic hydrodechlorination of 2,4-dichlorophenol over nanoscale Pd/Fe: Reaction pathway and some experimental parameters. *Water Res.* **2006**, *40*, 348-354.
49. Zhu, B.-W.; Lim, T.-T., Catalytic Reduction of Chlorobenzenes with Pd/Fe Nanoparticles: Reactive Sites, Catalyst Stability, Particle Aging, and Regeneration. *Environ. Sci. Technol.* **2007**, *41*, 7523-7529.
50. Wang, X.; Chen, C.; Chang, Y.; Liu, H., Dechlorination of chlorinated methanes by Pd/Fe bimetallic nanoparticles. *J. Hazard. Mater.* **2009**, *161*, 815-823.
51. Shin, E.-J.; Spiller, A.; Tavoularis, G.; A. Keane, M., Chlorine-nickel interactions in gas phase catalytic hydrodechlorination: catalyst deactivation and the nature of reactive hydrogen. *Phys. Chem. Chem. Phys.* **1999**, *1*, 3173-3181.
52. Schrick, B.; Blough, J. L.; Jones, A. D.; Mallouk, T. E., Hydrodechlorination of Trichloroethylene to Hydrocarbons Using Bimetallic Nickel−Iron Nanoparticles. *Chem. Mater.* **2002**, *14*, 5140-5147.

53. Wu, L.; Ritchie, S. M., Removal of trichloroethylene from water by cellulose acetate supported bimetallic Ni/Fe nanoparticles. *Chemosphere* **2006**, *63*, 285-92.
54. Tee, Y.-H.; Grulke, E.; Bhattacharyya, D., Role of Ni/Fe Nanoparticle Composition on the Degradation of Trichloroethylene from Water. *Ind. Eng. Chem. Res.* **2005**, *44*, 7062-7070.
55. Tee, Y.-H.; Bachas, L.; Bhattacharyya, D., Degradation of Trichloroethylene by Iron-Based Bimetallic Nanoparticles. *J. Phys. Chem. C* **2009**, *113*, 9454-9464.
56. Lin, C. J.; Liou, Y. H.; Lo, S. L., Supported Pd/Sn bimetallic nanoparticles for reductive dechlorination of aqueous trichloroethylene. *Chemosphere* **2009**, *74*, 314-9.
57. Sriwatanapongse, W.; Reinhard, M.; Klug, C. A., Reductive Hydrodechlorination of Trichloroethylene by Palladium-on-Alumina Catalyst: 13C Solid-State NMR Study of Surface Reaction Precursors. *Langmuir* **2006**, *22*, 4158-4164.
58. Kovalchuk, V. I.; d'Itri, J. L., Catalytic chemistry of chloro- and chlorofluorocarbon dehalogenation: from macroscopic observations to molecular level understanding. *Appl. Catal., A* **2004**, *271*, 13-25.
59. Rhodes, W. D.; Lázár, K.; Kovalchuk, V. I.; d'Itri, J. L., Hydrogen-Assisted 1,2-Dichloroethane Dechlorination Catalyzed by Pt–Sn/SiO_2: Effect of the Pt/Sn Atomic Ratio. *J. Catal.* **2002**, *211*, 173-182.
60. Heinrichs, B. t.; Noville, F.; Schoebrechts, J.-P.; Pirard, J.-P., Palladium–silver sol–gel catalysts for selective hydrodechlorination of 1,2-dichloroethane into ethylene: IV. Deactivation mechanism and regeneration. *J. Catal.* **2003**, *220*, 215-225.
61. Meshesha, B. T.; Barrabés, N.; Föttinger, K.; Chimentão, R. J.; Llorca, J.; Medina, F.; Rupprechter, G.; Sueiras, J. E., Gas-phase hydrodechlorination of trichloroethylene over Pd/NiMgAl mixed oxide catalysts. *Appl. Catal., B* **2012**, *117-118*, 236-245.
62. Meshesha, B. T.; Barrabés, N.; Llorca, J.; Dafinov, A.; Medina, F.; Föttinger, K., PdCu alloy nanoparticles on alumina as selective catalysts for trichloroethylene hydrodechlorination to ethylene. *Appl. Catal., A* **2013**, *453*, 130-141.
63. Barrabes, N.; Cornado, D.; Foettinger, K.; Dafinov, A.; Llorca, J.; Medina, F.; Rupprechter, G., Hydrodechlorination of trichloroethylene on noble metal promoted Cu-hydrotalcite-derived catalysts. *J. Catal.* **2009**, *263*, 239-246.
64. Ren, L.; Pan, X., Catalysts used for microwave-assisted TCE decomposition by hydrogen. *Catal. Commun.* **2011**, *12*, 1366-1369.
65. Takashima, H.; Karches, M.; Kanno, Y., Catalytic decomposition of trichloroethylene over Pt-/Ni-catalyst under microwave heating. *Appl. Surf. Sci.* **2008**, *254*, 2023-2030.
66. Jou, C.-J. G.; Hsieh, S.-C.; Lee, C.-L.; Lin, C.; Huang, H.-W., Combining zero-valent iron nanoparticles with microwave energy to treat chlorobenzene. *J. Taiwan Inst. Chem. Eng.* **2010**, *41*, 216-220.

67. Cobo, M.; González, C. A.; Sánchez, E. G.; Montes, C., Catalytic hydrodechlorination of trichloroethylene with 2-propanol over Pd/Al_2O_3. *Catal. Today* **2011**, *172*, 78-83.
68. Wo, J.-j.; Zhang, Z.; Xu, X.-h., Dechlorination mechanism of 2,4-dichlorophenol by Ni/Fe nanoparticles in the presence of humic acid. *J. Zhejiang Univ., Sci., A* **2009**, *10*, 121-126.
69. Díaz, E.; McCall, A.; Faba, L.; Sastre, H.; Ordóñez, S., Trichloroethylene Hydrodechlorination in Water Using Formic Acid as Hydrogen Source: Selection of Catalyst and Operation Conditions. *Environ. Prog. Sustainable Energy* **2013**, *32*, 1217-1222.
70. Kopinke, F.-D.; Mackenzie, K.; Koehler, R.; Georgi, A., Alternative sources of hydrogen for hydrodechlorination of chlorinated organic compounds in water on Pd catalysts. *Appl. Catal., A* **2004**, *271*, 119-128.
71. Yuan, S.; Chen, M.; Mao, X.; Alshawabkeh, A. N., Effects of reduced sulfur compounds on Pd-catalytic hydrodechlorination of trichloroethylene in groundwater by cathodic H_2 under electrochemically induced oxidizing conditions. *Environ. Sci. Technol.* **2013**, *47*, 10502-9.
72. Nishijima, W.; Ochi, Y.; Tsai, T.-Y.; Nakano, Y.; Okada, M., Catalytic hydrodechlorination of chlorinated ethylenes in organic solvents at room temperature and atmospheric pressure. *Appl. Catal., B* **2004**, *51*, 135-140.
73. Yuan, G.; Keane, M. A., Catalyst deactivation during the liquid phase hydrodechlorination of 2,4-dichlorophenol over supported Pd: influence of the support. *Catal. Today* **2003**, *88*, 27-36.
74. Barrabés, N.; Föttinger, K.; Dafinov, A.; Medina, F.; Rupprechter, G.; Llorca, J.; Sueiras, J. E., Study of $Pt–CeO_2$ interaction and the effect in the selective hydrodechlorination of trichloroethylene. *Appl. Catal., B* **2009**, *87*, 84-91.
75. Barrabés, N.; Föttinger, K.; Llorca, J.; Dafinov, A.; Medina, F.; Sá, J.; Hardacre, C.; Rupprechter, G. n., Pretreatment Effect on Pt/CeO_2 Catalyst in the selective hydrodechlorination of trichloroethylene. *J. Phys. Chem. C* **2010**, *114*, 17675-17682.
76. Navon, R.; Eldad, S.; Mackenzie, K.; Kopinke, F.-D., Protection of palladium catalysts for hydrodechlorination of chlorinated organic compounds in wastewaters. *Appl. Catal., B* **2012**, *119-120*, 241-247.
77. Kopinke, F.-D.; Angeles-Wedler, D.; Fritsch, D.; Mackenzie, K., Pd-catalyzed hydrodechlorination of chlorinated aromatics in contaminated waters—Effects of surfactants, organic matter and catalyst protection by silicone coating. *Appl. Catal., B* **2010**, *96*, 323-328.
78. Bacik, D. B.; Zhang, M.; Zhao, D.; Roberts, C. B.; Seehra, M. S.; Singh, V.; Shah, N., Synthesis and characterization of supported polysugar-stabilized palladium

nanoparticle catalysts for enhanced hydrodechlorination of trichloroethylene. *Nanotechnol.* **2012**, *23*, 294004.
79. Chen, N.; Rioux, R.; Ribeiro, F., Investigation of Reaction Steps for the Hydrodechlorination of Chlorine-Containing Organic Compounds on Pd Catalysts. *J. Catal.* **2002**, *211*, 192-197.
80. Reinhard, M.; Semadeni, M.; Sharma, P. K.; Haag, W. R., Dehalogenation of haloaliphatic hydrocarbon compounds in the aquatic and terrestrial environment. *Bioremediation of Contaminated Soils* **1999**, 133-174.
81. Edmiston, P. L. Swellable sol-gels, methods of making, and use thereof. US8119759 B2, 2012.
82. Edmiston, P. L. Swellable materials and methods of use US 8,367,793 B2, 2013.
83. Miller, F. A., Misassignment of the strong Raman band near 1000 cm^{-1} in some substituted benzenes, and the Herzberg versus Wilson convention for numbering the vibrations of benzene. *J. Raman Spectrosc.* **1988**, *19*, 219-221.
84. Oriero, D. A.; Weakley, A. T.; Aston, D. E., Rheological and micro-Raman time-series characterization of enzyme sol–gel solution toward morphological control of electrospun fibers. *Sci. Technol. Adv. Mater.* **2016**.
85. Colthup, N., *Introduction to infrared and Raman spectroscopy*; Elsevier, 2012.
86. Martinelli, A., Effects of a Protic Ionic Liquid on the Reaction Pathway during Non-Aqueous Sol–Gel Synthesis of Silica: A Raman Spectroscopic Investigation. *Int. J. Mol. Sci.* **2014**, *15*, 6488-6503.
87. Bertoluzza, A.; Fagnano, C.; Morelli, M. A.; Gottardi, V.; Guglielmi, M., Raman and infrared spectra on silica gel evolving toward glass. *J. Non-Cryst. Solids* **1982**, *48*, 117-128.
88. Lorenzi, R.; Brovelli, S.; Meinardi, F.; Lauria, A.; Chiodini, N.; Paleari, A., Role of sol-gel networking and fluorine doping in the silica Urbach energy. *J. Non-Cryst. Solids* **2011**, *357*, 1838-1841.
89. Little, D. J.; Ams, M.; Dekker, P.; Marshall, G. D.; Dawes, J. M.; Withford, M. J., Femtosecond laser modification of fused silica: the effect of writing polarization on Si-O ring structure. *Opt. Express* **2008**, *16*, 20029-20037.
90. Socrates, G., *Infrared and Raman characteristic group frequencies: tables and charts*; John Wiley & Sons, 2004.
91. Morrow, B. A., The Raman spectrum of chemisorbed methanol on silica. A comparison with the infrared technique. *J. Phys. Chem.* **1977**, *81*, 2663-2666.
92. Launer, P. J., Infrared analysis of organosilicon compounds: spectra-structure correlations. *Silicone compounds register and review* **1987**, *100*.
93. Galeener, F.; Lucovsky, G., Longitudinal Optical Vibrations in Glasses: GeO_2 and SiO_2. *Phys. Rev. Lett.* **1976**, *37*, 1474-1478.

94. Payne, M.; Inkson, J., Longitudinal-optic-transverse-optic vibrational mode splittings in tetrahedral network glasses. *J. Non-Cryst. Solids* **1984**, *68*, 351-360.
95. De Leeuw, S.; Thorpe, M. F., Coulomb splittings in glasses. *Phys. Rev. Lett.* **1985**, *55*, 2879.
96. Almeida, R. M.; Pantano, C. G., Structural investigation of silica gel films by infrared spectroscopy. *J. Appl. Phys.* **1990**, *68*, 4225-4232.
97. Lin-Vien, D.; Colthup, N. B.; Fateley, W. G.; Grasselli, J. G., *The handbook of infrared and Raman characteristic frequencies of organic molecules*; Elsevier, 1991.
98. Watanabe, H.; Hosoi, T., Fundamental Aspects of Silicon Carbide Oxidation. *Phys. Technol. Silicon Carbide Devices* **2013**, 235-250.
99. Kim, M.; Kim, J., Development of high power and energy density microsphere silicon carbide–MnO_2 nanoneedles and thermally oxidized activated carbon asymmetric electrochemical supercapacitors. *Phys. Chem. Chem. Phys.* **2014**, *16*, 11323-11336.
100. Yamashita, A.; Sato, Y.; Tsukamoto, T.; Suda, Y., p-Cu_2O/SiC_xO_y/n-SiC/n-Si memory diode having resistive nonvolatile memory and rectifying behaviors. *Appl. Phys. Express* **2014**, *7*, 074203.
101. Wojcieszak, R.; Ghazzal, M.; Gaigneaux, E. M.; Ruiz, P., Low temperature oxidation of methanol to methyl formate over Pd nanoparticles supported on γ-Fe_2O_3. *Catal. Sci. Technol.* **2014**, *4*, 738-745.
102. Wang, D.; Lu, S.; Kulesza, P. J.; Li, C. M.; De Marco, R.; Jiang, S. P., Enhanced oxygen reduction at Pd catalytic nanoparticles dispersed onto heteropolytungstate-assembled poly (diallyldimethylammonium)-functionalized carbon nanotubes. *Phys. Chem. Chem. Phys.* **2011**, *13*, 4400-4410.
103. Liu, X.; Xu, G.; Chen, Y.; Lu, T.; Tang, Y.; Xing, W., A Strategy for Fabricating Porous PdNi@ Pt Core-shell Nanostructures and Their Enhanced Activity and Durability for the Methanol Electrooxidation. *Scientific reports* **2015**, *5*.
104. Iacopi, F.; Beyer, G.; Travaly, Y.; Waldfried, C.; Gage, D. M.; Dauskardt, R. H.; Houthoofd, K.; Jacobs, P.; Adriaensens, P.; Schulze, K., Thermomechanical properties of thin organosilicate glass films treated with ultraviolet-assisted cure. *Acta Mater.* **2007**, *55*, 1407-1414.
105. Rulkens, R.; Ni, Y.; Manners, I., Living anionic ring-opening polymerization of silicon-bridged [1] ferrocenophanes: synthesis and characterization of poly (ferrocenylsilane)-polysiloxane block copolymers. *J. Am. Chem. Soc.* **1994**, *116*, 12121-12122.
106. Mabboux, P.-Y.; Gleason, K. K., Chemical Bonding Structure of Low Dielectric Constant Si:O:C:H Films Characterized by Solid-State NMR. *J. Electrochem. Soc.* **2005**, *152*, F7-F13.

107. Yang, J. J.; El-Nahhal, I. M.; Chuang, I.-S.; Maciel, G. E., Synthesis and solid-state NMR structural characterization of polysiloxane-immobilized amine ligands and their metal complexes. *J. Non-Cryst. Solids* **1997**, *209*, 19-39.
108. Shimojima, A.; Mochizuki, D.; Kuroda, K., Synthesis of silylated derivatives of a layered polysilicate kanemite with mono-, di-, and trichloro (alkyl) silanes. *Chem. Mater.* **2001**, *13*, 3603-3609.
109. Choi, S.; Kim, Y.; Kim, I.; Ha, C.-S., Effect of organosilica isomers on the interfacial interaction in polyimide/aromatic organosilica hybrids. *J. Appl. Polym. Sci.* **2007**, *103*, 2507-2513.
110. Kast, P.; Friedrich, M.; Teschner, D.; Girgsdies, F.; Lunkenbein, T.; Naumann d'Alnoncourt, R.; Behrens, M.; Schlögl, R., CO oxidation as a test reaction for strong metal–support interaction in nanostructured Pd/FeO_x powder catalysts. *Appl. Catal., A* **2015**, *502*, 8-17.
111. Mahata, N.; Vishwanathan, V., Influence of Palladium Precursors on Structural Properties and Phenol Hydrogenation Characteristics of Supported Palladium Catalysts. *J. Catal.* **2000**, *196*, 262-270.
112. Somboonthanakij, S.; Mekasuwandumrong, O.; Panpranot, J.; Nimmanwudtipong, T.; Strobel, R.; Pratsinis, S. E.; Praserthdam, P., Characteristics and Catalytic Properties of Pd/SiO_2 Synthesized by One-step Flame Spray Pyrolysis in Liquid-phase Hydrogenation of 1-Heptyne. *Catal. Lett.* **2007**, *119*, 346-352.
113. Verho, O.; Zheng, H.; Gustafson, K. P. J.; Nagendiran, A.; Zou, X.; Bäckvall, J.-E., Application of Pd Nanoparticles Supported on Mesoporous Hollow Silica Nanospheres for the Efficient and Selective Semihydrogenation of Alkynes. *ChemCatChem* **2016**, *8*, 773-778.
114. Wu, K.; Qian, X.; Chen, L.; Xu, Z.; Zheng, S.; Zhu, D., Effective liquid phase hydrodechlorination of diclofenac catalysed by Pd/CeO_2. *RSC Adv.* **2015**, *5*, 18702-18709.
115. Comandella, D.; Woszidlo, S.; Georgi, A.; Kopinke, F.-D.; Mackenzie, K., Efforts for long-term protection of palladium hydrodechlorination catalysts. *Appl. Catal., B* **2016**, *186*, 204-211.
116. Ardila A, A. N.; Reyes, J.; Arriola, E.; Hernández, J. A.; Fuentes, G. A., Liquid-phase chloroform hydrodechlorination catalyzed by Pd/TiO_2-Na. *Appl. Catal., A* **2015**, *497*, 211-215.
117. Choi, H.; Lawal, W.; Al-Abed, S. R., Desorption, partitioning, and dechlorination characteristics of PCBs in sediments in interaction with reactive activated carbon. *J. Hazard. Mater.* **2015**, *287*, 118-25.
118. Haryanto, A.; Ferno, S.; Murali, N.; Adhikari, S., Current status of hydrogen production techniques by steam reforming of ethanol: A Review. *Energy Fuels* **2005**, *19*, 2098-2106.

119. Mehta, V.; Cooper, J. S., Review and analysis of PEM fuel cell design and manufacturing. *J. Power Sources* **2003**, *114*, 32-53.
120. Das, D.; Veziroğlu, T. N., Hydrogen production by biological processes: a survey of literature. *Int. J. Hydrogen Energy* **2001**, *26*, 13-28.
121. Biswas, P.; Kunzru, D., Steam reforming of ethanol on Ni–CeO_2–ZrO_2 catalysts: Effect of doping with copper, cobalt and calcium *Catal. Lett.* **2007**, *118*, 36-49.
122. Song, H.; Zhang, L.; Watson, R.; Braden, D.; Ozkan, U., Investigation of bio-ethanol steam reforming over cobalt-based catalysts. *Catal. Today* **2007**, *129*, 346-354.
123. Song, H.; Bao, X.; Hadad, C. M.; Ozkan, U. S., Adsorption/Desorption Behavior of Ethanol Steam Reforming Reactants and Intermediates over Supported Cobalt Catalysts. *Catal. Lett.* **2011**, *141*, 43-54.
124. Nishiguchi, T.; Matsumoto, T.; Kanai, H.; Utani, K.; Matsumura, Y.; Shen, W.-J.; Imamura, S., Catalytic steam reforming of ethanol to produce hydrogen and acetone. *Appl. Catal., A* **2005**, *279*, 273-277.
125. de Lima, S. M.; da Cruz, I. O.; Jacobs, G.; Davis, B. H.; Mattos, L. V.; Noronha, F. B., Steam reforming, partial oxidation, and oxidative steam reforming of ethanol over Pt/$CeZrO_2$ catalyst. *J. Catal.* **2008**, *257*, 356-368.
126. de Lima, S. M.; Silva, A. M.; Graham, U. M.; Jacobs, G.; Davis, B. H.; Mattos, L. V.; Noronha, F. B., Ethanol decomposition and steam reforming of ethanol over $CeZrO_2$ and Pt/$CeZrO_2$ catalyst: Reaction mechanism and deactivation. *Appl. Catal., A* **2009**, *352*, 95-113.
127. Salge, J. R.; Deluga, G. A.; Schmidt, L. D., Catalytic partial oxidation of ethanol over noble metal catalysts. *J. Catal.* **2005**, *235*, 69-78.
128. Breen, J. P.; Burch, R.; Coleman, H. M., Metal-catalysed steam reforming of ethanol in the production of hydrogen for fuel cell applications. *Appl. Catal., B* **2002**, *39*, 65-74.
129. Diagne, C.; Idriss, H.; Pearson, K.; Gómez-García, M. A.; Kiennemann, A., Efficient hydrogen production by ethanol reforming over Rh catalysts. Effect of addition of Zr on CeO_2 for the oxidation of CO to CO_2. *C. R. Chim.* **2004**, *7*, 617-622.
130. de Lima, S. M.; Silva, A. M.; da Cruz, I. O.; Jacobs, G.; Davis, B. H.; Mattos, L. V.; Noronha, F. B., H_2 production through steam reforming of ethanol over Pt/ZrO_2, Pt/CeO_2 and Pt/$CeZrO_2$ catalysts. *Catal. Today* **2008**, *138*, 162-168.
131. Scott, M.; Goeffroy, M.; Chiu, W.; Blackford, M. A.; Idriss, H., Hydrogen Production from Ethanol over Rh-Pd/CeO_2 Catalysts. *Top. Catal.* **2008**, *51*, 13-21.
132. Cavallaro, S.; Chiodo, V.; Vita, A.; Freni, S., Hydrogen production by auto-thermal reforming of ethanol on Rh/Al_2O_3 catalyst. *J. Power Sources* **2003**, *123*, 10-16.
133. Sheng, P. Y.; Chiu, W. W.; Yee, A.; Morrison, S. J.; Idriss, H., Hydrogen production from ethanol over bimetallic Rh-M/CeO_2 (M=Pd or Pt). *Catal. Today* **2007**, *129*, 313-321.

134. Zhang, B.; Cai, W.; Li, Y.; Xu, Y.; Shen, W., Hydrogen production by steam reforming of ethanol over an Ir/CeO_2 catalyst: Reaction mechanism and stability of the catalyst. *Int. J. Hydrogen Energy* **2008**, *33*, 4377-4386.
135. Erdohelyi, A.; Rasko, J.; Kecskse, T.; Toth, M.; Domok, M.; Baan, K., Hydrogen formation in ethanol reforming on supported noble metal catalysts. *Catal. Today* **2006**, *116*, 367-376.
136. Kourtelesis, M.; Panagiotopoulou, P.; Verykios, X. E., Influence of structural parameters on the reaction of low temperature ethanol steam reforming over Pt/Al_2O_3 catalysts. *Catal. Today* **2015**, *258*, 247-255.
137. Aupretre, F.; Descorme, C.; Duprez, D., Bio-ethanol catalytic steam reforming over supported metal catalysts. *Catal. Commun.* **2002**, *3*, 263-267.
138. Frusteri, F.; Freni, S.; Spadaro, L.; Chiodo, V.; Bonura, G.; Donato, S.; Cavallaro, S., H_2 production for MC fuel cell by steam reforming of ethanol over MgO supported Pd, Rh, Ni and Co catalysts. *Catal. Commun.* **2004**, *5*, 611-615.
139. Fierro, V.; Akdim, O.; Mirodatos, C., On-board hydrogen production in a hybrid electric vehicle by bio-ethanol oxidative steam reforming over Ni and noble metal based catalysts. *Green Chem.* **2003**, *5*, 20-24.
140. Hou, T.; Yu, B.; Zhang, S.; Xu, T.; Wang, D.; Cai, W., Hydrogen production from ethanol steam reforming over Rh/CeO_2 catalyst. *Catal. Commun.* **2015**, *58*, 137-140.
141. Sheng, P. Y.; Yee, A.; Bowmaker, G. A.; Idriss, H., H_2 Production from Ethanol over $Rh-Pt/CeO_2$ Catalysts: The Role of Rh for the Efficient Dissociation of the Carbon-Carbon Bond. *J. Catal.* **2002**, *208*, 393-403.
142. Cifuentes, B.; Valero, M.; Conesa, J.; Cobo, M., Hydrogen Production by Steam Reforming of Ethanol on Rh-Pt Catalysts: Influence of CeO_2, ZrO_2, and La_2O_3 as Supports. *Catalysts* **2015**, *5*, 1872-1896.
143. Divins, N. J.; Casanovas, A.; Xu, W.; Senanayake, S. D.; Wiater, D.; Trovarelli, A.; Llorca, J., The influence of nano-architectured CeOx supports in $RhPd/CeO_2$ for the catalytic ethanol steam reforming reaction. *Catal. Today* **2015**, *253*, 99-105.
144. Mondal, T.; Pant, K. K.; Dalai, A. K., Catalytic oxidative steam reforming of bio-ethanol for hydrogen production over Rh promoted $Ni/CeO_2–ZrO_2$ catalyst. *Int. J. Hydrogen Energy* **2015**, *40*, 2529-2544.
145. Kugai, J.; Velu, S.; Song, C., Low-temperature reforming of ethanol over CeO_2-supported Ni-Rh bimetallic catalysts for hydrogen production. *Catal. Lett.* **2005**, *101*, 255-264.
146. Pereira, E. B.; Homs, N.; Marti, S.; Fierro, J. L. G.; Ramirez de la Piscina, P., Oxidative steam-reforming of ethanol over Co/SiO_2, $Co-Rh/SiO_2$ and Co–Ru/SiO_2 catalysts: Catalytic behavior and deactivation/regeneration processes. *J. Catal.* **2008**, *257*, 206-214.

147. Varga, E.; Ferencz, Z.; Oszkó, A.; Erdőhelyi, A.; Kiss, J., Oxidation states of active catalytic centers in ethanol steam reforming reaction on ceria based Rh promoted Co catalysts: An XPS study. *J. Mol. Catal. A: Chem.* **2015**, *397*, 127-133.
148. Llorca, J.; Homs, N.; Sales, J.; de la Piscina, P. R., Efficient Production of Hydrogen over Supported Cobalt Catalysts from Ethanol Steam Reforming. *J. Catal.* **2002**, *209*, 306-317.
149. Li, S.; Li, M.; Zhang, C.; Wang, S.; Ma, X.; Gong, J., Steam reforming of ethanol over Ni/ZrO_2 catalysts: Effect of support on product distribution. *Int. J. Hydrogen Energy* **2012**, *37*, 2940-2949.
150. Grzegorczyk, W.; Denis, A.; Gac, W.; Ioannides, T.; Machocki, A., Hydrogen Formation via Steam Reforming of Ethanol Over Cu/ZnO Catalyst Modified with Nickel, Cobalt and Manganese. *Catal. Lett.* **2009**, *128*, 443-448.
151. Chen, L.-C.; Lin, S. D., Effects of the pretreatment of $CuNi/SiO_2$ on ethanol steam reforming: Influence of bimetal morphology. *Appl. Catal., B* **2014**, *148-149*, 509-519.
152. Han, S. J.; Song, J. H.; Bang, Y.; Yoo, J.; Park, S.; Kang, K. H.; Song, I. K., Hydrogen production by steam reforming of ethanol over mesoporous $Cu–Ni–Al_2O_3–ZrO_2$ xerogel catalysts. *Int. J. Hydrogen Energy* **2016**, *41*, 2554-2563.
153. Carvalho, F. L. S.; Asencios, Y. J. O.; Bellido, J. D. A.; Assaf, E. M., Bio-ethanol steam reforming for hydrogen production over Co_3O_4/CeO_2 catalysts synthesized by one-step polymerization method. *Fuel Process. Technol.* **2016**, *142*, 182-191.
154. Vaidya, P. D.; Rodrigues, A. E., Insight into steam reforming of ethanol to produce hydrogen for fuel cells. *Chem. Eng. J. (Lausanne)* **2006**, *117*, 39-49.
155. Llorca, J.; Dalmon, J.-A.; Ramirez de la Piscina, P.; Homs, N., *In situ* magnetic characterisation of supported cobalt catalysts under steam-reforming of ethanol. *Appl. Catal., A* **2003**, *243*, 261-269.
156. Llorca, J.; de la Piscina, P. R.; Dalmon, J.-A.; Sales, J.; Homs, N., CO-free hydrogen from steam-reforming of bioethanol over ZnO-supported cobalt catalysts. *Appl. Catal., B* **2003**, *43*, 355-369.
157. Llorca, J.; Homs, N.; Sales, J.; Fierro, J.; Luis, G.; Ramirez de la Piscina, P., Effect of sodium addition on the performance of Co-ZnO-based catalysts for hydrogen production from bioethanol. *J. Catal.* **2004**, *222*, 470-480.
158. Llorca, J.; Piscina, P. R. d. l.; Dalmon, J.-A.; Homs, N., Transformation of Co_3O_4 during Ethanol Steam-Re-forming. Activation Process for Hydrogen Production. *Chem. Mater.* **2004**, *16*, 3573-3578.
159. Batista, M. S.; Santos, R. K. S.; Assaf, E. M.; Assaf, J. M.; Ticianelli, E. A., Characterization of the activity and stability of supported cobalt catalysts for the steam reforming of ethanol. *J. Power Sources* **2003**, *124*, 99-103.

160. Batista, M. S.; Santos, R. K. S.; Assaf, E. M.; Assaf, J. M.; Ticianelli, E. A., High efficiency steam reforming of ethanol by cobalt-based catalysts. *J. Power Sources* **2004**, *134*, 27-32.
161. Profeti, L. P. R.; Ticianelli, E. A.; Assaf, E. M., Production of hydrogen by ethanol steam reforming on Co/Al_2O_3 catalysts: Effect of addition of small quantities of noble metals. *J. Power Sources* **2008**, *175*, 482-489.
162. Benito, M.; Padilla, R.; Rodríguez, L.; Sanz, J. L.; Daza, L., Zirconia supported catalysts for bioethanol steam reforming: Effect of active phase and zirconia structure. *J. Power Sources* **2007**, *169*, 167-176.
163. Sun, J.; Karim, A. M.; Mei, D.; Engelhard, M.; Bao, X.; Wang, Y., New insights into reaction mechanisms of ethanol steam reforming on $Co–ZrO_2$. *Appl. Catal., B* **2015**, *162*, 141-148.
164. Kaddouri, A.; Mazzocchia, C., A study of the influence of the synthesis conditions upon the catalytic properties of Co/SiO_2 or Co/Al_2O_3 catalysts used for ethanol steam reforming. *Catal. Commun.* **2004**, *5*, 339-345.
165. Wang, H.; Liu, Y.; Wang, L.; Qin, Y. N., Study on the carbon deposition in steam reforming of ethanol over Co/CeO_2 catalyst. *Chem. Eng. J. (Lausanne)* **2008**, *145*, 25-31.
166. Martono, E.; Vohs, J. M., Support effects in cobalt-based ethanol steam reforming catalysts: Reaction of ethanol on Co/CeO_2/YSZ(100) model catalysts. *J. Catal.* **2012**, *291*, 79-86.
167. Karim, A. M.; Su, Y.; Engelhard, M. H.; King, D. L.; Wang, Y., Catalytic roles of Co^0 and Co^{2+} during steam reforming of ethanol on Co/MgO catalysts. *ACS Catal.* **2011**, *1*, 279-286.
168. Torres, J. A.; Llorca, J.; Casanovas, A.; Dominguez, M.; Salvado, J.; Montane, D., Steam reforming of ethanol at moderate temperature: Multifactorial design analysis of Ni/La_2O_3-Al_2O_3, and Fe- and Mn-promoted Co/ZnO catalysts. *J. Power Sources* **2007**, *169*, 158-166.
169. Yu, N.; Zhang, H.; Davidson, S. D.; Sun, J.; Wang, Y., Effect of ZnO facet on ethanol steam reforming over Co/ZnO. *Catal. Commun.* **2016**, *73*, 93-97.
170. Haga, F.; Nakajima, T.; Miya, H.; Mishima, S., Catalytic properties of supported cobalt catalysts for steam reforming of ethanol. *Catal. Lett.* **1997**, *48*, 223-227.
171. Moura, J. S.; Souza, M. O. G.; Bellido, J. D. A.; Assaf, E. M.; Opportus, M.; Reyes, P.; Rangel, M. d. C., Ethanol steam reforming over rhodium and cobalt-based catalysts: Effect of the support. *Int. J. Hydrogen Energy* **2012**, *37*, 3213-3224.
172. Trovarelli, A.; de Leitenburg, C.; Boaro, M.; Dolcetti, G., The utilization of ceria in industrial catalysis. *Catal. Today* **1999**, *50*, 353-367.
173. Yamasue, E.; Okumura, H.; Ishihara, K. N., Thermal Stability and Catalytic Performance of Pd, Pt and Rh Loaded on $CuO–CeO_2–Al_2O_3$ Support for Three-Way Catalysts. In *Zero-Carbon Energy Kyoto 2012*, Springer: 2013; pp 167-177.

174. Diwell, A.; Rajaram, R.; Shaw, H.; Truex, T., The role of ceria in three-way catalysts. *Stud. Surf. Sci. Catal.* **1991**, *71*, 139-152.
175. Kim, G., Ceria-promoted three-way catalysts for auto exhaust emission control. *Ind. Eng. Chem. Prod. Res. Dev.* **1982**, *21*, 267-274.
176. Trovarelli, A., Catalytic properties of ceria and CeO_2-containing materials. *Catal. Rev.-Sci. Eng.* **1996**, *38*, 439-520.
177. Lin, R.; Cao, C.; Zhang, H.; Huang, H.; Ma, J., Electro-catalytic activity of enhanced CO tolerant cerium-promoted Pt/C catalyst for PEM fuel cell anode. *Int. J. Hydrogen Energy* **2012**, *37*, 4648-4656.
178. Yang, F.; Graciani, J.; Evans, J.; Liu, P.; Hrbek, J.; Sanz, J. F.; Rodriguez, J. A., CO oxidation on inverse CeO(x)/Cu(111) catalysts: high catalytic activity and ceria-promoted dissociation of O_2. *J. Am. Chem. Soc.* **2011**, *133*, 3444-3451.
179. Torrente-Murciano, L.; Gilbank, A.; Puertolas, B.; Garcia, T.; Solsona, B.; Chadwick, D., Shape-dependency activity of nanostructured CeO_2 in the total oxidation of polycyclic aromatic hydrocarbons. *Appl. Catal., B* **2013**, *132-133*, 116-122.
180. Laosiripojana, N.; Assabumrungrat, S., Catalytic dry reforming of methane over high surface area ceria. *Appl. Catal., B* **2005**, *60*, 107-116.
181. da Silva, A. M.; de Souza, K. R.; Mattos, L. V.; Jacobs, G.; Davis, B. H.; Noronha, F. B., The effect of support reducibility on the stability of Co/CeO_2 for the oxidative steam reforming of ethanol. *Catal. Today* **2011**, *164*, 234-239.
182. Song, H.; Ozkan, U., Ethanol steam reforming over Co-based catalysts: Role of oxygen mobility. *J. Catal.* **2009**, *261*, 66-74.
183. Song, H.; Ozkan, U. S., Changing the Oxygen Mobility in Co/Ceria Catalysts by Ca Incorporation: Implications for Ethanol Steam Reforming. *J. Phys. Chem. A* **2010**, *114*, 3796-3801.
184. Song, H.; Tan, B.; Ozkan, U. S., Novel Synthesis Techniques for Preparation of Co/CeO_2 as Ethanol Steam Reforming Catalysts. *Catal. Lett.* **2009**, *132*, 422-429.
185. Lin, S. S. Y.; Kim, D. H.; Ha, S. Y., Metallic phases of cobalt-based catalysts in ethanol steam reforming: The effect of cerium oxide. *Appl. Catal., A* **2009**, *355*, 69-77.
186. Laosiripojana, N.; Assabumrungrat, S., Catalytic steam reforming of ethanol over high surface area CeO_2: The role of CeO_2 as an internal pre-reforming catalyst. *Appl. Catal., B* **2006**, *66*, 29-39.
187. Liu, Y.; Murata, K.; Inaba, M., Steam Reforming of Bio-Ethanol to Produce Hydrogen over Co/CeO_2 Catalysts Derived from $Ce_{1-x}Co_xO_{2-y}$ Precursors. *Catalysts* **2016**, *6*, 26.
188. Srisiriwat, N.; Therdthianwong, S.; Therdthianwong, A., Oxidative steam reforming of ethanol over Ni/Al_2O_3 catalysts promoted by CeO_2, ZrO_2 and CeO_2-ZrO_2. *Int. J. Hydrogen Energy* **2009**, *34*, 2224-2234.

189. Biswas, P.; Kunzru, D., Steam reforming of ethanol for production of hydrogen over Ni/CeO_2–ZrO_2 catalyst: Effect of support and metal loading. *Int. J. Hydrogen Energy* **2007**, *32*, 969-980.
190. Osorio-Vargas, P.; Campos, C. H.; Navarro, R. M.; Fierro, J. L. G.; Reyes, P., Rh/Al_2O_3–La_2O_3 catalysts promoted with CeO_2 for ethanol steam reforming reaction. *J. Mol. Catal. A: Chem.* **2015**, *407*, 169-181.
191. Sun, C.; Li, H.; Chen, L., Nanostructured ceria-based materials: synthesis, properties, and applications. *Energy Environ. Sci.* **2012**, *5*, 8475.
192. Yu, S.-W.; Huang, H.-H.; Tang, C.-W.; Wang, C.-B., The effect of accessible oxygen over Co_3O_4–CeO_2 catalysts on the steam reforming of ethanol. *Int. J. Hydrogen Energy* **2014**, *39*, 20700-20711.
193. Liang, C.; Ma, Z.; Lin, H.; Ding, L.; Qiu, J.; Frandsen, W.; Su, D., Template preparation of nanoscale $Ce_xFe_{1-x}O_2$ solid solutions and their catalytic properties for ethanol steam reforming. *J. Mater. Chem.* **2009**, *19*, 1417-1424.
194. Anupriya, K.; Vivek, E.; Subramanian, B., Facile synthesis of ceria nanoparticles by precipitation route for UV blockers. *J. Alloys Compd.* **2014**, *590*, 406-410.
195. Shih, S.-J.; Tzeng, W.-L.; Kuo, W.-L., Fabrication of ceria particles using glycine nitrate spray pyrolysis. *Surf. Coat. Technol.* **2014**, *259*, 302-309.
196. Christensen, J. M.; Deiana, D.; Grunwaldt, J.-D.; Jensen, A. D., Ceria Prepared by Flame Spray Pyrolysis as an Efficient Catalyst for Oxidation of Diesel Soot. *Catal. Lett.* **2014**, *144*, 1661-1666.
197. Hirano, M.; Inagaki, M., Preparation of monodispersed cerium (IV) oxide particles by thermal hydrolysis: influence of the presence of urea and Gd doping on their morphology and growth. *J. Mater. Chem.* **2000**, *10*, 473-477.
198. Bumajdad, A.; Zaki, M. I.; Eastoe, J.; Pasupulety, L., Microemulsion-based synthesis of CeO_2 powders with high surface area and high-temperature stabilities. *Langmuir* **2004**, *20*, 11223-11233.
199. Charojrochkul, S.; Nualpaeng, W.; Laosiripojana, N.; Assabumrungrat, S., Materials Challenges and Testing for Supply of Energy and Resources. Springer: Berlin, Germany: 2012.
200. Derakhshandeh, P. G.; Soleimannejad, J.; Janczak, J., Sonochemical synthesis of a new nano-sized cerium(III) coordination polymer and its conversion to nanoceria. *Ultrason. Sonochem.* **2015**, *26*, 273-80.
201. Cui, M. Y.; He, J. X.; Lu, N. P.; Zheng, Y. Y.; Dong, W. J.; Tang, W. H.; Chen, B. Y.; Li, C. R., Morphology and size control of cerium carbonate hydroxide and ceria micro/nanostructures by hydrothermal technology. *Mater. Chem. Phys.* **2010**, *121*, 314-319.
202. Zawadzki, M., Preparation and characterization of ceria nanoparticles by microwave-assisted solvothermal process. *J. Alloys Compd.* **2008**, *454*, 347-351.

203. Zhang, D.; Niu, F.; Li, H.; Shi, L.; Fang, J., Uniform ceria nanospheres: Solvothermal synthesis, formation mechanism, size-control and catalytic activity. *Powder Technol.* **2011**, *207*, 35-41.
204. Abbasi, Z.; Haghighi, M.; Fatehifar, E.; Rahemi, N., Comparative synthesis and physicochemical characterization of CeO_2 nanopowder via redox reaction, precipitation and sol–gel methods used for total oxidation of toluene. *Asia-Pacific Journal of Chemical Engineering* **2012**, *7*, 868-876.
205. Zhou, X. D.; Huebner, W., Size-induced lattice relaxation in CeO_2 nanoparticles. *Appl. Phys. Lett.* **2001**, *79*, 3512-3514.
206. Deshpande, S.; Patil, S.; Kuchibhatla, S. V. N. T.; Seal, S., Size dependency variation in lattice parameter and valency states in nanocrystalline cerium oxide. *Appl. Phys. Lett.* **2005**, *87*, 133113.
207. Zhang, F.; Chan, S.-W.; Spanier, J. E.; Apak, E.; Jin, Q.; Robinson, R. D.; Herman, I. P., Cerium oxide nanoparticles: size-selective formation and structure analysis. *Appl. Phys. Lett.* **2002**, *80*, 127-129.
208. Yi, N.; Si, R.; Saltsburg, H.; Flytzani-Stephanopoulos, M., Active gold species on cerium oxide nanoshapes for methanol steam reforming and the water gas shift reactions. *Energy Environ. Sci.* **2010**, *3*, 831-837.
209. Si, R.; Flytzani-Stephanopoulos, M., Shape and crystal-plane effects of nanoscale ceria on the activity of Au-CeO_2 catalysts for the water-gas shift reaction. *Angew. Chem.-Int. Edit.* **2008**, *47*, 2884-2887.
210. Yi, N.; Si, R.; Saltsburg, H.; Flytzani-Stephanopoulos, M., Steam reforming of methanol over ceria and gold-ceria nanoshapes. *Appl. Catal., B* **2010**, *95*, 87-92.
211. Lee, Y.; He, G.; Akey, A. J.; Si, R.; Flytzani-Stephanopoulos, M.; Herman, I. P., Raman analysis of mode softening in nanoparticle CeO(2-delta) and Au-CeO(2-delta) during CO oxidation. *J. Am. Chem. Soc.* **2011**, *133*, 12952-5.
212. Boucher, M. B.; Goergen, S.; Yi, N.; Flytzani-Stephanopoulos, M., 'Shape effects' in metal oxide supported nanoscale gold catalysts. *Phys. Chem. Chem. Phys.* **2011**, *13*, 2517-2527.
213. Soykal, I. I.; Bayram, B.; Sohn, H.; Gawade, P.; Miller, J. T.; Ozkan, U. S., Ethanol steam reforming over Co/CeO_2 catalysts: Investigation of the effect of ceria morphology. *Appl. Catal., A* **2012**, *449*, 47-58.
214. Soykal, I. I.; Sohn, H.; Ozkan, U. S., Effect of Support Particle Size in Steam Reforming of Ethanol over Co/CeO_2Catalysts. *ACS Catal.* **2012**, *2*, 2335-2348.
215. Jensen, J. R.; Johannessen, T.; Livbjerg, H., An improved N_2O-method for measuring Cu-dispersion. *Appl. Catal., A* **2004**, *266*, 117-122.
216. Jacobs, G.; Ji, Y.; Davis, B. H.; Cronauer, D.; Kropf, A. J.; Marshall, C. L., Fischer–Tropsch synthesis: Temperature programmed EXAFS/XANES investigation of the

influence of support type, cobalt loading, and noble metal promoter addition to the reduction behavior of cobalt oxide particles. *Appl. Catal., A* **2007**, *333*, 177-191.
217. Song, H.; Ozkan, U. S., The role of impregnation medium on the activity of ceria-supported cobalt catalysts for ethanol steam reforming. *J. Mol. Catal. A: Chem.* **2010**, *318*, 21-29.
218. Bayram, B.; Soykal, I. I.; von Deak, D.; Miller, J. T.; Ozkan, U. S., Ethanol steam reforming over Co-based catalysts: Investigation of cobalt coordination environment under reaction conditions. *J. Catal.* **2011**, *284*, 77-89.
219. Pena O'Shea, d. l. V. A.; Homs, N.; Pereira, E.; Nafria, R.; Piscina, P. R. d. l., X-ray diffraction study of Co_3O_4 activation under ethanol steam-reforming. *Catal. Today* **2007**, *126*, 148-152.
220. Kissinger, H. E., Reaction kinetics in differential thermal analysis. *Anal. Chem.* **1957**, *29*, 1702-1706.
221. Zhou, K.; Wang, X.; Sun, X.; Peng, Q.; Li, Y., Enhanced catalytic activity of ceria nanorods from well-defined reactive crystal planes. *J. Catal.* **2005**, *229*, 206-212.
222. Laachir, A., et al., REDUCTION OF CEO2 BY HYDROGEN - MAGNETIC-SUSCEPTIBILITY AND FOURIER-TRANSFORM INFRARED, ULTRAVIOLET AND X-RAY PHOTOELECTRON-SPECTROSCOPY MEASUREMENTS. *J. Chem. Soc.-Faraday Trans.* **1991**, *87*, 1601-1609.
223. Patnaik, P., *Handbook of inorganic chemicals*; McGraw-Hill: New York, 2003; Vol. 1, p 1062.
224. Lin, S. S. Y.; Kim, D. H.; Ha, S. Y., Hydrogen production from ethanol steam reforming over supported cobalt catalysts. *Catal. Lett.* **2008**, *122*, 295-301.
225. Perelygin, I. S.; Klimchuk, M. A., Infrared spectra of coordinated pyridine. *Journal of Applied Spectroscopy* **1976**, *24*, 43-46.
226. Zaki, M. I.; Hussein, G. A. M.; Mansour, S. A. A.; El-Ammawy, H. A., Adsorption and surface reactions of pyridine on pure and doped ceria catalysts as studied by infrared spectroscopy. *J. Mol. Catal.* **1989**, *51*, 209-220.
227. Bollinger, M. A.; Vannice, M. A., A kinetic and DRIFTS study of low-temperature carbon monoxide oxidation over Au-TiO_2 catalysts. *Appl. Catal., B* **1996**, *8*, 417-443.
228. Jacobs, G., Low temperature water–gas shift: *in situ* DRIFTS-reaction study of ceria surface area on the evolution of formates on Pt/CeO_2 fuel processing catalysts for fuel cell applications. *Appl. Catal., A* **2003**, *252*, 107-118.
229. Yee, A.; Morrison, S. J.; Idriss, H., A Study of the Reactions of Ethanol on CeO_2 and Pd/CeO_2 by Steady State Reactions, Temperature Programmed Desorption, and *In Situ* FT-IR. *J. Catal.* **1999**, *186*, 279-295.
230. Gangadharan, A.; Shen, M.; Sooknoi, T.; Resasco, D. E.; Mallinson, R. G., Condensation reactions of propanal over $Ce_xZr_{1-x}O_2$ mixed oxide catalysts. *Appl. Catal., A* **2010**, *385*, 80-91.

231. Soykal, I. I.; Sohn, H.; Singh, D.; Miller, J. T.; Ozkan, U. S., Reduction Characteristics of Ceria under Ethanol Steam Reforming Conditions: Effect of the Particle Size. *ACS Catal.* **2014**, *4*, 585-592.
232. Shan, J.-j.; Nguyen, L.; Zhang, S.; Tao, F.-F., Water–Gas Shift on Pd/α-MnO_2 and Pt/α-MnO_2. *Catal. Lett.* **2015**, *145*, 1571-1580.
233. Tao, F. F., Design of an in-house ambient pressure AP-XPS using a bench-top X-ray source and the surface chemistry of ceria under reaction conditions. *Chem. Commun. (Cambridge, U. K.)* **2012**, *48*, 3812-3814.
234. Wang, L.; Zhang, S.; Zhu, Y.; Patlolla, A.; Shan, J.; Yoshida, H.; Takeda, S.; Frenkel, A. I.; Tao, F., Catalysis and *In Situ* Studies of Rh_1/Co_3O_4Nanorods in Reduction of NO with H_2. *ACS Catal.* **2013**, *3*, 1011-1019.
235. Zhu, Y.; Zhang, S.; Ye, Y.; Zhang, X.; Wang, L.; Zhu, W.; Cheng, F.; Tao, F., Catalytic Conversion of Carbon Dioxide to Methane on Ruthenium–Cobalt Bimetallic Nanocatalysts and Correlation between Surface Chemistry of Catalysts under Reaction Conditions and Catalytic Performances. *ACS Catal.* **2012**, *2*, 2403-2408.
236. Song, H.; Zhang, L.; Ozkan, U. S., Investigation of the reaction network in ethanol steam reforming over supported cobalt catalysts. *Ind. Eng. Chem. Res.* **2010**, *49*, 8984-8989.
237. Llorca, J.; Homs, N.; de la Piscina, P. R., *In situ* DRIFT-mass spectrometry study of the ethanol steam-reforming reaction over carbonyl-derived Co/ZnO catalysts. *J. Catal.* **2004**, *227*, 556-560.
238. Zhang, B.; Tang, X.; Li, Y.; Xu, Y.; Shen, W., Hydrogen production from steam reforming of ethanol and glycerol over ceria-supported metal catalysts. *Int. J. Hydrogen Energy* **2007**, *32*, 2367-2373.
239. Saib, A. M.; Moodley, D. J.; Ciobîcă, I. M.; Hauman, M. M.; Sigwebela, B. H.; Weststrate, C. J.; Niemantsverdriet, J. W.; van de Loosdrecht, J., Fundamental understanding of deactivation and regeneration of cobalt Fischer–Tropsch synthesis catalysts. *Catal. Today* **2010**, *154*, 271-282.
240. Petitto, S. C.; Marsh, E. M.; Carson, G. A.; Langell, M. A., Cobalt oxide surface chemistry: The interaction of CoO(100), Co_3O_4(110) and Co_3O_4(111) with oxygen and water. *J. Mol. Catal. A: Chem.* **2008**, *281*, 49-58.
241. Qiu, L.; Liu, F.; Zhao, L.; Ma, Y.; Yao, J., Comparative XPS study of surface reduction for nanocrystalline and microcrystalline ceria powder. *Appl. Surf. Sci.* **2006**, *252*, 4931-4935.
242. Zhang, F.; Wang, P.; Koberstein, J.; Khalid, S.; Chan, S.-W., Cerium oxidation state in ceria nanoparticles studied with X-ray photoelectron spectroscopy and absorption near edge spectroscopy. *Surf. Sci.* **2004**, *563*, 74-82.

243. Burroughs, P.; Hamnett, A.; Orchard, A. F.; Thornton, G., Satellite structure in the X-ray photoelectron spectra of some binary and mixed oxides of lanthanum and cerium. *J. Chem. Soc., Dalton Trans.* **1976**, 1686-1698.
244. Bera, P.; Anandan, C., XRD and XPS studies of room temperature spontaneous interfacial reaction of CeO_2 thin films on Si and Si_3N_4 substrates. *RSC Adv.* **2014**, *4*, 62935-62939.
245. Zhang, C.; Lin, J., Visible-light induced oxo-bridged Zr^{IV}-O-Ce^{III} redox centre in tetragonal ZrO_2-CeO_2 solid solution for degradation of organic pollutants. *Phys. Chem. Chem. Phys.* **2011**, *13*, 3896-3905.
246. Chen, Y.; Zhao, S.; Liu, Z., Influence of the synergistic effect between Co-N-C and ceria on the catalytic performance for selective oxidation of ethylbenzene. *Phys. Chem. Chem. Phys.* **2015**, *17*, 14012-14020.
247. Baek, J. H.; Park, J. Y.; Hwang, A. R.; Kang, Y. C., Spectroscopic and Morphological Investigation of Co_3O_4 Microfibers Produced by Electrospinning Process. *Bull. Korean Chem. Soc.* **2012**, *33*, 1242-1246.
248. Domínguez, M.; Taboada, E.; Idriss, H.; Molins, E.; Llorca, J., Fast and efficient hydrogen generation catalyzed by cobalt talc nanolayers dispersed in silica aerogel. *J. Mater. Chem.* **2010**, *20*, 4875-4883.
249. Chuang, T.; Brundle, C.; Rice, D., Interpretation of the x-ray photoemission spectra of cobalt oxides and cobalt oxide surfaces. *Surf. Sci.* **1976**, *59*, 413-429.
250. Ernst, B.; Bensaddik, A.; Hilaire, L.; Chaumette, P.; Kiennemann, A., Study on a cobalt silica catalyst during reduction and Fischer–Tropsch reaction: *in situ* EXAFS compared to XPS and XRD. *Catal. Today* **1998**, *39*, 329-341.
251. Sexton, B.; Hughes, A.; Turney, T., An XPS and TPR study of the reduction of promoted cobalt-kieselguhr Fischer-Tropsch catalysts. *J. Catal.* **1986**, *97*, 390-406.
252. Kim, M. H.; Choo, K.-H., Low-temperature continuous wet oxidation of trichloroethylene over CoO_x/TiO_2 catalysts. *Catal. Commun.* **2007**, *8*, 462-466.
253. Divins, N. J.; Angurell, I.; Escudero, C.; Pérez-Dieste, V.; Llorca, J., Influence of the support on surface rearrangements of bimetallic nanoparticles in real catalysts. *Science* **2014**, *346*, 620-623.
254. Liu, Z., et al., Ambient pressure XPS and IRRAS investigation of ethanol steam reforming on Ni-CeO(111) catalysts: an *in situ* study of C-C and O-H bond scission. *Phys. Chem. Chem. Phys.* **2016**, *18*, 16621-16628.
255. Óvári, L.; Krick Calderon, S.; Lykhach, Y.; Libuda, J.; Erdőhelyi, A.; Papp, C.; Kiss, J.; Steinrück, H. P., Near ambient pressure XPS investigation of the interaction of ethanol with Co/CeO_2(111). *J. Catal.* **2013**, *307*, 132-139.
256. Binet, C.; Daturi, M.; Lavalley, J.-C., IR study of polycrystalline ceria properties in oxidised and reduced states. *Catal. Today* **1999**, *50*, 207-225.

257. Ebiad, M. A.; Abd El-Hafiz, D. R.; Elsalamony, R. A.; Mohamed, L. S., Ni supported high surface area CeO_2–ZrO_2 catalysts for hydrogen production from ethanol steam reforming. *RSC Adv.* **2012**, *2*, 8145-8156.
258. Levine, S.; Snyder, M. In *Microgravity Cube Lab Experiment Design: Setting New Precedents for Micro-Gravity Testing*, AIAA SPACE 2012 Conference & Exposition, 2012.
259. Ho, C. M.; Yu, J. C.; Kwong, T.; Mak, A. C.; Lai, S. Y., Morphology-controllable synthesis of mesoporous CeO_2 nano- and microstructures. *Chem. Mater.* **2005**, *17*, 4514-4522.
260. Huang, P. X.; Wu, F.; Zhu, B. L.; Gao, X. P.; Zhu, H. Y.; Yan, T. Y.; Huang, W. P.; Wu, S. H.; Song, D. Y., CeO_2 nanorods and gold nanocrystals supported on CeO_2 nanorods as catalyst. *J. Phys. Chem. B* **2005**, *109*, 19169-19174.
261. Liu, L.; Yao, Z.; Deng, Y.; Gao, F.; Liu, B.; Dong, L., Morphology and crystal-plane effects of nanoscale ceria on the activity of CuO/CeO_2 for NO reduction by CO. *Chem. Commun.* **2011**, *3*, 978-989.
262. Yang, Z.; Zhou, K.; Liu, X.; Tian, Q.; Lu, D.; Yang, S., Single-crystalline ceria nanocubes: size-controlled synthesis, characterization and redox property. *Nanotechnol.* **2007**, *18*, 185606.
263. Tok, A. I. Y.; Boey, F. Y. C.; Dong, Z.; Sun, X. L., Hydrothermal synthesis of CeO_2 nano-particles. *J. Mater. Process. Technol.* **2007**, *190*, 217-222.
264. Mai, H. X.; Sun, L. D.; Zhang, Y. W.; Si, R.; Feng, W.; Zhang, H. P.; Liu, H. C.; Yan, C. H., Shape-selective synthesis and oxygen storage behavior of ceria nanopolyhedra, nanorods, and nanocubes. *J. Phys. Chem. B* **2005**, *109*, 24380-24385.
265. Wu, N. C.; Shi, E. W.; Zheng, Y. Q.; Li, W. J., Effect of pH of medium on hydrothermal synthesis of nanocrystalline cerium (IV) oxide powders. *J. Am. Ceram. Soc.* **2002**, *85*, 2462-2468.
266. Sano, T.; Mizukami, F.; Kawamura, M.; Takaya, H.; Mouri, T.; Inaoka, W.; Toida, Y.; Watanabe, M.; Toyoda, K., Crystallization of ZSM-5 zeolite under microgravity. *Zeolites* **1992**, *12*, 801-805.
267. Li, J.-G.; Ikegami, T.; Wang, Y.; Mori, T., Reactive Ceria Nanopowders via Carbonate Precipitation. *J. Am. Ceram. Soc.* **2002**, *85*, 2376-2378.
268. Wu, Z.; Li, M.; Schwartz, V.; Overbury, S. H. In *Shape effect in metal oxide catalysis: Ceria nanoshapes as catalysts and supports*, American Chemical Society: 2013; pp CATL-96.
269. Rivière, J. C.; Myhra, S., *Handbook of surface and interface analysis: methods for problem-solving*; CRC Press, 2009.
270. Leofanti, G.; Padovan, M.; Tozzola, G.; Venturelli, B., Surface area and pore texture of catalysts. *Catal. Today* **1998**, *41*, 207-219.

271. Tauster, S.; Fung, S.; Baker, R.; Horsley, J., Strong interactions in supported-metal catalysts. *Science* **1981**, *211*, 1121-1125.
272. KLANČNIK, G.; Medved, J.; MRVAR, P., Differential thermal analysis (DTA) and differential scanning calorimetry (DSC) as a method of material investigation. *RMZ–Materials and Geoenvironment* **2010**, *57*, 127-142.
273. Höhne, G. W. H.; Hemminger, W.; Flammersheim, H.-J., Theoretical Fundamentals of Differential Scanning Calorimeters. In *Differential Scanning Calorimetry*, Springer: 1996; pp 21-40.
274. Watson, E. S.; O'Neill, M. J.; Justin, J.; Brenner, N., A Differential Scanning Calorimeter for Quantitative Differential Thermal Analysis. *Anal. Chem.* **1964**, *36*, 1233-1238.
275. Harwalkar, V.; Ma, C., Thermal analysis: principles and applications. *Food proteins: Properties and characterization* **1996**, 405.
276. Jae Chul, R.; In, J. C., Structures and properties of silica gels prepared by the sol—gel method. *J. Non-Cryst. Solids* **1991**, *130*, 8-17.
277. Young, S. K., Sol-Gel Science for Ceramic Materials. *Mater. Matters* **2006**.
278. Rahman, I. A.; Padavettan, V., Synthesis of Silica Nanoparticles by Sol-Gel: Size-Dependent Properties, Surface Modification, and Applications in Silica-Polymer Nanocomposites—A Review. *J. Nanomater.* **2012**, *2012*, 1-15.
279. Nair, B. N.; Elferink, W. J.; Keizer, K.; Verweij, H., Sol–gel synthesis and characterization of microporous silica membranes I: SAXS study on the growth of polymeric structures. *J. Colloid Interface Sci.* **1996**, *178*, 565-570.
280. Buckley, A.; Greenblatt, M., The sol-gel preparation of silica gels. *J. Chem. Educ.* **1994**, *71*, 599-602.
281. Trewyn, B. G.; Slowing, I. I.; Giri, S.; Chen, H.-T.; Lin, V. S. Y., Synthesis and Functionalization of a Mesoporous Silica Nanoparticle Based on the Sol–Gel Process and Applications in Controlled Release. *Acc. Chem. Res.* **2007**, *40*, 846-853.
282. Zhang, Q.; Ariga, K.; Okabe, A.; Aida, T., A condensable amphiphile with a cleavable tail as a “lizard” template for the sol-gel synthesis of functionalized mesoporous silica. *J. Am. Chem. Soc.* **2004**, *126*, 988-989.
283. Vacassy, R.; Flatt, R. J.; Hofmann, H.; Choi, K. S.; Singh, R. K., Synthesis of Microporous Silica Spheres. *J. Colloid Interface Sci.* **2000**, *227*, 302-315.
284. Khramov, A. N.; Collinson, M. M., Sol–gel preparation of macroporous silica films by templating with polystyrene microspheres. *Chem. Commun.* **2001**, 767-768.
285. Liu, J.; He, F.; Durham, E.; Zhao, D.; Roberts, C. B., Polysugar-stabilized Pd nanoparticles exhibiting high catalytic activities for hydrodechlorination of environmentally deleterious trichloroethylene. *Langmuir* **2008**, *24*, 328-336.
286. Chen, J.-L.; Al-Abed, S. R.; Ryan, J. A.; Li, Z., Effects of pH on dechlorination of trichloroethylene by zero-valent iron. *J. Hazard. Mater.* **2001**, *83*, 243-254.

287. He, F.; Zhao, D., Hydrodechlorination of trichloroethene using stabilized Fe-Pd nanoparticles: Reaction mechanism and effects of stabilizers, catalysts and reaction conditions. *Appl. Catal., B* **2008**, *84*, 533-540.
288. Díaz, E.; Faba, L.; Ordóñez, S., Effect of carbonaceous supports on the Pd-catalyzed aqueous-phase trichloroethylene hydrodechlorination. *Appl. Catal., B* **2011**, *104*, 415-417.
289. Wei, J.; Qian, Y.; Liu, W.; Wang, L.; Ge, Y.; Zhang, J.; Yu, J.; Ma, X., Effects of particle composition and environmental parameters on catalytic hydrodechlorination of trichloroethylene by nanoscale bimetallic Ni-Fe. *J. Environ. Sci.* **2014**, *26*, 1162-1170.
290. López, E.; Ordóñez, S.; Sastre, H.; Díez, F. V., Kinetic study of the gas-phase hydrogenation of aromatic and aliphatic organochlorinated compounds using a Pd/Al_2O_3 catalyst. *J. Hazard. Mater.* **2003**, *97*, 281-294.
291. Ordóñez, S.; Díez, F. V.; Sastre, H., Catalytic hydrodechlorination of chlorinated olefins over a Pd/Al_2O_3 catalyst: kinetics and inhibition phenomena. *Ind. Eng. Chem. Res.* **2002**, *41*, 505-511.
292. Chen, N.; Rioux, R. M.; Barbosa, L. A.; Ribeiro, F. H., Kinetic and theoretical study of the hydrodechlorination of $CH_{4-x}Cl_x$ (x = 1-4) compounds on palladium. *Langmuir* **2010**, *26*, 16615-16624.